Spectrum Sharing between Radar and Communication Systems

Awais Khawar

Dissertation submitted to the Faculty of the
Virginia Polytechnic Institute and State University
in partial fulfillment of the requirements for the degree of

Doctor of Philosophy
in
Electrical Engineering

Charles Clancy, Chair
Jeffrey Reed
Michael Roan
Robert McGwier
Sandeep Shukla

June 22, 2015
Arlington, Virginia

Keywords: spectrum sharing, MIMO radar, null steering, radar waveform design, channel modeling

Spectrum Sharing between Radar and Communication Systems

Awais Khawar

ABSTRACT

Radio frequency spectrum is a scarce natural resource that is utilized for many services including surveillance, navigation, communication, and broadcasting. Recent years have seen tremendous growth in use of spectrum especially by commercial cellular operators. As a result, cellular operators are experiencing a shortage of radio spectrum to meet bandwidth demands of users. Spectrum sharing is a promising approach to solve the problem of spectrum congestion as it allows cellular operators access to more spectrum in order to satisfy the ever growing bandwidth demands of commercial users. The US spectrum regulatory bodies are working on an initiative to share 150 MHz of spectrum, held by federal agencies, in the 3.5 GHz band with commercial wireless operators. This band is primarily used by radar systems that are critical to national defense. Field tests have shown that spectrum sharing between radars and communication systems require large separation distance in order to protect them from harmful interference. Thus, novel methods are required to ensure spectrum sharing between the two systems without the need of large protection distances.

In order to efficiently share spectrum between radars and communication systems at the same time and in the same geographical area, a novel method is proposed that transforms radar signal in such a way that it does not interfere with communication systems. This is accomplished by projecting the radar signal onto null space of the wireless channel between radar and communication system. In order to understand the effects of the proposed sharing mechanism – in urban, sub-urban, and littoral areas – new channel models, specifically, two- and three-dimensional channel models are designed that capture azimuth and elevation angles of communication systems and helps in placing accurate nulls. In addition, interference coming from communication systems into radar receivers is analyzed and radar performance is accessed. Using this information, resource allocation schemes are designed for communication systems that take advantage of the carrier aggregation feature of the LTE-Advanced systems. This further helps in dynamic sharing of spectrum between radars and communication systems. The proposed signal projection approach not only meets radar objectives but also meets spectrum sharing objectives. However, there is a trade-off as signal projection results in some performance degradation for radars. Performance metrics such as probability of target detection, Cramer Rao bound and maximum likelihood estimate of target's angle of arrival, and beampattern of radar are studied for performance degradation. The results show minimal degradation in radar performance and reduction in exclusion zones, thus, showing the efficacy of the proposed approach.

Preface

All praise is due to Allah, the All Knowing, the Wise

"And of Knowledge, you (mankind) have been given only a little"

[Verse 85, Chapter 17, The Holy Quran]

Acknowledgments

This doctoral dissertation, a milestone in my career, would not have been possible without the help and support of many mentors, lab-mates, friends, and family members over the past three and a half year. I would like to take this opportunity to express my gratitude and appreciation to them.

First and foremost, I would like to thank the Almight Allah for giving me strength and wisdom to pursue PhD studies. Next, I would like to thank my PhD adviser Dr. Charles Clancy for giving me a great research topic to work on. His continuous support, guidance, and liberty to explore new research areas is highly appreciated. I would also like to thank my PhD advisory committee members for their valuable suggestions and feedback to improve quality of my dissertation. I am also very grateful to my funding sources including Defense Advanced Research Projects Agency (DARPA), USA, and NWFP University of Engineering and Technology, Pakistan, for financially supporting portions of my graduate studies.

Additionally, I would like to thank Dr. Ahmed Abdelhadi, previously a Postdoctoral Researcher and now a Research Scientist at Hume Center, with whom I have co-authored many papers, for his help and support. I also wish to express gratitude to my lab-mates Ms. Haya Shajaiah (co-author on one paper), Ms. Jasmin Mahal (co-author on one paper), and Dr. Chowdhury Shahriar. It was a fruitful and great experience working with them.

Moreover, I am very fortunate to find very knowledgeable, helping, supporting, and loving friends during my graduate studies. I would like to thank Dr. Waseem Ansar Malik (APL), Dr. Hamza Shakeel (NIST), Dr. M. Akbar, Mr. Tamoor Gandapur (Samsung), and Mr. Shafiq Ur Rahman for the memorable experiences. I would also like to thank my friends and their families in Northern Virginia for making my social life very enjoyable and memorable.

Finally, I thank all my family members for their love and support. I am very grateful to my beautiful wife, Sana Awais, for her unending love, support, and encouragement, and for making my life very manageable and happy throughout my PhD studies. I would like to thank my parents, Khawar and Sajida, for encouraging me to pursue higher education and their never ending support and love. I would also like to acknowledge the continuous support of my brother and sister, uncles and aunts, father-in-law, mother-in-law, and brothers-in-law.

Dedication

To my Parents, my beloved wife Sana, and our beautiful daughter Raneem.

Contents

List of Figures

List of Algorithms

List of Tables

Chapter 1

Introduction

Radio frequency spectrum is a scarce natural resource that is utilized for many services including surveillance, navigation, communication, and broadcasting. The RF spectrum upto 6 GHz is considered as prime spectrum due to its favorable propagation properties. Due to this reason this portion of RF spectrum is heavily congested as numerous federal and commercial systems are deployed, as shown in Figure 1.1. Recent years have seen tremendous growth in use of spectrum especially by commercial cellular operators. Ubiquitous use of smartphones and tablets is one of the reasons behind an all-time high utilization of spectrum. As a result, cellular operators are experiencing a shortage of radio spectrum to meet bandwidth demands of users. On the other hand, spectrum measurements have shown that much spectrum – not held by cellular operators – is underutilized even in dense urban areas. This has motivated shared access to spectrum by secondary systems with no or minimal impact to incumbent systems. Spectrum sharing is a promising approach to solve the problem of spectrum congestion as it allows cellular operators access to more spectrum in order to satisfy the ever growing bandwidth demands of commercial users.

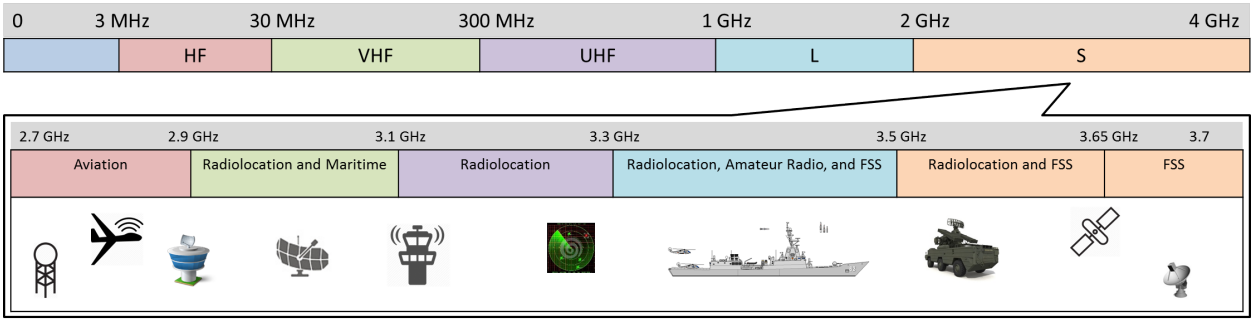

User	0 – 300 MHz	300 MHz – 1 GHz	1 GHz – 2 GHz	2 GHz – 4 GHz
Federal	Tactical and non-tactical mobile communications Mobile-satellite communications Air traffic control communications	Instrument Landing System (ILS) Mobile-satellite communications Space research Meteorological aids Earth exploration-satellite Meteorological-satellite Radio astronomy Enhanced Position Location Reporting System (EPLRS) Public Safety Perimeter protection radars Wind profiler radars RFID for container tracking and port security Low-capacity voice and/or data point-to-point and point-to-multipoint microwave communication Aeronautical radio navigation service (ARNS) Distance Measuring Equipment (DME) Tactical Air Navigation (TACAN) system	Distance Measuring Equipment (DME) Tactical Air Navigation (TACAN) system Air Traffic Control Radar Beacon System (ATCRBS) Identification Friend or Foe (IFF) System Global Navigation Satellite System (GNSS) Positioning, Navigation, and Timing (PNT) Joint Tactical Information Distribution System (JTIDS) Air traffic control (ATC) in the national airspace, border surveillance, early warning missile detection, and drug interdiction Ship-to-ship communication systems, nuclear burst detection system, remote sensing, and radio astronomy Passive remote sensing of ocean salinity and soil moisture content Medical telemetry devices Aeronautical mobile telemetry (AMT) Deep Space Network system	Tracking Data and Relay Satellite System (TDRSS) Military research, law enforcement video surveillance, control of robotic systems for explosive ordnance neutralization and disposal, and the testing of robotic ground vehicles Aeronautical telemetry Aeronautical mobile telemetry (AMT) Flight test missions Flight testing of aircraft, missiles, or major components Video link operations from the land mobile robot to the human control station, thus dealing with unexploded ordnance safely for explosive ordnance disposal Air-to-ground-to-air communication, flight telemetry, point-to-point data links, and ship-to-shore communication Airport surveillance radar (ASR) systems and meteorological radars such as Next Generation Weather Radar (NEXRAD) Maritime radio navigation Shipborne, land-based, and aeronautical mobile radar systems used for fleet air defense, missile and gunfire control, bomb scoring, battlefield weapon locations, air traffic control, and range safety Satellite earth stations
Non-Federal	AM and FM broadcast TV RFID Amateur Radio	ZigBee DECT/Cordless telephone GPS GSM UMTS LTE/LTE-A WLAN Bluetooth BAN/WBAN/BSN UWB Modern Cordless telephone		

Figure 1.1: Spectrum occupancy and utilization by federal and commercial users

1.1 Motivation and Background

Recent studies by the US spectrum regulatory bodies, Federal Communications Commission (FCC) and the National Telecommunications and Information Administration (NTIA), have noticed that huge chunks of spectrum held by federal agencies have low average utilization, especially in urban areas. On the other hand, spectrum held by commercial operators, including cellular operators, have heavy utilization in urban areas than federal agencies. The demands for bandwidth from wireless operators have led to proposals to reduce or share spectrum allocated for federal radar operations [1, 2]. In order to efficiently utilize spectrum currently in-use by federal agencies, FCC and NTIA are working on an initiative to share 150 MHz of spectrum, held by federal agencies, in the band 3550–3700 MHz with commercial

Radar-Mount	Type	Receiver Noise Level (dBm)	I/N Criteria (dB)	Interference Threshold (dBm)	Radar to BS (km)			Radar to UE (km)	BS/UE to Radar (km)	
					EC	WC	GC		WiMAX Systems	LTE Small Cells
Shipborne	1	-108	-6	-114	361	343	339	68 (EC)	310 (GC)	77% reduction in the size of exclusion zones
	2	-95	-6	-101	154	235	106	32 (EC)	45 (WC)	
	3	-94	-6	-100	224	286	200	47 (WC)	53 (WC)	
	4	Not Available			448	404	458	143 (GC)	305 (EC)	
	5	Not Available			455	415	557	309 (GC)	N/A	
Ground-based	1	-103	-6	-109	40			<1	24	1
	2	-100	15	-85	<1			<1	<1	
	3	-96	-6	-102	63			3.5	32	
Airborne	1	-92.5	30	-62.5	<1			<1	<1	<<1
	2	-100	40	-60	<1			<1	<1	

Figure 1.2: Statistics of exclusion zones required in the 3.5 GHz band to protect radar and WiMAX BSs/small cells from each other's harmful interference.

wireless operators [3]. This band is primarily used by the Department of Defense for air, ground, and shipborne radar systems that are critical to national defense, see Figure 1.2. More spectrum for commercial operators will result in huge economic and social prospects for the nation. However, field tests have shown that spectrum sharing between radars and WiMAX systems require large separation distance in order to protect them from harmful interference that may compromise sensitive or classified information or operations of federal incumbents [4]. This is due to high signal power used by radars and high-peak sidelobes which saturate communication system receivers, which are traditionally designed to handle power levels in watts rather than kilo watts or mega watts. Such high peak powers are typical of airport surveillance radars, weather radars, and military phased array radars such as SPY-1 radar of Aegis system. On the other hand, due to highly sensitive radar receivers, see Figure 1.2, designed to detect even the faintest of returned signal, has in the past mandated for exclusive rights to radio spectrum allocations since its operation can be affected by commercial wireless system interference [5]. This excludes large population of the US,

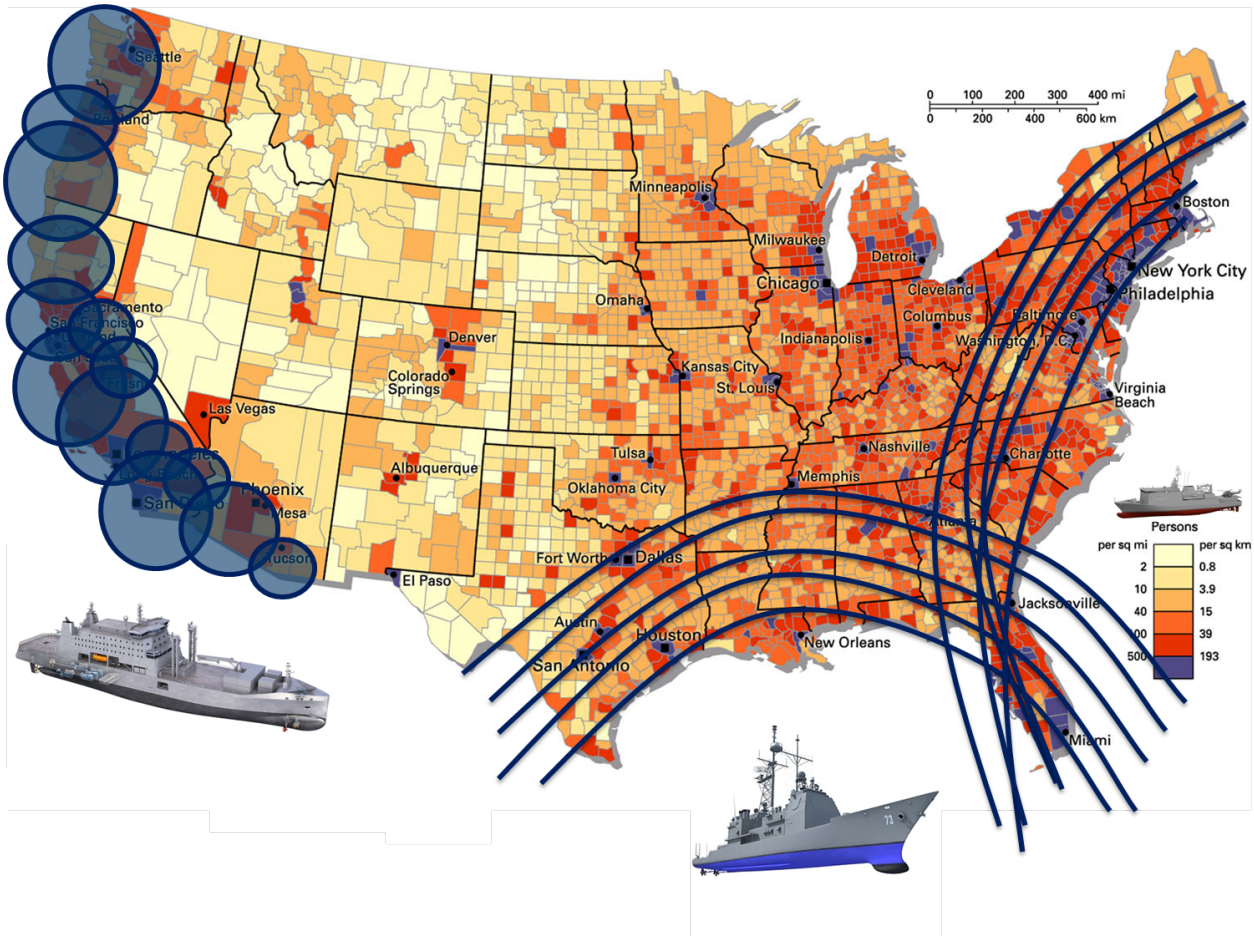

Figure 1.3: Exclusion zones required to protect radar and WiMAX systems from each other's harmful interference.

approximately 60%, from reaping benefits of spectrum sharing and has little to no business value for commercial operators, see Figure 1.3. These exclusion zones can be considerably reduced if low power small cells are deployed instead of high power WiMAX base stations. Studies have reported upto 77% reduction in the size of exclusion zones with this configuration but still excludes approximately 40% of the US population. This can be seen in Table 1.2. However, the need for exclusion zones in not eliminated by this approach. Thus, novel methods are required to ensure spectrum sharing between the two systems without the need of large protect distances.

1.2 Regulatory Efforts to Share Radar Spectrum

Spectrum sharing between radars and communication systems is an important cross-disciplinary research area of federal and commercial interest. In March 2010, the National Broadband Plan recommended that the FCC and NTIA work together to identify spectrum that can be used for wireless broadband services on an exclusive, shared, licensed, and/or unlicensed basis. In addition, the FCC make 500 MHz of spectrum available by 2020, with 300 MHz to be made available by 2015 [1]. This was followed by a Presidential Memorandum which directed NTIA to collaborate with the FCC to make available 500 MHz of Federal spectrum for commercial wireless services [6]. In compliance with the Presidential directive, NTIA in its *Fast Track* Report identified a number of bands compatible for commercial utilization including the 3500-3650 MHz band which is primarily used by federal radar systems [4].

The 3550-3650 MHz band, currently used for military and satellite operations, is a possible candidate for spectrum sharing between military radars and broadband wireless access (BWA) communication systems such as LTE and WiMAX, according to the NTIA's 2010 Fast Track Report [4]. Electromagnetic interference to military radar operations is expected from spectrum sharing. However, one simply can't relocate these federal radar systems to other bands since the nature of the said band contains many frequencies which work best for highly sensitive fixed, airborne, and maritime radar systems and are essential for superior performance. Moreover, cost to relocate can be unbearable. The problem of EMI mitigation is possible due to advancements in transmitter and receiver design technology, of cellular systems, which has made real-time spectrum reassignment possible.

In the past, it has been made possible for wireless systems to share government bands such that they operate under a low-power constraint in order to protect incumbents from interference. Example includes: Wi-Fi and Bluetooth in the 2450-2490 MHz band, wireless

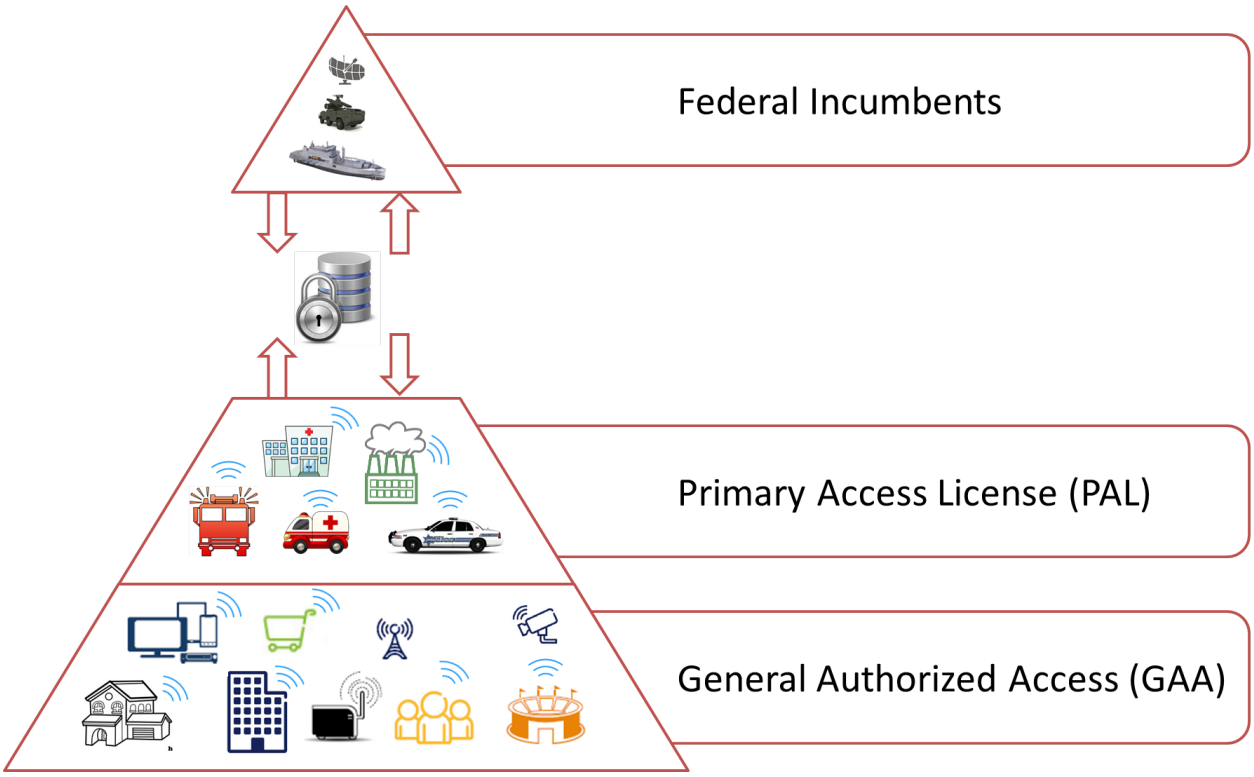

Figure 1.4: FCC's spectrum sharing hierarchy: FCC proposes to use the 3.5 GHz band in a hierarchical manner where federal incumbents, primary access license (PAL) holders, and general authorized access (GAA) users coordinate through a spectrum access system (SAS) for channel assignment.

local area network (WLAN) in the 5.25-5.35 and 5.47-5.725 GHz radar bands [7], and recently the FCC has proposed small cells, i.e. wireless base stations operating on a low power, to operate in the 3550-3650 MHz radar band [3]. FCC proposes to use the 3.5 GHz band in a hierarchical manner where federal incumbents, primary access license (PAL) holders, and general authorized access (GAA) users coordinate through a spectrum access system (SAS) for channel assignment. This hierarchy is shown in Figure 1.4.

1.3 State-of-the-art in Spectrum Sharing

In this section, state-of-the-art approaches for spectrum sharing are discussed in the context of radar and communication systems.

1.3.1 Waveform Shaping

In spectrum sharing perspective between radars and communication systems, EMI needs to be mitigated at both the systems. Communication systems due to their advancements give more freedom to mitigate interference from radar systems. For example, in order to counter radar interference on WiMAX systems, interference mitigation in four domains namely space, time, frequency, and system-level modification is proposed by Lackpour et. al. [8]. Radar systems due to their sensitivity are more susceptible to interference from communication systems. So far, as previously discussed, in order to protect radar operations, communication systems operate on a low-power basis to avoid interference to radars or operate by sensing the availability of radar channel at a power level which doesn't exceed the allowed interference limit [7, 9].

Radar systems are also evolving, with recent trend in design of MIMO radars and cognitive radars, radar systems are becoming more resilient in handling interference and jamming as they are more aware about their radio environment map (REM). This has motivated researchers to propose beamforming approaches to mitigate interference from wireless communication systems to MIMO radar [10]. In addition, spatial domain can also be used to mitigate MIMO radar interference to wireless communication system. One such technique was proposed by Shabnam et al. [11] which projected radar signal onto null space of interference channel between MIMO radar and MIMO communication system. Moreover, radar

waveforms can also designed such that they don't cause interference to cellular systems, in addition to meeting their mission objectives [12].

1.3.2 Waveform Design

The problem of waveform design for MIMO radars has gained considerable attention in the last few years. This is due to the fact that MIMO radars allow to transmit a very diverse set of waveforms through each transmit element independently, thus providing extra degrees of freedom (DoF). In contrast, a phased array radar transmits waveforms that are correlated in phase or time. This capability of MIMO radar gives it superiority over phased array radars when it comes to target's spatial diversity and resolution [13]. Moreover, with the help of extra DoF an efficient transmit beampattern or waveform can be designed.

One way to design desired MIMO radar waveform is by synthesis of covariance matrix of waveform. This is also known as beampattern matching problem where the actual beams are matched to the desired beams. A practical constraint in design of radar waveform is for them to have constant envelope (CE) property in order to allow radio frequency amplifiers operate at maximum efficiency. Therefore, in practical systems, waveforms with the CE property are desirable.

Waveforms with constant-envelope (CE) are very desirable, in radar and communication system, from an implementation perspective, i.e., they allow power amplifiers to operate at or near saturation levels. CE waveforms are also popular due to their ability to be used with power efficient class C and class E power amplifiers and also with linear power amplifiers with no average power back-off into power amplifier. As a result, various researchers have proposed CE waveforms for communication systems; for example, CE multi-carrier modulation waveforms [14], such as CE orthogonal frequency division multiplexing (CE-OFDM) wave-

forms [15]; and radar systems, for example, CE waveforms [16], CE binary-phase shift keying (CE-BPSK) waveforms [17], and CE quadrature-phase shift keying (CE-QPSK) waveforms [18].

Transmit beampattern design problem, to realize a given covariance matrix subject to various constraints, for MIMO radars is an active area of research; many researchers have proposed algorithms to solve this beampattern matching problem. Fuhrmann et al. proposed waveforms with arbitrary cross-correlation matrix by solving beampattern optimization problem, under the constant-modulus constraint, using various approaches [19]. Aittomaki et al. proposed to solve beampattern optimization problem under the total power constraint as a least squares problem [20]. Gong et al. proposed an optimal algorithm for omnidirectional beampattern design problem with the constraint to have sidelobes smaller than some predetermined threshold values [21]. Hua et al. proposed transmit beampatterns with constraints on ripples, within the energy focusing section, and the transition bandwidth [22]. However, many of the above approaches don't consider designing waveforms with finite alphabet and constant-envelope property, which is very desirable from an implementation perspective. Ahmed et al. proposed a method to synthesize covariance matrix of BPSK waveforms with finite alphabet and constant-envelope property [17]. They also proposed a similar solution for QPSK waveforms but it didn't satisfy the constant-envelope property. A method to synthesize covariance matrix of QPSK waveforms with finite alphabet and constant-envelope property was proposed by Sodagari et al. [18].

1.3.3 Interference Modeling

Spectrum sharing promises huge economic and social prospects but also brings in new challenges for the optimal operation of incumbents and commercial users, from a harmful in-

terference perspective. In order to analyze the interference coming from communication systems into radar systems an accurate model for the distribution of aggregate interference is required. This also helps in cellular system planning to reduce the harmful effects of interference and ensures performance of both cellular and radar systems. In determining a model of aggregate interference, from cellular system, several factors need to be considered which includes their spatial distribution, total number of transmitters, power control, and channel parameters. In wireless communications, interference is usually characterized by sum of log-normal random variables. This is why the distribution of sum of log-normal random variables has been an active topic of research since 1960s [23]. Since then, many people have used approximation techniques to approximate distribution of log-normal sums. Some of the most commonly used approximation methods include Wilkinson's [24], a moment matching approach for the first two moments, and Schwartz and Yeh's exact first two moment expressions for a sum of two log-normal random variables. In the context of cellular communications, aggregate interference has been approximated using various approximations and moment matching techniques, see [25] and references therein. The authors in [26], propose an exclusion-region and secondary-user-density based model to share spectrum between an aeronautical radar, operating in the 960-1215 MHz band, and indoor femto cell users. The operation of femto cell users is limited by the interference threshold established by the central network in order to protect the radar.

1.3.4 Channel Modeling

Channel modeling for wireless communications is a fundamental area of research as it allows performance evaluation of transmission techniques. A comprehensive introduction to SISO and MIMO wireless channel modeling, propagation modeling, and statistical description of channels can be found in [27] and references there in. However, the efforts so far have been

limited to model channels between wireless communication systems and to the best of my knowledge no work exists on channel modeling between wireless communication and radar systems. In order to study performance evaluation and interference mitigation techniques in a spectrum sharing scenario between radar and communication systems the problem of channel modeling is of prime importance. Traditionally, wireless channel models have been designed to capture azimuth i.e. 2D channels. A comprehensive introduction to 2D wireless channel modeling, propagation modeling, and statistical description of channels can be found in [27] and references there in. Recently, there has been a surge in modeling wireless channels that capture both the azimuth and elevation directions known as 3D channels. 3D channels allow very precise beamforming for users on ground and in buildings. As a result wireless research community is heavily involved in designing and standardizing 3D channel models that can reap the benefits of both the azimuth and elevation beamforming [28]. However, efforts so far have been limited to model 3D channels between wireless communication systems and to the best of my knowledge no work exists on 3D channel modeling between wireless communication and radar systems. A 3D channel model can enable radar systems to place accurate nulls in azimuth and elevation angles of BSs in order to mitigate radar interference. Therefore, in order to study performance evaluation and interference mitigation techniques in a spectrum sharing scenario, the problem of 3D channel modeling is of prime importance.

1.3.5 Resource Allocation

Optimal allocation of resources has been a classical problem in communication systems. This problem has gained renewed interest in modern cellular systems. For example, a new feature, carrier aggregation, was added to the 3GPP LTE standard in Release 10 [29]. With the inclusion of this new feature LTE is now refereed to as LTE Advanced or 4G-LTE, two terms used interchangeably. Carrier aggregation allows users to employ multiple carriers to achieve

higher bandwidth. The carrier aggregation approach can exploit the highly segmented spectrum and provide higher bandwidth to users running multiple applications. This feature of LTE Advanced can also be used to share spectrum with radar systems by using resource allocation with the aggregation of LTE Advanced and radar bands. A utility proportional fairness resource allocation approach is proposed in [30]. Users with elastic and inelastic traffic are considered. Each user application is represented by a utility function based on the user application type. Delay-tolerant applications are presented by logarithmic utility function whereas real-time applications are presented by sigmoidal-like utility functions. A tractable optimal solution to the optimization problem exists as the authors have proven that the optimizations problem is convex. Additionally, a resource allocation algorithm is proposed by the authors to allocate the eNodeB resources optimally among users. No user is allocated zero rate by the algorithm. This was achieved by using a proportional fairness approach to guarantee a minimum QoS to each user even in the case of scarce resources. A resource allocation optimization problem with carrier aggregation is formulated in [31]. The proposed resource allocation algorithm allocates the primary carrier resources optimally among users. It then starts allocating the secondary carrier resources optimally among users based on the user utility functions and the optimal rate allocated to that user by the primary carrier. The final optimal rate allocated to each user is the aggregated rates given by both the primary and secondary carriers. The algorithm uses proportional fairness approach to guarantee that no user is allocated zero rate.

In [32], the authors introduced a bandwidth proportional fairness algorithm. The algorithm is an iterative process that allows users to bid for resources until the allocated rate is almost equivalent to the optimal rate. The algorithm determines the price that the user should pay for its allocated resources. In [33], the authors used sigmoidal-like utility functions to represent real-time applications. An optimization problem is formulated in [34] and

[35] to allocate the network resources optimally among real-time applications. In [36], a resource allocation optimization problem is presented for two groups of users. The first group is a public safety users group and the second one is a commercial users group. Each user is running either delay-tolerant or real-time application at a time and each public safety user application is assigned an application target rate. The proposed algorithm gives priority to public safety users when allocating the eNodeB resources. Once each public safety user is allocated its application target rate the algorithm starts allocating the remaining eNodeB resources among all users based on proportional fairness approach. In [37], the authors presented a resource allocation algorithm to allocate the eNodeB resources optimally among VIP users and regular users running multiple applications. The rate allocation algorithm is a two cases algorithm. The fist case is performed when the eNodeB available resources does not exceed the total VIP users applications target rates whereas the second case is performed when it exceeds that total. Each case is a two-stage algorithm, In the first stage the eNodeB allocates optimal rates to multi-application users subscribing for a service based on the user type, the user applications types and the applications target rates. In the second stage, each UE allocates the rate assigned to it by the eNodeB optimally among its applications. An optimal rate allocation algorithm is presented in [30], [38] and [39] to allocate a single carrier resources optimally among mobile users. Users applications are delay-tolerant applications and real-time applications presented by logarithmic utility functions and sigmoidal-like utility functions, respectively. A rate allocation optimization problem using a proportional fairness approach is considered to allocate the eNodeB resources optimally among users with a minimum QoS given to each user when allocating resources.

In the past, cellular networks were dominated by voice-only traffic. However, in recent years, there has been a significant growth in the amount of multimedia-rich traffic over cellular networks. In order to support such traffic, networks require higher data rates which can

be achieved by using higher modulation schemes. This is the reason current and emerging cellular standards are supporting various higher modulation schemes. For example, Long term evolution (LTE), the fourth-generation (4G) wireless standard specified by 3rd Generation Partnership Project (3GPP), supports higher modulation schemes such as QPSK, 16-QAM, and 64-QAM according to 3GPP Release 10 or more commonly known as LTE-Advanced (LTE-A). The next evolution of LTE – LTE Release 12 and beyond – also refereed to as LTE-B supports higher modulation schemes upto 256-QAM [40, 41]. Higher modulation schemes require higher transmit power to achieve a certain signal-to-noise ratio (SNR) which can guarantee minimum successful transmission probability of packets. This motivates numerous research efforts to optimally allocate power for users seeking better quality-of-service (QoS), where QoS can be the minimum successful transmission probability of packets. In a cellular network, different users can run different services, requiring different modulation schemes, and thus can have different power and QoS requirements.

One aspect of improving power allocation and achieving better QoS is to use network utility maximization framework. This framework was first explored by the seminal works of Kelly et al. [42] and Low et al. [43] for wired networks, such as the Internet, and later by Marbach et al. [44] and Lee et al. [35] for wireless networks, such as Code Division Multiple Access (CDMA)-based systems. The utility function can be considered as a controlling parameter through which a user's QoS can be guaranteed. In this treatment, each user's utility function is a function of its power allocation and the goal is to allocate powers in order to maximize network utility, which is defined as a product of all users' utilities. The traditional approaches to model network utility maximization problem is by the summation of users' utility functions [44][35]. However, such a formulation can drop users in order to maximize system performance and thus all users are not treated fairly, as an example consult [35].

A utility function is a representation of QoS of a user. For example, utility functions have been defined to maximize signal-to-interference-plus-noise ratio (SINR) [35], Shannon capacity [45], ratio of throughput to transmit power [46] etc. Thus, the type of utility function represents each user's QoS characteristics and it is possible that in a network supporting different services one has to deal with various types of utility functions. The shape of a utility function depends upon the characteristics of service it is representing and thus can have many shapes including concave, convex, sigmoidal-like or S-shaped, and inverse-S-shaped [47]. The optimality of the solution of network utility maximization problem depends upon the shape of a utility function. For example, services represented by concave utility functions satisfy the convexity conditions of network utility maximization problem, when it is represented by sum of users' utility functions, and thus yields optimal solution. This is not the case for non-concave utility functions. Moreover, algorithms proposed for downlink power allocation are utility function specific and can't be generalized to other utility functions due to the various shapes a utility function can take. Thus, an algorithm can be optimal for one class of utility functions and at the same time sub-optimal for other classes of utility functions.

This work considers sigmoidal-like, or S-shaped, utility functions, which are first convex and then concave, for network utility maximization problem because QoS criterion is probability of successful packet transmission and its cumulative distribution function is also S-shaped i.e. first convex and then concave. Thus, sigmoidal-like utility function is a natural choice to represent probability of successful packet transmission which can be a function of SINR [35] or signal-to-interference ratio (SIR) [48].

The wireless broadcast channel is random in nature and users experience independent and heterogeneous communication environment. In such a challenging propagation environment it is difficult to design resource allocation algorithms that maximize system efficiency, ensure fairness, and meet QoS requirements of all users. For example, in order to improve system

efficiency, opportunistic resource allocation algorithms are used [49]. These algorithms favor users with whom they share good channel quality or those typically closer to the base station (BS), and tend to avoid users that are in deep-fade or the ones at cell edges. Despite of maximizing system efficiency such algorithms fail to (a) satisfy QoS requirements of users and (b) maintain fair allocation of resources among users. This can be avoided by fair allocation of resources among all users and thus utility proportional fairness problems are of more interest [50].

Pricing can be used as a control measure by network providers i.e. users can be motivated to make rational decisions on the usage of network resources in order to maximize network utility. It has been successfully applied to control congestion in the Internet [51] and rate and power in wireless networks [52, 53]. In network utility maximization problems it is typical of network providers to set shadow prices for its resources.

In [54], the authors consider a proportional fairness scheduling problem in a network supporting different users' modulation schemes. However, their approach is limited since they propose a two-user opportunistic proportional fairness scheduling and utility maximization problem. Their algorithm for opportunistic proportional fairness scheduling is optimal but for utility maximization their proposed algorithm is suboptimal.

Lee et al. consider a downlink utility-based power allocation algorithm for Code Division Multiple Access (CDMA)-based systems in [35]. The algorithm maximizes the total system utility but can drop users to maximize the overall system utilization, therefore, it does not guarantee minimum QoS for all users. Moreover, they use an approximation to solve non-concave sigmoidal-like utility maximization problem which is Pareto optimal. An alternate approach to approximate concave and non-concave utility functions using minimum mean-square error was proposed by [34]. The approximated utility function is used to solve

the power allocation problem using a modified version of the distributed power allocation algorithm presented in [42]. The same problem is considered by Tychogiorgos et al. with a non-convex optimization formulation for maximization of utility function [55, 56]. The proposed algorithm solves the problem when the duality gap is zero but doesn't converge to the optimal solution for a positive duality gap.

evolved NodeB (eNodeB) can also be used to allocate powers fairly among users by taking into account user positions. This utility proportional fairness problem can achieve QoS targets both in terms of fairness and throughput [57]. In addition, the authors have shown that their signal-to-interference-plus-noise ratio (SINR)-based fair power allocation algorithm, which starts from the cell-edge users and converges to the center, can achieve maximum sum rate and optimal fairness. On the other hand, an alternate approach to improve the throughput for the cell-edge user, an uplink power control and resource allocation scheme is considered in [58]. The algorithm takes into account the interference to and from adjacent cells. It first allocates resources independently among the cells and then adjusts resources and powers for the center users based on resource allocation and users' position among adjacent cells. In [59], the authors propose a utility max-min fairness power allocation for users with elastic and real-time traffic sharing a single path in the network. In [60], the authors proposed a utility proportional fair optimization formulation for high-SINR wireless networks using a utility max-min architecture. They compare their algorithm to the traditional bandwidth proportional fair algorithms [61] and present a closed form solution that prevents oscillations in the network.

In [62, 63], the authors consider downlink power allocation for semi-elastic applications, for example video conferencing, in 4G cellular networks using a sigmoidal-like utility function. They consider a utility maximization problem over multiple time slots since their algorithm allocates powers and subcarriers in each time slot in order to optimize average user utility

over time by an exchange of price and demand among users, the network, and an intermediate power allocation module. A similar network utility maximization problem for video streaming over cellular networks, for both uplink and downlink, is considered in [64]. The authors consider a joint optimization of video and network resources to maximize total video reception quality of a limited number of users without interrupting the service of other voice users. the convergence of their algorithms.

1.4 Contributions

In order to efficiently share spectrum between radars and communication systems at the same time and in the same geographical area, a novel method is proposed that transforms radar signal in such a way that it does not interfere with communication systems. This is accomplished by projecting the radar signal onto null space of the wireless channel between radar and communication system. Basically, nulls are formed in radar beampattern in the direction of communication systems. Previous approaches either allow spectrum sharing in time or space but not both. In order to understand the effects of the proposed sharing mechanism – in urban, sub-urban, and littoral areas – new channel models are designed keeping in view the different antenna geometries of radar and communication systems. In this regard two- and three-dimensional channel models are designed that capture azimuth and elevation angles of communication systems and helps in placing accurate nulls. In addition, interference coming from communication systems into radar receivers is analyzed and radar performance is accessed. Using this information, resource allocation schemes are designed for communication systems that take advantage of the carrier aggregation feature of the LTE-Advanced systems. This further helps in dynamic sharing of spectrum between radars and communication systems.

The proposed signal shaping/design approach not only meets radar objectives but also meets spectrum sharing objectives. However, there is a tradeoff as signal shaping or designing new radar signal, with spectrum sharing constraint, results in some performance degradation for radars. Therefore, it is of interest to study the impact of projection on radar performance. Performance metrics such as probability of target detection, Cramér Rao bound and maximum likelihood estimate of target's angle of arrival, and beampattern of radar are studied for performance degradation. The results show minimal degradation in radar performance and reduction in exclusion zones, thus, showing the efficacy of the proposed approach. At the same time, resource allocation schemes benefit from extra spectrum provided by radars, thus, resulting in capacity gains for communication systems.

An outline of area-wise contributions made in this research is as follows.

1.4.1 Waveform Shaping

In this area, the following contributions are made:

- A spectrum sharing environment in which MIMO radar is sharing spectrum with a single MIMO communication system is considered [11]. For this model, a projection algorithm to project radar waveform onto null space of interference channel is proposed which guarantees zero interference to communication system.

- The above spectrum sharing scenario is modified and instead of one, multiple MIMO communication systems or cellular system is considered and a new projection algorithm is proposed for this case [65].

- In order to evaluate radar performance, when its waveform is subject to projection or shaping, probability of target detection [66], Cramér Rao bound and maximum

likelihood estimates of target's angle of arrival [67], and beampatterns [68] are studied.

1.4.2 Waveform Design

In this area, the following contributions are made:

- Finite alphabet binary phase shift keying (BPSK) waveforms are designed with spectrum sharing constraints. Waveforms are designed for both moving and stationary MIMO radars in a way that radar doesn't cause interference to cellular systems [12].
- Finite alphabet quadrature phase shift keying (QPSK) waveforms are designed with spectrum sharing constraints. Waveforms are designed for both moving and stationary MIMO radars in a way that radar doesn't cause interference to cellular systems [69].
- It is shown that it is possible to design finite alphabet constant envelope QPSK waveforms [69]. This is of practical importance in both radar and communication systems.

1.4.3 Interference Modeling

In this area, the following contributions are made:

- It is shown that interference originating from cellular systems in a correlated fading environment has a log-normal distribution [70].
- Using the above information, the impact of cellular interference on radar's probability of missing a target is studied under various operating conditions [70].

1.4.4 Channel Modeling

In this area, the following contributions are made:

- Two-dimensional (2D) channel model between MIMO radar and MIMO communication system is designed by considering a 1D antenna array at both the radar and cellular system. Using the proposed 2D channel model the efficacy of eigen-nulling over spatial-nulling, for radar interference mitigation at cellular systems, is demonstrated [71].
- Power received at communication system in 2D line-of-sight (LoS) channel model is studied. In addition, coherence time of channel is computed for various radar models [72].
- Performance of MIMO radar is studied when interference channel between radar and communication system is perturbed by the motion of sea waves [73].
- Three-dimensional (3D) MIMO channel model between MIMO radar and MIMO cellular system is formulated by considering a 2D antenna array at the radar and a 1D array at the BS. Using the proposed channel model the efficacy of a novel null space projection algorithm in 2D which mitigates radar interference is demonstrated. In addition, the volume illuminated by spectrum sharing MIMO radars that are subject to interference mitigation is studied [74].

1.4.5 Resource Allocation

In this area, the following contributions are made:

- Rate allocation algorithms for cellular systems are designed which exploit carrier aggregation to increase system capacity and avoid radar interference [75].

- Power allocation algorithms for cellular systems are designed which exploit carrier aggregation to optimally allocate power to users [76].

1.5 Technical Challenges in Spectrum Sharing

During the course of this research several technical issues regarding spectrum sharing between radars and communication systems were identified and solutions were presented. However, significant work is still required at both radar and communication systems to realize spectrum sharing. Some of these technical issues are mentioned in this section in the light of regulatory statutes.

The FCC has proposed that small cell based PAL and GAA users operate in such a way that they do not interfere with federal incumbent operations. This is made sure by having each small cell register with a central database or SAS and report its transmission characteristics, as shown in Figure 1.4. The SAS can utilize this information to apprise federal incumbents, perform channel allocation, calculate exclusion zones required for incumbent protection, and inform small cells accordingly on whether they are allowed to operate. In the context of this research MIMO radars can utilize this information for placing nulls at small cells and model interference coming from small cells into radar receivers. At the same time, such information can be utilized by small cells for resource allocation. However, these are very challenging task due to the following reasons:

- **MIMO Radar Antennas and Power Limitations** – This research considered the use of MIMO radars due to its enhanced angular resolution, target detection, parameter identifiability, and flexible transmit/receive beamforming capabilities as compared to a phased array radar [13]. However, MIMO radars have considerably less transmit

coherent processing gain which translates into beam-shape loss which results in performance degradation for the target's RCS fading in addition to loss in signal-to-noise ratio (SNR) [77]. This problem is further aggravated if a larger MIMO antenna array is employed to place nulls at a large number of systems. A solution to over come this problem in MIMO radars is proposed in [77] and for the case of spectrum sharing MIMO radars is proposed in [78].

- **Deployment Information** – Small cell devices that are used in high rise buildings or mounted on billboards or used for point-to-point links have the potential to cause interference to federal incumbents on a larger scale as they'll be highly likely to operate in-line with the antenna of radar. Therefore, each small cell should report its exact location (co-ordinates), height, and building floor information. This information would be used for interference modeling. In addition, such information can be utilized by radars to place nulls in a spatial sector to protect small cells from radar interference.

- **Propagation Modeling** – Propagation modeling for rural, sub-urban, and urban area is quite different due to the presence of crops, forest, buildings, etc. Therefore, the database should take this information into account when calculating exclusion zones.

- **Real-time Interference Modeling** – Wireless traffic is very dynamic in nature and can have busy and idle periods on a given day. Therefore, exclusion zone calculation should be done in real time. This means exclusion zones won't be static over time.

- **Security** – Wireless links are prone to eavesdroppers and other malicious users that may falsely report their characteristics to a database [79]. Bad data would lead to inaccurate calculation of exclusion zones. Therefore, in order to protect incumbent operations, security of the database and information conveyed to database must be

ensured.

- **Static vs. Mobile Operations** – A mobile small cell would be continuously changing its location and thus needs to report its characteristics more often than static small cells. It would be very challenging for the database to accommodate such a user for exclusion zone calculations that is changing its characteristics too rapidly. Moreover, it would be challenging for a radar system to place nulls at moving small cell terminals.

- **Power Control and Beamforming** – Modern wireless systems frequently use power control and beamforming to maximize its throughput and enhance user experience. Both factors are very important for exclusion zone calculation. For example, a small cell might want to use maximum transmit power for a certain user at a certain angle that is also in line-of-sight to a federal system. This is an undesirable scenario which is harmful for federal operations and thus the database has to play its role in avoiding this situation. Therefore, both power control and beamforming information must also be reported to the database. This information can also be exploited by MIMO radars when forming projection matrix and calculating null space of interference channel.

1.6 Organization of Dissertation

This dissertation is organized as follows. Chapter 2 presents radar model, communication system model, spectrum sharing environment along with projection and spectrum sharing algorithms. Chapter 3 presents performance metrics of spectrum sharing MIMO radars and this includes probability of target detection, Cramér Rao bound and maximum likelihood estimates of target's angle of arrival, and beampatterns. Chapter 4 presents waveform design approaches and designs BPSK and QPSK waveforms by considering spectrum sharing

constraints. Chapter 5 models cellular interference and evaluates its impact on radar's target detection performance. Chapter 6 models channel between radar and communication systems. Chapter 7 presents resource allocation algorithms. Chapter 8 concludes this dissertation and points out some future extensions of this work. Appendix A contains a list of book, journal articles, conference proceedings, and technical reports published during the course of this research.

Chapter 2

Spectrum Sharing via a Projection Based Approach

In wireless communications, multiple access schemes have played a vital role in enabling multiple users access spectrum simultaneously. Some of the very common and widely used multiple access schemes include frequency division duplexing (FDD) and time division duplexing (TDD). However, the emergence of MIMO systems made it possible to exploit spatial domain. This gave rise to spatial division duplexing (SDD) in which users coexist in the same channel by exploiting orthogonal spatial dimensions, that are not in use by the other user. This results in an interference free environment and is also known as null space based coexistence method.

Projection of signals onto null space of interference channels for avoiding secondary user interference to primary system has been proposed within the cognitive radio context. The idea is to estimate the null space of the channel matrix, between secondary user (SU) and primary user (PU). This process is done at the SU transmitter. In the case when channel is

assumed to be reciprocal, between PU transmitter and receiver, null space can be estimated by SU transmitter by using second order statistics of the PU's transmitted signal [80, 81]. However, the above approach is restricted to PUs using Time Division Duplexing (TDD), for example, WiMax systems. If the assumption of channel reciprocity is removed, channel estimation requires cooperation between the PU and the SU.

The distinction of this work lies in first showing that projection based spectrum sharing method can be applied to MIMO radar systems, to avoid interfering with communication systems, and secondly, studying its effects on radar both analytically and quantitatively. This chapter introduces preliminaries of system models for MIMO radar and cellular system, that will be used in the subsequent chapters. This chapter is organized as follows. Section 2.1 introduces radar signal model. Section 2.4 introduces cellular system model. Section 2.2 defines interference channel. Section 2.3 introduces spectrum sharing environment. Section 2.5 defines null space projection and spectrum sharing algorithms.

2.1 Radar Signal Model

Let $\mathbf{x}(t)$ be the signal transmitted from the M-element MIMO radar array, defined as

$$\mathbf{x}(t) = \begin{bmatrix} x_1(t)e^{j\omega_c t} & x_2(t)e^{j\omega_c t} & \cdots & x_M(t)e^{j\omega_c t} \end{bmatrix}^T \tag{2.1}$$

where $x_k(t)e^{j\omega_c t}$ is the baseband signal from the k^{th} transmit element, ω_c is the carrier angular frequency, $t \in [0, T_o]$, with T_o being the observation time. The transmit steering vector is defined as

$$\mathbf{a}_T(\theta) \triangleq \begin{bmatrix} e^{-j\omega_c \tau_{T_1}(\theta)} & e^{-j\omega_c \tau_{T_2}(\theta)} & \cdots & e^{-j\omega_c \tau_{T_M}(\theta)} \end{bmatrix}^T. \tag{2.2}$$

Table 2.1: Table of Notations

Notation	Description
$\mathbf{x}(t)$	Transmitted radar (orthogonal) waveform
$\mathbf{a}_T(\theta)$	Transmit steering vector to target angle θ
$\mathbf{a}_R(\theta)$	Receive steering vector to target angle θ
$\mathbf{A}(\theta)$	Transmit-receive steering matrix
$\mathbf{y}(t)$	Received radar waveform
$\mathbf{R}_\mathbf{x}$	Correlation matrix of orthogonal waveforms
$\mathbf{s}_j^{\mathrm{UE}}(t)$	Signal transmitted by the j^{th} UE in the i^{th} BS
$\mathcal{L}_i^{\mathrm{UE}}$	Total number of user equipments (UEs) in the i^{th} BS
$\mathcal{K}$	Total number of BSs
M	Radar transmit antennas
N	Radar receive antennas
N^{BS}	BS transmit/receive antennas
$\mathbf{H}_i$	Channel between radar and i^{th} BS
$\mathbf{H}_{i,j}$	Channel between j^{th} UE and i^{th} cell
$\mathbf{r}_i(t)$	Received signal at the i^{th} BS
$\mathbf{P}_i$	Projection matrix for the i^{th} channel

Then, the transmit-receive steering matrix can be written as

$$\mathbf{A}(\theta) \triangleq \mathbf{a}_R(\theta)\mathbf{a}_T^T(\theta). \tag{2.3}$$

Since, M transmit and receive elements are used, $\mathbf{a}(\theta) \triangleq \mathbf{a}_T(\theta) \triangleq \mathbf{a}_R(\theta)$. The signal received from a single point target, in far-field with constant radial velocity v_r, at an angle θ can be written as

$$\mathbf{y}(t) = \alpha\, e^{-j\omega_D t}\mathbf{A}(\theta)\, \mathbf{x}(t-\tau(t)) + \mathbf{n}(t) \tag{2.4}$$

where $\tau(t) = \tau_{T_k}(t) + \tau_{R_l}(t)$, denoting the sum of propagation delays between the target and the k^{th} transmit element and the l^{th} receive element, respectively; ω_D is the Doppler frequency shift, and α represents the complex path loss including the propagation loss and the coefficient of reflection.

2.1.1 Modeling Assumptions

In order to keep the analysis tractable, the following assumptions about the signal model are made:

- The path loss α is assumed to be identical for all transmit and receive elements, due to the far-field assumption [13].
- The angle θ is the azimuth angle of the target.
- After compensating the range-Doppler parameters, equation (2.4) can be simplified as

$$\mathbf{y}(t) = \alpha\, \mathbf{A}(\theta)\, \mathbf{x}(t) + \mathbf{n}(t). \tag{2.5}$$

2.1.2 Target Model/Channel

A point target model is considered which is defined for targets having a scatterer with infinitesimal spatial extent. This model is a good assumption and is widely used in radar theory for the case when radar elements are colocated and their exists a large distance between the radar array and the target as compared to inter-element distance [82]. The signal reflected from a point target with unit radar cross-section (RCS) is mathematically represented by the Dirac delta function.

2.1.3 Statistical Assumptions

The following assumptions for the received signal model in equation (2.5) are made:

- θ and α are deterministic unknown parameters representing the target's direction of arrival and the complex amplitude of the target, respectively.
- The noise vector $\mathbf{n}(t)$ is independent, zero-mean complex Gaussian with known covariance matrix $\mathbf{R_n} = \sigma_n^2\mathbf{I}_M$, i.e. $\mathbf{n}(t) \sim \mathcal{N}^c(\mathbf{0}_M, \sigma_n^2\mathbf{I}_M)$, where $\mathcal{N}^c$ denotes the complex Gaussian distribution.
- With the above assumptions, the received signal model in equation (2.5) has an independent complex Gaussian distribution, i.e., $\mathbf{y}(t) \sim \mathcal{N}^c(\alpha\mathbf{A}(\theta)\,\mathbf{x}(t), \sigma_n^2\mathbf{I}_M)$.

2.1.4 Orthogonal Waveforms

In this work, with the exception of Chapter 4, it is assumed that orthogonal waveforms are transmitted by MIMO radars, i.e.,

$$\mathbf{R_x} = \int_{T_o} \mathbf{x}(t)\mathbf{x}^H(t)dt = \mathbf{I}_M. \tag{2.6}$$

The transmission of orthogonal signals gives MIMO radar advantages in terms of digital beamforming at the transmitter in addition to receiver, improved angular resolution, extended array aperture in the form of virtual arrays, increased number of resolvable targets, lower sidelobes, and lower probability of intercept as compared to coherent waveforms [13].

2.2 Interference Channel Model

In the spectrum sharing model, radar shares $\mathcal{K}$ interference channels with cellular system. Let's define the i^{th} interference channel as

$$\mathbf{H}_i \triangleq \begin{bmatrix} h_i^{(1,1)} & \cdots & h_i^{(1,M)} \\ \vdots & \ddots & \vdots \\ h_i^{(N^{\text{BS}},1)} & \cdots & h_i^{(N^{\text{BS}},M)} \end{bmatrix} \quad (N^{\text{BS}} \times M) \tag{2.7}$$

where $i = 1, 2, \ldots, \mathcal{K}$, and $h_i^{(l,k)}$ denotes the channel coefficient from the k^{th} antenna element at the MIMO radar to the l^{th} antenna element at the i^{th} BS. It is assumed that elements of $\mathbf{H}_i$ are independent, identically distributed (i.i.d.) and circularly symmetric complex Gaussian random variables with zero-mean and unit-variance, thus, having a i.i.d. Rayleigh distribution.

2.3 Cooperative RF Environment

In the wireless communications literature, it is usually assumed that the transmitter (mostly BS) has channel state information (CSI) either by feedback from the receiver (mostly UE), in FDD systems [83], or transmitters can reciprocate the channel, in TDD systems [83]. The feedback and reciprocity are valid and practical as long as the feedback has a reasonable overhead and coherence time of the RF channel is larger than the two-way communication time, respectively.

In the case of radars sharing their spectrum with communications systems one way to

get CSI is that radar estimates $\mathbf{H}_i$ based on the training symbols sent by communication receivers (or BSs in this case) [84]. Another approach is that radar aids communication systems in channel estimation, with the help of a low-power reference signal, and they feed back the estimated channel to radar [67]. Since, radar signal is treated as interference at communication system, one can characterize the channel as interference channel and refer to information about it as interference-channel state information (ICSI).

Spectrum sharing between radars and communications systems can be envisioned in two domains: military radars sharing spectrum with military communication systems, *Mil2Mil* sharing; another possibility is military radars sharing spectrum with commercial communication systems, *Mil2Com* sharing. In *Mil2Mil* sharing, ICSI can be acquired by radars fairly easily as both systems belong to military. In *Mil2Com* sharing, ICSI can be acquired by giving incentives to commercial communication system. The biggest incentive in this scenario is null-steering and protection from radar interference. Thus, regardless of the sharing scenario, *Mil2Mil* or *Mil2Com*, ICSI is available for the sake of mitigating radar interference at communication systems.

2.4 Cellular System Model

In this work, MIMO cellular system, with $\mathcal{K}$ base stations is considered. Each BS is equipped with N^{BS} transmit and receive antennas, with i^{th} BS supporting $\mathcal{L}_i^{\text{UE}}$ user equipments (UEs). The UEs are also multi-antenna systems with N^{UE} transmit and receive antennas. If $\mathbf{s}_j^{\text{UE}}(t)$ is the signals transmitted by the j^{th} UE in the i^{th} cell, then the received signal at the i^{th} BS

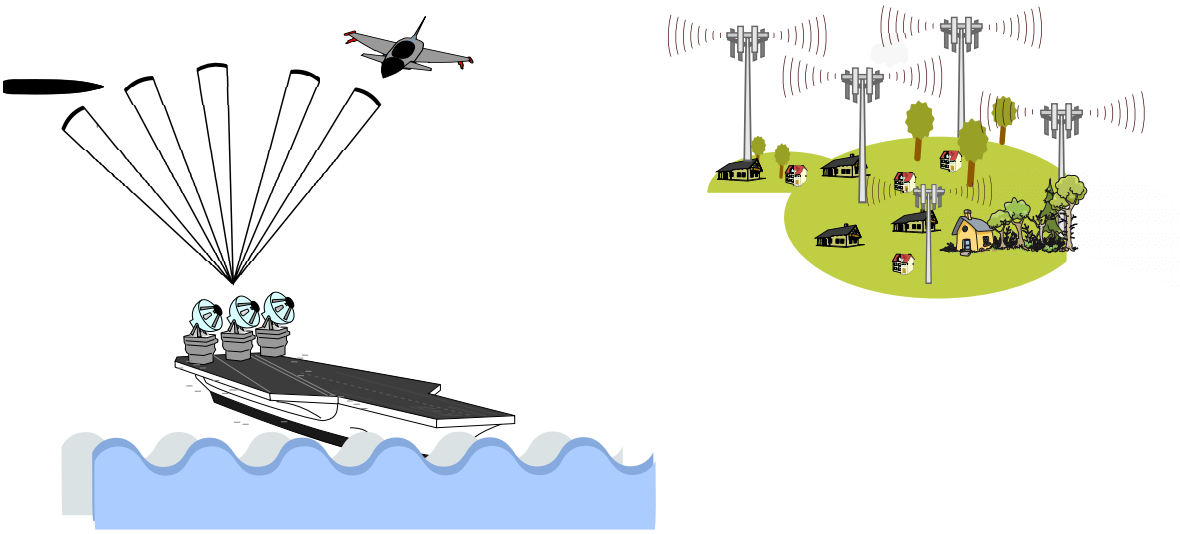

Figure 2.1: Spectrum Sharing Scenario: Seaborne MIMO radar detecting a point target while simultaneously sharing spectrum with a MIMO cellular system.

receiver can be written as

$$\mathbf{r}_i(t) = \sum_j \mathbf{H}_{i,j}^{N^{\mathrm{BS}} \times N^{\mathrm{UE}}} \mathbf{s}_j^{\mathrm{UE}}(t) + \mathbf{H}_i \mathbf{x}(t) + \mathbf{w}(t) \tag{2.8}$$

$$\text{for } 1 \leq i \leq \mathcal{K} \text{ and } 1 \leq j \leq \mathcal{L}_i^{\mathrm{UE}}$$

where $\mathbf{w}(t)$ is the additive white Gaussian noise, $\mathbf{H}_{i,j}$ is the channel between i^{th} BS and j^{th} UE, and $\mathbf{H}_i$ is the channel between i^{th} BS and radar. In order to avoid interference to the i^{th} BS, the radar shapes its waveform $\mathbf{x}(n)$ such that it is in the null-space of $\mathbf{H}_i$, i.e. $\mathbf{H}_i \mathbf{x}(n) = \mathbf{0}$.

Lets consider two spectrum sharing scenarios which are discussed as follows.

Case 1 ($M \ll \mathcal{K}N^{\mathrm{BS}}$ but $M > N^{\mathrm{BS}}$): Consider a scenario in which a MIMO radar has a very small antenna array as compared to the combined antenna array of $\mathcal{K}$ BSs, i.e. $M \ll \mathcal{K}N^{\mathrm{BS}}$, but is larger than individual BS antenna array, i.e. $M > N^{\mathrm{BS}}$. In such a

scenario, it is not possible for the MIMO radar to simultaneously mitigate interference to all the $\mathcal{K}$ BSs present in the network because of insufficient degrees of freedom (DoF) available. However, the available DoF allow simultaneous target detection and interference mitigation to one of the BS among $\mathcal{K}$ BSs. The choice of BS selection depends upon the performance metric which radar wants to optimize. In this work, we consider numerous performance metrics that are discussed in the next chapter.

A drawback of this approach is that interference is not mitigated to $\mathcal{K}-1$ BSs present in the network and the radar has to utilize higher transmit power to achieve the same performance level which can increase the level of interference at BSs not part of the mitigation scheme. This drawback is addressed in the literature by moving $\mathcal{K}-1$ BSs to non-radar frequency bands by using resource allocation and carrier aggregation techniques [75, 85].

It is worth mentioning that when $M \ll \mathcal{K}N^{\mathrm{BS}}$ traditional colocated MIMO radar architecture is not suitable for mitigation of interference by using NSP approaches because sufficient DoF are not available and doing so will result in performance degradation of radar systems. However, the MIMO radar architecture can be modified into an overlapped-MIMO radar architecture where the transmit array of colocated MIMO radar is partitioned into a number of subarrays that are allowed to overlap. The overlapped-MIMO radar architecture increases the DoF and enjoys the advantages of the MIMO radar while mitigating interference to communication systems without sacrificing the main desirable characteristics for its own transmission [78].

Case 2 ($M \gg \mathcal{K}N^{\mathrm{BS}}$): Consider a scenario in which a MIMO radar has a very large antenna array as compared to the combined antenna array of $\mathcal{K}$ BSs, i.e. $M \gg \mathcal{K}N^{\mathrm{BS}}$. In such a scenario, it is feasible for the MIMO radar to simultaneously mitigate interference to all the $\mathcal{K}$ BSs present in the network while reliably detecting targets. This is because

sufficient degrees of freedom are available for both the tasks. In such a scenario the combined interference channel that the MIMO radar shares with $\mathcal{K}$ BSs in the networks is given as

$$\mathbf{H} = \begin{bmatrix} \mathbf{H}_1 & \mathbf{H}_2 & \cdots & \mathbf{H}_{\mathcal{K}} \end{bmatrix}. \tag{2.9}$$

2.5 Switched Null Space Projection (SNSP)

In this section, null space projection algorithm for multi-cell BS systems is introduced along with spectrum sharing and projection algorithms.

2.5.1 Projection Matrix

This section introduces formation of projection matrices for Case 1 and Case 2.

Projection for Case 1 ($M \ll \mathcal{K}N^{\mathbf{BS}}$ but $M > N^{\mathbf{BS}}$): This section defines projection algorithm for 'Case 1' which projects radar signal onto the null space of interference channel $\mathbf{H}_i$. Assuming, the MIMO radar has channel state information of all $\mathbf{H}_i$ interference channels, through feedback, in *Mil2Mil* or *Mil2Com* scenario, singular value decomposition (SVD) is performed to find the null space and then construct a projector matrix. Lets proceed by first finding SVD of $\mathbf{H}_i$, i.e.,

$$\mathbf{H}_i = \mathbf{U}_i \mathbf{\Sigma}_i \mathbf{V}_i^H. \tag{2.10}$$

Now, define

$$\widetilde{\mathbf{\Sigma}}_i \triangleq \mathrm{diag}(\widetilde{\sigma}_{i,1}, \widetilde{\sigma}_{i,2}, \ldots, \widetilde{\sigma}_{i,p}) \tag{2.11}$$

where $p \triangleq \min(N^{\mathrm{BS}}, M)$ and $\widetilde{\sigma}_{i,1} > \widetilde{\sigma}_{i,2} > \cdots > \widetilde{\sigma}_{i,q} > \widetilde{\sigma}_{i,q+1} = \widetilde{\sigma}_{i,q+2} = \cdots = \widetilde{\sigma}_{i,p} = 0$ are

the singular values of $\mathbf{H}_i$. Next, define

$$\widetilde{\mathbf{\Sigma}}_i' \triangleq \text{diag}(\widetilde{\sigma}_{i,1}', \widetilde{\sigma}_{i,2}', \ldots, \widetilde{\sigma}_{i,M}') \tag{2.12}$$

where

$$\widetilde{\sigma}_{i,u}' \triangleq \begin{cases} 0, & \text{for } u \leq q, \\ 1, & \text{for } u > q. \end{cases} \tag{2.13}$$

Using above definitions one can now define projection matrix, i.e.,

$$\mathbf{P}_i \triangleq \mathbf{V}_i \widetilde{\mathbf{\Sigma}}_i' \mathbf{V}_i^H. \tag{2.14}$$

In order to show that $\mathbf{P}_i$ is a valid projection matrix two results on projection matrices are proved below.

Property 2.5.1. *$\mathbf{P}_i \in \mathbb{C}^{M \times M}$ is a projection matrix if and only if $\mathbf{P}_i = \mathbf{P}_i^H = \mathbf{P}_i^2$.*

Proof. Let's start by showing the 'only if' part. First, lets show $\mathbf{P}_i = \mathbf{P}_i^H$. Taking Hermitian of equation (2.14) yields

$$\mathbf{P}_i^H = (\mathbf{V}_i \widetilde{\mathbf{\Sigma}}_i' \mathbf{V}_i^H)^H = \mathbf{P}_i. \tag{2.15}$$

Now, squaring equation (2.14) gives

$$\mathbf{P}_i^2 = \mathbf{V}_i \widetilde{\mathbf{\Sigma}}_i \mathbf{V}_i^H \times \mathbf{V}_i \widetilde{\mathbf{\Sigma}}_i \mathbf{V}_i^H = \mathbf{P}_i \tag{2.16}$$

where above equation follows from $\mathbf{V}_i^H \mathbf{V}_i = \mathbf{I}$ (since they are orthonormal matrices) and $(\widetilde{\mathbf{\Sigma}}_i')^2 = \widetilde{\mathbf{\Sigma}}_i'$ (by construction). From equations (2.15) and (2.16) it follows that $\mathbf{P}_i = \mathbf{P}_i^H = \mathbf{P}_i^2$. Next, lets show $\mathbf{P}_i$ is a projector by showing that if $\mathbf{v} \in$ range $(\mathbf{P}_i)$, then $\mathbf{P}_i \mathbf{v} = \mathbf{v}$, i.e.,

for some $\mathbf{w}, \mathbf{v} = \mathbf{P}_i\mathbf{w}$, then

$$\mathbf{P}_i\mathbf{v} = \mathbf{P}_i(\mathbf{P}_i\mathbf{w}) = \mathbf{P}_i^2\mathbf{w} = \mathbf{P}_i\mathbf{w} = \mathbf{v}. \tag{2.17}$$

Moreover, $\mathbf{P}_i\mathbf{v} - \mathbf{v} \in \text{null}(\mathbf{P}_i)$, i.e.,

$$\mathbf{P}_i(\mathbf{P}_i\mathbf{v} - \mathbf{v}) = \mathbf{P}_i^2\mathbf{v} - \mathbf{P}_i\mathbf{v} = \mathbf{P}_i\mathbf{v} - \mathbf{P}_i\mathbf{v} = \mathbf{0}. \tag{2.18}$$

This concludes the proof.

□

Property 2.5.2. $\mathbf{P}_i \in \mathbb{C}^{M\times M}$ *is an orthogonal projection matrix onto the null space of* $\mathbf{H}_i \in \mathbb{C}^{N^{BS}\times M}$.

Proof. Since $\mathbf{P}_i = \mathbf{P}_i^H$, one can write

$$\mathbf{H}_i\mathbf{P}_i^H = \mathbf{U}_i\widetilde{\mathbf{\Sigma}}_i\mathbf{V}_i^H \times \mathbf{V}_i\widetilde{\mathbf{\Sigma}}_i'\mathbf{V}_i^H = \mathbf{0}. \tag{2.19}$$

The above results follows from noting that $\widetilde{\mathbf{\Sigma}}_i\widetilde{\mathbf{\Sigma}}_i' = \mathbf{0}$ by construction. □

'Case 1' deals with $\mathcal{K}$ interference channels. Therefore, one needs to select the interference channel which results in least degradation of radar waveform in a minimum norm sense, i.e.,

$$i_{\min} \triangleq \underset{1\leq i\leq \mathcal{K}}{\arg\min} \left|\left|\mathbf{P}_i\mathbf{x}(t) - \mathbf{x}(t)\right|\right|_2 \tag{2.20}$$

$$\breve{\mathbf{P}} \triangleq \mathbf{P}_{i_{\min}}. \tag{2.21}$$

Once projection matrix is selected it is straight forward to project radar signal onto the null

space of interference channel via

$$\breve{\mathbf{x}}(t) = \breve{\mathbf{P}}\,\mathbf{x}(t). \tag{2.22}$$

The correlation matrix of our NSP waveform is given as

$$\mathbf{R}_{\breve{\mathbf{x}}} = \int_{T_o} \breve{\mathbf{x}}(t)\breve{\mathbf{x}}^H(t)dt \tag{2.23}$$

which is no longer identity, because the projection does not preserve the orthogonality, and its rank depends upon the rank of the projection matrix.

Projection for Case 2 ($M \gg \mathcal{K}N^{\mathbf{BS}}$): In this section, lets define the projection algorithm for 'Case 2' which projects radar signal onto the null space of combined interference channel $\mathbf{H}$. The SVD of $\mathbf{H}$ is given as

$$\mathbf{H} = \mathbf{U}\mathbf{\Sigma}\mathbf{V}^H. \tag{2.24}$$

Now, lets define

$$\widetilde{\mathbf{\Sigma}} \triangleq \mathrm{diag}(\widetilde{\sigma}_1, \widetilde{\sigma}_2, \ldots, \widetilde{\sigma}_p) \tag{2.25}$$

where $p \triangleq \min(N^{\mathrm{BS}}, M)$ and $\widetilde{\sigma}_1 > \widetilde{\sigma}_2 > \cdots > \widetilde{\sigma}_q > \widetilde{\sigma}_{q+1} = \widetilde{\sigma}_{q+2} = \cdots = \widetilde{\sigma}_p = 0$ are the singular values of $\mathbf{H}$. Next, define

$$\widetilde{\mathbf{\Sigma}}'_i \triangleq \mathrm{diag}(\widetilde{\sigma}'_1, \widetilde{\sigma}'_2, \ldots, \widetilde{\sigma}'_M) \tag{2.26}$$

where

$$\widetilde{\sigma}'_u \triangleq \begin{cases} 0, & \text{for } u \leq q, \\ 1, & \text{for } u > q. \end{cases} \tag{2.27}$$

Using above definitions one can now define projection matrix, i.e.,

$$\mathbf{P} \triangleq \mathbf{V}\widetilde{\mathbf{\Sigma}}'\mathbf{V}^H. \tag{2.28}$$

It is straightforward to see that $\mathbf{P}$ is a valid projection matrix by using Properties 1 and 2.

2.5.2 Spectrum Sharing and Projection Algorithms

In this section, spectrum sharing and projection algorithms for 'Case 1' and 'Case 2' are explained.

Algorithms for Case 1 ($M \ll \mathcal{K}N^{\mathbf{BS}}$ but $M > N^{\mathbf{BS}}$): For this case, the process of spectrum sharing by forming projection matrices and selecting interference channels is executed with the help of Algorithms (1) and (2). First, at each pulse repetition interval (PRI), the radar obtains ICSI of all $\mathcal{K}$ interference channels. This information is sent to Algorithm (2) for the calculation of null spaces and formation of projection matrices. Algorithm (1) process $\mathcal{K}$ projection matrices, received from Algorithm (2), to find the projection matrix which results in least degradation of radar waveform in a minimum norm sense. This step is followed by the projection of radar waveform onto the null space of the selected BS, i.e, the BS to the corresponding selected projection matrix, and waveform transmission.

Projection for Case 2 ($M \gg \mathcal{K}N^{\mathbf{BS}}$): For this case, the process of spectrum sharing is executed with the help of Algorithms (3) and (4). First, at each pulse repetition interval (PRI), the radar obtains ICSI of all $\mathcal{K}$ interference channels. This information is sent to Algorithm (4) for the calculation of null space of $\mathbf{H}$ and the formation of projection matrix $\mathbf{P}$. The projection of radar waveform onto the null space of $\mathbf{H}$ is performed by Algorithm 3.

Algorithm 1 Spectrum Sharing Algorithm for Case 1

loop
  for $i = 1 : \mathcal{K}$ **do**
    Get CSI of $\mathbf{H}_i$ through feedback from the i^{th} BS.
    Send $\mathbf{H}_i$ to Algorithm (2) for the formation of projection matrix $\mathbf{P}_i$.
    Receive the i^{th} projection matrix $\mathbf{P}_i$ from Algorithm (2).
  end for
  Find $i_{\min} = \underset{1 \leq i \leq \mathcal{K}}{\arg\min} \left|\left| \mathbf{P}_i \mathbf{x}(t) - \mathbf{x}(t) \right|\right|_2$.
  Set $\breve{\mathbf{P}} = \mathbf{P}_{i_{\min}}$ as the desired projector.
  Perform null space projection, i.e., $\breve{\mathbf{x}}(t) = \breve{\mathbf{P}}\mathbf{x}(t)$.
end loop

Algorithm 2 Projection Algorithm for Case 1

if $\mathbf{H}_i$ received from Algorithm (1) **then**
  Perform SVD on $\mathbf{H}_i$ (i.e. $\mathbf{H}_i = \mathbf{U}_i \mathbf{\Sigma}_i \mathbf{V}_i^H$)
  Construct $\widetilde{\mathbf{\Sigma}}_i = \text{diag}(\widetilde{\sigma}_{i,1}, \widetilde{\sigma}_{i,2}, \ldots, \widetilde{\sigma}_{i,p})$
  Construct $\widetilde{\mathbf{\Sigma}}_i' = \text{diag}(\widetilde{\sigma}'_{i,1}, \widetilde{\sigma}'_{i,2}, \ldots, \widetilde{\sigma}'_{i,M})$
  Setup projection matrix $\mathbf{P}_i = \mathbf{V}_i \widetilde{\mathbf{\Sigma}}_i' \mathbf{V}_i^H$.
  Send $\mathbf{P}_i$ to Algorithm (1).
end if

Algorithm 3 Spectrum Sharing Algorithm for Case 2

loop
  Get CSI of $\mathbf{H}$ through feedback from $\mathcal{K}$ BSs.
  Send $\mathbf{H}$ to Algorithm (4) for the formation of projection matrix $\mathbf{P}$.
  Receive the projection matrix $\mathbf{P}$ from Algorithm (4).
  Perform null space projection, i.e., $\breve{\mathbf{x}}(t) = \mathbf{P}\mathbf{x}(t)$.
end loop

Algorithm 4 Projection Algorithm for Case 2

if $\mathbf{H}$ received from Algorithm (3) **then**
  Perform SVD on $\mathbf{H}$ (i.e. $\mathbf{H} = \mathbf{U}\mathbf{\Sigma}\mathbf{V}^H$)
  Construct $\widetilde{\mathbf{\Sigma}} = \text{diag}(\widetilde{\sigma}_1, \widetilde{\sigma}_2, \ldots, \widetilde{\sigma}_p)$
  Construct $\widetilde{\mathbf{\Sigma}}_i' = \text{diag}(\widetilde{\sigma}'_1, \widetilde{\sigma}'_2, \ldots, \widetilde{\sigma}'_M)$
  Setup projection matrix $\mathbf{P} = \mathbf{V}\widetilde{\mathbf{\Sigma}}'\mathbf{V}^H$.
  Send $\mathbf{P}$ to Algorithm (3).
end if

Chapter 3

Spectrum Sharing: Performance Metrics

In Chapter 2, a projection based approach was presented to mitigate radar interference by projecting radar signal onto null space of interference channel between radar and communication system. Since this approach modifies radar signal, it is important to study the impact of projection on radar performance. Therefore, in this chapter, radar performance metrics are considered. The focus is on four performance metrics which are target detection, Cramér Rao bound and maximum likelihood estimate of target's angle of arrival, and beampattern of null space projected MIMO radar waveform.

This chapter is organized as follows. Section 3.1 discusses target detection performance of spectrum sharing MIMO radars. It presents the generalized likelihood ratio test (GLRT) for target detection and derives detector statistic for NSP and orthogonal waveform. Sections 3.2 and 3.3 discusses Cramér Rao bound and maximum likelihood estimate of target's direction of arrival. Section 3.4 discusses beampattern of null space projected MIMO radar waveform.

Section 3.5 concludes this chapter.

3.1 Target Detection

The problem of target estimation, detection, and tracking lies at the heart of radar signal processing. This problem becomes critically important when radar is sharing spectrum with other systems, say cellular systems. In this section, target detection performance of radar that is subject to shape its waveform in a way that it doesnt cause interference to cellular systems is evaluated. Target detection capabilities of null-space projected (NSP) waveform are compared with orthogonal waveform. For this purpose, generalized likelihood ratio test (GLRT) for target detection along with detector statistic for NSP and orthogonal waveform are derived. The target detection performance for NSP and orthogonal waveform is studied theoretically and via Monte Carlo simulations.

3.1.1 Statistical Decision Test for Target Detection

In this section, a statistical decision test is derived for targets illuminated with the orthogonal radar waveforms and the NSP projected radar waveforms. The goal is to compare the performance of the two waveforms by looking at the test decision on whether the target is present or not in the range-Doppler cell of interest. A system-level architecture of the spectrum sharing radar is shown in Figure 3.1. In this architecture, the transmitter performs the functions of waveform generation, channel selection, and projection; and the receiver performs the functions of signal detection and estimation.

For target detection and estimation, a hypothesis test is constructed where the goal is to choose between two hypothesis: the null hypothesis $\mathcal{H}_0$ which represents the case when the

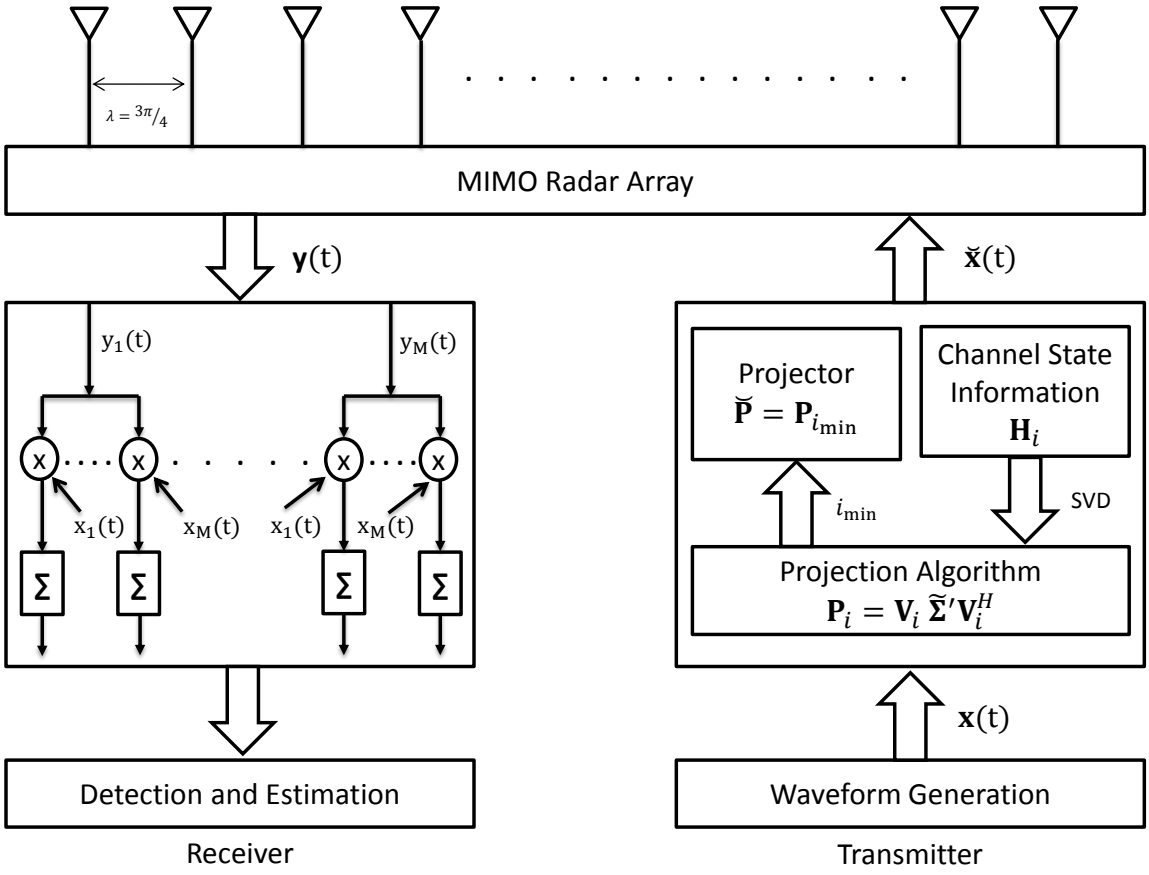

Figure 3.1: System-level architecture of spectrum sharing MIMO radar: The transmitter is modified to perform the functions of ICSI collection, projection matrix formation, interference channel selection, and radar waveform projection on to the selected interference channel for spectrum sharing. On the other hand, the receiver is a traditional radar receiver performing functions of parameter detection and estimation on radar returns.

target is absent or the alternate hypothesis $\mathcal{H}_1$ which represents the case when the target is present. The hypothesis for a single target model in equation (2.5) can be written as

$$\mathbf{y}(t) = \begin{cases} \mathcal{H}_1 : \alpha \, \mathbf{A}(\theta) \, \mathbf{x}(t) + \mathbf{n}(t), & 0 \leq t \leq T_o, \\ \mathcal{H}_0 : \mathbf{n}(t), & 0 \leq t \leq T_o. \end{cases} \tag{3.1}$$

The generalize likelihood ratio test (GLRT) is used because θ and α are unknown but deter-

ministic. The advantage of using GLRT is that unknown parameters can be replaced with their maximum likelihood (ML) estimates. The ML estimate of α and θ are found for various signal models, targets, and interference sources in [13, 86] when using orthogonal signals. In this section, a simpler model is considered with one target and no interference sources in order to study the impact of NSP on target detection in a tractable manner. Therefore, a simpler derivation of ML estimation and GLRT is presented.

The received signal model in equation (2.5) can be written as

$$\mathbf{y}(t) = \mathbf{Q}(t, \theta)\alpha + \mathbf{n}(t) \tag{3.2}$$

where

$$\mathbf{Q}(t, \theta) = \mathbf{A}(\theta)\mathbf{x}(t). \tag{3.3}$$

Karhunen-Loève expansion are used for derivation of the log-likelihood function for estimating θ and α. Let Ω denote the space of the elements of $\{\mathbf{y}(t)\}, \{\mathbf{Q}(t, \theta)\}$, and $\{\mathbf{n}(t)\}$. Moreover, let ψ_z, $z = 1, 2, \ldots$, be an orthonormal basis function of Ω satisfying

$$< \psi_z(t), \psi_{z'}(t) >= \int_{T_0} \psi_z(t), \psi^*_{z'}(t) = \delta_{zz'} \tag{3.4}$$

where $\delta_{zz'}$ is the Krönecker delta function. Then, the following series can be used to expand

the processes, $\{\mathbf{y}(t)\}, \{\mathbf{Q}(t,\theta)\}$, and $\{\mathbf{n}(t)\}$, as

$$\mathbf{y}(t) = \sum_{z=1}^{\infty} \mathbf{y}_z \psi_z(t) \tag{3.5}$$

$$\mathbf{Q}(t,\theta) = \sum_{z=1}^{\infty} \mathbf{Q}_z(\theta) \psi_z(t) \tag{3.6}$$

$$\mathbf{n}(t) = \sum_{z=1}^{\infty} \mathbf{n}_z \psi_z(t) \tag{3.7}$$

where $\mathbf{y}_z, \mathbf{Q}_z$, and $\mathbf{n}_z$ are the coefficients in the Karhunen-Loève expansion of the considered processes obtained by taking the corresponding inner product with basis function $\phi_z(t)$. Thus, an equivalent discrete model of equation (3.2) can be obtained as

$$\mathbf{y}_z = \mathbf{Q}_z(\theta)\alpha + \mathbf{n}_z, \quad z = 1, 2, \ldots \tag{3.8}$$

For white circular complex Gaussian processes, i.e, $\mathbb{E}[\mathbf{n}(t)\mathbf{n}(t-\tau(t))] = \sigma_n^2 \mathbf{I}_M \delta(\tau(t))$, the sequence $\{n_z\}$ is i.i.d. and $\mathbf{n}_z \sim \mathcal{N}^c(\mathbf{0}_M, \sigma_n^2 \mathbf{I}_M)$. Thus, the log-likelihood function can be expressed as

$$L_{\mathbf{y}}(\theta, \alpha) = \sum_{z=1}^{\infty} \left(- M \log(\pi\sigma_n^2) - \frac{1}{\sigma_n^2} \big|\big| \mathbf{y}_z - \mathbf{Q}_z(\theta)\alpha \big|\big|^2 \right). \tag{3.9}$$

Maximizing with respect to α yields

$$L_{\mathbf{y}}(\theta, \hat{\alpha}) = \Gamma - \frac{1}{\sigma_n^2} \Big(E_{\mathbf{yy}} - \mathbf{e}_{\mathbf{Qy}}^H \mathbf{E}_{\mathbf{QQ}}^{-1} \mathbf{e}_{\mathbf{Qy}} \Big) \tag{3.10}$$

where

$$\Gamma \triangleq -M \log(\pi \sigma_n^2) \tag{3.11}$$

$$E_{\mathbf{yy}} \triangleq \sum_{z=1}^{\infty} \left|\left|\mathbf{y}_z\right|\right|^2 \tag{3.12}$$

$$\mathbf{e}_{\mathbf{Qy}} \triangleq \sum_{z=1}^{\infty} \mathbf{Q}_z^H \mathbf{y}_z \tag{3.13}$$

$$\mathbf{E}_{\mathbf{QQ}}^{-1} \triangleq \sum_{z=1}^{\infty} \mathbf{Q}_z^H \mathbf{Q}_z. \tag{3.14}$$

Note that, in equation (3.10), apart from the constant Γ, the remaining summation goes to infinity. However, due to the non-contribution of higher order terms in the estimation of θ and α the summation can be finite. Using the identity

$$\int_{T_o} \mathbf{v}_1(t) \mathbf{v}_2^H(t) dt = \sum_{z=1}^{\infty} \mathbf{v}_{1z} \mathbf{v}_{2z}^H \tag{3.15}$$

for $\mathbf{v}_i(t) = \sum_{z=1}^{\infty} \mathbf{v}_{1z} \psi_z(t), i = 1, 2$, equations (3.12)-(3.14) can be written as

$$E_{\mathbf{yy}} \triangleq \int_{T_o} \left|\left|\mathbf{y}(t)\right|\right|^2 dt \tag{3.16}$$

$$\mathbf{e}_{\mathbf{Qy}} \triangleq \int_{T_o} \mathbf{Q}^H(t, \theta) \mathbf{y}(t) dt \tag{3.17}$$

$$\mathbf{E}_{\mathbf{QQ}} \triangleq \int_{T_o} \mathbf{Q}^H(t, \theta) \mathbf{Q}(t, \theta) dt. \tag{3.18}$$

Using the definition of $\mathbf{Q}(t, \theta)$ in equation (3.3), the f^{th} element of $\mathbf{e}_{\mathbf{Qy}}$ can be written as

$$[\mathbf{e}_{\mathbf{Qy}}]_f = \mathbf{a}^H(\theta_f) \mathbf{E}^T \mathbf{a}(\theta_f) \tag{3.19}$$

where

$$\mathbf{E} = \int_{T_o} \mathbf{y}(t)\mathbf{x}^H(t)dt. \tag{3.20}$$

Similarly, the fg^{th} element of $\mathbf{E_{QQ}}$ can be written as

$$[\mathbf{E_{QQ}}]_{fg} = \mathbf{a}^H(\theta_f)\mathbf{a}(\theta_g)\mathbf{a}^H(\theta_f)\mathbf{R}_x^T\mathbf{a}(\theta_g). \tag{3.21}$$

Since, $\mathbf{e_{Qy}}$ and $\mathbf{E_{QQ}}$ are independent of the received signal, the sufficient statistic to calculate θ and α is given by $\mathbf{E}$. Using equations (3.19)-(3.21), the ML estimate in matrix-vector form can be written as

$$L_{\mathbf{y}}(\hat{\theta}_{\text{ML}}) = \arg\max_{\theta} \frac{\left|\mathbf{a}^H(\hat{\theta}_{\text{ML}})\mathbf{E}\mathbf{a}^*(\hat{\theta}_{\text{ML}})\right|^2}{M\mathbf{a}^H(\hat{\theta}_{\text{ML}})\mathbf{R}_{\mathbf{x}}^T\mathbf{a}(\hat{\theta}_{\text{ML}})}. \tag{3.22}$$

Then, the GLRT for the hypothesis testing model in equation (3.1) is given as

$$L_{\mathbf{y}} = \max_{\theta,\alpha}\{\log f_{\mathbf{y}}(\mathbf{y},\theta,\alpha;\mathcal{H}_1)\} - \log f(\mathbf{y};\mathcal{H}_0) \underset{\mathcal{H}_0}{\overset{\mathcal{H}_1}{\gtrless}} \delta \tag{3.23}$$

where $f_{\mathbf{y}}(\mathbf{y},\theta,\alpha;\mathcal{H}_1)$ and $f(\mathbf{y};\mathcal{H}_0)$ are the probability density functions of the received signal under hypothesis $\mathcal{H}_1$ and $\mathcal{H}_0$, respectively. Hence, the GLRT can be expressed as

$$L_{\mathbf{y}}(\hat{\theta}_{\text{ML}}) = \arg\max_{\theta} \frac{\left|\mathbf{a}^H(\hat{\theta}_{\text{ML}})\mathbf{E}\mathbf{a}^*(\hat{\theta}_{\text{ML}})\right|^2}{M\mathbf{a}^H(\hat{\theta}_{\text{ML}})\mathbf{R}_{\mathbf{x}}^T\mathbf{a}(\hat{\theta}_{\text{ML}})} \underset{\mathcal{H}_0}{\overset{\mathcal{H}_1}{\gtrless}} \delta. \tag{3.24}$$

The asymptotic statistics of $L(\hat{\theta}_{\text{ML}})$ for both the hypothesis is given by [87]

$$L(\hat{\theta}_{\text{ML}}) \sim \begin{cases} \mathcal{H}_1 : \chi_2^2(\rho), \\ \mathcal{H}_0 : \chi_2^2, \end{cases} \tag{3.25}$$

where

- $\chi_2^2(\rho)$ is the noncentral chi-squared distributions with two degrees of freedom,
- χ_2^2 is the central chi-squared distributions with two degrees of freedom,
- and ρ is the noncentrality parameter, which is given by

$$\rho = \frac{|\alpha|^2}{\sigma_n^2} |\mathbf{a}^H(\theta) \mathbf{R}_{\mathbf{x}}^T \mathbf{a}(\theta)|^2. \tag{3.26}$$

For the general signal model, δ is set according to a desired probability of false alarm P_{FA}, i.e.,

$$P_{\text{FA}} = P(L(\mathbf{y}) > \delta | \mathcal{H}_0) \tag{3.27}$$

$$\delta = \mathcal{F}_{\chi_2^2}^{-1}(1 - P_{\text{FA}}) \tag{3.28}$$

where $\mathcal{F}_{\chi_2^2}^{-1}$ is the inverse central chi-squared distribution function with two degrees of freedom. The probability of detection is given by

$$P_{\text{D}} = P(L(\mathbf{y}) > \delta | \mathcal{H}_1) \tag{3.29}$$

$$P_{\text{D}} = 1 - \mathcal{F}_{\chi_2^2(\rho)} \left(\mathcal{F}_{\chi_2^2}^{-1}(1 - P_{\text{FA}}) \right) \tag{3.30}$$

where $\mathcal{F}_{\chi_2^2(\rho)}$ is the noncentral chi-squared distribution function with two degrees of freedom and noncentrality parameter ρ.

3.1.1.1 P_D for Orthogonal Waveforms

For orthogonal waveforms $\mathbf{R}_{\mathbf{x}}^T = \mathbf{I}_M$, therefore, the GLRT can be expressed as

$$L_{\text{Orthog}}(\hat{\theta}_{\text{ML}}) = \frac{\left|\mathbf{a}^H(\hat{\theta}_{\text{ML}})\mathbf{E}\mathbf{a}^*(\hat{\theta}_{\text{ML}})\right|^2}{M\mathbf{a}^H(\hat{\theta}_{\text{ML}})\mathbf{a}(\hat{\theta}_{\text{ML}})} \underset{\mathcal{H}_0}{\overset{\mathcal{H}_1}{\gtrless}} \delta_{\text{Orthog}} \tag{3.31}$$

and the statistics of $L(\hat{\theta}_{\text{ML}})$ for this case is

$$L_{\text{Orthog}}(\hat{\theta}_{\text{ML}}) \sim \begin{cases} \mathcal{H}_1 : \chi_2^2(\rho_{\text{Orthog}}), \\ \mathcal{H}_0 : \chi_2^2, \end{cases} \tag{3.32}$$

where

$$\rho_{\text{Orthog}} = \frac{M^2|\alpha|^2}{\sigma_n^2}. \tag{3.33}$$

δ_{Orthog} is set according to a desired probability of false alarm $P_{\text{PF-Orthog}}$, i.e.,

$$\delta_{\text{Orthog}} = \mathcal{F}_{\chi_2^2}^{-1}(1 - P_{\text{PF-Orthog}}) \tag{3.34}$$

and then the probability of detection for orthogonal waveforms is given by

$$P_{\text{D-Orthog}} = 1 - \mathcal{F}_{\chi_2^2(\rho_{\text{Orthog}})}\left(\mathcal{F}_{\chi_2^2}^{-1}(1 - P_{\text{PF-Orthog}})\right). \tag{3.35}$$

3.1.1.2 P_D for NSP Waveforms

For spectrum sharing waveforms $\mathbf{R}_{\mathbf{x}}^T = \mathbf{R}_{\check{\mathbf{x}}}^T$, therefore, the GLRT can be expressed as

$$L_{\text{NSP}}(\hat{\theta}_{\text{ML}}) = \frac{\left|\mathbf{a}^H(\hat{\theta}_{\text{ML}})\mathbf{E}\mathbf{a}^*(\hat{\theta}_{\text{ML}})\right|^2}{M\mathbf{a}^H(\hat{\theta}_{\text{ML}})\mathbf{R}_{\check{\mathbf{x}}}^T\mathbf{a}(\hat{\theta}_{\text{ML}})} \underset{\mathcal{H}_0}{\overset{\mathcal{H}_1}{\gtrless}} \delta_{\text{NSP}} \tag{3.36}$$

and the statistics of $L(\hat{\theta}_{\mathrm{ML}})$ for this case is

$$L_{\mathrm{NSP}}(\hat{\theta}_{\mathrm{ML}}) \sim \begin{cases} \mathcal{H}_1 : \chi^2_2(\rho_{\mathrm{NSP}}), \\ \mathcal{H}_0 : \chi^2_2, \end{cases} \tag{3.37}$$

where

$$\rho_{\mathrm{NSP}} = \frac{|\alpha|^2}{\sigma_n^2} |\mathbf{a}^H(\theta) \mathbf{R}_{\tilde{\mathbf{x}}}^T \mathbf{a}(\theta)|^2. \tag{3.38}$$

δ_{NSP} is set according to a desired probability of false alarm $P_{\text{PF-NSP}}$, i.e.,

$$\delta_{\mathrm{NSP}} = \mathcal{F}^{-1}_{\chi^2_2}(1 - P_{\text{PF-NSP}}) \tag{3.39}$$

and then the probability of detection for orthogonal waveforms is given by

$$P_{\text{D-NSP}} = 1 - \mathcal{F}_{\chi^2_2(\rho_{\mathrm{NSP}})} \left(\mathcal{F}^{-1}_{\chi^2_2}(1 - P_{\text{PF-NSP}}) \right). \tag{3.40}$$

3.1.2 Numerical Examples

In order to study the detection performance of spectrum sharing MIMO radars, we carry out Monte Carlo simulation using the radar parameters mentioned in Table 3.1.

3.1.3 Analysis of Case 1

For this case, at each run of Monte Carlo simulation we generate $\mathcal{K}$ Rayleigh interference channels each with dimensions $N^{\mathrm{BS}} \times M$, calculate their null spaces and construct corresponding projection matrices using Algorithm (2), determine the best channel to perform projection of radar signal using Algorithm (1), transmit NSP signal, estimate parameters θ

Table 3.1: MIMO Radar System Parameters

Parameters	Notations	Values
Radar/Communication System RF band	-	$3550 - 3650$ MHz
Radar antennas	M	8, 4
Communication System Antennas	N^{BS}	2
Carrier frequency	f_c	3.55 GHz
Wavelength	λ	8.5 cm
Inter-element antenna spacing	$3\lambda/4$	6.42 cm
Radial velocity	v_r	2000 m/s
Speed of light	c	3×10^8 m/s
Target distance from the radar	r_0	500 Km
Target angle	θ	$\hat{\theta}$
Doppler angular frequency	ω_D	$2\omega_c v_r/c$
Two way propagation delay	τ_r	$2r_0/c$
Path loss	α	$\hat{\alpha}$

and α from the received signal, and calculate the probability of detection for orthogonal and NSP waveforms.

Performance of Algorithms (1) **and** (2)**:** In Figure 3.2, we demonstrate the use of Algorithms (1) and (2) in improving target detection performance when multiple BSs are present in detection space of radar and the radar has to reliably detect target while not interfering with communication system of interest. As an example, we consider a scenario with five BSs and the radar has to select a projection channel which minimizes degradation in its waveform, thus, maximizing its probability of detection of the target.

In Figure 3.2(a), we consider the case when $\dim \mathcal{N}(\mathbf{H}_i) = 2$. We show detection results for five different NSP signals, i.e, radar waveform projected onto five different BSs. Note

that, in order to achieve a detection probability of 90%, we need 6 dB to 13 dB more gain in SNR as compared to the orthogonal waveform, depending upon which channel we select. Using Algorithms (1) and (2) we can select interference channel that results in minimum degradation of radar waveform and results in enhanced target detection performance with the minimum additional gain in SNR required. For example, Algorithms (1) and (2) would select BS#5 because in this case NSP waveform requires least gain in SNR to achieve a detection probability of 90% as compared to other BSs.

In Figure 3.2(b), we consider the case when $\dim \mathcal{N}(\mathbf{H}_i) = 6$. Similar to Figure 3.2(a) we show detection results for five different NSP signals but now MIMO radar has a larger array of antennas as compared to the previous case. In this case, in order to achieve a detection probability of 90%, we need 3 dB to 5 dB more gain in SNR as compared to the orthogonal waveform. As in the previous case, using Algorithms (1) and (2) we can select interference channel that results in minimum degradation of radar waveform and results in enhanced target detection performance with the minimum additional gain in SNR required. For example, Algorithms (1) and (2) would select BS#2 because in this case NSP waveform requires least gain in SNR to achieve a detection probability of 90% as compared to the other BSs.

The above two examples demonstrate the importance of Algorithms (1) and (2) in selecting interference channel for radar signal projection to maximize detection probability and minimize gain in SNR required as a result of NSP of radar waveforms for spectrum sharing.

Case 1(a): $\dim \mathcal{N}(\mathbf{H}_i) = 2$: In Figure 3.3, we plot the variations of probability of detection P_{D} as a function of signal-to-noise ratio (SNR) for various values of probability of false alarm P_{FA}. Each sub-plot represents the P_{D} for a fixed P_{FA}. We choose to evaluate P_{D} against P_{FA} values of $10^{-1}, 10^{-3}, 10^{-5}$ and 10^{-7} when the interference channel $\mathbf{H}_i$ has dimensions 2×4,

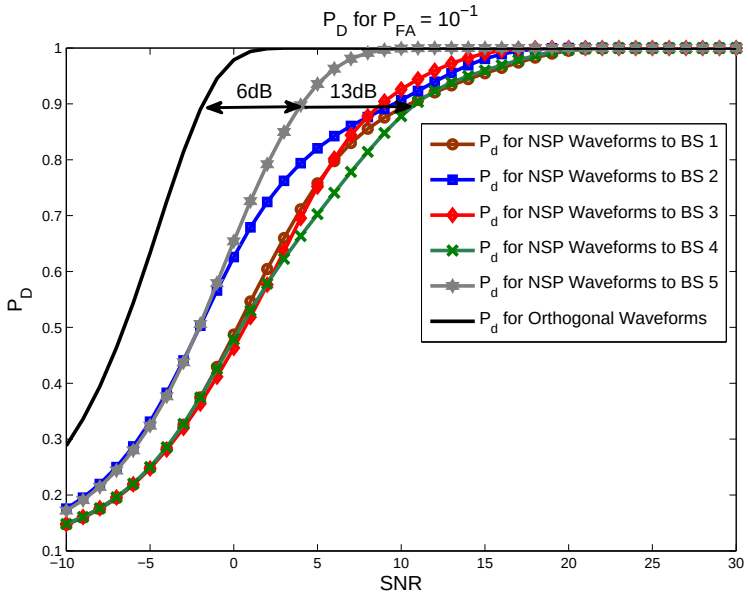

(a) Probability of detection when $\dim \mathcal{N}(\mathbf{H}_i) = 2$. Note that 6 dB to 13 dB of additional gain in SNR is required to detect target with 90% probability, depending upon the NSP waveform transmitted.

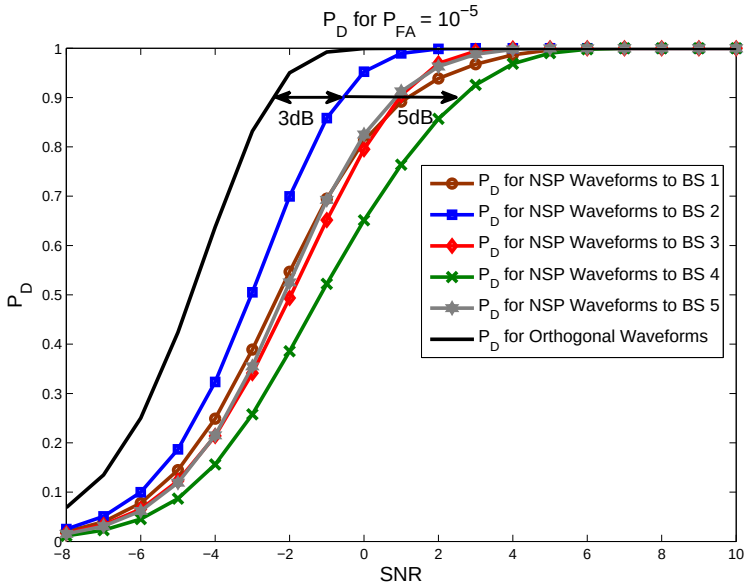

(b) Probability of detection when $\dim \mathcal{N}(\mathbf{H}_i) = 6$. Note that 3 dB to 5 dB of additional gain in SNR is required to detect target with 90% probability, depending upon the NSP waveform transmitted.

Figure 3.2: Case 1 – Performance of Algorithms (1) and (2): Using our spectrum sharing and projection algorithms, we can select interference channel for radar signal projection to maximize detection probability and minimize gain in SNR required as a result of NSP of radar waveforms. For example, Algorithms (1) and (2) select BS#5 and BS#2 for $\dim \mathcal{N}(\mathbf{H}_i) = 2$ and $\dim \mathcal{N}(\mathbf{H}_i) = 6$ cases, respectively, as they require minimum additional gain in SNR.

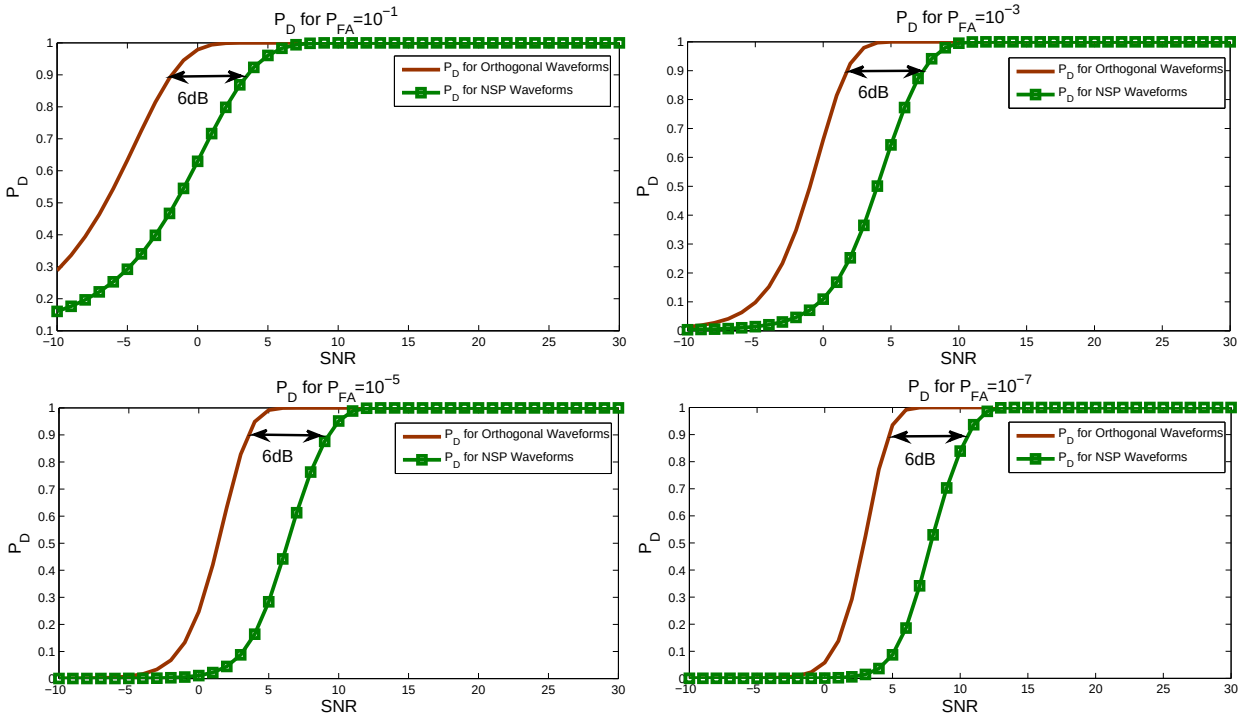

Figure 3.3: Case 1(a): $\dim \mathcal{N}(\mathbf{H}_i) = 2$ – P_{D} as a function of SNR: P_{D} as a function of SNR for various values of probability of false alarm P_{FA}, i.e., $P_{\mathrm{FA}} = 10^{-1}, 10^{-3}, 10^{-5}$ and 10^{-7}. The interference channel $\mathbf{H}_i$ has dimensions 2×4, i.e., the radar has $M = 4$ antennas and the communication system has $N^{\mathrm{BS}} = 2$ antennas, thus, we have a null space dimension of '$\dim \mathcal{N}(\mathbf{H}_i) = 2$'. Note that we need 6 dB more gain in SNR for the NSP waveform to get the same result produced by the orthogonal waveform.

i.e., the radar has $M = 4$ antennas and the communication system has $N^{\mathrm{BS}} = 2$ antennas, thus, we have a null space dimension of '$\dim \mathcal{N}(\mathbf{H}_i) = 2$'. When we compare the detection performance of two waveforms we note that in order to get a desired P_D for a fixed P_{FA} we need more SNR for NSP than orthogonal waveforms. For example, say we desire $P_D = 0.9$, then according to Figure 3.3 we need 6 dB more gain in SNR for NSP waveform to get the same result produced by the orthogonal waveform.

Case 1(b): $\dim \mathcal{N}(\mathbf{H}_i) = 6$: In Figure 3.4, similar to Figure 3.3, we do an analysis of P_{D} against the same values of P_{FA} but for interference channel $\mathbf{H}_i$ having dimensions 2×8, i.e., now the radar has $M = 8$ antennas and the communication system has $N^{\mathrm{BS}} = 2$ antennas,

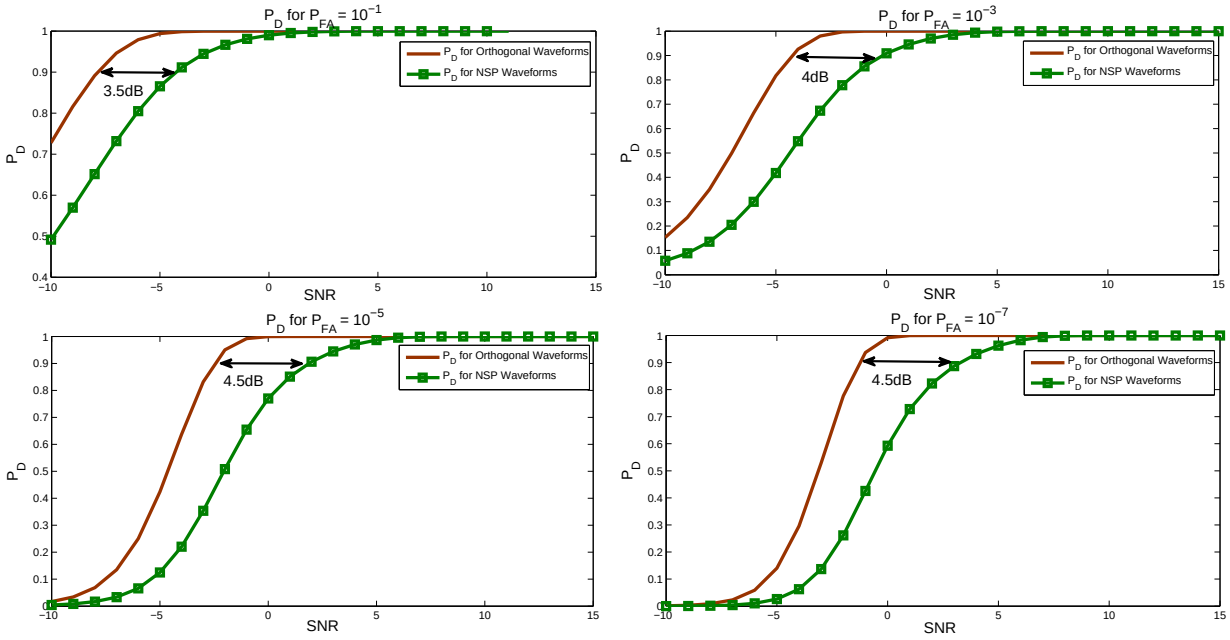

Figure 3.4: Case 1(b): $\dim \mathcal{N}(\mathbf{H}_i) = 6$ – P_{D} as a function of SNR: P_{D} as a function of SNR for various values of probability of false alarm P_{FA}, i.e., $P_{\mathrm{FA}} = 10^{-1}, 10^{-3}, 10^{-5}$ and 10^{-7}. The interference channel $\mathbf{H}_i$ has dimensions 2×8, i.e., the radar has $M = 8$ antennas and the communication system has $N^{\mathrm{BS}} = 2$ antennas, thus, we have a null space dimension of '$\dim \mathcal{N}(\mathbf{H}_i) = 6$'. Note that we need 3.5 to 4.5 dB more gain in SNR for the NSP waveform to get the same result produced by the orthogonal waveform.

thus, we have a null space dimension of '$\dim \mathcal{N}(\mathbf{H}_i) = 6$'. Similar to Case 1, when we compare the detection performance of two waveforms we note that in order to get a desired P_D for a fixed P_{FA} we need more SNR for NSP than the orthogonal waveforms. For example, say we desire $P_D = 0.9$, then according to Figure 3.4 we need 3.5 to 4.5 dB more gain in SNR for the NSP waveform to get the same result produced by the orthogonal waveform.

Comparison of Case 1(a) and Case 1(b): As expected, when SNR increases detection performance increases for both waveforms. However, when we compare the two waveforms at a fixed value of SNR, the orthogonal waveforms perform much better than the NSP waveform in detecting target. This is because our transmitted waveforms are no longer orthogonal and we lose the advantages promised by orthogonal waveforms when used in MIMO radars as

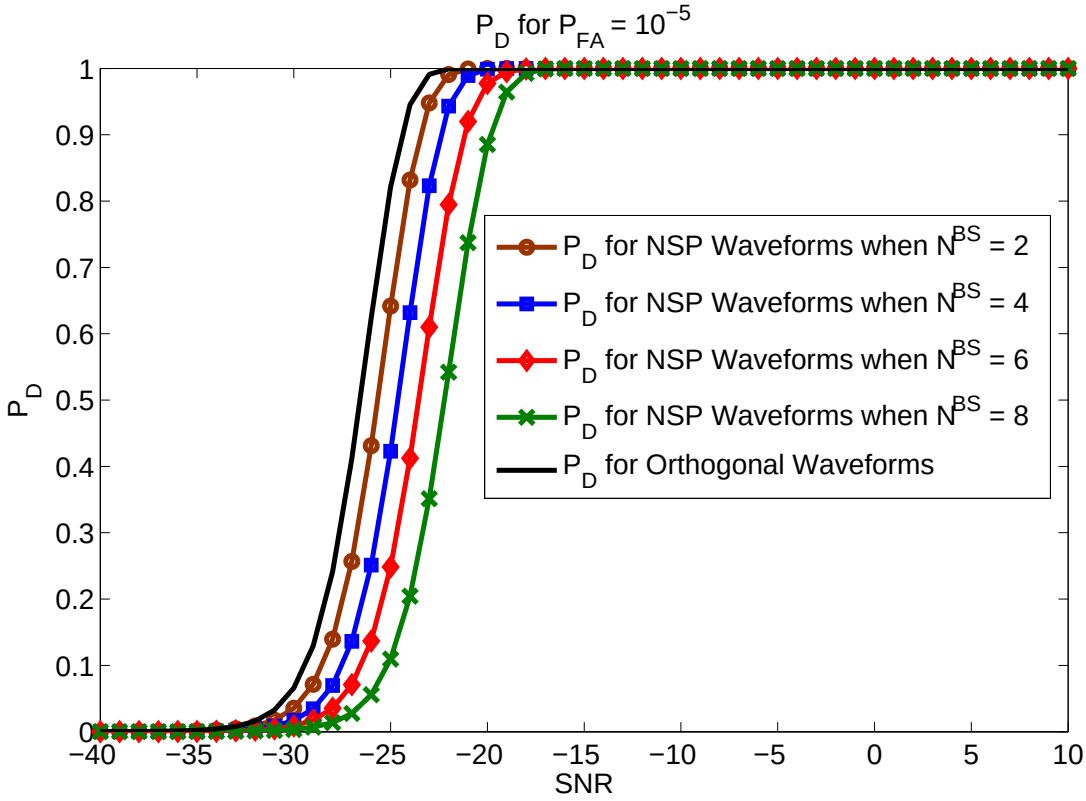

Figure 3.5: Case 2: P_{D} as a function of SNR for $P_{\mathrm{FA}} = 10^{-5}$. The MIMO radar mitigates interference to all the BSs in the network. As an example, we consider $M = 100$, $\mathcal{K} = 5$, and $N^{\mathrm{BS}} = \{2, 4, 6, 8\}$.

discussed in Section 2.1.4, but, we ensure zero interference to the BS of interest, thus, sharing radar spectrum at an increased cost of target detection in terms of SNR.

In Case 1(a), in order to achieve a desired P_D for a fixed P_{FA} we need more SNR for NSP as compared to Case 1(b). This is because we are using more radar antennas, while the antennas at the BS remain fixed in Case 1(b) which increases the dimension of the null space of the interference channel. This yields better detection performance even for NSP waveform. So, in order to mitigate the effect of NSP on radar performance one way is to employ a larger array at the radar transmitter.

3.1.4 Analysis of Case 2

For this case, at each run of Monte Carlo simulation we generate $\mathcal{K}$ Rayleigh interference channels, combine them into one interference channel with dimensions $\mathcal{K}N^{\mathrm{BS}} \times M$, calculate its null space and construct corresponding projection matrix using Algorithm (4), perform projection of radar signal using Algorithm (3), transmit NSP signal, estimate parameters θ and α from the received signal, and calculate the probability of detection for orthogonal and NSP waveforms.

In Figure 3.5, we consider the case when the radar has a very large antenna array as compared to the combined antenna array of $\mathcal{K}$ BSs. In such a scenario, we have enough degrees of freedom at the radar for reliable target detection and simultaneously nulling out interference to all the BSs present in the network. As an example, in Figure 3.5, we consider $M = 100$, $\mathcal{K} = 5$, and $N^{\mathrm{BS}} = \{2, 4, 6, 8\}$. We do an analysis of P_{D} against $P_{\mathrm{FA}} = 10^{-5}$ for the combined interference channel $\mathbf{H}$ having dimensions $\mathcal{K}N^{\mathrm{BS}} \times M$. When we compare the detection performance of original waveform and NSP waveform onto the combined channel we note that in order to get a desired P_D for a fixed P_{FA} we need more SNR for NSP than the orthogonal waveforms. For example, say we desire $P_D = 0.95$, then according to Figure 3.5 we need 1, 2, 3.5, and 4.5 dB more gain in SNR for the NSP waveform when N^{BS} is $2, 4, 6$, and 8, respectively, to get the same result produced by the orthogonal waveforms.

3.2 Cramér Rao bound (CRB)

In this section, a second performance metric i.e. Cramér Rao bound (CRB) for estimating target direction, i.e., angle of arrival or parameter θ is considered as a performance metric for the MIMO radar system. Degradation in the estimate of the target's angle of arrival

due to null space projection of the radar waveform is studied. The CRB for a single target, no-interference case, is given as in [13],

$$\mathrm{CRB}(\theta) = \frac{1}{2\,\mathrm{SNR}}\left(M_R \dot{\mathbf{a}}_T^H(\theta)\mathbf{R}_{\mathbf{x}}^T\dot{\mathbf{a}}_T(\theta) + \mathbf{a}_T^H(\theta)\mathbf{R}_{\mathbf{x}}^T\mathbf{a}_T(\theta)\|\dot{\mathbf{a}}_R(\theta)\|^2 - \frac{M_R\left|\mathbf{a}_T^H(\theta)\mathbf{R}_{\mathbf{x}}^T\dot{\mathbf{a}}_T(\theta)\right|^2}{\mathbf{a}_T^H(\theta)\mathbf{R}_{\mathbf{x}}^T\mathbf{a}_T(\theta)} \right)^{-1} \tag{3.41}$$

Numerical Example

In this section, an example of CRB for direction estimation is provided and effects of NSP on the radar performance are studied. In Figure 3.6, root-mean-square-error (RMSE) of different radar waveforms is shown. The performance of original radar waveform is compared with the NSP waveform projected onto $\mathbf{H}_{\mathrm{Best}}$ and $\mathbf{H}_{\mathrm{Worst}}$. Note that by using Algorithms (1) and (2) degradation in the radar performance can be minimized as the NSP waveform onto $\mathbf{H}_{\mathrm{Best}}$ is closer to the original radar waveform in RMSE sense than the NSP waveform onto $\mathbf{H}_{\mathrm{Worst}}$. Thus, by an appropriate selection of the interference channel degradation in the radar performance, due to the NSP of its waveform, can be minimized.

3.3 Maximum-Likelihood (ML) Estimation

In this section, a third performance metric is introduced which is the ML estimate of various target parameters including angle. The ML estimate for the case of no interference and a single target can be written as in [13],

$$(\hat{\theta}, \hat{\tau}_r, \hat{\omega}_D)_{\mathrm{ML}} = \underset{\theta,\tau_r,\omega_D}{\arg\max} \frac{\left|\mathbf{a}_R^H(\theta)\mathbf{E}(\tau_r,\omega_D)\mathbf{a}_T^*(\theta)\right|^2}{M_R\mathbf{a}_T^H(\theta)\mathbf{R}_{\mathbf{x}}^T\mathbf{a}_T(\theta)} \tag{3.42}$$

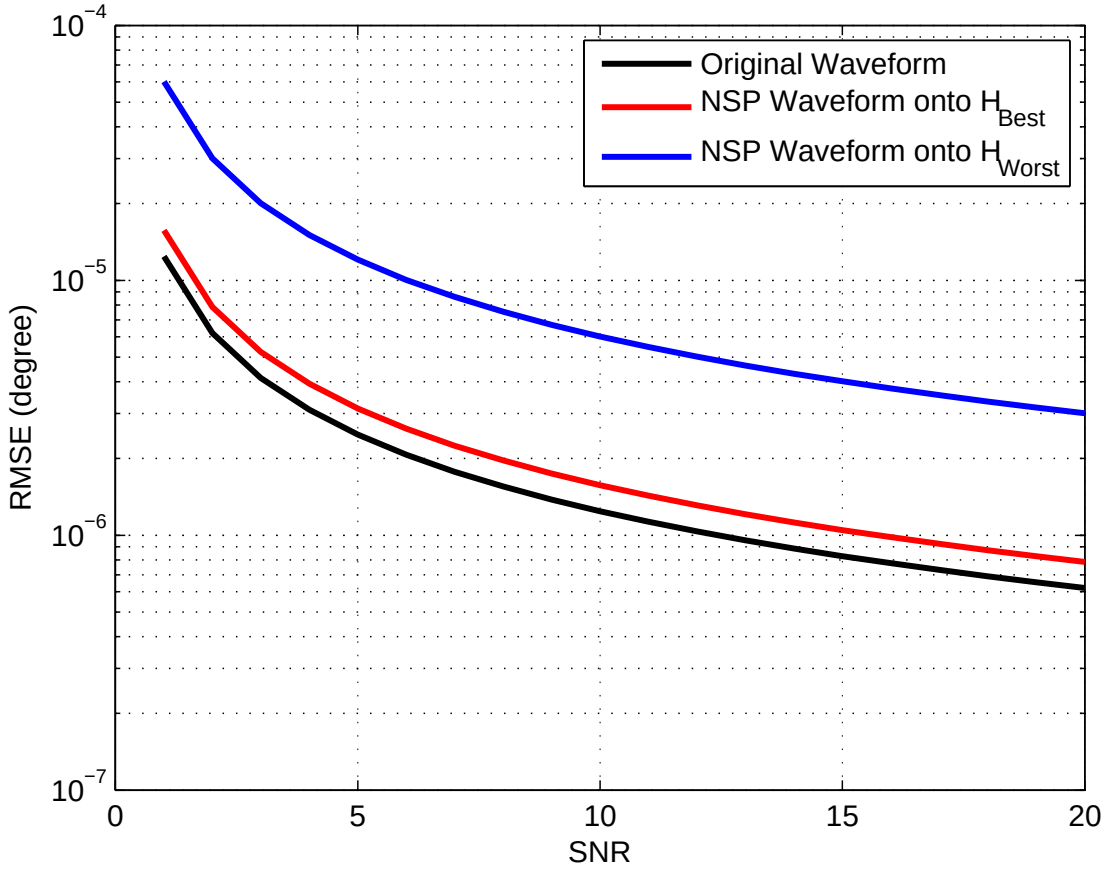

Figure 3.6: CRB on target direction estimation RMSE as a function of the SNR. $\mathbf{H}_{\text{Best}}$ and $\mathbf{H}_{\text{Worst}}$ channels are selected using Algorithms (1) and (2).

where

$$\dot{\mathbf{a}}_R(\theta) = \frac{d\mathbf{a}_R(\theta)}{d\theta}$$

$$\dot{\mathbf{a}}_T(\theta) = \frac{d\mathbf{a}_T(\theta)}{d\theta}$$

$$\mathbf{R}_{\mathbf{x}} = \int_{T_0} \mathbf{x}(t)\,\mathbf{x}^H(t)\,dt$$

$$\mathbf{E}(\tau_r, \omega_D) = \int_{T_0} \mathbf{y}(t)\,\mathbf{x}^H(t-\tau_r)\,e^{j\omega_D t}\,dt$$

τ_r is the propagation delay, two-way, between the target and the reference point, and ω_D is the Doppler frequency shift as defined in Table 3.1.

Numerical Example

In this section, a numerical example is discussed in which ML estimate of angle of arrival of a target is considered for a radar in a spectrum sharing environment. The interest is the estimation error of the angle due to the NSP of radar waveform. In Figure 3.7, original angles and estimated angles using ML estimation for different radar waveforms are compared. Using Algorithms (1) and (2) almost similar ML results for original waveform and the NSP waveform can be achieved which shows that by choosing $\mathbf{H}_{\text{Best}}$ to project degradation in radar performance can be kept at minimum. Note that the ML estimate for the NSP waveform onto $\mathbf{H}_{\text{Worst}}$ is much degraded from the original waveform and the NSP waveform onto $\mathbf{H}_{\text{Best}}$.

3.4 Beampattern

In addition to performance metrics like CRB and ML, changes in beampattern of the MIMO radar due to null space projection of the radar waveform is also of interest. Beampattern is a measure of beamformer's response to a target at direction θ given by, as in [13],

$$G(\theta, \theta_D) = \Gamma \frac{|\mathbf{a}_T^H(\theta)\mathbf{R}_{\mathbf{x}}^T\mathbf{a}_T(\theta_D)|^2}{\mathbf{a}_T^H(\theta_D)\mathbf{R}_{\mathbf{x}}^T\mathbf{a}_T(\theta_D)} \frac{|\mathbf{a}_R^H(\theta)\mathbf{a}_R(\theta_D)|^2}{M_R} \tag{3.43}$$

where Γ is the normalization constant and θ_D represents the digital steering direction of the main beam.

Numerical Example

In this section, a numerical example is discussed in which beampattern of MIMO radar

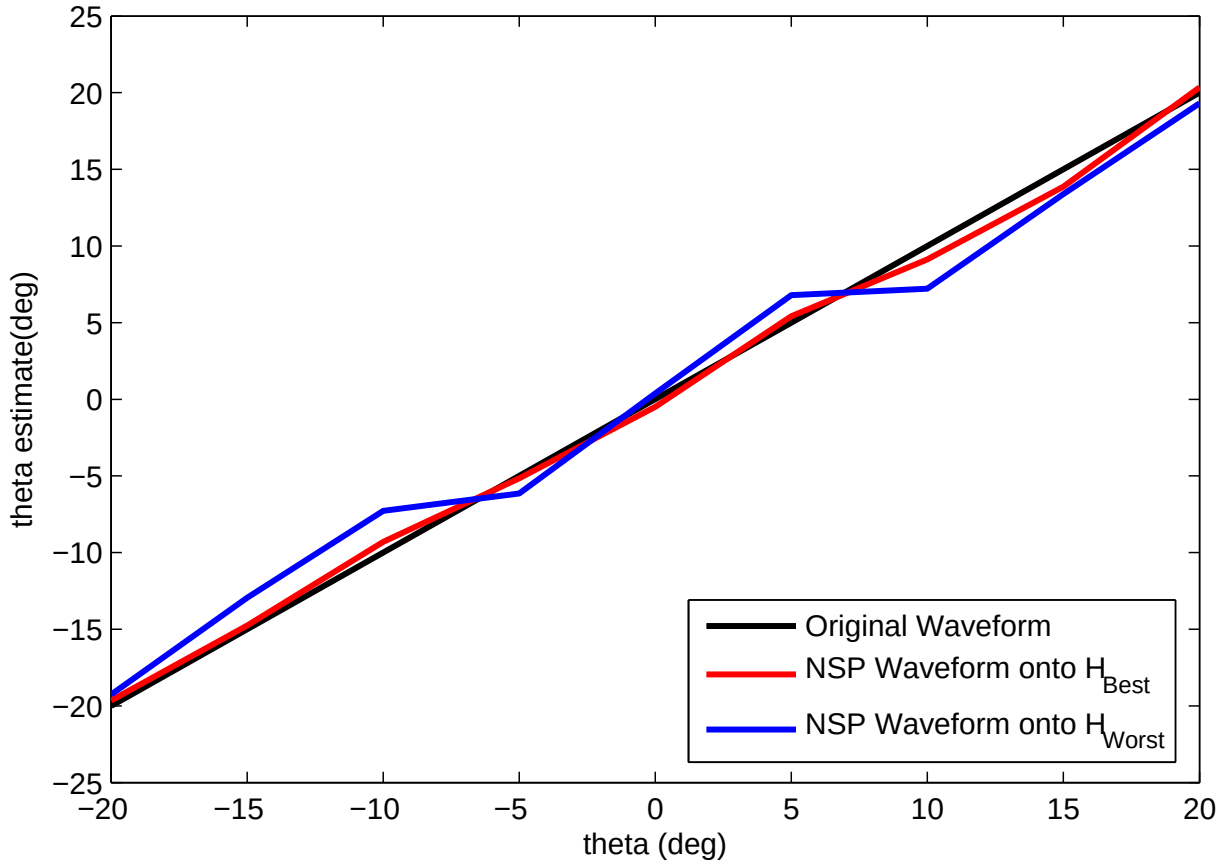

Figure 3.7: ML on target direction estimation. $\mathbf{H}_{\text{Best}}$ and $\mathbf{H}_{\text{Worst}}$ channels are selected using Algorithms (1) and (2).

for best and worst channel is compared with the original beampattern. The larger value of null space corresponds to the best channel and the smaller value corresponds to the worst channel. Note that by selecting appropriate channel for signal projection radar sidelobes can be manipulated. Thus, for the best radar performance, it is desirable to select interference channel with the maximum null space i.e. according to Algorithms (1) and (2).

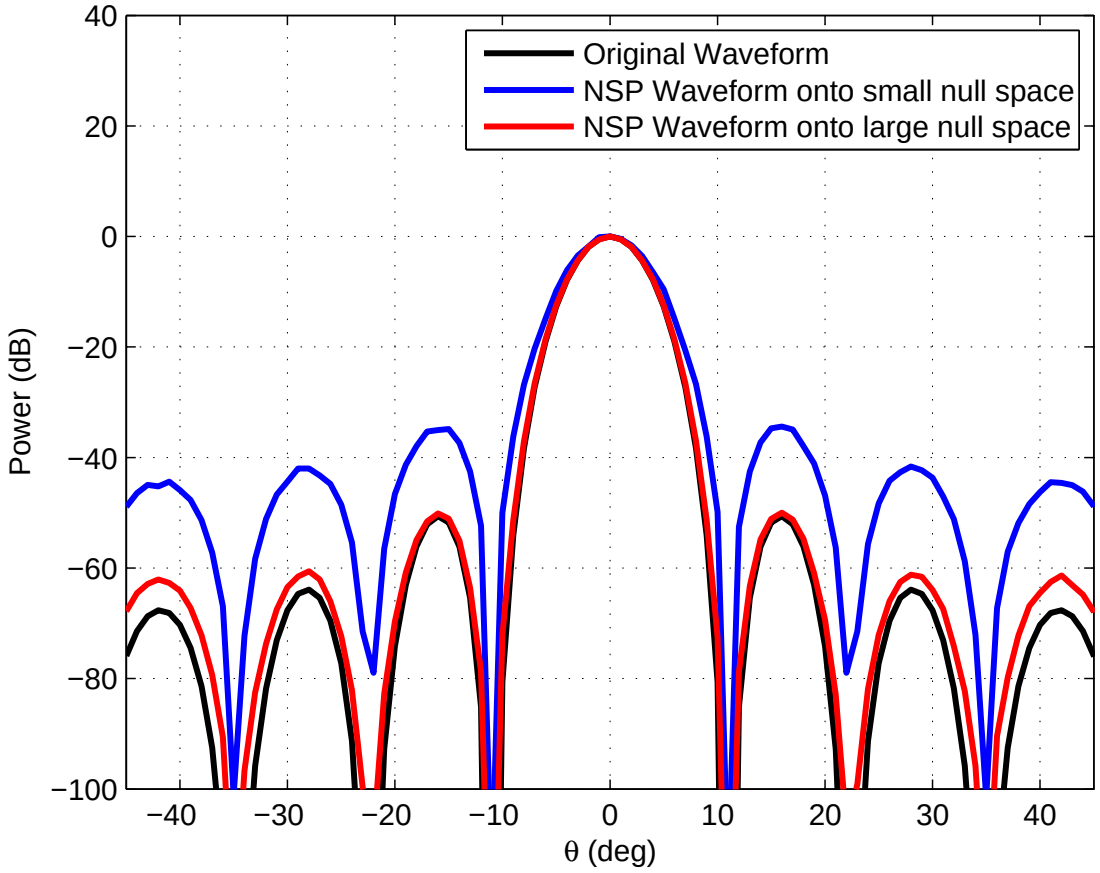

Figure 3.8: Beampattern of spectrum sharing MIMO radar. Beampattern of MIMO radar when different values of threshold are used to calculate the null space of interference channels in Algorithm (2).

3.5 Conclusion

In the future, radar RF spectrum will be shared with wireless communication systems to meet the growing bandwidth demands and mitigate the effects of spectrum congestion for commercial wireless services. In this chapter various performance metrics of a spectrum sharing MIMO radar were analyzed. First, an evaluation of the detection performance of spectrum sharing MIMO radars was provided. The statistical detection problem for target

detection was formulated and generalized likelihood ratio test was used to decide about the presence of target when using orthogonal waveforms and null-space projected (NSP) waveforms. Two spectrum sharing cases were considered. For 'Case 1', when $M \ll \mathcal{K}N^{\mathrm{BS}}$ but $M > N^{\mathrm{BS}}$, the radar had not sufficient degrees of freedom (DoF) available to simultaneously detect target and mitigate interference to $\mathcal{K}$ BSs in the network. For this case, interference was mitigated to one of the BS in the network and algorithms for interference channel selection and projection of radar waveform onto the selected interference channel were proposed in order to mitigate interference to the selected BS. Results showed that, about 6 dB of gain in SNR was required when $\dim \mathcal{N}(\mathbf{H}_i) = 2$ and 3.5 to 4.5 dB of gain in SNR was required when $\dim \mathcal{N}(\mathbf{H}_i) = 6$ when NSP waveforms were used instead of orthogonal waveforms for spectrum sharing. Analysis showed that this degradation in performance can be mitigated by using a larger array at the MIMO radar transmitter. For 'Case 2', when $M \gg \mathcal{K}N^{\mathrm{BS}}$, the radar had sufficient DoF available to simultaneously detect target and mitigate interference to all $\mathcal{K}$ BSs in the network. Results showed that when the interference channel has a large null space the amount of SNR required to achieve a desired detection probability is low and vice versa. It was shown that by using the proposed spectrum sharing and projection algorithms the radar was able to maximize target detection probability and minimize additional gain in SNR required to detect the target. For both the cases it was shown that when using the NSP waveforms, the detection performance degraded as compared to the orthogonal waveforms and more SNR to detect reliably was required. However, this resulted in co-channel spectrum sharing with communication systems which solved the spectrum congestion problem. Similarly, CRB, ML, and beampattern of spectrum sharing MIMO radar were analyzed and it was shown that by using the proposed algorithms the degradation in radar performance can be minimized.

Chapter 4

Radar Waveform Design for Spectrum Sharing

The design of multiple-input multiple-output (MIMO) radar waveforms with specified properties has a number of applications including clutter suppression and interference mitigation. In this chapter, binary phase shift keying (BPSK) and quadrature phase shift keying (QPSK) radar waveforms are designed with the aim to mitigate radar interference to communication system. BPSK and QPSK transmit beampattern of a MIMO radar are designed, when it is sharing its spectrum with a cellular system, with the constraint that the waveform is in the null space of interference channel between radar and communication system. The desired beampatterns are designed by unconstrained nonlinear optimization of the desired covariance matrix. This chapter considers waveform design problem for a stationary maritime MIMO radar when interference channels are changing slowly and thus they can be included in the beampattern matching optimization problem. In addition, this chapter considers the case when the maritime MIMO radar is moving and thus experiences interference channels that are changing fast enough to be not included in the optimization problem. For this

case, CE waveform are designed first and then projected onto the null space of interference channel, before transmission, in order to have zero interference to the communication system. Through simulations the effect of including the constraint of spectrum sharing or the waveform be in the null space of interference channel on the BPSK and QPSK waveform design is studied.

4.1 BPSK Radar Waveform

In this section, BPSK radar waveforms for spectrum sharing are designed, i.e., the problem of designing MIMO radar BPSK waveform to match a given beampattern in the presence of a cellular system is considered. The classical problem of beampattern matching is modified to include the constraint that the designed waveform should not cause interference to cellular system. So in addition to maximizing the received power at a number of given target locations and minimizing at all other locations this work also seeks to null out interference to cellular system through waveform design. The problem of waveform design for MIMO radars to coexist with a single communication system is considered in [18]. This work extends this approach and designs MIMO radar waveforms that can coexist with a cellular system, i.e., waveforms that support coexistence with many communication systems. Two types of radar platforms are considered. First, radar waveform is designed for stationary maritime MIMO radar which experiences stationary or slowly moving interference channels. Due to the tractability of interference channels, null space projection (NSP) is included in the unconstrained nonlinear optimization problem for waveform design. Second, radar waveform for moving maritime MIMO radar which experiences interference channels that are fast enough not to be included in the optimization problem due to their intractability. For this case, FACE waveforms are designed first and then projected onto null space of

interference channel before transmission. The performance of BPSK radar waveform for spectrum sharing is evaluated via numerical examples.

4.1.1 Finite Alphabet BPSK Beampattern Matching

In this section, finite alphabet BPSK waveforms are designed for spectrum sharing by considering a uniform linear array of M transmit antennas with inter-element spacing of half-wavelength. Then, the transmit signal is given as

$$\mathbf{x}(n) = \begin{bmatrix} x_1(n) & x_2(n) & \cdots & x_M(n) \end{bmatrix} \tag{4.1}$$

where $x_m(n)$ is the baseband signal from the m^{th} transmit element at time index n. Then the received signal from a target at location θ_k is given as

$$r_k(n) = \sum_{m=1}^{M} e^{-j(m-1)\pi \sin\theta_k} x_m(n), \qquad k = 1, 2, ..., K. \tag{4.2}$$

The above received signal can be represented compactly as

$$r_k(n) = \mathbf{a}^H(\theta_k)\mathbf{x}(n) \tag{4.3}$$

where $\mathbf{a}(\theta_k)$ is the steering vector defined as

$$\mathbf{a}(\theta_k) = \begin{bmatrix} 1 & e^{-j\pi \sin\theta_k} & e^{-j2\pi \sin\theta_k} & \cdots & e^{-j(M-1)\pi \sin\theta_k} \end{bmatrix} \tag{4.4}$$

Now, the power received from the target at location θ_k is given as

$$\begin{aligned} P(\theta_k) &= \mathbb{E}\{\mathbf{a}^H(\theta_k)\,\mathbf{x}(n)\,\mathbf{x}^H(n)\,\mathbf{a}(\theta_k)\} \\ &= \mathbf{a}^H(\theta_k)\,\mathbf{R}\,\mathbf{a}(\theta_k) \end{aligned} \tag{4.5}$$

where $\mathbf{R}$ is the correlation matrix of the transmitted signal. The desired beampattern $\phi(\theta_k)$ is formed by minimizing the square of the error between $P(\theta_k)$ and $\phi(\theta_k)$ through a cost function defined as

$$J(\mathbf{R}) = \frac{1}{K}\sum_{k=1}^{K}\Big(\mathbf{a}^H(\theta_k)\,\mathbf{R}\,\mathbf{a}(\theta_k) - \phi(\theta_k)\Big)^2. \tag{4.6}$$

It is important to realize that $\mathbf{R}$ can not be chosen freely since it is a covariance matrix of the transmitted waveform and thus it must be positive semidefinite. In addition, the interest is in constant envelope waveform, i.e., all antennas are required to transmit at same power level which translates to same diagonal elements of $\mathbf{R}$. Thus, $\mathbf{R}$ is subject to two constraints, namely,

$$\begin{aligned} &C_1 : \mathbf{v}^H\mathbf{R}\mathbf{v} \geq 0, && \forall\,\mathbf{v} \\ &C_2 : \mathbf{R}(m,m) = c, && m = 1, 2, \ldots, M. \end{aligned}$$

Thus, under the given constraints, a constrained nonlinear optimization problem can be setup to solve beampattern matching problem

$$\begin{aligned} \min_{\mathbf{R}} \quad & \frac{1}{K}\sum_{k=1}^{K}\Big(\mathbf{a}^H(\theta_k)\,\mathbf{R}\,\mathbf{a}(\theta_k) - \phi(\theta_k)\Big)^2 \\ \text{subject to} \quad & \mathbf{v}^H\mathbf{R}\mathbf{v}, && \forall\,\mathbf{v} \\ & \mathbf{R}(m,m) = c, && m = 1, 2, ..., M. \end{aligned} \tag{4.7}$$

For radar waveform design, this constrained nonlinear optimization problem can be transformed into an unconstrained nonlinear optimization problem by bounding the variables using multidimensional spherical coordinates [88]. Once $\mathbf{R}$ is synthesized, the waveform matrix $\mathbf{X}$ with N samples defined as

$$\mathbf{X} = \begin{bmatrix} \mathbf{x}(1) & \mathbf{x}(2) & \cdots & \mathbf{x}(N) \end{bmatrix}^T \tag{4.8}$$

can be realized from

$$\mathbf{X} = \boldsymbol{\mathcal{X}} \boldsymbol{\Lambda}^{1/2} \mathbf{W}^H \tag{4.9}$$

where $\boldsymbol{\mathcal{X}} \in \mathcal{C}^{N \times M}$ is a matrix of zero mean and unit variance Gaussian random variables, $\boldsymbol{\Lambda} \in \mathcal{R}^{M \times M}$ is the diagonal matrix of eigenvalues and $\mathbf{W} \in \mathcal{C}^{M \times M}$ is the matrix of eigenvectors of $\mathbf{R}$ [17]. Due to the distribution of $\boldsymbol{\mathcal{X}}$, the distribution of the random variables in the columns of $\mathbf{X}$ is also Gaussian but the waveform produced is not guaranteed to have the CE property.

4.1.2 Gaussian Covariance Matrix Synthesis for Desired Beampattern

An algorithm to directly synthesize covariance matrix of Gaussian random variables to generate finite alphabet constant envelope binary phase shift keying (BPSK) waveform for a desired beampattern was proposed by Ahmed et al [88]. Using the same approach, the Gaussian random variables with zero mean and unit variance, x_m, can be mapped onto BPSK symbol, z_m, through a simple relation

$$z_m = \text{sign}(x_m), \quad m \in \{1, 2, ..., M\}. \tag{4.10}$$

Using results from [88]

$$\begin{aligned}\mathbb{E}(z_p z_q) &= \mathbb{E}\Big(\text{sign}(x_p)\text{sign}(x_q)\Big) \\ &= \frac{2}{\pi}\sin^{-1}\big(\mathbb{E}(x_p x_q)\big)\end{aligned} \tag{4.11}$$

where x_p and x_q are Gaussian random variables and z_p and z_q are BPSK random variables. Therefore, the relation between real covariance matrix of beampattern $\mathbf{R}$ and Gaussian covariance matrix $\mathbf{R}_g$ is given by

$$\mathbf{R} = \frac{2}{\pi}\sin^{-1}(\mathbf{R}_g). \tag{4.12}$$

The Gaussian covariance matrix $\mathbf{R}_g$ is generated by the matrix $\mathbf{X}$ of Gaussian random variables using (4.9). Then BPSK random variables are generated directly by

$$\mathbf{Z} = \text{sign}(\mathbf{X}). \tag{4.13}$$

In [17], the authors propose to synthesize $\mathbf{R}_g$ as $\mathbf{R}_g = \mathbf{U}^H\mathbf{U}$ which transforms equation (4.7) as

$$\min_{\psi_{ij}} \frac{1}{K}\sum_{k=1}^{K}\Big(\frac{2}{\pi}\mathbf{a}^H(\theta_k)\sin^{-1}(\mathbf{U}^H\mathbf{U})\mathbf{a}(\theta_k) - \phi(\theta_k)\Big)^2 \tag{4.14}$$

where ψ_{ij} are the variables of the optimization problem and $\mathbf{U}$ is given by

$$\mathbf{U} = \begin{pmatrix} 1 & \sin(\psi_{21}) & \sin(\psi_{31})\sin(\psi_{32}) & \cdots & \prod_{m=1}^{M-1}\sin(\psi_{Mm}) \\ 0 & \cos(\psi_{21}) & \sin(\psi_{31})\cos(\psi_{32}) & \cdots & \prod_{m=1}^{M-2}\sin(\psi_{Mm})\cos(\psi_{M,M-1}) \\ 0 & 0 & \cos(\psi_{31}) & \ddots & \vdots \\ \vdots & \vdots & \ddots & \cdots & \sin(\psi_{M1})\cos(\psi_{M2}) \\ 0 & 0 & \cdots & \cdots & \cos(\psi_{M1}) \end{pmatrix} \tag{4.15}$$

4.1.3 BPSK Waveform Design for Spectrum Sharing

This section considers the design of MIMO radar waveforms for spectrum sharing. Two waveform design approaches are considered: one includes spectrum sharing constraint in the optimization problem and the other does not. The motivation and reasons for these two approaches and their impact on radar waveform performance is discussed in the following sections.

4.1.3.1 BPSK Waveform for Stationary MIMO Radar

Consider the case of a maritime MIMO radar when a ship is docked or is stationary and thus radar platform is stationary. In this case, interference channels have little to no variations and thus it is feasible to include the constraint of NSP into the optimization problem. The new optimization problem is formulated by the combination of projection matrix, equation

(2.22), into the optimization problem in equation (4.14) as

$$\min_{\psi_{ij}} \frac{1}{K} \sum_{k=1}^{K} \Big(\frac{2}{\pi} \mathbf{a}^H(\theta_k) \mathbf{P}_{\check{\mathbf{V}}} \sin^{-1}(\mathbf{U}^H \mathbf{U}) \mathbf{P}_{\check{\mathbf{V}}}^H \mathbf{a}(\theta_k) - \phi(\theta_k) \Big)^2. \tag{4.16}$$

This optimization problem does not guarantee to generate constant envelope radar waveform but guarantees that the designed waveform is in the null space of the interference channel or the designed waveform does not cause interference to the communication system. In addition, it is an evaluation of the impact of the NSP on the CE radar waveforms. The waveform generation process is shown using the block diagram of Figure 4.1. The waveform generated by solving the optimization problem in equation (4.16) and then using equation (4.9) is denoted by $\mathbf{X}_{\text{opt}}$. The corresponding BPSK waveform is denoted by $\mathbf{Z}_{\text{opt}}$ which is obtained using equation (4.13). Then, the output NSP waveform is given by

$$\mathbf{Z}_{\text{opt-NSP}} = \mathbf{Z}_{\text{opt}} \mathbf{P}_{\check{\mathbf{V}}}^H. \tag{4.17}$$

4.1.3.2 BPSK Waveform for Moving MIMO Radar

Consider the case of a maritime radar which is moving and thus experiences interference channels that change too fast. In this case, it is not feasible to include the NSP in the optimization problem. Alternately, one can design CE waveforms by solving the optimization problem in equation (4.14) and then projection the waveform onto the null space of interference channel. The waveform generation process is shown using the block diagram of Figure 4.2. Thus, the CE waveform is generated according to the method explained in Section 4.1.2

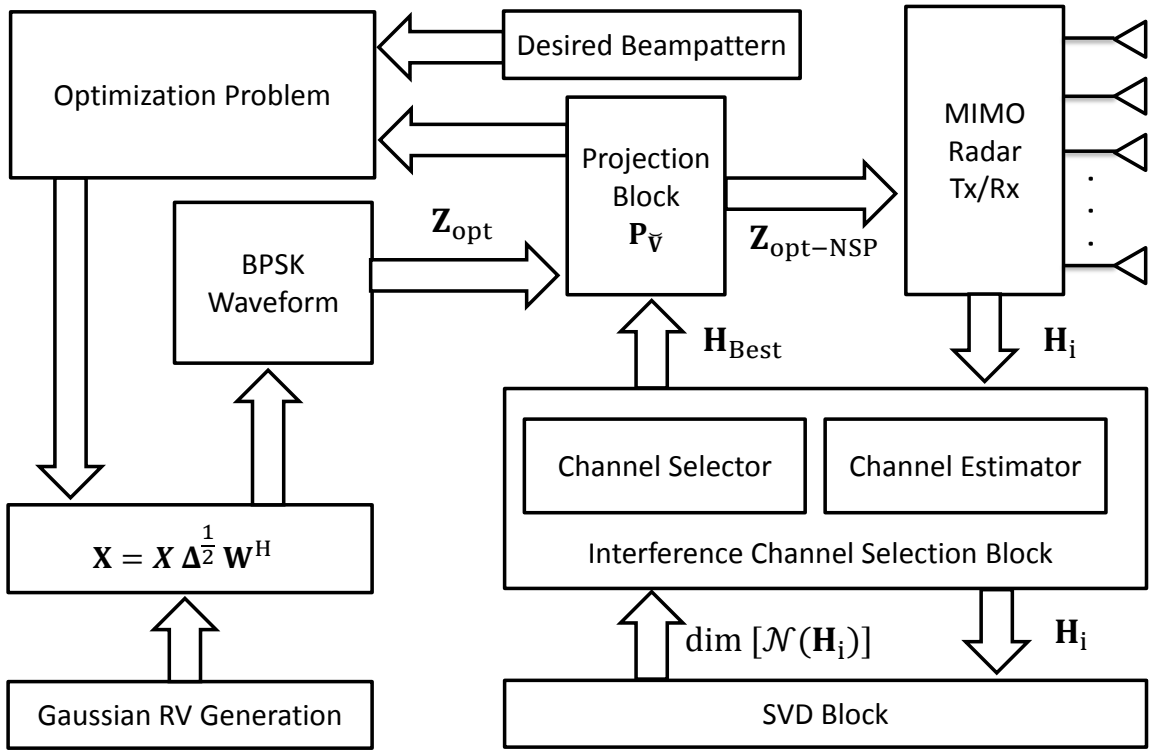

Figure 4.1: Block diagram of the transmit beampattern design problem for a stationary maritime MIMO radar. The desired waveform is generated by including the projection matrix $\mathbf{P}_{\check{\mathbf{V}}}$, for the candidate interference channel $\mathbf{H}_{\text{Best}}$, in the optimization process. For this waveform constant envelope property is not guaranteed. The candidate interference channel is selected by Algorithms (1) and (2).

and then projected onto the null space of the interference channel according to

$$\mathbf{Z}_{\text{NSP}} = \mathbf{Z}\mathbf{P}_{\check{\mathbf{V}}}^{H}. \tag{4.18}$$

This formulation projects the CE waveform onto the null space of the interference channel.

In the next section, the impact of projection on the radar waveform performance is studied.

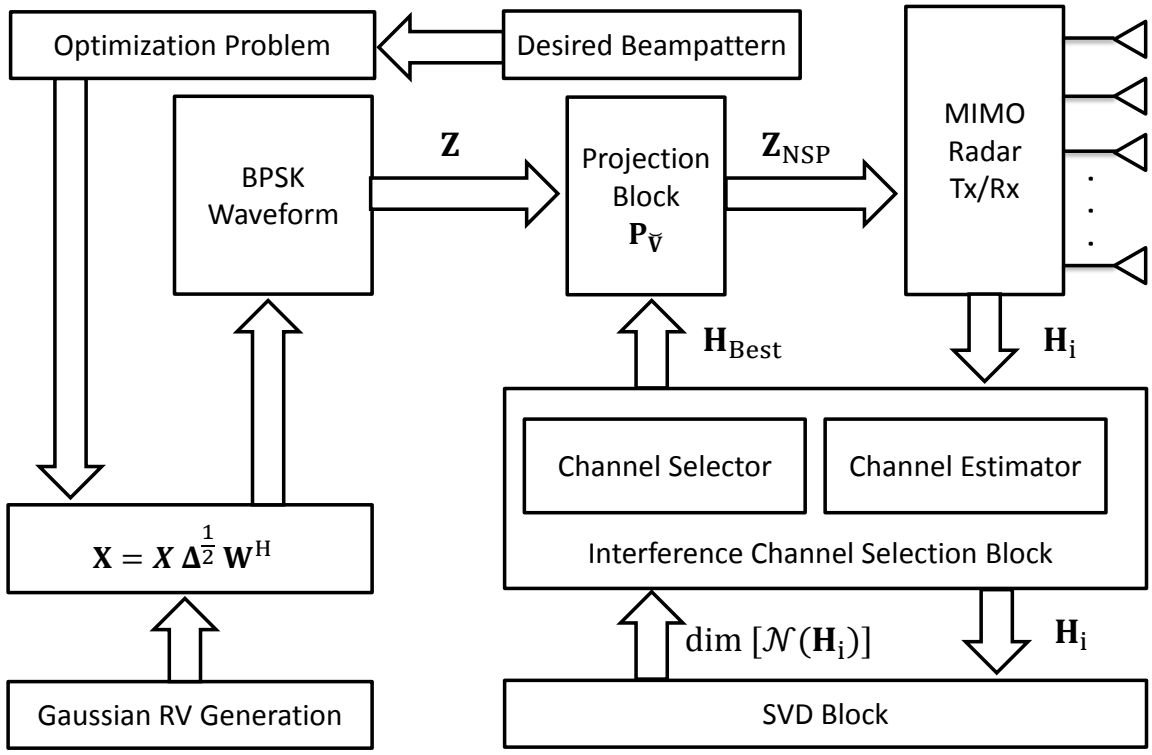

Figure 4.2: Block diagram of the transmit beampattern design problem for a moving maritime MIMO radar. The desired waveform is generated with constant envelope property and then projected onto the candidate interference channel $\mathbf{H}_{\mathrm{Best}}$ via projection matrix $\mathbf{P}_{\check{\mathbf{V}}}$. The candidate interference channel is selected by Algorithms (1) and (2).

4.1.4 Numerical Examples

This section provides numerical examples discussing BPSK waveforms for spectrum sharing. A uniform linear array (ULA) of ten elements, i.e., $M = 10$, is considered with an interelement spacing of half-wavelength. In addition, all antennas transmit at the same power level which is fixed to unity. Each antenna transmits a waveform with $N = 100$ symbols and the resulting beampattern is the average of 100 Monte-Carlo trials of BPSK waveforms. The

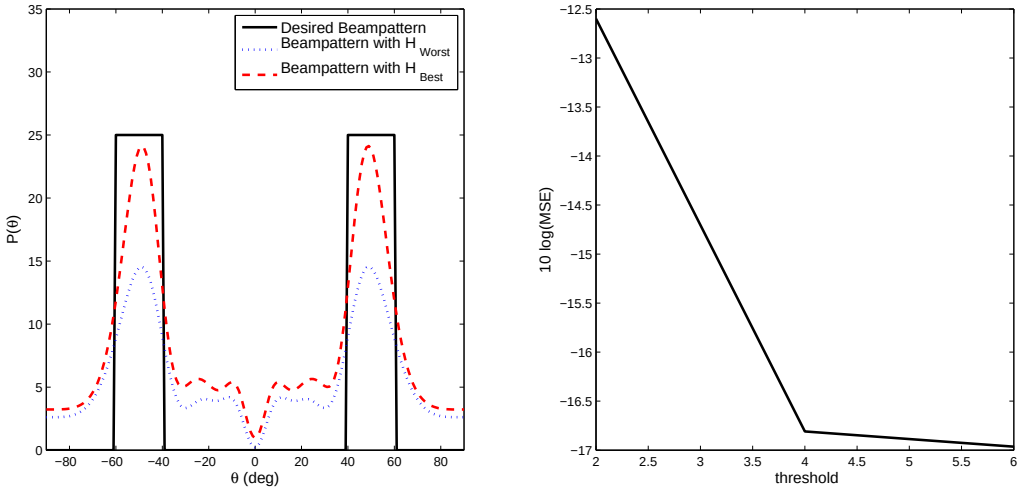

Figure 4.3: Transmit beampattern and its MSE for a *stationary* maritime MIMO radar. The figure compares the desired beampattern with the average beampattern of BPSK waveforms for null space projection *included* in beampattern matching optimization problem for candidate interference channel $\mathbf{H}_{\text{Best}}$.

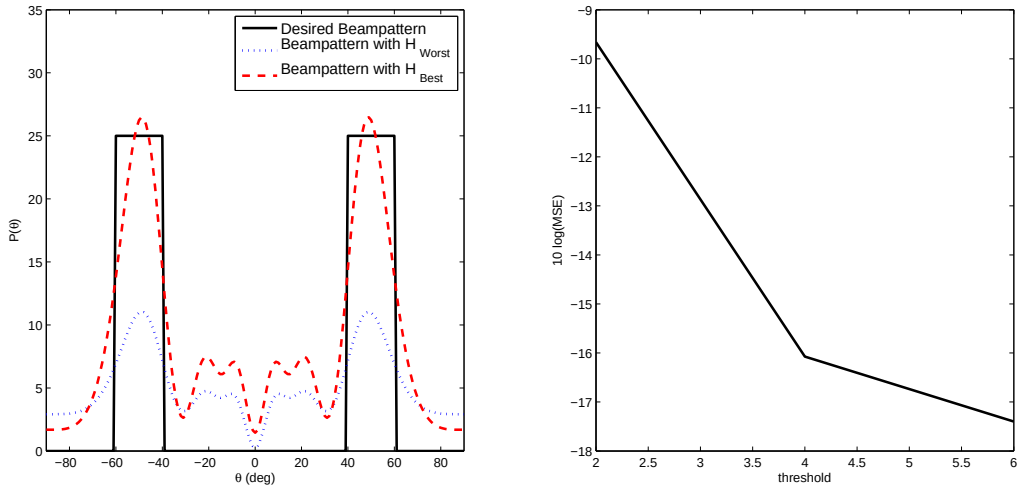

Figure 4.4: Transmit beampattern and its MSE for a *moving* maritime MIMO radar. The figure compares the desired beampattern with the average beampattern of BPSK waveforms for null space projection *after* optimization for candidate interference channel $\mathbf{H}_{\text{Best}}$.

mean-squared error (MSE) between the desired, $\phi(\theta_k)$, and actual beampatterns, $P(\theta_k)$, is given by

$$\text{MSE} = \frac{1}{K}\sum_{k=1}^{K}\Big(P(\theta_k) - \phi(\theta_k)\Big)^2.$$

The interference channels, $\mathbf{H}_i$, are modeled as a Rayleigh fading channels with Rayleigh probability density function (pdf) given by

$$f(h|\rho) = \frac{h}{\rho^2}e^{\frac{-h^2}{2\rho^2}}$$

where ρ is the mode of the Rayleigh distribution. The candidate interference channel, $\breve{\mathbf{H}}$, for waveform design is selected using Algorithm (1) and its null space is computed using SVD according to Algorithm (2).

In Figure 4.3, the desired beampattern has two main lobes from $-60°$ to $-40°$ and from $40°$ to $60°$. It is the beampattern for stationary maritime MIMO radar obtained by solving the optimization problem in equation (2.22). The resulting waveform covariance matrix is given by

$$\mathbf{R}_{\text{opt-NSP}} = \frac{1}{N}\mathbf{Z}_{\text{opt-NSP}}^H\mathbf{Z}_{\text{opt-NSP}}$$

Note that the desired beampattern and the beampattern obtained by including the projection matrix inside the optimization problem match closely for interference channel $\mathbf{H}_{\text{Best}}$ than $\mathbf{H}_{\text{Worst}}$.

In Figure 4.4, the desired beampattern has two main lobes from $-60°$ to $-40°$ and from $40°$ to $60°$. It represents the beampattern of a moving maritime MIMO radar. Since interference channels are evolving fast, beampattern is obtained by solving the optimization problem in equation (4.14) and then projecting the resulting waveform onto the null space of $\breve{\mathbf{H}}$ using the projection matrix in equation (2.22). The resulting waveform covariance matrix is given

by

$$\mathbf{R}_{\text{NSP}} = \frac{1}{N}\mathbf{Z}_{\text{NSP}}^{H}\mathbf{Z}_{\text{NSP}}.$$

Note that the desired beampattern and the beampattern obtained by projecting the waveform onto the null space of interference channel match closely for interference channel $\mathbf{H}_{\text{Best}}$ than $\mathbf{H}_{\text{Worst}}$.

In Figures 4.3 and 4.4, MSE of beampattern matching design problem is shown. It shows that interference channel with the largest null space have the least MSE. This is in accordance with the methodology to select $\mathbf{H}_{\text{Best}}$ among $\mathbf{N}_{\text{BS}}$ interference channels using Algorithms (1) and (2).

In Figures 4.3 and 4.4, the desired beampattern match closely the actual beampattern when interference channel $\mathbf{H}_{\text{Best}}$ is used. Thus, by careful selection of interference channel using Algorithms (1) and (2), when sharing spectrum with a cellular system, we can obtain a beampattern which is very close to the desired beampattern and in addition do not interfere with the communication system

4.2 QPSK Radar Waveform

In this section, it is proved that finite alphabet constant-envelope (FACE) quadrature-pulse shift keying (QPSK) waveforms can be designed to realize a given covariance matrix by transforming a constrained nonlinear optimization problem into an unconstrained nonlinear optimization problem. In addition, QPSK waveforms are designed in a way that they don't cause interference to a cellular system, by steering nulls towards a selected base station (BS). The BS is selected according to our algorithm which guarantees minimum degradation in radar performance due to null space projection (NSP) of radar waveforms. QPSK waveforms

Table 4.1: Table of Notations for Waveform Design

Notation	Description
$\widetilde{\mathbf{x}}(n)$	Transmitted QPSK radar waveform
$\mathbf{a}(\theta_k)$	Steering vector to steer signal to target angle θ_k
$\widetilde{\mathbf{r}}_k(n)$	Received radar waveform from target at θ_k
$\widetilde{\mathbf{R}}$	Correlation matrix of QPSK waveforms
$\mathbf{s}_j(n)$	Signal transmitted by the j^{th} UE in the i^{th} cell
$\mathcal{L}_i$	Total number of user equipments (UEs) in the i^{th} cell
$\mathcal{K}$	Total number of BSs
M	Radar transmit/receive antennas
N_{BS}	BS transmit/receive antennas
N_{UE}	UE transmit/receive antennas
$\mathbf{H}_i$	i^{th} interference channel
H_n	Hermite Polynomial
$\mathbf{y}_i(n)$	Received signal at the i^{th} BS
$\mathbf{P}_i$	Projection matrix for the i^{th} channel

are designed with spectrum sharing constraints for a stationary and moving radar platform. It is shown that the waveform designed for stationary MIMO radar matches the desired beampattern closely, when the number of BS antennas N^{BS} is considerably less than the number of radar antennas M, due to quasi-static interference channel. However, for moving radar the difference between designed and desired waveforms is larger than stationary radar, due to rapidly changing channel.

4.2.1 Finite Alphabet Constant-Envelope QPSK Beampattern Design

In this section, QPSK waveforms having finite alphabets and constant-envelope property are designed. A uniform linear array (ULA) of M transmit antennas with inter-element spacing of half-wavelength is considered. Then, the transmitted QPSK signal is given as

$$\widetilde{\mathbf{x}}(n) = \begin{bmatrix} \widetilde{x}_1(n) & \widetilde{x}_2(n) & \cdots & \widetilde{x}_M(n) \end{bmatrix}^T \tag{4.19}$$

where $\widetilde{x}_m(n)$ is the QPSK signal from the m^{th} transmit element at time index n. Then, the received signal from a target at location θ_k is given as

$$\widetilde{r}_k(n) = \sum_{m=1}^{M} e^{-j(m-1)\pi \sin\theta_k} \widetilde{x}_m(n), \quad k = 1, 2, ..., K, \tag{4.20}$$

where K is the total number of targets. The received signal can be compactly written as

$$\widetilde{r}_k(n) = \mathbf{a}^H(\theta_k)\widetilde{\mathbf{x}}(n) \tag{4.21}$$

where $\mathbf{a}(\theta_k)$ is the steering vector defined as

$$\mathbf{a}(\theta_k) = \begin{bmatrix} 1 & e^{-j\pi \sin\theta_k} & \cdots & e^{-j(M-1)\pi \sin\theta_k} \end{bmatrix}^T. \tag{4.22}$$

The power received at the target located at θ_k is given as

$$\begin{aligned} P(\theta_k) &= \mathbb{E}\{\mathbf{a}^H(\theta_k)\, \widetilde{\mathbf{x}}(n)\, \widetilde{\mathbf{x}}^H(n)\, \mathbf{a}(\theta_k)\} \\ &= \mathbf{a}^H(\theta_k)\, \widetilde{\mathbf{R}}\, \mathbf{a}(\theta_k) \end{aligned} \tag{4.23}$$

where $\widetilde{\mathbf{R}}$ is correlation matrix of the transmitted QPSK waveform. The desired QPSK beampattern $\phi(\theta_k)$ is formed by minimizing the square of the error between $P(\theta_k)$ and $\phi(\theta_k)$ through a cost function defined as

$$J(\widetilde{\mathbf{R}}) = \frac{1}{K}\sum_{k=1}^{K}\Big(\mathbf{a}^H(\theta_k)\,\widetilde{\mathbf{R}}\,\mathbf{a}(\theta_k) - \phi(\theta_k)\Big)^2. \tag{4.24}$$

Since, $\widetilde{\mathbf{R}}$ is covariance matrix of the transmitted signal it must be positive semi-definite. Moreover, due to the interest in constant-envelope property of waveforms, all antennas must transmit at the same power level. The optimization problem in equation (4.24) has some constraints and, thus, can't be chosen freely. In order to design finite alphabet constant-envelope waveforms, the following constraints must be satisfied:

$$\begin{aligned} &C_1 : \mathbf{v}^H\widetilde{\mathbf{R}}\mathbf{v} \geq 0, && \forall\,\mathbf{v}, \\ &C_2 : \widetilde{\mathbf{R}}(m,m) = c, && m = 1,2,\ldots,M, \end{aligned}$$

where C_1 satisfies the 'positive semi-definite' constraint and C_2 satisfies the 'constant-envelope' constraint. Thus, a constrained nonlinear optimization problem given as

$$\begin{aligned} \min_{\widetilde{\mathbf{R}}} \quad & \frac{1}{K}\sum_{k=1}^{K}\Big(\mathbf{a}^H(\theta_k)\,\widetilde{\mathbf{R}}\,\mathbf{a}(\theta_k) - \phi(\theta_k)\Big)^2 \\ \text{subject to} \quad & \mathbf{v}^H\widetilde{\mathbf{R}}\mathbf{v} \geq 0, \qquad \forall\,\mathbf{v}, \\ & \widetilde{\mathbf{R}}(m,m) = c, \qquad m = 1,2,...,M. \end{aligned} \tag{4.25}$$

Ahmed et al. showed that, by using multi-dimensional spherical coordinates, this constrained nonlinear optimization can be transformed into an unconstrained nonlinear optimization [17].

Once $\widetilde{\mathbf{R}}$ is synthesized, the waveform matrix $\widetilde{\mathbf{X}}$ with N samples is given as

$$\widetilde{\mathbf{X}} = \begin{bmatrix} \widetilde{\mathbf{x}}(1) & \widetilde{\mathbf{x}}(2) & \cdots & \widetilde{\mathbf{x}}(N) \end{bmatrix}^T. \tag{4.26}$$

This can be realized from

$$\widetilde{\mathbf{X}} = \mathfrak{X}\mathbf{\Lambda}^{1/2}\mathbf{W}^H \tag{4.27}$$

where $\mathfrak{X} \in \mathcal{C}^{N\times M}$ is a matrix of zero mean and unit variance Gaussian random variables, $\mathbf{\Lambda} \in \mathcal{R}^{M\times M}$ is the diagonal matrix of eigenvalues, and $\mathbf{W} \in \mathcal{C}^{M\times M}$ is the matrix of eigenvectors of $\widetilde{\mathbf{R}}$ [89]. Note that $\widetilde{\mathbf{X}}$ has Gaussian distribution due to $\mathfrak{X}$ but the waveform produced is not guaranteed to have the CE property.

4.2.2 Finite Alphabet Constant-Envelope QPSK Waveforms

In [18], an algorithm to synthesize FACE QPSK waveforms to realize a given covariance matrix, $\widetilde{\mathbf{R}}$, with complex entries was presented. However, it was not proved that such a covariance matrix is positive semi-definite and the constrained nonlinear optimization problem can be transformed into an un-constrained nonlinear optimization problem, this claim is proved in this section.

Consider zero mean and unit variance Gaussian random variables (RVs) $\widetilde{x}_m$ and $\widetilde{y}_m$ that can be mapped onto a QPSK RV $\widetilde{z}_m$ through, as in [18],

$$\widetilde{z}_m = \frac{1}{\sqrt{2}}\Big[\text{sign}(\widetilde{x}_m) + \jmath\,\text{sign}(\widetilde{y}_m)\Big]. \tag{4.28}$$

Then, it is straight forward to write the (p,q)th element of the complex covariance matrix

as

$$\mathbb{E}\{\widetilde{z}_p\widetilde{z}_q\} = \gamma_{pq} = \gamma_{\Re_{pq}} + \jmath\,\gamma_{\Im_{pq}} \tag{4.29}$$

where $\gamma_{\Re_{pq}}$ and $\gamma_{\Im_{pq}}$ are the real and imaginary parts of γ_{pq}, respectively. If, Gaussian RVs $\widetilde{x}_p, \widetilde{x}_q, \widetilde{y}_p$, and $\widetilde{y}_q$ are chosen such that

$$\begin{aligned}\mathbb{E}\{\widetilde{x}_p\widetilde{x}_q\} &= \mathbb{E}\{\widetilde{y}_p\widetilde{y}_q\}\\ \mathbb{E}\{\widetilde{x}_p\widetilde{y}_q\} &= -\mathbb{E}\{\widetilde{y}_p\widetilde{x}_q\}\end{aligned} \tag{4.30}$$

then real and imaginary parts of γ_{pq} can be written as

$$\begin{aligned}\gamma_{\Re_{pq}} &= \mathbb{E}\Big\{\text{sign}(\widetilde{x}_p)\text{sign}(\widetilde{x}_q)\Big\}\\ \gamma_{\Im_{pq}} &= \mathbb{E}\Big\{\text{sign}(\widetilde{y}_p)\text{sign}(\widetilde{x}_q)\Big\}.\end{aligned} \tag{4.31}$$

Then, from equation (4.74) Section 4.2.4

$$\mathbb{E}\{\widetilde{z}_p\widetilde{z}_q\} = \frac{2}{\pi}\left[\sin^{-1}\left(\mathbb{E}\{\widetilde{x}_p\widetilde{x}_q\}\right) + \jmath\,\sin^{-1}\left(\mathbb{E}\{\widetilde{y}_p\widetilde{x}_q\}\right)\right]. \tag{4.32}$$

The complex Gaussian covariance matrix $\widetilde{\mathbf{R}}_g$ is defined as

$$\widetilde{\mathbf{R}}_g \triangleq \Re(\mathbf{R}_g) + \jmath\,\Im(\mathbf{R}_g) \tag{4.33}$$

where $\Re(\mathbf{R}_g)$ and $\Im(\mathbf{R}_g)$ both have real entries, since $\mathbf{R}_g$ is a real Gaussian covariance matrix. Then, equation (4.32) can be written as

$$\widetilde{\mathbf{R}} = \frac{2}{\pi}\left[\sin^{-1}\Big(\Re(\mathbf{R}_g)\Big) + \jmath\,\sin^{-1}\Big(\Im(\mathbf{R}_g)\Big)\right]. \tag{4.34}$$

In [18], it is proposed to construct complex Gaussian covariance matrix via transform $\widetilde{\mathbf{R}}_g = \widetilde{\mathbf{U}}^H\widetilde{\mathbf{U}}$, where $\widetilde{\mathbf{U}}$ is given by equation (4.37). Then, $\widetilde{\mathbf{U}}$ can be written as

$$\widetilde{\mathbf{U}} = \Re(\widetilde{\mathbf{U}}) + \jmath\Im(\widetilde{\mathbf{U}}) \tag{4.35}$$

where $\Re(\widetilde{\mathbf{U}})$ and $\Im(\widetilde{\mathbf{U}})$ are given by equations (4.38) and (4.39), respectively. Alternately, $\widetilde{\mathbf{R}}_g$ can also be expressed as

$$\widetilde{\mathbf{R}}_g = \Big[\Re(\widetilde{\mathbf{U}})^H\Re(\widetilde{\mathbf{U}}) + \Im(\widetilde{\mathbf{U}})^H\Im(\widetilde{\mathbf{U}})\Big] + \jmath\Big[\Re(\widetilde{\mathbf{U}})^H\Im(\widetilde{\mathbf{U}}) - \Im(\widetilde{\mathbf{U}})^H\Re(\widetilde{\mathbf{U}})\Big]. \tag{4.36}$$

$$\widetilde{\mathbf{U}} = \begin{pmatrix} e^{j\psi_1} & e^{j\psi_2}\sin(\psi_{21}) & e^{j\psi_3}\sin(\psi_{31})\sin(\psi_{32}) & \cdots & e^{j\psi_M}\prod_{m=1}^{M-1}\sin(\psi_{Mm}) \\ 0 & e^{j\psi_2}\cos(\psi_{21}) & e^{j\psi_3}\sin(\psi_{31})\cos(\psi_{32}) & \cdots & e^{j\psi_M}\prod_{m=1}^{M-2}\sin(\psi_{Mm})\cos(\psi_{M,M-1}) \\ 0 & 0 & e^{j\psi_3}\cos(\psi_{31}) & \ddots & \vdots \\ \vdots & \vdots & \ddots & \cdots & e^{j\psi_M}\sin(\psi_{M1})\cos(\psi_{M2}) \\ 0 & 0 & \cdots & \cdots & e^{j\psi_M}\cos(\psi_{M1}) \end{pmatrix} \tag{4.37}$$

$$\Re\big(\widetilde{\mathbf{U}}\big) = \begin{bmatrix} \cos(\psi_1) & \cos(\psi_2)\sin(\psi_{21}) & \cos(\psi_3)\sin(\psi_{31})\sin(\psi_{32}) & \cdots & \cos(\psi_M)\prod_{m=1}^{M-1}\sin(\psi_{Mm}) \\ 0 & \cos(\psi_2)\cos(\psi_{21}) & \cos(\psi_3)\sin(\psi_{31})\cos(\psi_{32}) & \cdots & \cos(\psi_M)\prod_{m=1}^{M-2}\sin(\psi_{Mm})\cos(\psi_{M,M-1}) \\ 0 & 0 & \cos(\psi_3)\cos(\psi_{31}) & \ddots & \vdots \\ \vdots & \vdots & \ddots & \cdots & \cos(\psi_M)\sin(\psi_{M1})\cos(\psi_{M2}) \\ 0 & 0 & \cdots & \cdots & \cos(\psi_M)\cos(\psi_{M1}) \end{bmatrix} \tag{4.38}$$

$$\Im\big(\widetilde{\mathbf{U}}\big) = \begin{bmatrix} \sin(\psi_1) & \sin(\psi_2)\sin(\psi_{21}) & \sin(\psi_3)\sin(\psi_{31})\sin(\psi_{32}) & \cdots & \sin(\psi_M)\prod_{m=1}^{M-1}\sin(\psi_{Mm}) \\ 0 & \sin(\psi_2)\cos(\psi_{21}) & \sin(\psi_3)\sin(\psi_{31})\cos(\psi_{32}) & \cdots & \sin(\psi_M)\prod_{m=1}^{M-2}\sin(\psi_{Mm})\cos(\psi_{M,M-1}) \\ 0 & 0 & \sin(\psi_3)\cos(\psi_{31}) & \ddots & \vdots \\ \vdots & \vdots & \ddots & \cdots & \sin(\psi_M)\sin(\psi_{M1})\cos(\psi_{M2}) \\ 0 & 0 & \cdots & \cdots & \sin(\psi_M)\cos(\psi_{M1}) \end{bmatrix} \tag{4.39}$$

Lemma 4.2.1. *If* $\mathbf{R}_g$ *is a covariance matrix and*

$$\widetilde{\mathbf{R}}_g = \Re(\mathbf{R}_g) + \jmath\,\Im(\mathbf{R}_g) \tag{4.40}$$

then the complex covariance matrix $\widetilde{\mathbf{R}}_g$ *will always be positive semi-definite.*

Proof. Please see Appendix 4.2.5. □

Lemma 4.2.1 satisfies constraint C_1 and $\widetilde{\mathbf{R}}_g$ also satisfies constraint C_2 for $c = 1$. This helps to transform constrained nonlinear optimization into unconstrained nonlinear optimization in the following section.

In order to generate QPSK waveforms define $N \times 2M$ matrix $\widetilde{\mathbf{S}}$, of Gaussian RVs, as

$$\widetilde{\mathbf{S}} \triangleq \begin{bmatrix} \widetilde{\mathbf{X}} & \widetilde{\mathbf{Y}} \end{bmatrix} \tag{4.41}$$

where $\widetilde{\mathbf{X}}$ and $\widetilde{\mathbf{Y}}$ are of each size $N \times M$, representing real and imaginary parts of QPSK waveform matrix, which is given as

$$\widetilde{\mathbf{Z}} = \frac{1}{\sqrt{2}} \Big[\text{sign}(\widetilde{\mathbf{X}}) + \jmath \, \text{sign}(\widetilde{\mathbf{Y}}) \Big]. \tag{4.42}$$

The covariance matrix of $\widetilde{\mathbf{S}}$ is given as

$$\widetilde{\mathbf{R}}_{\widetilde{\mathbf{S}}} = \mathbb{E}\{\widetilde{\mathbf{S}}^H \widetilde{\mathbf{S}}\} = \begin{bmatrix} \Re(\mathbf{R}_g) & \Im(\mathbf{R}_g) \\ -\Im(\mathbf{R}_g) & \Re(\mathbf{R}_g) \end{bmatrix}. \tag{4.43}$$

QPSK waveform matrix $\widetilde{\mathbf{Z}}$ can be realized by the matrix $\widetilde{\mathbf{S}}$ of Gaussian RVs which can be generated using equation (4.27) by utilizing $\widetilde{\mathbf{R}}_{\widetilde{\mathbf{S}}}$.

4.2.3 Gaussian Covariance Matrix Synthesis for Desired QPSK Beampattern

This section proves that the desired QPSK beampattern can be directly synthesized by using the complex covariance matrix, $\widetilde{\mathbf{R}}_g$, for complex Gaussian RVs. This generates M QPSK

waveforms for the desired beampattern which satisfy the property of finite alphabet and constant-envelope. By exploiting the relationship between the complex Gaussian RVs and QPSK RVs one has

$$\widetilde{\mathbf{R}} = \frac{2}{\pi}\left[\sin^{-1}\left(\Re(\mathbf{R}_g)\right) + \jmath\,\sin^{-1}\left(\Im(\mathbf{R}_g)\right)\right]. \tag{4.44}$$

Lemma 4.2.2. *If $\widetilde{\mathbf{R}}_g$ is a complex covariance matrix and*

$$\widetilde{\mathbf{R}} = \frac{2}{\pi}\left[\sin^{-1}\left(\Re(\mathbf{R}_g)\right) + \jmath\,\sin^{-1}\left(\Im(\mathbf{R}_g)\right)\right]$$

then $\widetilde{\mathbf{R}}$ will always be positive semi-definite.

Proof. Please see Section 4.2.5. □

Using equation (4.44), the optimization problem in equation (4.25) can be rewritten as

$$\begin{aligned}
\min_{\widetilde{\mathbf{R}}} \quad & \frac{1}{K}\sum_{k=1}^{K}\left[\frac{2}{\pi}\mathbf{a}^H(\theta_k)\left\{\sin^{-1}\left(\Re(\mathbf{R}_g)\right)\jmath\sin^{-1}\left(\Im(\mathbf{R}_g)\right)\right\}\mathbf{a}(\theta_k) - \phi(\theta_k)\right]^2 \\
\text{subject to} \quad & \mathbf{v}^H\widetilde{\mathbf{R}}\mathbf{v} \geq 0, \qquad \forall\,\mathbf{v}, \\
& \widetilde{\mathbf{R}}(m,m) = c, \qquad m = 1,2,...,M.
\end{aligned} \tag{4.45}$$

Since, the matrix $\widetilde{\mathbf{U}}$ is already known, $\widetilde{\mathbf{R}}_g$ can be formulated via equation (4.36) as

$$\begin{aligned}
J(\boldsymbol{\Theta}) = \frac{1}{K}\sum_{k=1}^{K}\Bigg[\frac{2}{\pi}\mathbf{a}^H(\theta_k)\Bigg\{\sin^{-1}\Big(\Re(\widetilde{\mathbf{U}})^H\Re(\widetilde{\mathbf{U}}) + \Im(\widetilde{\mathbf{U}})^H\Im(\widetilde{\mathbf{U}})\Big) \\
+ \jmath\sin^{-1}\Big(\Re(\widetilde{\mathbf{U}})^H\Im(\widetilde{\mathbf{U}}) - \Im(\widetilde{\mathbf{U}})^H\Re(\widetilde{\mathbf{U}})\Big)\Bigg\} \times \mathbf{a}^H(\theta_k) - \alpha\phi(\theta_k)\Bigg]^2
\end{aligned} \tag{4.46}$$

Moreover, the (p,q)th element of the upper triangular matrix $\widetilde{\mathbf{R}}_g$ can be written by first writing the (p,q)th element of the upper triangular matrix $\Re\big(\mathbf{R}_g(p,q)\big)$ as

$$\Re\big(\mathbf{R}_g(p,q)\big) = \begin{cases} \prod_{l=1}^{q-1}\sin(\Psi_{ql})\prod_{s=1}^{p}\prod_{u=1}^{q} f(s,u), & p>q \\ 1, & p=q \end{cases} \tag{4.47}$$

where $f(s,u) = \cos(\Psi_s)\cos(\Psi_u) + \sin(\Psi_s)\sin(\Psi_u)$; and the (p,q)th element of the upper triangular matrix $\Im\big(\mathbf{R}_g(p,q)\big)$ as

$$\Im\big(\mathbf{R}_g(p,q)\big) = \begin{cases} g(p,q)\prod_{l=1}^{q-1}\sin(\Psi_{ql}), & p>q \\ 0, & p=q \end{cases} \tag{4.48}$$

where $g(p,q) = \cos(\Psi_p)\sin(\Psi_q) + \sin(\Psi_p)\cos(\Psi_q)$. Thus, the (p,q)th element of the upper triangular matrix $\widetilde{\mathbf{R}}_g$ can be written as

$$\widetilde{\mathbf{R}}_g(p,q) = \begin{cases} \Re\big(\mathbf{R}_g(p,q)\big) + \jmath\Im\big(\mathbf{R}_g(p,q)\big), & p>q \\ 1, & p=q. \end{cases} \tag{4.49}$$

By utilizing the information of $\widetilde{\mathbf{U}}$, the constrained optimization problem in equation (4.45) can be transformed into an unconstrained optimization problem that can be written as equation (4.46), where

$$\boldsymbol{\Theta} = \begin{bmatrix} \boldsymbol{\Psi}^T & \widetilde{\boldsymbol{\Psi}}^T & \alpha \end{bmatrix}^T, \tag{4.50}$$

and

$$\boldsymbol{\Psi}^T = \begin{bmatrix} \Psi_{21} & \Psi_{21} & \cdots & \Psi_{21} \end{bmatrix}^T,$$
$$\widetilde{\boldsymbol{\Psi}}^T = \begin{bmatrix} \Psi_1 & \Psi_2 & \cdots & \Psi_M \end{bmatrix}^T.$$

The optimization is over $M(M-1)/2 + M$ elements Ψ_{mn} and Ψ_l. The advantage of this approach lies in the free selection of elements of $\boldsymbol{\Theta}$ without effecting the positive semi-definite property and diagonal elements of $\widetilde{\mathbf{R}}_g$. Noting that $\widetilde{\mathbf{U}}$ and $\widetilde{\mathbf{R}}_g$ are functions of $\boldsymbol{\Theta}$, one can alternately write the cost-function, in equation (4.46), as

$$J(\boldsymbol{\Theta}) = \frac{1}{K}\sum_{k=1}^{K}\left[\frac{2}{\pi}\mathbf{a}^H(\theta_k)\sin^{-1}\Big(\Re(\mathbf{R}_g)\Big)\mathbf{a}(\theta_k) + \frac{2\jmath}{\pi}\mathbf{a}^H(\theta_k)\sin^{-1}\Big(\Im(\mathbf{R}_g)\Big)\mathbf{a}(\theta_k) - \alpha\phi(\theta_k)\right]^2. \tag{4.51}$$

First, the partial differentiation of $J(\boldsymbol{\Theta})$ with respect to any element of $\boldsymbol{\Psi}$, say Ψ_{mn}, can be found as

$$\begin{aligned}\frac{\partial J(\boldsymbol{\Theta})}{\partial \Psi_{mn}} = &\left[\frac{2}{K}\sum_{k=1}^{K}\left\{\frac{2}{\pi}\mathbf{a}^H(\theta_k)\sin^{-1}\big(\Re(\mathbf{R}_g)\big)\mathbf{a}(\theta_k)\right.\right.\\ &\left.\left.+\frac{2\jmath}{\pi}\mathbf{a}^H(\theta_k)\sin^{-1}\big(\Im(\mathbf{R}_g)\big)\mathbf{a}(\theta_k) - \alpha\phi(\theta_k)\right\}\right]\\ &\times\left[\frac{\partial}{\partial\Psi_{mn}}\left\{\frac{2}{\pi}\mathbf{a}^H(\theta_k)\sin^{-1}\big(\Re(\mathbf{R}_g)\big)\mathbf{a}(\theta_k)\right.\right.\\ &\left.\left.+\frac{2\jmath}{\pi}\mathbf{a}^H(\theta_k)\sin^{-1}\big(\Im(\mathbf{R}_g)\big)\mathbf{a}(\theta_k)\right\}\right].\end{aligned} \tag{4.52}$$

The matrix $\Re(\mathbf{R}_g)$ is real and symmetric, i.e., $\Re\big(\mathbf{R}_g(p,q)\big) = \Re\big(\mathbf{R}_g(q,p)\big)$, at the same time, $\Im(\mathbf{R}_g)$ has real entries but is skew-symmetric, i.e., $\Im\big(\mathbf{R}_g(p,q)\big) = -\Im\big(\mathbf{R}_g(q,p)\big)$. These

observations enables us to write equation (4.52) in a simpler form

$$\frac{\partial J(\boldsymbol{\Theta})}{\partial \Psi_{mn}} = \Bigg[\frac{4}{K}\sum_{k=1}^{K}\Bigg\{\frac{2}{\pi}\mathbf{a}^H(\theta_k)\sin^{-1}\big(\Re(\mathbf{R}_g)\big)\mathbf{a}(\theta_k) + \frac{2\jmath}{\pi}\mathbf{a}^H(\theta_k)\sin^{-1}\big(\Im(\mathbf{R}_g)\big)\mathbf{a}(\theta_k) - \alpha\phi(\theta_k)\Bigg\}\Bigg] \times \Bigg[\frac{2}{\pi}\sum_{p=1}^{M-1}\sum_{q=p+1}^{M}\frac{\cos\big(\pi|p-q|\sin(\theta_k)\big)}{\sqrt{1-\Re\big(\mathbf{R}_g^2(p,q)\big)}}\frac{\partial\Re\big(\mathbf{R}_g(p,q)\big)}{\partial\Psi_{mn}}\Bigg]. \tag{4.53}$$

Moreover, $\Re(\mathbf{R}_g)$ contains only $(M-1)$ terms which depend on Ψ_{mn}, thus, equation (4.53) further simplifies as

$$\frac{\partial J(\boldsymbol{\Theta})}{\partial \Psi_{mn}} = \frac{8}{\pi K}\Bigg[\sum_{k=1}^{K}\Bigg\{\frac{2}{\pi}\mathbf{a}^H(\theta_k)\sin^{-1}\big(\Re(\mathbf{R}_g)\big)\mathbf{a}(\theta_k) + \frac{2\jmath}{\pi}\mathbf{a}^H(\theta_k)\sin^{-1}\big(\Im(\mathbf{R}_g)\big)\mathbf{a}(\theta_k) - \alpha\phi(\theta_k)\Bigg\}\Bigg] \times \Bigg[\Bigg\{\sum_{p=1}^{m-1}\frac{\cos\big(\pi|p-m|\sin(\theta_k)\big)}{\sqrt{1-\Re\big(\mathbf{R}_g^2(p,m)\big)}}\frac{\partial\Re\big(\mathbf{R}_g(p,m)\big)}{\partial\Psi_{mn}} + \sum_{q=m+1}^{M}\frac{\cos\big(\pi|m-q|\sin(\theta_k)\big)}{\sqrt{1-\Re\big(\mathbf{R}_g^2(m,q)\big)}}\frac{\partial\Re\big(\mathbf{R}_g(m,q)\big)}{\partial\Psi_{mn}}\Bigg\}\Bigg]. \tag{4.54}$$

Second, the partial differentiation of $J(\boldsymbol{\Theta})$ with respect to any element of $\widetilde{\boldsymbol{\Psi}}$, say Ψ_l, can be

found in the same manner as was found for Ψ_{mn}, i.e.,

$$\frac{\partial J(\boldsymbol{\Theta})}{\partial \Psi_l} = \frac{8}{\pi K}\Bigg[\sum_{k=1}^{K}\Bigg\{\frac{2}{\pi}\mathbf{a}^H(\theta_k)\sin^{-1}\big(\Re(\mathbf{R}_g)\big)\mathbf{a}(\theta_k) + \frac{2\jmath}{\pi}\mathbf{a}^H(\theta_k)\sin^{-1}\big(\Im(\mathbf{R}_g)\big)\mathbf{a}(\theta_k) - \alpha\phi(\theta_k)\Bigg\}\Bigg] \times \Bigg[\sum_{p=1}^{M-1}\sum_{q=p+1}^{M}\frac{\cos\big(\pi|p-q|\sin(\theta_k)\big)}{\sqrt{1-\Re\big(\mathbf{R}_g^2(p,q)\big)}}\frac{\partial\Re\big(\mathbf{R}_g(p,q)\big)}{\partial\Psi_l}\Bigg]. \tag{4.55}$$

Finally, the partial differentiation of $J(\boldsymbol{\Theta})$ with respect to α is

$$\frac{\partial J(\boldsymbol{\Theta})}{\partial \alpha} = \frac{-2\phi(\theta_k)}{K}\Bigg[\sum_{k=1}^{K}\Bigg\{\frac{2}{\pi}\mathbf{a}^H(\theta_k)\sin^{-1}\big(\Re(\mathbf{R}_g)\big)\mathbf{a}(\theta_k) + \frac{2\jmath}{\pi}\mathbf{a}^H(\theta_k)\sin^{-1}\big(\Im(\mathbf{R}_g)\big)\mathbf{a}(\theta_k) - \alpha\phi(\theta_k)\Bigg\}\Bigg]. \tag{4.56}$$

4.2.4 Generating CE QPSK Random Processes From Gaussian Random Variables

Assuming identically distributed Gaussian RV's $\widetilde{x}_p, \widetilde{y}_p, \widetilde{x}_q$ and $\widetilde{y}_q$ that are mapped onto QPSK RV's $\widetilde{z}_p$ and $\widetilde{z}_q$ using

$$\widetilde{z}_p = \frac{1}{\sqrt{2}}\Bigg[\text{sign}\bigg(\frac{\widetilde{x}_p}{\sqrt{2}\sigma}\bigg) + \jmath\,\text{sign}\bigg(\frac{\widetilde{y}_p}{\sqrt{2}\sigma}\bigg)\Bigg] \tag{4.57}$$

$$\widetilde{z}_q = \frac{1}{\sqrt{2}}\Bigg[\text{sign}\bigg(\frac{\widetilde{x}_q}{\sqrt{2}\sigma}\bigg) + \jmath\,\text{sign}\bigg(\frac{\widetilde{y}_q}{\sqrt{2}\sigma}\bigg)\Bigg] \tag{4.58}$$

where σ^2 is the variance of Gaussian RVs. The cross-correlation between QPSK and Gaussian RVs can be derived as

$$\mathbb{E}\{\widetilde{z}_p\widetilde{z}_q^*\} = \frac{1}{2}\mathbb{E}\Bigg[\Big\{\text{sign}\Big(\frac{\widetilde{x}_p}{\sqrt{2}\sigma}\Big) + \jmath\,\text{sign}\Big(\frac{\widetilde{y}_p}{\sqrt{2}\sigma}\Big)\Big\}\Big\{\text{sign}\Big(\frac{\widetilde{x}_q}{\sqrt{2}\sigma}\Big) + \jmath\,\text{sign}\Big(\frac{\widetilde{y}_q}{\sqrt{2}\sigma}\Big)\Big\}\Bigg]. \quad (4.59)$$

Using equation (4.30) one can write the above equation as

$$\mathbb{E}\{\widetilde{z}_p\widetilde{z}_q^*\} = \mathbb{E}\Big\{\text{sign}\Big(\frac{\widetilde{x}_p}{\sqrt{2}\sigma}\Big)\text{sign}\Big(\frac{\widetilde{x}_q}{\sqrt{2}\sigma}\Big)\Big\} + \jmath\,\mathbb{E}\Big\{\text{sign}\Big(\frac{\widetilde{y}_p}{\sqrt{2}\sigma}\Big)\text{sign}\Big(\frac{\widetilde{x}_q}{\sqrt{2}\sigma}\Big)\Big\}. \quad (4.60)$$

The cross-correlation relationship between Gaussian and QPSK RVs can be derived by first considering

$$\mathbb{E}\Big\{\text{sign}\Big(\frac{\widetilde{x}_p}{\sqrt{2}\sigma}\Big)\text{sign}\Big(\frac{\widetilde{x}_q}{\sqrt{2}\sigma}\Big)\Big\} = \int_{-\infty}^{\infty}\int_{-\infty}^{\infty}\Bigg[\text{sign}\Big(\frac{\widetilde{x}_p}{\sqrt{2}\sigma}\Big) \times \text{sign}\Big(\frac{\widetilde{x}_q}{\sqrt{2}\sigma}\Big)p(\widetilde{x}_p, \widetilde{x}_q, \rho_{\widetilde{x}_p\widetilde{x}_q})\Bigg]\, d\widetilde{x}_p\, d\widetilde{x}_q \quad (4.61)$$

where $p(\widetilde{x}_p, \widetilde{x}_q, \rho_{\widetilde{x}_p\widetilde{x}_q})$ is the joint probability density function of $\widetilde{x}_p$ and $\widetilde{x}_q$, and $\rho_{\widetilde{x}_p\widetilde{x}_q} = \frac{\mathbb{E}\{\widetilde{x}_p\widetilde{x}_q^*\}}{\sigma^2}$ is the cross-correlation coefficient of $\widetilde{x}_p$ and $\widetilde{x}_q$. Using Hermite polynomials [90], the above double integral can be transformed as in [17]. Thus,

$$\mathbb{E}\Big\{\text{sign}\Big(\frac{\widetilde{x}_p}{\sqrt{2}\sigma}\Big)\text{sign}\Big(\frac{\widetilde{x}_q}{\sqrt{2}\sigma}\Big)\Big\} = \sum_{n=0}^{\infty}\frac{\rho^n_{\widetilde{x}_p\widetilde{x}_q}}{2\pi\sigma^2 2^n n!}\int_{-\infty}^{\infty}\text{sign}\Big(\frac{\widetilde{x}_p}{\sqrt{2}\sigma}\Big) \times e^{\widetilde{x}_p^2/2\sigma^2}H_n\Big(\frac{\widetilde{x}_p}{\sqrt{2}\sigma}\Big)\, d\widetilde{x}_p \times \int_{-\infty}^{\infty}\text{sign}\Big(\frac{\widetilde{x}_q}{\sqrt{2}\sigma}\Big)e^{\widetilde{x}_q^2/2\sigma^2}H_n\Big(\frac{\widetilde{x}_q}{\sqrt{2}\sigma}\Big)\, d\widetilde{x}_q \quad (4.62)$$

where

$$H_n(\widetilde{x}_m) = (-1)^n e^{\frac{\widetilde{x}_m^2}{2}}\frac{d^n}{d\widetilde{x}_m^n}e^{\frac{-\widetilde{x}_m^2}{2}} \quad (4.63)$$

is the Hermite polynomial. By substituting $\hat{x}_p = \frac{\widetilde{x}_p}{\sqrt{2}\sigma}$ and $\hat{x}_q = \frac{\widetilde{x}_q}{\sqrt{2}\sigma}$, and splitting the limits of integration into two parts, equation (4.62) can be simplified as

$$\mathbb{E}\Big\{\text{sign}(\hat{x}_p)\text{sign}(\hat{x}_q)\Big\} = \sum_{n=0}^{\infty} \frac{\rho^n_{\hat{x}_p\hat{x}_q}}{\pi 2^n n!}\left(\int_0^{\infty} e^{\hat{x}_p^2}\Big[H_n(\hat{x}_p) - H_n(-\hat{x}_p)\Big]\, d\hat{x}_p\right)^2. \tag{4.64}$$

Using $H_n(-\hat{x}_p) = (-1)^n H_n(\hat{x}_p)$ [91], equation (4.64) can be written as

$$\mathbb{E}\Big\{\text{sign}(\hat{x}_p)\text{sign}(\hat{x}_q)\Big\} = \sum_{n=0}^{\infty} \frac{\rho^n_{\hat{x}_p\hat{x}_q}}{\pi 2^n n!}\left(\int_0^{\infty} e^{\hat{x}_p^2} H_n(\hat{x}_p)\big(1 - (-1)^n\big)\, d\hat{x}_p\right)^2. \tag{4.65}$$

The above equation is non-zero for odd n only, therefore, one can rewrite it as

$$\mathbb{E}\Big\{\text{sign}(\hat{x}_p)\text{sign}(\hat{x}_q)\Big\} = \sum_{n=0}^{\infty} \frac{\rho^{2n+1}_{\hat{x}_p\hat{x}_q}}{\pi 2^{2n}(2n+1)!}\left(\int_0^{\infty} e^{\hat{x}_p^2} H_{2n+1}(\hat{x}_p)\, d\hat{x}_p\right)^2. \tag{4.66}$$

Then using $\int_0^{\infty} e^{\hat{x}_p^2} H_{2n+1}(\hat{x}_p)\, d\hat{x}_p = (-1)^n \frac{(2n)!}{n!}$ from [91], one can write equation (4.66) as

$$\begin{aligned}
\mathbb{E}\Big\{\text{sign}\Big(\frac{\widetilde{x}_p}{\sqrt{2}\sigma}\Big)\text{sign}\Big(\frac{\widetilde{x}_q}{\sqrt{2}\sigma}\Big)\Big\} &= \sum_{n=0}^{\infty} \frac{\rho^{2n+1}_{\widetilde{x}_p\widetilde{x}_q}}{\pi 2^{2n}(2n+1)!}\left((-1)^n \frac{2n!}{n!}\right)^2 \\
&= \frac{2}{\pi}\left[\rho_{\widetilde{x}_p\widetilde{x}_q} + \frac{\rho^3_{\widetilde{x}_p\widetilde{x}_q}}{2\cdot 3} + \frac{1\cdot 3\rho^5_{\widetilde{x}_p\widetilde{x}_q}}{2\cdot 4\cdot 5} + \frac{1\cdot 3\cdot 5\rho^7_{\widetilde{x}_p\widetilde{x}_q}}{2\cdot 4\cdot 6\cdot 7} + \cdots\right] \\
&= \frac{2}{\pi}\sin^{-1}\Big(\mathbb{E}\{\widetilde{x}_p\widetilde{x}_q\}\Big)
\end{aligned} \tag{4.67}$$

In equation (4.61), the first part of equation (4.60) was expanded. Now, similarly expanding the second part of equation (4.60), i.e.,

$$\mathbb{E}\Big\{\text{sign}\Big(\frac{\widetilde{y}_p}{\sqrt{2}\sigma}\Big)\text{sign}\Big(\frac{\widetilde{x}_q}{\sqrt{2}\sigma}\Big)\Big\} = \int_{-\infty}^{\infty}\int_{-\infty}^{\infty}\left[\text{sign}\Big(\frac{\widetilde{y}_p}{\sqrt{2}\sigma}\Big)\text{sign}\Big(\frac{\widetilde{x}_q}{\sqrt{2}\sigma}\Big)p(\widetilde{y}_p,\widetilde{x}_q,\rho_{\widetilde{y}_p\widetilde{x}_q})\right]d\widetilde{y}_p\,d\widetilde{x}_q \tag{4.68}$$

where $p(\widetilde{y}_p,\widetilde{x}_q,\rho_{\widetilde{y}_p\widetilde{x}_q})$ is the joint probability density function of $\widetilde{y}_p$ and $\widetilde{x}_q$, and $\rho_{\widetilde{y}_p\widetilde{x}_q} = \frac{\mathbb{E}\{\widetilde{y}_p\widetilde{x}_q^*\}}{\sigma^2}$ is the cross-correlation coefficient of $\widetilde{y}_p$ and $\widetilde{x}_q$. Using Hermite polynomials, equation (4.63), equation (4.68) can be written as

$$\mathbb{E}\Big\{\text{sign}\Big(\frac{\widetilde{y}_p}{\sqrt{2}\sigma}\Big)\text{sign}\Big(\frac{\widetilde{x}_q}{\sqrt{2}\sigma}\Big)\Big\} = \sum_{n=0}^{\infty}\frac{\rho^n_{\widetilde{y}_p\widetilde{x}_q}}{2\pi\sigma^2 2^n n!}\int_{-\infty}^{\infty}\text{sign}\Big(\frac{\widetilde{y}_p}{\sqrt{2}\sigma}\Big)\times e^{\widetilde{y}_p^2/2\sigma^2}H_n\Big(\frac{\widetilde{y}_p}{\sqrt{2}\sigma}\Big)\,d\widetilde{y}_p\times$$
$$\int_{-\infty}^{\infty}\text{sign}\Big(\frac{\widetilde{x}_q}{\sqrt{2}\sigma}\Big)e^{\widetilde{x}_q^2/2\sigma^2}H_n\Big(\frac{\widetilde{x}_q}{\sqrt{2}\sigma}\Big)\,d\widetilde{x}_q. \tag{4.69}$$

By substituting $\hat{y}_p = \frac{\widetilde{y}_p}{\sqrt{2}\sigma}$ and $\hat{x}_q = \frac{\widetilde{x}_q}{\sqrt{2}\sigma}$, and splitting the limits of integration into two parts, equation (4.69) can be simplified as

$$\mathbb{E}\Big\{\text{sign}(\hat{y}_p)\text{sign}(\hat{x}_q)\Big\} = \sum_{n=0}^{\infty}\frac{\rho^n_{\hat{y}_p\hat{x}_q}}{\pi 2^n n!}\left(\int_0^{\infty}e^{\hat{y}_p^2}\Big[H_n(\hat{y}_p) - H_n(-\hat{y}_p)\Big]\,d\hat{y}_p\right)^2. \tag{4.70}$$

Using $H_n(-\hat{y}_p) = (-1)^n H_n(\hat{y}_p)$, above equation can be written as

$$\mathbb{E}\Big\{\text{sign}(\hat{y}_p)\text{sign}\hat{x}_q)\Big\} = \sum_{n=0}^{\infty}\frac{\rho^n_{\hat{y}_p\hat{x}_q}}{\pi 2^n n!}\left(\int_0^{\infty}e^{\hat{y}_p^2}H_n(\hat{y}_p)\big(1-(-1)^n\big)\,d\hat{y}_p\right)^2. \tag{4.71}$$

The above equation is non-zero for odd n only, therefore, it can be rewritten as

$$\mathbb{E}\Big\{\text{sign}(\hat{y}_p)\text{sign}(\hat{x}_q)\Big\} = \sum_{n=0}^{\infty} \frac{\rho_{\hat{y}_p\hat{x}_q}^{2n+1}}{\pi 2^{2n}(2n+1)!}\left(\int_0^{\infty} e^{\hat{y}_p^2} H_{2n+1}(\hat{y}_p)\, d\hat{y}_p\right)^2. \tag{4.72}$$

Then using $\int_0^{\infty} e^{\hat{y}_p^2} H_{2n+1}(\hat{y}_p)\, d\hat{y}_p = (-1)^n \frac{(2n)!}{n!}$, equation (4.72) can be rewritten as

$$\begin{aligned}\mathbb{E}\Big\{\text{sign}\Big(\frac{\widetilde{y}_p}{\sqrt{2}\sigma}\Big)\text{sign}\Big(\frac{\widetilde{x}_q}{\sqrt{2}\sigma}\Big)\Big\} &= \sum_{n=0}^{\infty} \frac{\rho_{\widetilde{y}_p\widetilde{x}_q}^{2n+1}}{\pi 2^{2n}(2n+1)!}\left((-1)^n \frac{2n!}{n!}\right)^2 \\ &= \frac{2}{\pi}\left[\rho_{\widetilde{y}_p\widetilde{x}_q} + \frac{\rho_{\widetilde{y}_p\widetilde{x}_q}^3}{2\cdot 3} + \frac{1\cdot 3\rho_{\widetilde{y}_p\widetilde{x}_q}^5}{2\cdot 4\cdot 5} + \frac{1\cdot 3\cdot 5\rho_{\widetilde{y}_p\widetilde{x}_q}^7}{2\cdot 4\cdot 6\cdot 7} + \cdots\right] \\ &= \frac{2}{\pi}\sin^{-1}\Big(\mathbb{E}\{\widetilde{y}_p\widetilde{x}_q\}\Big). \end{aligned} \tag{4.73}$$

Combining equations (4.67) and (4.73), gives the cross-correlation of equation (4.60) as

$$\mathbb{E}\{\widetilde{z}_p\widetilde{z}_q\} = \frac{2}{\pi}\left[\sin^{-1}\Big(\mathbb{E}\{\widetilde{x}_p\widetilde{x}_q\}\Big) + \jmath\,\sin^{-1}\Big(\mathbb{E}\{\widetilde{y}_p\widetilde{x}_q\}\Big)\right]. \tag{4.74}$$

4.2.5 Proof of Constant Envelope Property of QPSK Waveforms

4.2.5.1 Preliminaries to Proofs

This section presents some preliminary results used in the proofs throughout the section. For proofs of the following theorems, please see the corresponding references.

Theorem 4.2.1. *The matrix $\mathbf{A} \in \mathbb{C}^{n\times n}$ is positive semi-definite if and only if $\Re(\mathbf{A})$ is positive semi-definite [92].*

Theorem 4.2.2. *A necessary and sufficient condition for $\mathbf{A} \in \mathbb{C}^{n\times n}$ to be positive definite*

is that the Hermitian part

$$\mathbf{A}_H = \frac{1}{2}\left[\mathbf{A} + \mathbf{A}^H\right]$$

be positive definite [92].

Theorem 4.2.3. *If* $\mathbf{A} \in \mathbb{C}^{n\times n}$ *and* $\mathbf{B} \in \mathbb{C}^{n\times n}$ *are positive semi-definite matrices then the matrix* $\mathbf{C} = \mathbf{A} + \mathbf{B}$ *is guaranteed to be positive semi-definite matrix [93].*

Theorem 4.2.4. *If the matrix* $\mathbf{A} \in \mathbb{C}^{n\times n}$ *is positive semi-definite then the* p *times Schur product of* $\mathbf{A}$*, denoted by* $\mathbf{A}_\circ^p$*, will also be positive semi-definite [93].*

4.2.5.2 Proofs

Proof of Lemma 4.2.1. To prove Lemma 4.2.1, note that the real part of $\widetilde{\mathbf{R}}_g$ is $\mathbf{R}_g$ which is positive semi-definite by definition, thus, by Theorem 4.2.1, the complex covariance matrix $\widetilde{\mathbf{R}}_g$ is also positive semi-definite. □

Proof of Lemma 4.2.2. To prove Lemma 4.2.2, one can individually expand the sum, $\sin^{-1}\left(\Re(\widetilde{\mathbf{R}}_g)\right) + \jmath\,\sin^{-1}\left(\Im(\widetilde{\mathbf{R}}_g)\right)$, using Taylor series, i.e., first expanding $\sin^{-1}\left(\Re(\widetilde{\mathbf{R}}_g)\right)$

$$\begin{aligned}\sin^{-1}\left(\Re(\mathbf{R}_g)\right) = \Re(\mathbf{R}_g) + \frac{1}{2\cdot 3}\Re(\mathbf{R}_g)_\circ^3 + \frac{1\cdot 3}{2\cdot 4\cdot 5}\Re(\mathbf{R}_g)_\circ^5 \\ + \frac{1\cdot 3\cdot 5}{2\cdot 4\cdot 6\cdot 7}\Re(\mathbf{R}_g)_\circ^7 + \cdots\end{aligned} \tag{4.75}$$

Then using Theorem 4.2.3, each term or matrix, on the right hand side, is positive semi-definite, since, $\Re(\mathbf{R}_g)$ is positive semi-definite by definition. Moreover, $\sin^{-1}\left(\Re(\mathbf{R}_g)\right)$ is also positive semi-definite since its a sum of positive semi-definite matrices, this follows from Theorem 4.2.1.

Similarly, expanding $\jmath \sin^{-1}(\Im(\mathbf{R}_g))$ as

$$\begin{aligned}\jmath \sin^{-1}(\Im(\mathbf{R}_g)) = \jmath[\Im(\mathbf{R}_g) + \frac{1}{2\cdot 3}\Im(\mathbf{R}_g)_\circ^3 + \frac{1\cdot 3}{2\cdot 4\cdot 5}\Im(\mathbf{R}_g)_\circ^5 \\ + \frac{1\cdot 3\cdot 5}{2\cdot 4\cdot 6\cdot 7}\Im(\mathbf{R}_g)_\circ^7 + \cdots]\end{aligned} \tag{4.76}$$

Now, $\widetilde{\mathbf{R}}$ is positive semi-definite since real part of it is positive semidefinite, from equation (4.75) and Theorem 4.2.4.

□

Alternate proof of Lemma 4.2.2. Alternately, Lemma 4.2.2 can be proved by combining equations (4.75) and (4.76) as

$$\begin{aligned}&\sin^{-1}(\Re(\mathbf{R}_g)) + \jmath \sin^{-1}(\Im(\mathbf{R}_g)) \\ &= [\Re(\mathbf{R}_g) + \jmath\Im(\mathbf{R}_g)] + \frac{1}{2\cdot 3}\left[\Re(\mathbf{R}_g)_\circ^3 + \jmath\Im(\mathbf{R}_g)_\circ^3\right] \\ &\quad + \frac{1\cdot 3}{2\cdot 4\cdot 5}\left[\Re(\mathbf{R}_g)_\circ^5 + \jmath\Im(\mathbf{R}_g)_\circ^5\right] \\ &\quad + \frac{1\cdot 3\cdot 5}{2\cdot 4\cdot 6\cdot 7}\left[\Re(\mathbf{R}_g)_\circ^7 + \jmath\Im(\mathbf{R}_g)_\circ^7\right] + \cdots \\ &= \widetilde{\mathbf{R}}_g + \frac{1}{2\cdot 3}(\widetilde{\mathbf{R}}_g)_\circ^3 + \frac{1\cdot 3}{2\cdot 4\cdot 5}(\widetilde{\mathbf{R}}_g)_\circ^5 + \frac{1\cdot 3\cdot 5}{2\cdot 4\cdot 6\cdot 7}(\widetilde{\mathbf{R}}_g)_\circ^7 + \cdots\end{aligned} \tag{4.77}$$

Then, using Theorem 4.2.3, each term or matrix, on the right hand side, is positive semi-definite, since, $\widetilde{\mathbf{R}}_g$ is positive semi-definite by Lemma 1. Moreover, $\sin^{-1}(\Re(\mathbf{R}_g)) + \jmath \sin^{-1}(\Im(\mathbf{R}_g))$ is also positive semi-definite since its a sum of positive semi-definite matrices, this follows from Theorem 4.2.1.

□

4.2.6 Waveform Design for Spectrum Sharing

In the previous section, finite alphabet constant-envelope QPSK waveforms were designed by solving a beampattern matching optimization problem. This section extends the beampattern matching optimization problem and introduces new constraints in order to tailor waveforms that don't cause interference to communication systems when MIMO radar and communication systems are sharing spectrum. Spectrum sharing waveforms are designed for two cases: the first case is for a stationary maritime MIMO radar and the second case is for moving maritime MIMO radar. The waveform design in these contexts is and its performance is discussed in the following sections.

4.2.6.1 Stationary maritime MIMO radar

Consider a naval ship docked at the harbor. The radar mounted on top of that ship is also stationary. The interference channels are also stationary due to non-movement of ship and BSs. In such a scenario, the CSI has little to no variations and thus it is feasible to include the constraint of NSP, equation (4.78), into the optimization problem. Thus, the new optimization problem is formulated as equation (4.16).

A drawback of this approach is that it does not guarantee to generate constant-envelope radar waveform. However, the designed waveform is in the null space of the interference channel, thus, satisfying spectrum sharing constraints. The waveform generation process is shown using the block diagram of Figure 4.5. Note that, $\mathcal{K}$ waveforms are designed, as $\mathcal{K}$ interference channels exist that are static. Using the projection matrix $\mathbf{P}_i$, the NSP projected waveform can be obtained as

$$\breve{\widetilde{\mathbf{Z}}}_{\text{NSP}}^{\text{opt}} = \widetilde{\mathbf{Z}}_i^{\text{opt}} \mathbf{P}_i^H. \tag{4.78}$$

The correlation matrix of the NSP waveform is given as

$$\breve{\widetilde{\mathbf{R}}}_i = \frac{1}{N}\left(\breve{\widetilde{\mathbf{Z}}}^{\text{opt}}_{\text{NSP}}\right)^H \breve{\widetilde{\mathbf{Z}}}^{\text{opt}}_{\text{NSP}}. \tag{4.79}$$

It is proposed to select the transmitted waveform with covariance matrix $\breve{\widetilde{\mathbf{R}}}_i$ as close as possible to the desired covariance matrix, i.e.,

$$i_{\min} \triangleq \underset{1\le i\le \mathcal{K}}{\arg\min}\left[\frac{1}{K}\sum_{k=1}^{K}\left(\mathbf{a}^H(\theta_k)\,\breve{\widetilde{\mathbf{R}}}_i\,\mathbf{a}(\theta_k)-\phi(\theta_k)\right)^2\right] \tag{4.80}$$

$$\widetilde{\mathbf{R}}^{\text{opt}}_{\text{NSP}} \triangleq \breve{\widetilde{\mathbf{R}}}_{i_{\min}}. \tag{4.81}$$

Equivalently, $\mathbf{P}_i$ projects maximum power at target locations. Thus, for stationary MIMO radar waveform with spectrum sharing constraints Algorithm (5) is proposed.

Algorithm 5 Stationary MIMO Radar Waveform Design Algorithm with Spectrum Sharing Constraints

loop
  for $i = 1 : \mathcal{K}$ **do**
    Get CSI of $\mathbf{H}_i$ through feedback from the i^{th} BS.
    Send $\mathbf{H}_i$ to Algorithm (2) for the formation of projection matrix $\mathbf{P}_i$.
    Receive the i^{th} projection matrix $\mathbf{P}_i$ from Algorithm (2).
    Design QPSK waveform $\widetilde{\mathbf{Z}}^{\text{opt}}_i$ using the optimization problem in equation (4.16).
    Project the QPSK waveform onto the null space of i^{th} interference channel using $\breve{\widetilde{\mathbf{Z}}}^{\text{opt}}_{\text{NSP}} = \widetilde{\mathbf{Z}}^{\text{opt}}_i \mathbf{P}_i^H$.
  end for
  Find $i_{\min} = \underset{1\le i\le \mathcal{K}}{\arg\min}\left[\frac{1}{K}\sum_{k=1}^{K}\left(\mathbf{a}^H(\theta_k)\,\breve{\widetilde{\mathbf{R}}}_i\,\mathbf{a}(\theta_k)-\phi(\theta_k)\right)^2\right]$.
  Set $\widetilde{\mathbf{R}}^{\text{opt}}_{\text{NSP}} = \breve{\widetilde{\mathbf{R}}}_{i_{\min}}$ as the covariance matrix of the desired NSP QPSK waveforms to be transmitted.
end loop

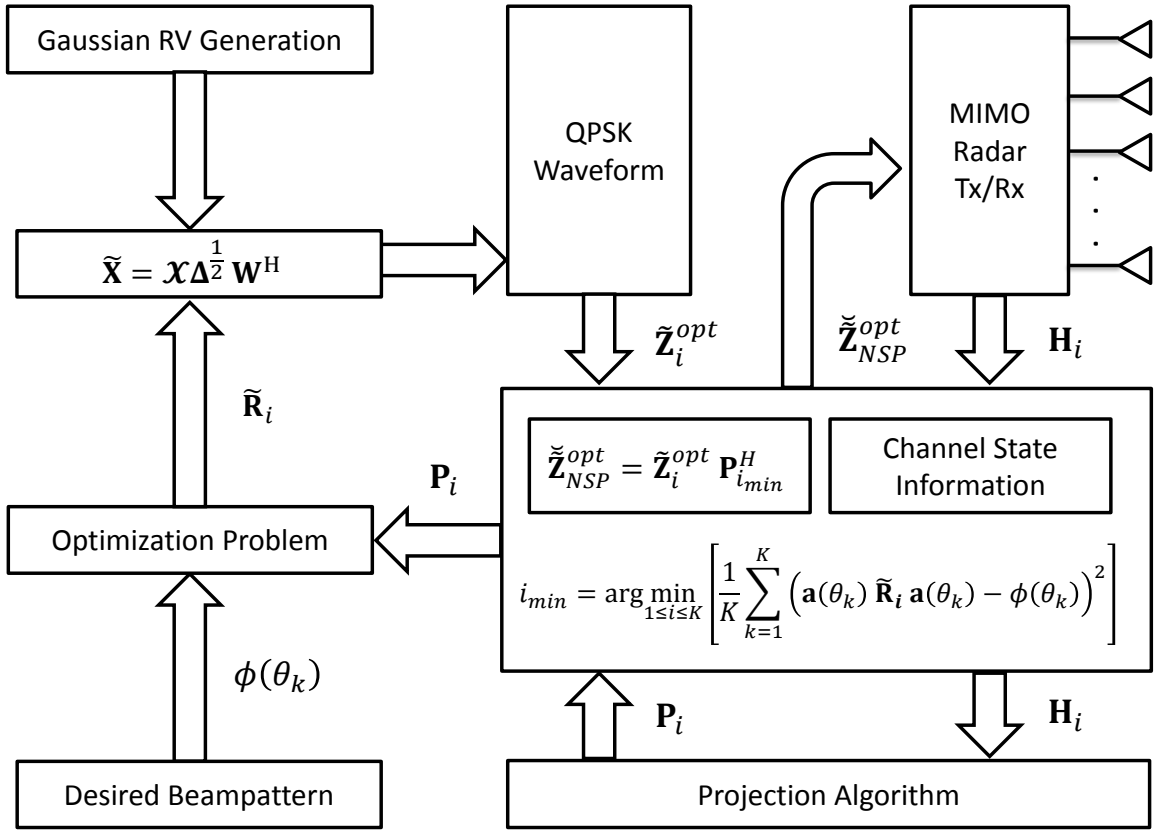

Figure 4.5: Block diagram of QPSK waveform generation process for a stationary MIMO radar with spectrum sharing constraints.

4.2.6.2 Moving maritime MIMO radar

Consider the case of a moving naval ship. The radar mounted on top of the ship is also moving, thus, the interference channels are varying due to the motion of ship. Due to time-varying ICSI, it is not feasible to include the NSP in the optimization problem. For this case, first design finite alphabet constant-envelope QPSK waveforms, using the optimization problem in equation (4.46), and then use NSP to satisfy spectrum sharing constraints using

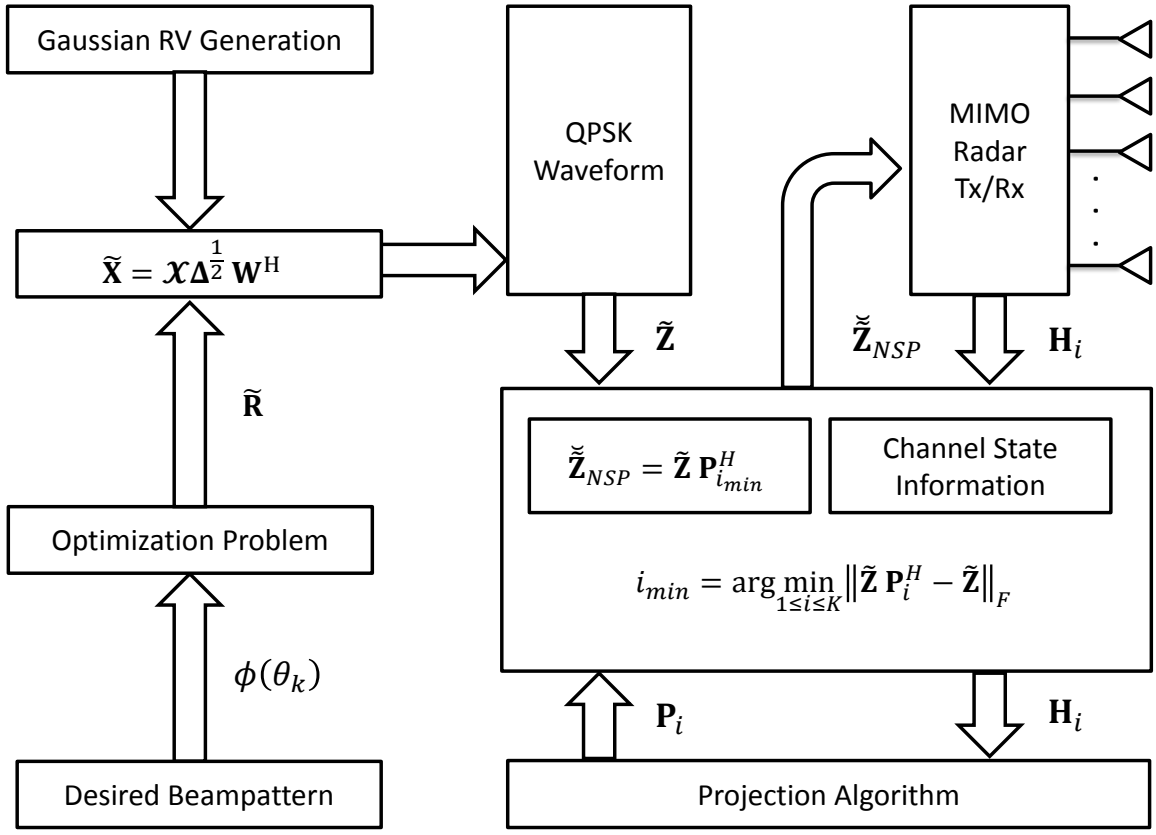

Figure 4.6: Block diagram of QPSK waveform generation process for a moving MIMO radar with spectrum sharing constraints.

transform

$$\breve{\tilde{\mathbf{Z}}}_i = \widetilde{\mathbf{Z}}\mathbf{P}_i^H. \tag{4.82}$$

The waveform generation process is shown using the block diagram of Figure 4.6. Note that only one waveform is designed using the optimization problem in equation (4.46) but $\mathcal{K}$ projection operations are performed via equation (4.82). The transmitted waveform is selected on the basis of minimum Forbenius norm with respect to the designed waveform

using the optimization problem in equation (4.46), i.e.,

$$i_{\min} \triangleq \underset{1\leq i\leq \mathcal{K}}{\arg\min} ||\widetilde{\mathbf{Z}}\mathbf{P}_i^H - \widetilde{\mathbf{Z}}||_F \tag{4.83}$$

$$\breve{\widetilde{\mathbf{Z}}}_{\text{NSP}} \triangleq \breve{\widetilde{\mathbf{Z}}}_{i_{\min}}. \tag{4.84}$$

The correlation matrix of this transmitted waveform is given as

$$\widetilde{\mathbf{R}}_{\text{NSP}} = \frac{1}{N}\breve{\widetilde{\mathbf{Z}}}_{\text{NSP}}^H \breve{\widetilde{\mathbf{Z}}}_{\text{NSP}}. \tag{4.85}$$

Thus, for moving MIMO radar waveform with spectrum sharing constraints Algorithm (6) is proposed.

Algorithm 6 Moving MIMO Radar Waveform Design Algorithm with Spectrum Sharing Constraints

Design FACE QPSK waveform $\widetilde{\mathbf{Z}}$ using the optimization problem in equation (4.46).
loop
  for $i = 1 : \mathcal{K}$ **do**
    Get CSI of $\mathbf{H}_i$ through feedback from the i^{th} BS.
    Send $\mathbf{H}_i$ to Algorithm (2) for the formation of projection matrix $\mathbf{P}_i$.
    Receive the i^{th} projection matrix $\mathbf{P}_i$ from Algorithm (2).
    Project the FACE QPSK waveform onto the null space of i^{th} interference channel using $\breve{\widetilde{\mathbf{Z}}}_i = \widetilde{\mathbf{Z}}\mathbf{P}_i^H$.
  end for
  Find $i_{\min} = \underset{1\leq i\leq \mathcal{K}}{\arg\min} ||\widetilde{\mathbf{Z}}\mathbf{P}_i^H - \widetilde{\mathbf{Z}}||_F$.
  Set $\widetilde{\mathbf{R}}_{\text{NSP}}$ as the covariance matrix of the desired NSP QPSK waveforms to be transmitted.
end loop

4.2.7 Numerical Examples

In order to design QPSK waveforms with spectrum sharing constraints, this section uses a uniform linear array (ULA) of ten elements, i.e., $M = 10$, with an inter-element spacing of half-wavelength. Each antenna transmits waveform with unit power and $N = 100$ symbols. The resulting beampattern is averaged over 100 Monte-Carlo trials of QPSK waveforms. At each run of Monte Carlo simulation this setup generates a Rayleigh interference channel with dimensions $N_{\text{BS}} \times M$, calculates its null space, and solves the optimization problem for stationary and moving maritime MIMO radar.

4.2.7.1 Waveform for stationary radar

This section designs the transmit beampattern for a stationary MIMO radar. The desired beampattern has two main lobes from -60° to -40° and from 40° to 60°. The QPSK transmit beampattern for stationary maritime MIMO radar is obtained by solving the optimization problem in equation (4.16). Different examples are given to cover various scenarios involving different number of BSs and different configuration of MIMO antennas at the BSs. In addition an example is given to demonstrate the efficacy of Algorithms (2) and (5) in BS selection and its impact on the waveform design problem.

Example 1: Cellular System with five BSs and $\{3, 5, 7\}$ MIMO antennas

In this example, waveform for a stationary MIMO radar is designed in the presence of a cellular system with five BSs. Three cases are addressed where the number of BS antennas are varied from 3 to 7. Figure 4.7 shows the designed waveforms for all five BSs each equipped with 3 MIMO antennas. Note that, due to channel variations there is a large variation in the amount of power projected onto target locations for different BSs. But for certain BSs, the projected waveform is close to the desired waveform. Figure 4.8 shows the designed

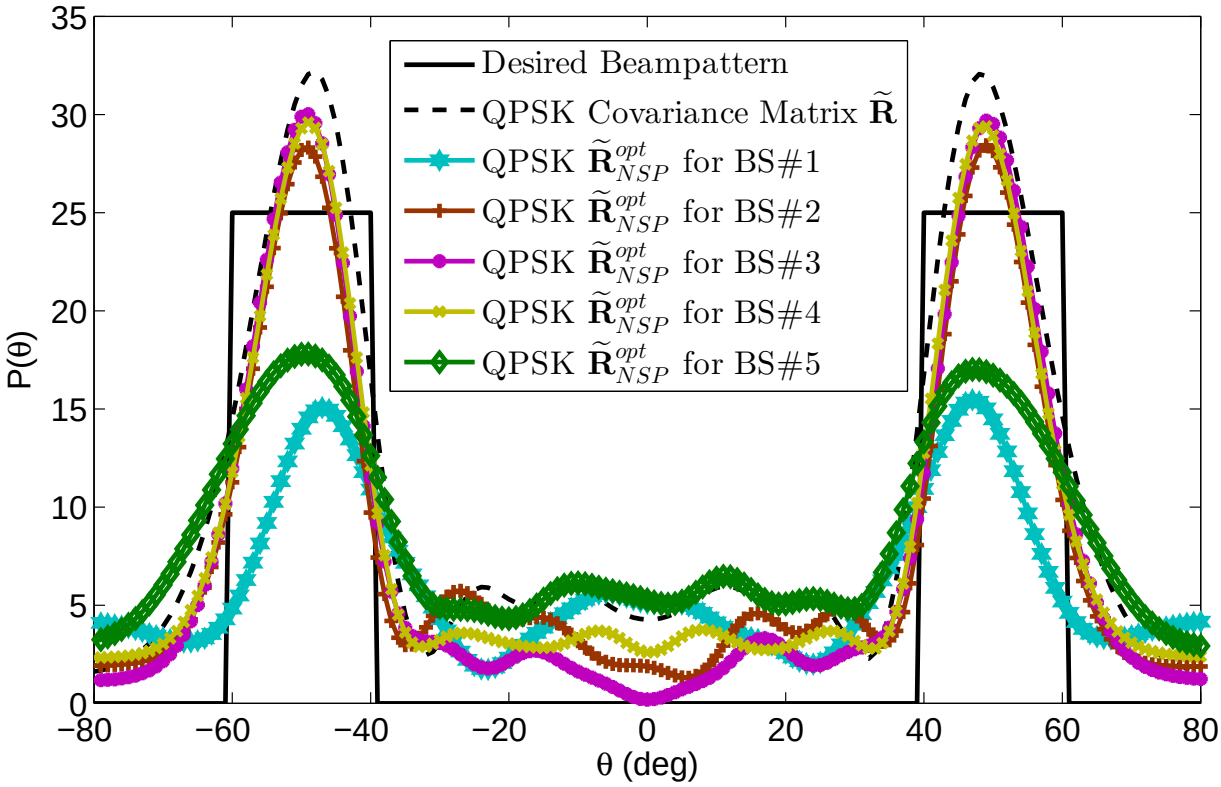

Figure 4.7: QPSK waveform for stationary MIMO radar, sharing RF environment with five BSs each equipped with *three* antennas.

waveforms for all five BSs each equipped with 5 MIMO antennas. Similar to the previous case, due to channel variations there is a large variation in the amount of power projected onto target locations for different BSs. However, the power projected onto the target is less when compared with the previous case. The number of antennas is increased to 7 in Figure 4.9; notice that the amount of power projected onto the targets is least as compared to previous two cases. This is because when $N_{\text{BS}} \ll M$ there is a larger null space to project radar waveform and this results in the projected waveform closer to the desired waveform. However, when $N_{\text{BS}} < M$, this is not the case.

Example 2: Performance of Algorithms (2) **and** (5) **in BS selection**

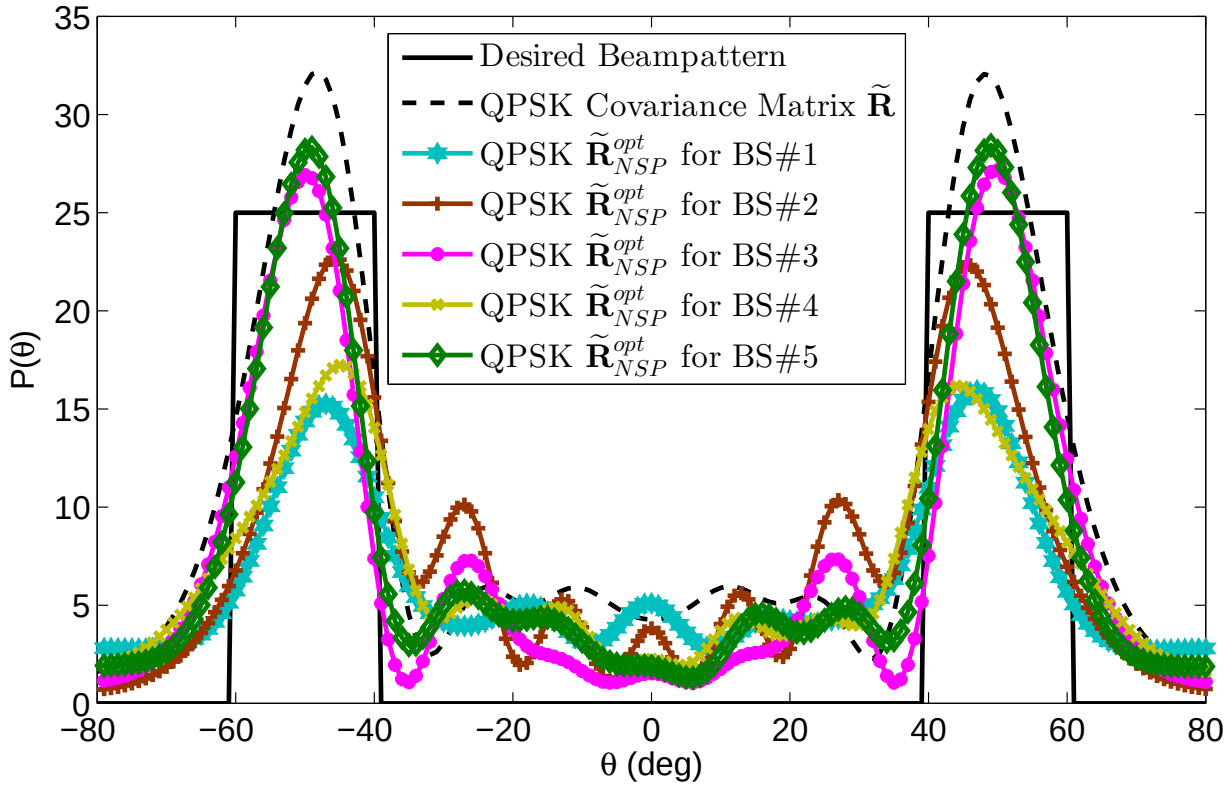

Figure 4.8: QPSK waveform for stationary MIMO radar, sharing RF environment with five BSs each equipped with *five* antennas.

In Example 1, waveforms for different number of BSs with different antenna configurations were designed. It was showed that for some BSs the designed waveform was close to the desired waveform but for other it wasn't and the projected waveform was closer to the desired waveform when $N_{\text{BS}} \ll M$ then when $N_{\text{BS}} < M$. Figure 4.10 uses Algorithms (2) and (5) to select the waveform which projects maximum power on the targets or equivalently the projected waveform is closest to the desired waveform. Algorithms (2) and (5) are applied to the cases when $N_{\text{BS}} = \{3, 5, 7\}$ and select the waveform which projects maximum power on the targets. It can be seen that Algorithm (5) helps to select waveform for stationary MIMO radar which results in best performance for radar in terms of projected waveform as close as possible to the desired waveform in addition of meeting spectrum sharing constraints.

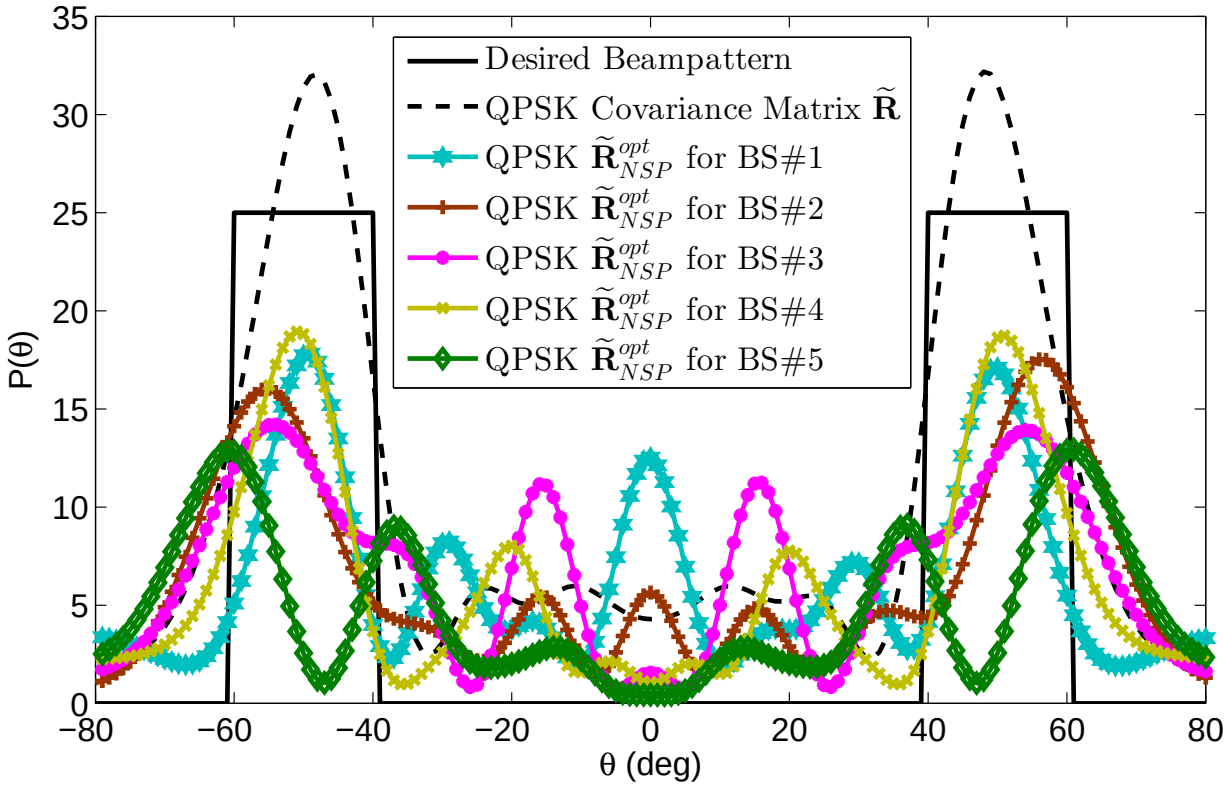

Figure 4.9: QPSK waveform for stationary MIMO radar, sharing RF environment with five BSs each equipped with *seven* antennas.

4.2.7.2 Waveform for moving radar

This section designs transmit beampattern for a moving MIMO radar. The desired beampattern has two main lobes from $-60°$ to $-40°$ and from $40°$ to $60°$. The QPSK transmit beampattern for moving maritime MIMO radar is obtained by solving the optimization problem in equation (4.51) and then projecting the resulting waveform onto the null space of $\mathbf{H}_i$ using the projection matrix in equation (4.82). Different examples are given to cover various scenarios involving different number of BSs and different configuration of MIMO antennas at the BSs. In addition an example is given to demonstrate the efficacy of Algorithms (2) and (6) in BS selection and its impact on the waveform design problem.

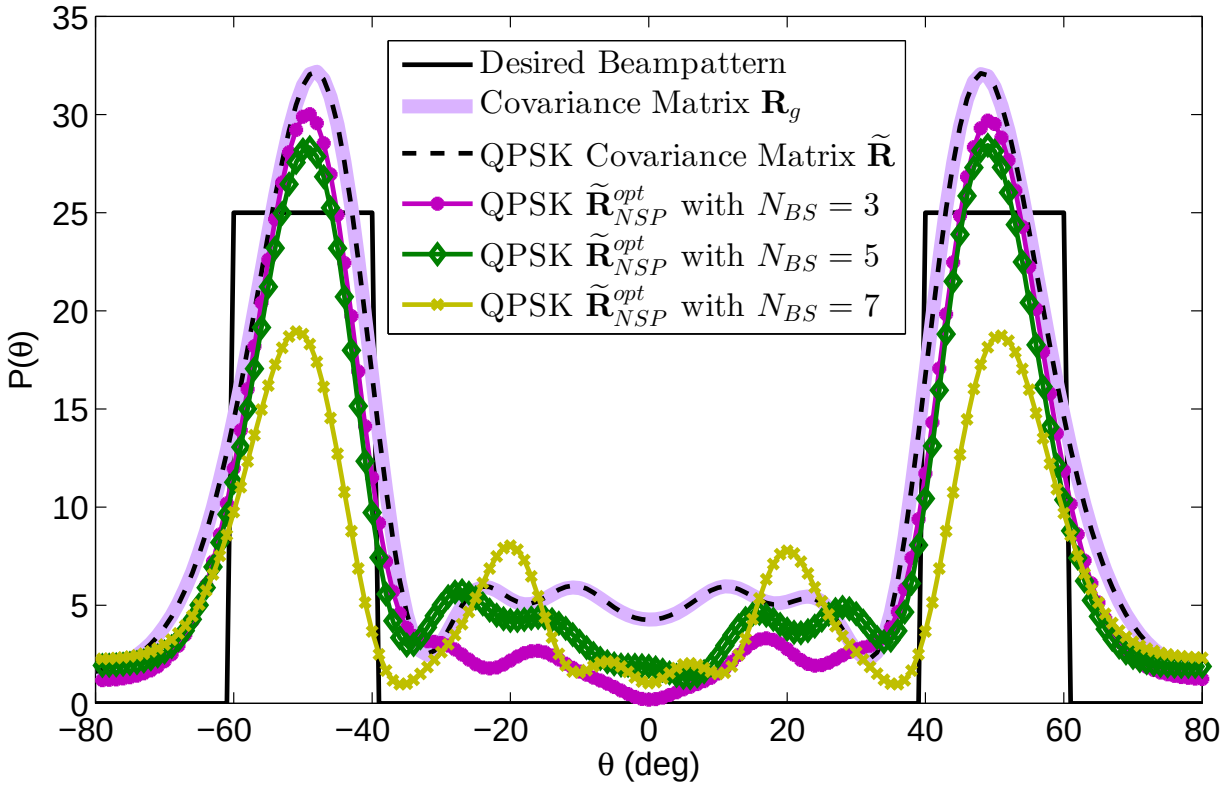

Figure 4.10: Algorithm (5) is used to select the waveform which projects maximum power on the targets when $N_{\text{BS}} = \{3, 5, 7\}$ in the presence of five BSs.

Example 3: Cellular System with five BSs each with $\{3, 5, 7\}$ MIMO antennas and moving MIMO radar

This example designs waveform for a moving MIMO radar in the presence of a cellular system with five BSs. Three cases are addressed where the number of BS antennas are varied from 3 to 7. Figure 4.11 shows the designed waveforms for all five BSs each equipped with 3 MIMO antennas. Note that, due to channel variations there is a large variation in the amount of power projected onto target locations for different BSs. When compared with Figure 4.7, the power projected onto the target by NSP waveform is less due to the mobility of radar. Figure 4.12 shows the designed waveforms for all five BSs each equipped with 5 MIMO

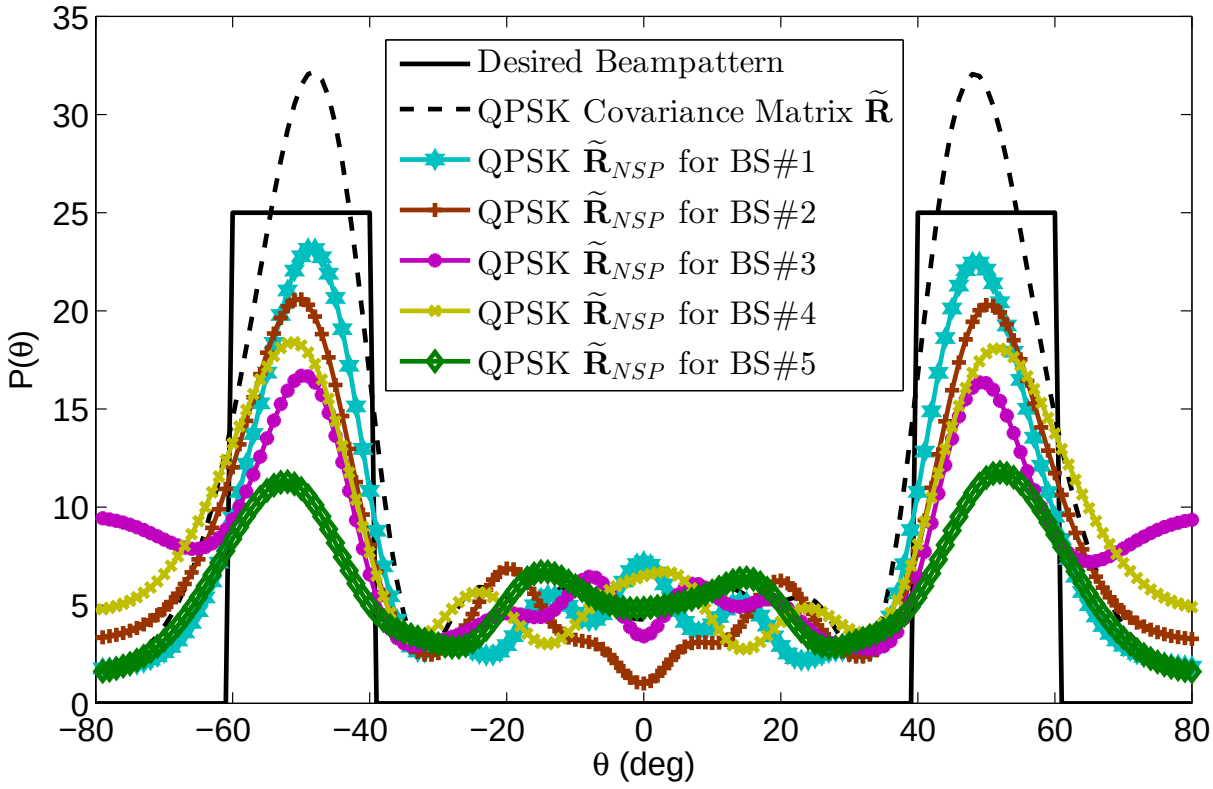

Figure 4.11: QPSK waveform for moving MIMO radar, sharing RF environment with five BSs each equipped with *three* antennas.

antennas. Similar to the previous case, due to channel variations there is a large variation in the amount of power projected onto target locations for different BSs. However, the power projected onto the target is less when compared with the previous case. The number of antennas is increased to 7 in Figure 4.13, note that the amount of power projected onto the targets is least as compared to previous two cases. This is because when $N_{\text{BS}} \ll M$ there exists a larger null space to project radar waveform and this results in the projected waveform closer to the desired waveform. However, when $N_{\text{BS}} < M$, this is not the case. Moreover, due to mobility of the radar, the amount of power projected for all three cases considered in this example are less than the similar example considered for stationary radar.

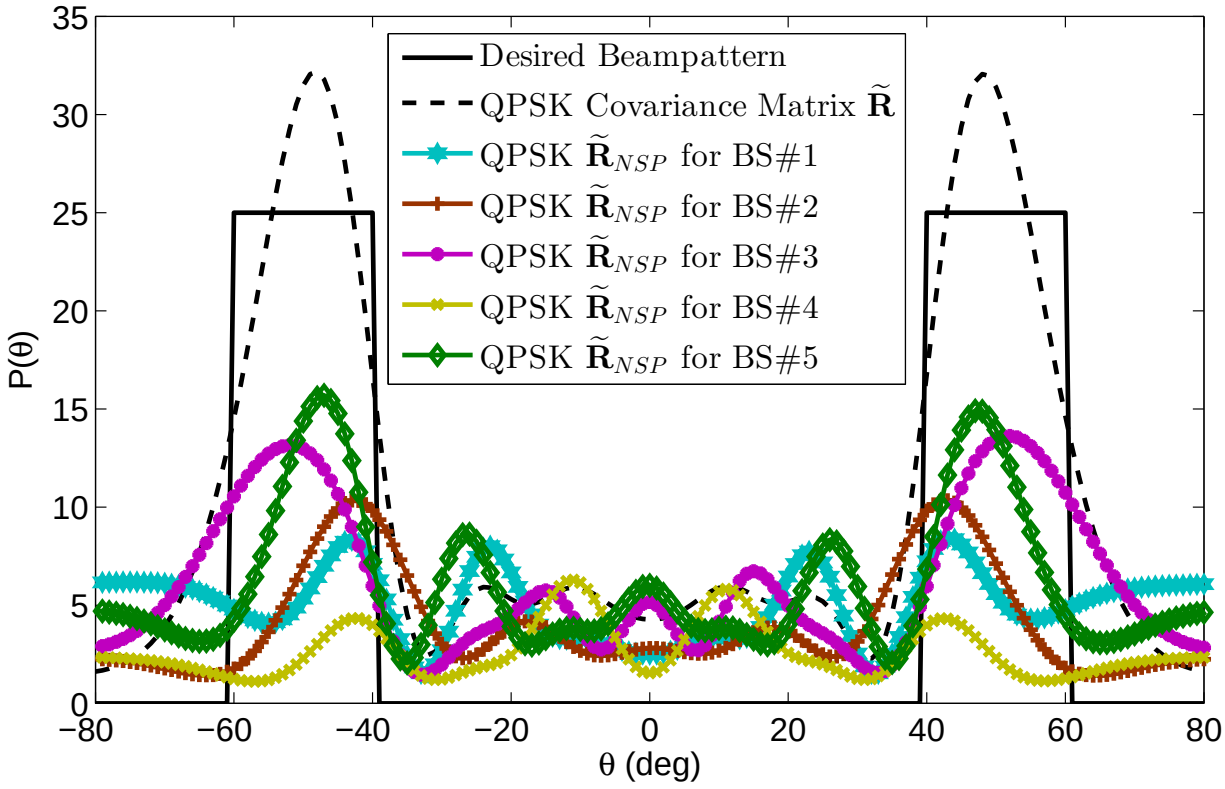

Figure 4.12: QPSK waveform for moving MIMO radar, sharing RF environment with five BSs each equipped with *five* antennas.

Example 4: Performance of Algorithms (2) **and** (6) **in BS selection for spectrum sharing with moving MIMO radar**

In Example 3, waveforms for different number of BSs with different antenna configurations were designed. It was shown that for some BSs the designed waveform was close to the desired waveform but for other it wasn't and the projected waveform was closer to the desired waveform when $N_{\text{BS}} \ll M$ then when $N_{\text{BS}} < M$. Figure 4.14 uses Algorithms (2) and (6) to select the waveform which has the least Forbenius norm with respect to the designed waveform. Algorithms (2) and (6) are applied to the cases when $N_{\text{BS}} = \{3, 5, 7\}$ and select the waveform which has minimum Forbenius norm. It can be seen that Algorithm

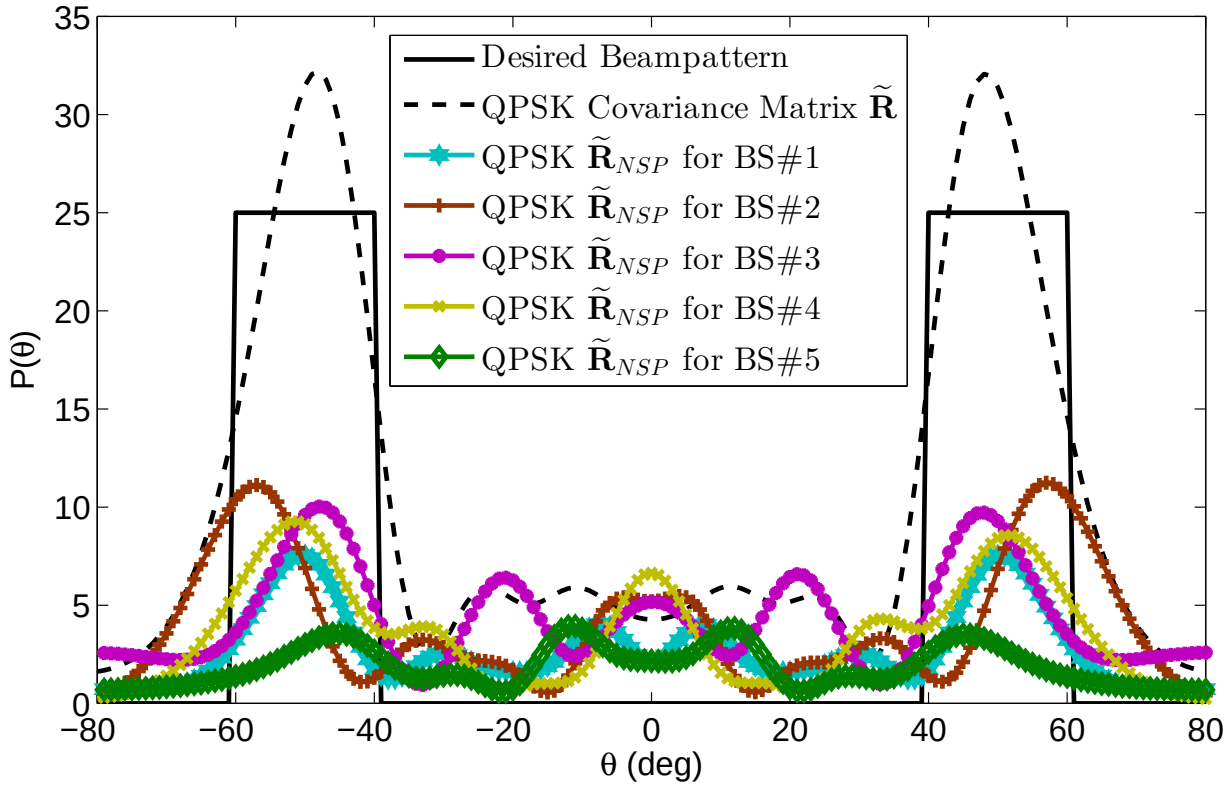

Figure 4.13: QPSK waveform for moving MIMO radar, sharing RF environment with five BSs each equipped with *seven* antennas.

(6) helps to select waveform for stationary MIMO radar which results in best performance for radar in terms of projected waveform as close as possible to the desired waveform in addition of meeting spectrum sharing constraints.

4.3 Conclusion

Waveform design for MIMO radar is an active topic of research in the signal processing community. This work addressed the problem of designing MIMO radar waveforms with spectrum sharing constraints. BPSK and QPSK waveforms were designed to allow radars

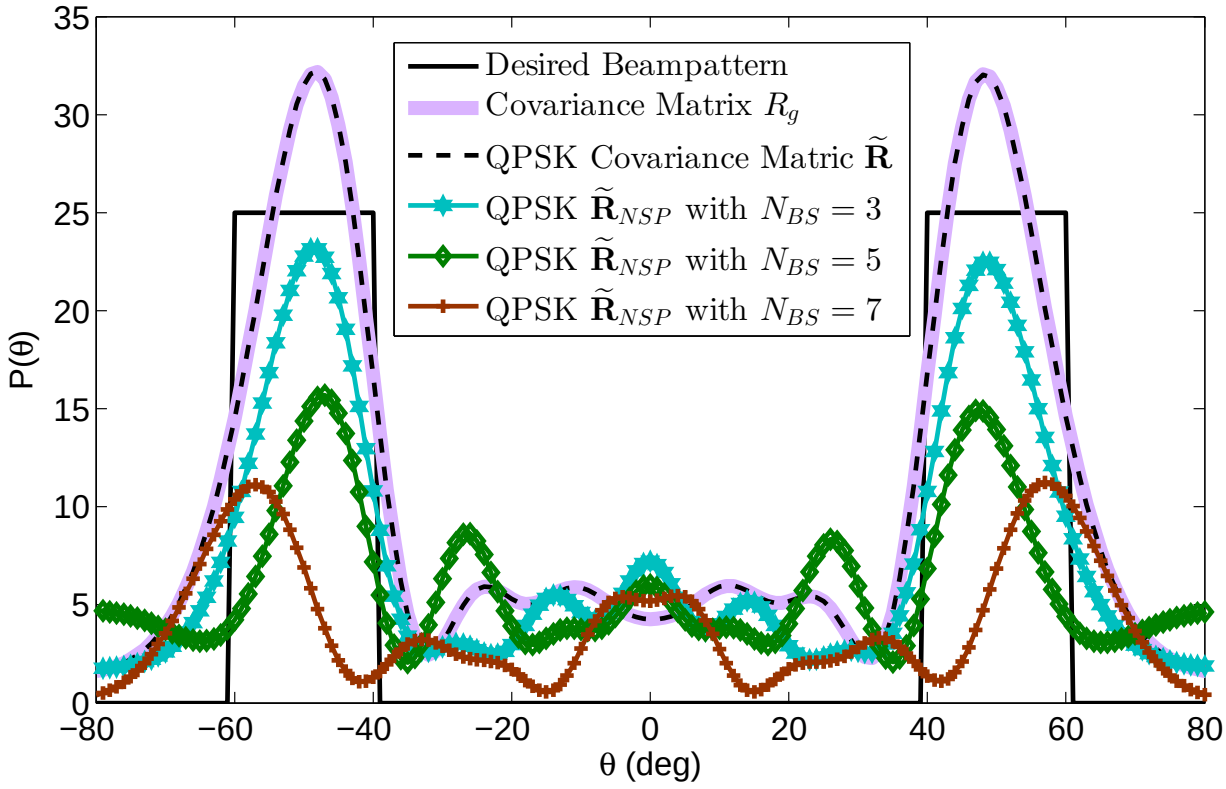

Figure 4.14: Algorithm (6) is used to select the waveform which projects maximum power on the targets when $N_{\text{BS}} = \{3, 5, 7\}$ in the presence of five BSs.

to share spectrum with communication systems without causing interference, which are very desirable for spectrum congested RF environments. In addition, constant-envelope QPSK waveforms were designed which are very desirable from practical perspectives.

In this chapter, BPSK and QPSK waveforms were designed for spectrally congested RF environments where radar and communication systems are sharing the same frequency band. The waveforms were shaped in a way that it is in the null space of communication system to avoid interference to communication system. A multi-BS MIMO cellular system was considered and algorithms for the formation of projection matrices and selection of interference channels were proposed. Waveforms for stationary and moving MIMO radar systems

were designed. For stationary MIMO radar, algorithms for BPSK and QPSK waveforms were proposed by considering the spectrum sharing constraints. The algorithms selected the waveform capable to project maximum power at the targets. For moving MIMO radar, algorithms for BPSK and QPSK waveforms were proposed by considering spectrum sharing constraints. The algorithms selected the waveform with the minimum Forbenius norm with respect to the designed waveform. This metric helped to select the projected waveform closest to the designed waveform.

In addition, it was shown that it is possible to realize finite alphabet constant-envelope quadrature-pulse shift keying (QPSK) MIMO radar waveforms. It was proved that such the covariance matrix for QPSK waveforms is positive semi-definite and the constrained nonlinear optimization problem can be transformed into an un-constrained nonlinear optimization problem, to realize finite alphabet constant-envelope QPSK waveforms. This result is of importance for both communication and radar waveform designs where constant-envelope is highly desirable.

Chapter 5

Cellular Interference Modeling for Spectrum Sharing

This chapter presents a framework for the analysis of radar performance under cellular interference. The impact on the performance of radar due to cellular interference is studied by deriving bounds on the probability of detection and probability of miss detection. For this purpose, first the distribution of aggregate cellular interference is derived, in a correlated shadow fading environment, at the radar receiver. It is proved that the sum of interference signals from a cellular system has a log-normal distribution with probability 1. A lower bound on the probability of miss target is derived where a ship target is consider and target returns are modeled by a log-normal distribution. Along with the analytical results this chapter also provide the corresponding simulation results showing degradation in radar performance due to interference from cellular systems.

This chapter first provides a spectrum sharing model in Section 5.1. Sections 5.2 and 5.2.1 state and prove that the aggregate interference from a cellular system has a log-normal

distribution, respectively. Section 5.2.2 computes the interference parameters. Section 5.3 explains radar system and target model. Section 5.4 derives bounds on the probability of detection. Section 5.5 presents simulation results along with the discussion and Section 5.6 concludes the chapter.

5.1 System Model and Notations

A spectrum sharing model in which a cellular system with N base stations (BS) is sharing radar spectrum to increase its capacity. However, this sharing of spectrum results in cellular interference to radar system. It is assumed the radar is at a distance of $r_i, i = 1, 2, \cdots, N$, from the i^{th} BS. This model is general in nature as any specific spatial distribution of the cellular system is not considered. In addition, all the BS are capable of transmitting at arbitrary power levels of their interest. The only assumption is that the location of all the BSs is known to the radar at which interference needs to be characterized. This is a fair assumption since in macro cellular systems BS locations are subject to network planning.

The wireless propagation environment that exists between shipborne radars and BSs of cellular systems is significantly different than that of a typical mobile in a cellular system. This is due to the fact that radar is located far away and only path loss, which is significant over large distances, and shadow fading, due to blockage of signals from large obstacles, affect the received signal strength at radar receiver. Due to the same reason, radar receiver is insensitive to the effect of small scale fading, due to mulipath propagation. These factors bring in novelty in the problem of aggregate cellular interference analysis for radar system and makes it different from analyzing interference at a particular receiver inside a cellular system. Thus, in order to consider a realistic interference scenario, we consider mean path loss and log-normal shadow fading models, which are commonly used in interference analysis

treatments [94]. Then, the interference power received from the i^{th} BS is

$$I_i = P_i r_i^{-\alpha} e^{X_i}, \qquad i = 1, 2, \cdots, N, \tag{5.1}$$

where P_i denotes the power transmitted, $r_i^{-\alpha}$ is the path loss exponent, and e^{X_i} is the log-normal random variable, where X_i is the transmitted signal from the i^{th} BS. In this chapter, X_i's that are jointly correlated Gaussian random variables with mean, μ_{X_i}, and variance, $\sigma^2_{X_i}$, are considered. It is assumed that the jointly correlated Gaussian random variables have a specific correlation structure, as specified in [95],

$$\rho_{ij} = \frac{\mathbb{E}\left[(X_i - \mu_{X_i})(X_j - \mu_{X_j})\right]}{\sigma_{X_i}\sigma_{X_j}} = \beta_i \beta_j. \tag{5.2}$$

The model under consideration has some other practical applications. It can be used to characterize interference from a secondary cellular system to a primary TV system where the cellular system is opportunistically using the TV white spaces to enhance its capacity [96]. Another application is the IEEE 802.22 digital TV (DTV) [97] scenario in which a cellular system is used to broadcast a TV signal and the interest is in the interference from this system to cognitive radios using spectrum opportunistically.

5.2 Aggregate Interference Distribution

In order to evaluate the impact of cellular interference on radar's performance it is necessary to characterize the statistic of the interference. The interference from N BSs, at radar, is

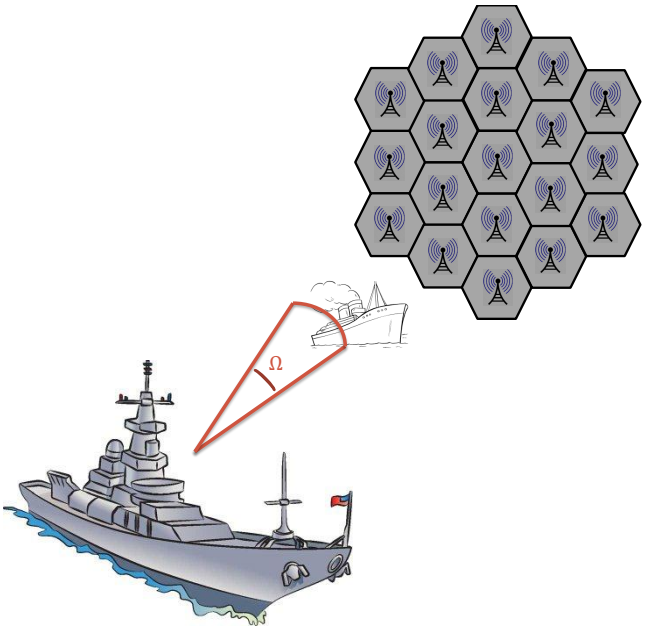

Figure 5.1: Shipborne phased array radar and onshore cellular system: Shipborne electrically-steered phased array radar is experiencing interference from an onshore cellular system while detecting a seaborne target that is a ship. The radar's main beam is subject to interference from cellular system.

the sum of individual interference powers and can be written as

$$\begin{aligned} I &= \sum_{i=1}^{N} I_i \\ &= \sum_{i=1}^{N} P_i r_i^{-\alpha} e^{X_i}. \end{aligned} \tag{5.3}$$

Then, the distribution of aggregate interference, described by equation (5.3), follows the log-normal distribution according to the following theorem.

Theorem 5.2.1. *The probability distribution of the normalized aggregate interference, at a radar system, has a limit distribution which is log-normal with probability 1, i.e.*

$$I = \frac{\sum_{i=1}^{N} I_i}{N} \xrightarrow{w.p.1} \ln \mathcal{N}(\mu_I, \sigma_I^2)$$

where the parameters μ_I and σ_I^2 are given as

$$\mu_I = \frac{1}{N}\sum_{i=1}^{N} P_i r_i^{-\alpha} e^{\left(\mu_{X_i} + \frac{\sigma_{X_i}^2}{2}\right)}$$

and

$$\sigma_I^2 = \mu_I^2 \left(e^{\zeta^2} - 1\right)$$

where

$$\zeta^2 = \sigma_{X_i}\sigma_{X_j}\beta_i\beta_j.$$

The cumulative probability density function (cdf) is given as

$$\mathbb{F}_I(i;\mu_I,\zeta) = \mathbb{P}(I \leq i) = 1 - \mathbb{Q}\left(\frac{\ln i - \ln \mu_I}{\zeta} + \frac{\zeta}{2}\right)$$

where $\mathbb{Q}(\cdot)$ is the Marcum's Q-function defined as

$$\mathbb{Q}(x) = \frac{1}{\sqrt{2\pi}}\int_x^{\infty} e^{-t^2/2} dt.$$

5.2.1 Proof of the Aggregate Interference Distribution

Let $Y_i, i = 0, 1, \cdots, N$, be independent Gaussian random variables with mean μ_{Y_i} and variance $\sigma_{Y_i}^2$. The first step is to create jointly correlated Gaussian random variables $X_i, i = 1, \cdots, N$, with a transformation

$$X_i = \zeta Y_0 + Y_i \tag{5.4}$$

where ζ is a positive real number and set $\mu_{Y_0} = 0$ and $\sigma_{Y_0}^2 = 1$. With this transformation $\mu_{X_i} = \mu_{Y_i}$ and $\sigma_{X_i}^2 = \zeta^2 + \sigma_{Y_i}^2$.

In order to proceed with the proof, independent log-normal random variables are first defined as

$$Z_i = P_i r_i^{-\alpha} e^{Y_i} \quad i = 1, 2, \cdots, N \tag{5.5}$$

with mean

$$\mu_{Z_i} = P_i r_i^{-\alpha} e^{\mu_{Y_i} + \sigma_{Y_i}^2/2}$$

and variance

$$\sigma_{Z_i}^2 = \left(P_i r_i^{-\alpha}\right)^2 e^{\left(2\mu_{Y_i} + \sigma_{Y_i}^2\right)} \left(e^{\sigma_{Y_i}^2} - 1\right).$$

Second, jointly correlated log-normal random variables are defined as

$$I_i = P_i r_i^{-\alpha} e^{X_i} \quad i = 1, 2, \cdots, N$$

with mean

$$\mu_{I_i} = \mu_{Z_i} e^{\zeta^2/2} \tag{5.6}$$

and variance

$$\sigma_{I_i}^2 = \left(P_i r_i^{-\alpha}\right)^2 e^{\left(2\mu_{Y_i} + \sigma_{Y_i}^2\right)} \left(e^{\sigma_{Y_i}^2} - 1\right).$$

Using (5.3), normalized aggregate interference can be written as

$$\begin{aligned} I &= \frac{1}{N} \sum_{i=1}^{N} I_i \\ &= \frac{1}{N} \sum_{i=1}^{N} P_i r_i^{-\alpha} e^{X_i}. \end{aligned} \tag{5.7}$$

Substituting X_i from equation (5.4) in (5.7) results in

$$\begin{aligned} I &= \frac{1}{N}\sum_{i=1}^{N} P_i r_i^{-\alpha} e^{(\zeta Y_0 + Y_i)} \\ &= \frac{1}{N} e^{\zeta Y_0} \sum_{i=1}^{N} P_i r_i^{-\alpha} e^{Y_i} \\ &= e^{\zeta Y_0} \frac{\sum_{i=1}^{N} Z_i}{N}. \end{aligned} \tag{5.8}$$

Applying the strong law of large numbers on equation (5.8) yields

$$\begin{aligned} \lim_{N\to\infty} I &= e^{\zeta Y_0} \lim_{N\to\infty} \frac{\sum_{i=1}^{N} Z_i}{N} \\ &= e^{\zeta Y_0} \frac{\sum_{i=1}^{N} \mathbb{E}[Z_i]}{N} \\ &= e^{\zeta Y_0} \frac{\sum_{i=1}^{N} \mu_{Z_i}}{N} \\ &= e^{\zeta Y_0} \bar{\mu}_{Z_i} \\ &= e^{(\zeta Y_0 + \ln \bar{\mu}_{Z_i})} \triangleq \widetilde{I} \end{aligned} \tag{5.9}$$

where $\widetilde{I}$ is a log-normal random variable with mean $\mu_{\widetilde{I}}$ and variance $\sigma^2_{\widetilde{I}}$. Note that equation (5.9) follows with probability one if Z_i's are independent, this follows from our definition of Z_i's in equation (5.5), and if the series $\sum_{i=0}^{\infty} \sigma^2_{Z_i}/i^2$ converges. To prove that, let

$$\begin{aligned} \sigma^2_{max} &= \max_i \sigma^2_{Z_i} \\ &= \max_i \left\{ \left(P_i r_i^{-\alpha}\right)^2 e^{\left(2\mu_{Y_i} + \sigma^2_{Y_i}\right)} \left(e^{\sigma^2_{Y_i}} - 1\right) \right\}. \end{aligned}$$

Since $P_i, r_i^{-\alpha}, \mu_{Y_i}$, and $\sigma_{Y_i}^2$ are all bounded so $\sigma_{max}^2 < \infty$. Then

$$\begin{aligned}\sum_{i=0}^{\infty} \frac{\sigma_{Z_i}^2}{i^2} &\leq \sum_{i=0}^{\infty} \frac{\sigma_{max}^2}{i^2} \\ &= \sigma_{max}^2 \sum_{i=0}^{\infty} \frac{1}{i^2} = \sigma_{max}^2 \frac{\pi^2}{6} < \infty\end{aligned}$$

where the last equality follows from [95].

5.2.2 Parameters of the Aggregate Interference Distribution

In this section, parameters for the aggregate interference in terms of signal parameters, $P_i, r_i^{-\alpha}, \mu_{X_i}, \sigma_{X_i}^2$, as described by equation (5.3) are found. In the last section it was showed that the aggregate interference has a joint log-normal distribution with parameters μ_I and σ_I^2 which can be calculated from equation (5.9) by first noting

$$\mu_{\widetilde{I}} = e^{\zeta^2/2} \bar{\mu}_{Z_i}. \tag{5.10}$$

Using definition of $\bar{\mu}_{Z_i}$ it can written that

$$\bar{\mu}_{Z_i} = \frac{1}{N} \sum_{i=1}^{N} \mu_{Z_i} = e^{-\zeta^2/2} \frac{1}{N} \sum_{i=1}^{N} \mu_{I_i} \tag{5.11}$$

where (5.11) follows from (5.6). Substituting (5.11) in (5.10) yields

$$\begin{aligned}\mu_{\widetilde{I}} &= \frac{1}{N} \sum_{i=1}^{N} \mu_{I_i} \\ &= \frac{1}{N} \sum_{i=1}^{N} P_i r_i^{-\alpha} e^{\left(\mu_{X_i} + \frac{\sigma_{X_i}^2}{2}\right)} \triangleq \mu_I.\end{aligned} \tag{5.12}$$

Similarly, the variance of the aggregate interference is given as

$$\sigma_{\widetilde{I}}^2 = \mathbb{E}\left[\left(\widetilde{I} - \mu_{\widetilde{I}}\right)^2\right] = \bar{\mu}_{Z_i}^2 e^{\zeta^2}\left(e^{\zeta^2} - 1\right). \tag{5.13}$$

Now, using equations (5.10) to (5.12), (5.13) can be written in terms of interference parameters as

$$\sigma_{\widetilde{I}}^2 = \mu_I^2\left(e^{\zeta^2} - 1\right) \triangleq \sigma_I^2.$$

Next, in order to determine ζ^2, equations (5.4) and (5.7) can be used as

$$\begin{aligned}\rho_{ij} &= \frac{\mathbb{E}\left[(X_i - \mu_{X_i})(X_j - \mu_{X_j})\right]}{\sigma_{X_i}\sigma_{X_j}} \\ &= \frac{\mathbb{E}\left[(\zeta Y_0 + Y_i - \mu_{Y_i})(\zeta Y_0 + Y_j - \mu_{Y_j})\right]}{\sigma_{X_i}\sigma_{X_j}} \\ &= \frac{\zeta^2}{\sigma_{X_i}\sigma_{X_j}} = \beta_i\beta_j.\end{aligned} \tag{5.14}$$

The last equality follows from our assumptions, introduced at the beginning of this proof, i.e. $\mu_{Y_0} = 0$, $\sigma_{Y_0}^2 = 1$, and $Y_i, i = 0, 1, \cdots, N$, being independent Gaussian random variables. Then ζ^2 follows from (5.14) as

$$\zeta^2 = \sigma_{X_i}\sigma_{X_j}\beta_i\beta_j.$$

The cdf of aggregate interference follows from the definition of cdf of log-normal random variables and the definitions of μ_I and σ_I^2 after some algebraic manipulations.

5.3 Radar System and Target Model

In this section, a shipborne electronically-steered phased array radar with four phased arrays, each capable to carry a 45° azimuth scan, is considered. Phased array radars are capable

of performing multiple functions at the same time. Some of the functions include complete search of hemisphere, track multiple targets; illuminate multiple targets and guide missiles towards them; they also have flexible search and track rates and frequency agility.

A seaborne target which is a ship is considered in this analysis. The detection of fluctuating target signals, in the presence of Gaussian noise, is a well studied problem in radar literature [98]. Usually it is assumed that the amplitude of the fluctuating signal has a Rayleigh distribution. This assumption is justified since radar returns from a target are composed of numerous and diverse reflecting elements. Then, statistically, the sum of these large number of independent random vectors, each having a uniform phase and a Rayleigh amplitude distribution, is a Rayleigh vector [99]. However, the Rayleigh assumption is generally true for targets having small radar cross section (RCS) because targets with high RCS exhibit a heavier tail than the Rayleigh distribution [100].

It is observed that certain target signals are best modeled by a log-normal distribution, for example, targets like ships, satellites and space vehicles. Assuming a Rayleigh distributed signal for such targets lead to significant errors in the probability of detection [101]. Therefore, a log-normal target model is used, which is constant within a scan but fluctuates log-normally from scan to scan. Since, the maximum effect of interference on radar will be during the azimuth search/track/detect operation and that is where the target is located it is appropriate to use a log-normal target model. Any other target model for such a scenario may not give accurate results due to mismatch in target models. Thus, the reflected signal from the target ship has a log-normal distribution and can be expressed as

$$x = P_r e^{-\psi}$$

where P_r is the power of the received signal from the target, ψ is normally distributed with

mean μ_ψ and variance σ_ψ^2. The probability of detection for such a target, no-interference case, is given as [101]

$$\mathbb{P}_D(\mathrm{SNR}, \Gamma, n_p, \psi) = \int_0^\infty \mathbb{P}_{n_p}(x, \Gamma) f(x|\mathrm{SNR}, \psi)\, dx \tag{5.15}$$

where

$$\mathbb{P}_{n_p}(\mathrm{SNR}, \Gamma) = \int_\gamma^\infty (v|\mathrm{SNR})^{(n_p-1)/2} e^{-(v-n_p\mathrm{SNR})} \mathbb{I}_{n_p-1}\left(2\sqrt{\mathrm{SNR} n_p v}\right)\, dv$$

is the probability of detection for n_p integrated pulses with some signal to noise ratio (SNR) at some detector threshold Γ, $\mathbb{I}_K(\cdot)$ is the modified Bessel function of order K, and

$$f(x|\mathrm{SNR}, \psi) = \frac{1}{\sqrt{2\pi}\sigma_\psi x} \exp\left(-\frac{\ln^2(\psi x/\mathrm{SNR})}{2\sigma_\psi^2}\right), \quad \psi \geq 1$$

is the probability density function for the log-normally fluctuating signal with ψ being the fluctuation parameter and $\sigma_\psi^2 = 2\ln\psi$.

The radar range equation is a useful metric for estimating the range of a radar, as a function of radar parameters. The interest is in the maximum radar range, $R_{\max}$, that can be achieved in a cellular interference scenario. The simple form of the radar equation is given as [82],

$$R_{\max}^4 = \frac{P_{t,\max} G_t G_r \bar{\sigma} \lambda^2}{(4\pi)^3 P_{r,\min}} \tag{5.16}$$

where $P_{t,\max}$ is the peak transmitted power from the transmit antenna of gain G_t, G_r is the gain of the receive antenna, λ is the wavelength, $\bar{\sigma}$ is the RCS of the target ship, and $P_{r,\min}$ is the smallest received power that can be detected by the radar. Since target is considered

to be a ship, its RCS can be approximated by the ship's displacement in tons. An empirical relation to calculate RCS is given by [82]

$$\bar{\sigma} = 52 f^{1/2} D^{3/2}\,\mathrm{m}^2$$

where f is the radar operating frequency in megahertz (MHz), and D is the ship's (full load) displacement in kilotons.

5.4 Receiver Operating Curves (ROC)

Assume the target is located in the same azimuth as that of cellular system. It is of interest to find the distribution of signal-to-interference-plus-noise ratio (SINR) so as to evaluate the radar's ROC. The SINR at the radar can be written as

$$\begin{aligned}\mathrm{SINR} &= \frac{P_r e^{-\psi}}{P_n + \sum_{i=1}^{N} P_i r_i^{-\alpha} e^{X_i}} \\ &= \frac{e^{-\psi}}{\dfrac{P_n}{P_r} + \dfrac{1}{P_r}\sum_{i=1}^{N} P_i r_i^{-\alpha} e^{X_i}}.\end{aligned}$$

Let's define $\gamma \triangleq P_r/P_n$, so that

$$\mathrm{SINR} = \frac{e^{-\psi}}{\dfrac{1}{\gamma} + \dfrac{1}{P_r}\sum_{i=1}^{N} P_i r_i^{-\alpha} e^{X_i}}. \tag{5.17}$$

Then, the probability of detection $\mathbb{P}_D$ can be expressed as

$$\mathbb{P}_D = 1 - \mathbb{P}_{\mathrm{Miss}} = 1 - \mathbb{P}(\mathrm{SINR} < \Gamma) \tag{5.18}$$

where $\mathbb{P}_{\text{Miss}}$ is the probability of miss detection. The analog to $\mathbb{P}_{\text{Miss}}$ in wireless communications is the outage probability. In order to characterize $\mathbb{P}_{\text{Miss}}$ and consequently $\mathbb{P}_D$ we are interested in the distribution of SINR for which no closed form expression exists and only approximations are used. However, a lower bound on the $\mathbb{P}_D$ of radar can be achieved by using similar arguments as in [102].

In order to simplify equation (5.17) let's define

$$\Delta \triangleq \frac{1}{\gamma} + \frac{1}{P_r}\sum_{i=1}^{N} P_i r_i^{-\alpha}$$
$$\xi_i \triangleq \frac{P_i r_i^{-\alpha}}{P_r \Delta}$$
$$\xi_0 \triangleq \frac{1}{\gamma\Delta}$$

where $\sum_{i=0}^{N} \xi_i = 1$. The SINR, in equation (5.17), can be rewritten using above definitions as

$$\text{SINR} = \frac{1}{\Delta}\frac{e^{-\psi}}{\xi_0 + \sum_{i=1}^{N} \xi_i e^{X_i}}.$$

Without loss of generality it is assumed that $\mu_\psi = 0$ and $\mu_{X_i} = 0$. Then, the lower bound on the probability of miss detection can be calculated by utilizing arithmatic-geometric mean

inequality, as in [102]:

$$\begin{aligned}
\mathbb{P}_{\text{Miss}} &= \mathbb{P}(\text{SINR} < \Gamma) \\
&= \mathbb{P}\left(e^{-\psi} < \Gamma\Delta\left(\xi_0 + \sum_{i=1}^{N} \xi_i e^{X_i}\right)\right) \\
&\geq \mathbb{P}\left(e^{-\psi} < \Gamma\Delta \prod_{i=1}^{N} e^{\xi_i X_i}\right) \\
&= \mathbb{P}\left(e^{-\left(\psi + \sum_{i=1}^{N} \xi_i X_i\right)} < \Gamma\Delta\right) \\
&= \mathbb{P}\left(\psi + \sum_{i=1}^{N} \xi_i X_i > -\big(\ln\Gamma + \ln\Delta\big)\right) \\
&= 1 - \mathbb{Q}\left(\frac{\ln\Gamma + \ln\Delta}{\sigma}\right). \qquad (5.19)
\end{aligned}$$

The variance σ^2 can be evaluated as

$$\begin{aligned}
\sigma^2 &= \mathbb{E}\left[\left(\psi + \sum_{i=1}^{N} \xi_i X_i\right)^2\right] \\
&= \sigma_\psi^2 + \sum_{i=1}^{N}\sum_{j=1}^{N} \xi_i \xi_j \rho_{ij} \sigma_{X_i} \sigma_{X_j} \\
&= \sigma_\psi^2 + \zeta^2 \sum_{i=1}^{N}\sum_{j=1}^{N} \xi_i \xi_j \qquad (5.20)
\end{aligned}$$

where equation (5.20) follows from the definition of jointly correlated Gaussian random variables X_i and X_j, see equation (5.4), the definition of ζ^2 in Theorem 1, and the assumption that target reflections and interference are independent. Then, the bound on probability of detection $\mathbb{P}_D$ can be evaluated from equation (5.18) by using the result of equation (5.19).

Table 5.1: Radar System Parameters

Parameters	Notations	Values
Carrier Frequency	f	3.5 GHz
Bandwidth	B	10 MHz
Peak Transmit Power	$P_{t,\max}$	6 MW
Target RCS	$\bar{\sigma}$	86084 m^2
Radar Noise Floor	F_n	-100 dBm
Noise Power	P_n	kT_0F_nB
Boltzmann Constant	k	1.38×10^{-23} J/K
Standard Temperature	T_0	290 K
Transmit Antenna Gain	G_t	42 dBi
Receive Antenna Gain	G_r	36 dBi

Table 5.2: Cellular System Parameters

Parameters	Notations	Values
Number of BSs	N	100
Distance from Radar	r_i	5-6 Km
BS Power	P_i	60 W
Path Loss Exponent	α	3.5
Frequency Reuse Factor	-	1

5.5 Numerical Examples

In this section, quantitative results to complement the analytical results are presented. Simplified assumption on radar and cellular system parameters and their deployments are used in order to facilitate quantitative analysis. The military radar under consideration, SPY-1 of Aegis system, has a bandwidth of 10 MHz and has approximately 6 dB more gain on

the transmit array. Moreover, they are capable to transmit at peak power levels of up to 6 MW. Some other parameters, including carrier frequency and noise floor are not necessarily exact, due to the unavailability of such parameters, but this does not affect in any way the results and the conclusions drawn. The radar and cellular system simulation parameters are mentioned in Tables 5.1 and 5.2, respectively.

For the cellular system, it is assumed that the BS signals, X_i's, are zero-mean i.e. $\mu_{X_i} = 0$ for $i = 1, 2, \ldots, N$, and has the following variance and correlation structure:

$$\sigma^2_{X_i} = \begin{cases} 6\,\text{dB}, & \text{for } 1 \leq i \leq \left\lfloor \frac{N}{2} \right\rfloor \\ 12\,\text{dB}, & \text{for } \left\lfloor \frac{N}{2} \right\rfloor + 1 \leq i \leq N \end{cases}$$

and

$$\rho_{ij} = \begin{cases} 0.80, & \text{for } 1 \leq i, j \leq \left\lfloor \frac{N}{2} \right\rfloor \text{ and } i \neq j \\ 0.20, & \text{for } \left\lfloor \frac{N}{2} \right\rfloor + 1 \leq i, j \leq N \text{ and } i \neq j \\ 0.40, & \text{elsewhere.} \end{cases}$$

For the radar system, it is assumed without loss of generality, the log-normal target has zero mean, $\mu_\psi = 0$, and the variance is determined by the fluctuating parameter ψ.

In Figure 5.2, a log-normal probability paper to compare our results with the limiting distribution is used. It is a useful tool to compare two distributions especially for log-normal distributions which form a straight line when plotted on a log-normal paper [95]. The absicca is transformed into *log*(absicca) and the corresponding probabilities are plotted on vertical axis. It is observed that the curve for 100 BSs is close to the limit distribution for values of cdf between 10^{-6} and 1. This value is very realistic for a search radar which employs large beamwidths, i.e. larger Ω in Figure 5.1, and thus is capable to scan a large azimuth which can cover areas containing hundreds of BSs.

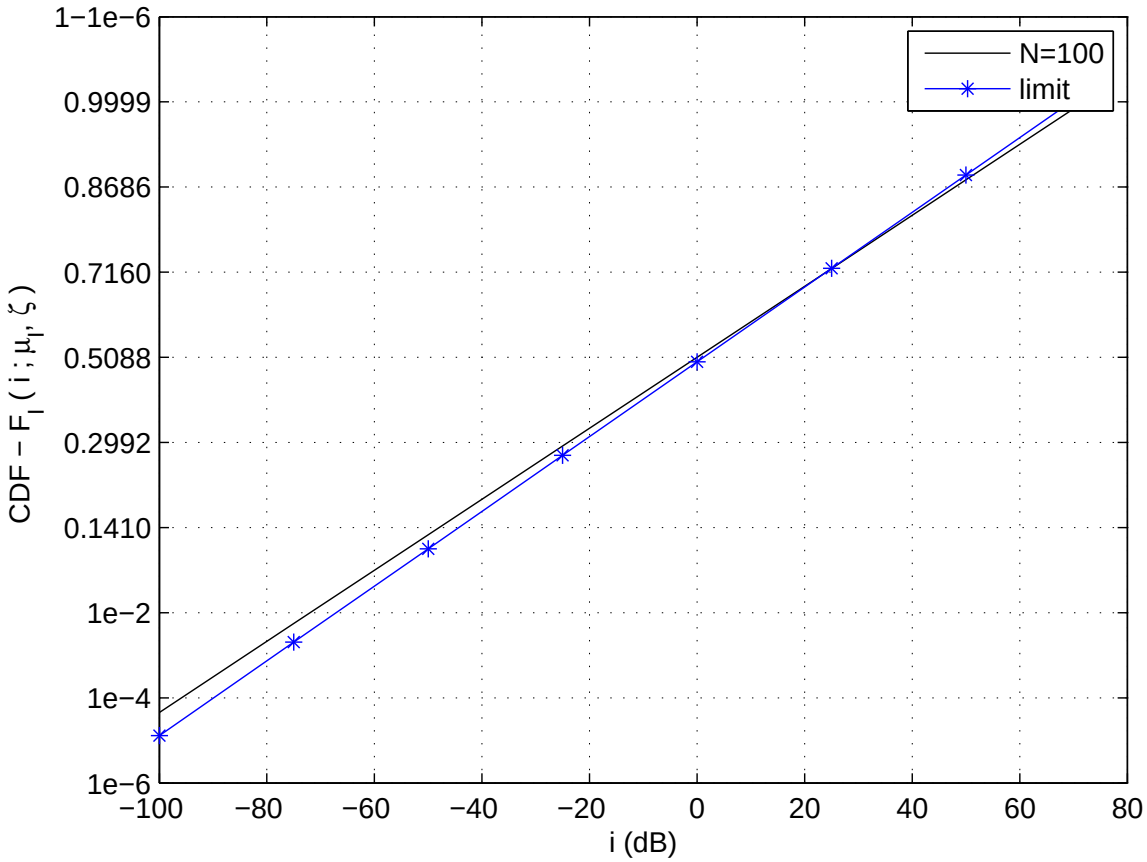

Figure 5.2: Distribution of aggregate cellular interference: The cdf, $F_I(i; \mu_I, \zeta)$, of the aggregate interference for $N = 100$ cellular base stations and the limit distribution. The limit distribution is reached for a large number of BSs but it is possible for radars which employ large beamwidths to scan azimuth for targets and can easily cover hundreds of BSs.

It is expected that the radar performance degrades when subject to interference from a cellular system operating in the same band. The lower bound on the probability of miss detection for a log-normal target is given by equation (5.19). This is used to compare the performance in Figure 5.3 for a log-normal target with and without interference with different detector threshold levels. These threshold levels are selected based on a desired probability of false alarm. The results indicate that under cellular interference radar's performance is degraded considerably. This serves as a motivation to introduce tolerable interference levels

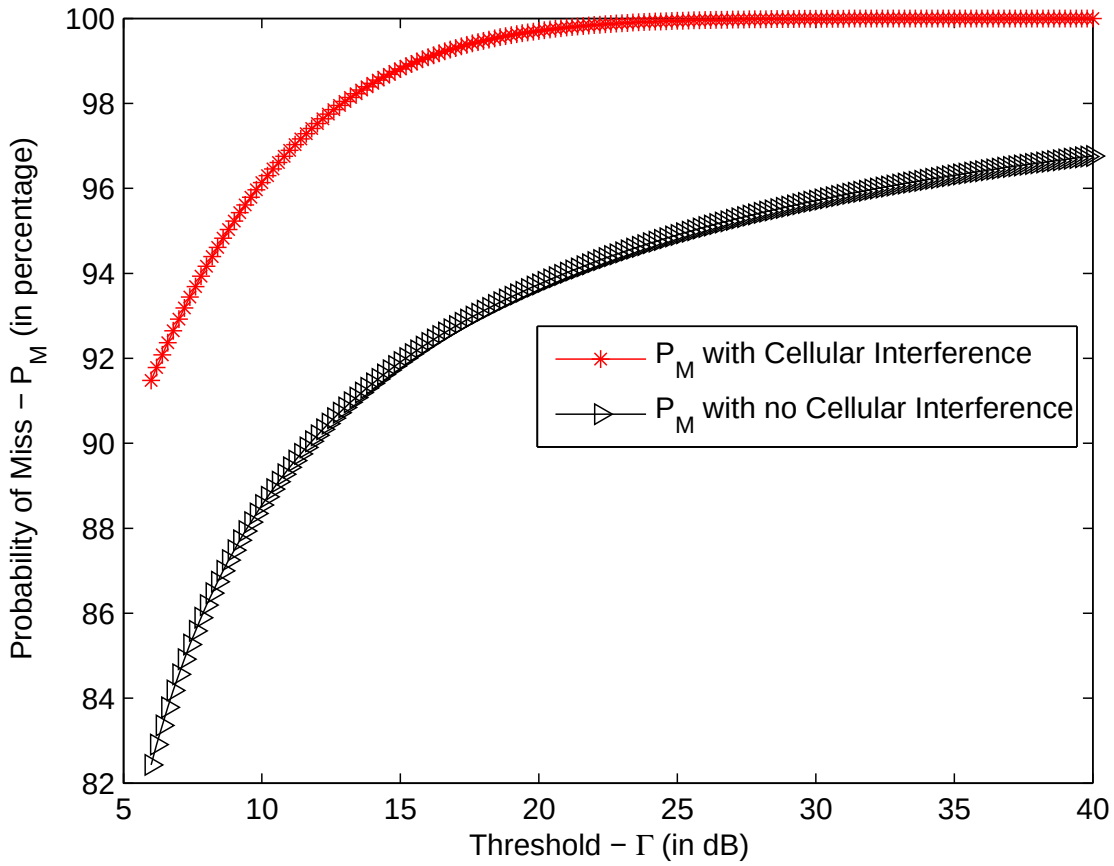

Figure 5.3: Comparison of probability of miss with and without interference. The probability of miss curve without interference is an exact curve but with interference is a lower bound on the probability of miss targets.

at the radar receiver and design considerations for deployment of cellular systems in order to protect the radar from cellular interference.

Figure 5.4 analyzes probability of miss when radar engineer varies its transmit power, $P_{t,\max}$, from 1 MWs to 4 MWs, in order to counter cellular interference. As the radar's transmit power is increased, SINR increases, and performance increases. It is also noted from Figure 5.4 that when the transmit power increases probability of miss detection drops. This can be used to counter interference from cellular systems.

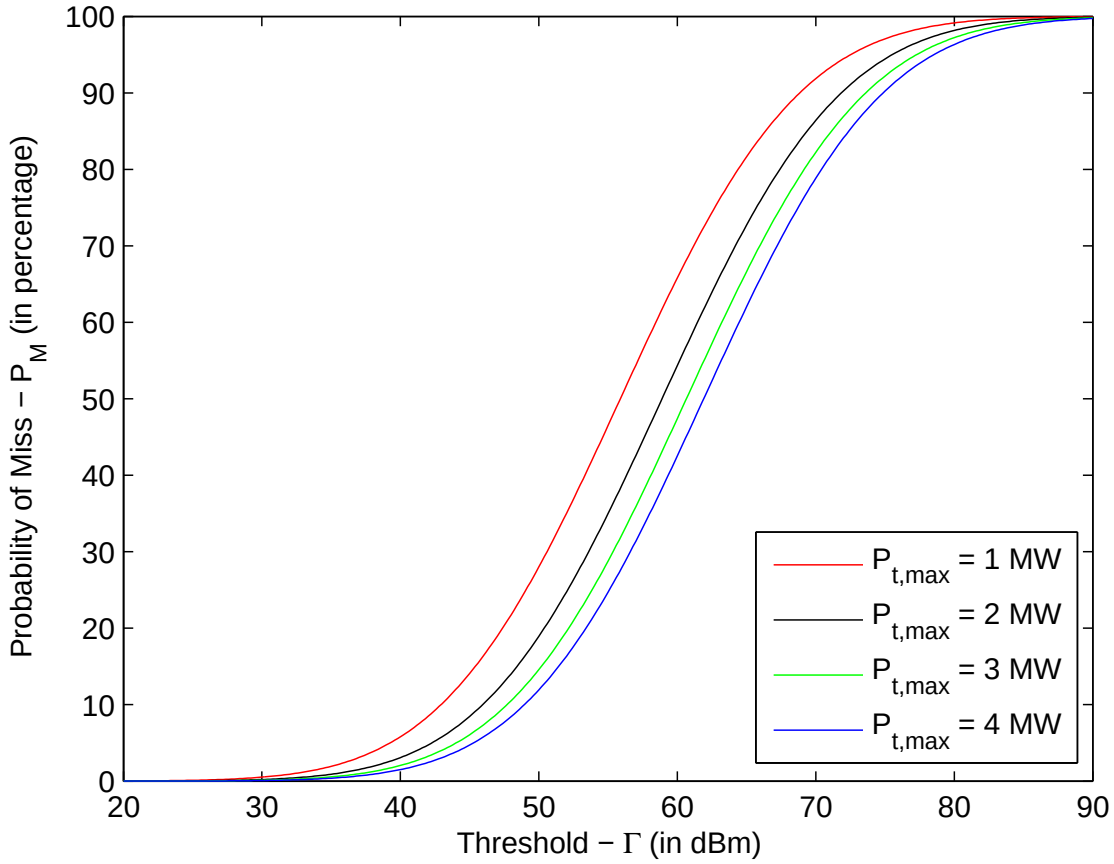

Figure 5.4: Probability of detection for different radar power parameters. Impact of cellular interference on the radar's detection performance when the radar has freedom to choose transmitted power in order to counter interference. The target is present at a distance of 100 Kms.

Figure 5.5 analyzes probability of miss for targets at different ranges. As expected, by increasing the target range from the radar the SINR decreases and the probability of miss increases. Hence, detection of far away targets will be a challenge for radar in cellular interference. One way to counter this is to increase transmit power in order to improve SINR so as to get better detection performance.

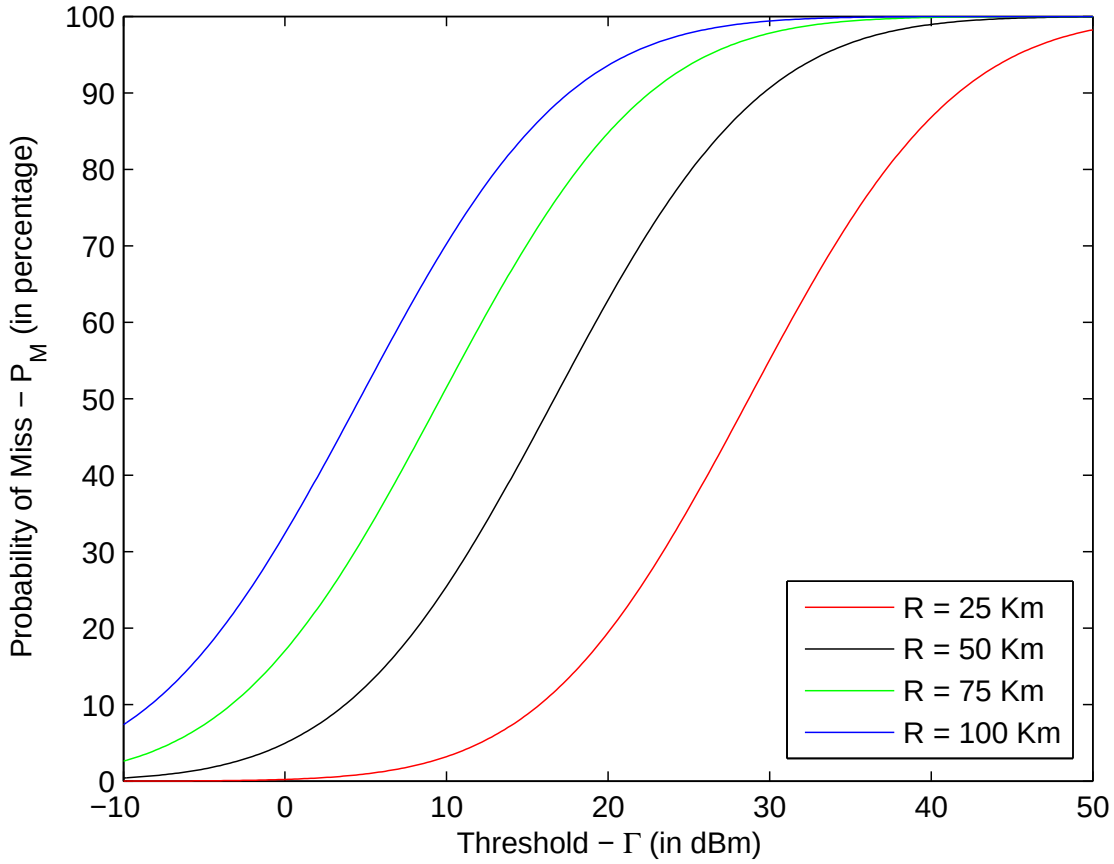

Figure 5.5: Impact of cellular interference on the radar's detection performance when targets are present at different distances. The simulation parameters of Tables 5.1 and 5.2 are used except that the radar transmits a 4 MW signal.

5.6 Conclusion

This chapter investigated the performance of S-band seaborne military radar when the incumbent is sharing its frequency band with commercial cellular system. The radar is subject to interference from the cellular system and its performance is evaluated under these new operating conditions.

First, aggregate distribution of cellular interference is derived and it is proved that it is

log-normal with probability 1. The proposed method does not rely on approximations and moment matching methods which were commonly used to characterize aggregate interference distribution. Using this result bounds on the probability of detection and the probability of miss detection under cellular interference were derived.

The analytical results were complemented with the simulation results where detection performance of radar under cellular interference was evaluated. It was shown that for smaller SINR values the difference in performance of radar detector with and without interference was much more than at higher SINR values. In addition, the targets that were far away were more hard to detect due to low SINR in interference regimes. The impact of interference could be minimized by using higher transmit powers at the radar terminal to increase SINR and thus have better detection performance.

The results presented serve as a motivation for further exploration of spectrum sharing between radar and commercial cellular systems so that both the systems can perform in an optimum way. In addition to innovative interference mitigation methods, policy level decisions, from regulators and cellular operators, are required in order to make such a sharing possible.

Chapter 6

Channel Modeling between MIMO Radar and MIMO Cellular System

Recent years have seen tremendous growth in wireless data traffic due to the ubiquitous use of smart phones and tablets. Cellular network operators are finding it hard to cope up with the growing user data requirements given the limited amount of spectrum available to them. Up till now, in order to meet bandwidth requirements, regulators usually free up spectrum held by various incumbents by relocating them to some other band. However, not only this process is time consuming it is also very expensive for incumbents to relocate. That is why regulators are now looking into the option of sharing spectrum across government agencies and commercial services. For example, the Federal Communications Commission (FCC) is considering to allow commercial wireless operation in the 3.5 GHz radar band [3]. This initiative has the potential to leverage new methods of spectrum sharing among heterogeneous systems such as small cells, radars, and satellite systems. However, a fundamental limitation for spectrum sharing is interference caused to coexisting systems. Novel interference mitigation methods are required for coexistence of these fundamentally different systems. This

chapter addresses this issue by modeling channel between radar and communication systems and studies the impact of a proposed interference mitigation scheme.

Channel modeling for wireless communications is a fundamental area of research as it allows performance evaluation of transmission techniques. A comprehensive introduction to SISO and MIMO wireless channel modeling, propagation modeling, and statistical description of channels can be found in [27] and references there in. However, the efforts so far have been limited to model channels between wireless communication systems and to the best of my knowledge no work exists on channel modeling between wireless communication and radar systems. In order to study performance evaluation and interference mitigation techniques in a spectrum sharing scenario between radar and communication systems the problem of channel modeling is of prime importance. Traditionally, wireless channel models have been designed to capture the azimuth i.e. 2D channels. A comprehensive introduction to 2D wireless channel modeling, propagation modeling, and statistical description of channels can be found in [27] and references there in. Recently, there has been a surge in modeling wireless channels that capture both the azimuth and elevation directions known as 3D channels. 3D channels allow very precise beamforming for users on ground and in buildings. As a result the wireless research community is heavily involved in designing and standardizing 3D channel models that can reap the benefits of both the azimuth and elevation beamforming [28]. However, the efforts so far have been limited to model 3D channels between wireless communication systems and to the best of my knowledge no work exists on 3D channel modeling between wireless communication and radar systems. A 3D channel model can enable radar systems to place accurate nulls in azimuth and elevation angles of BSs in order to mitigate radar interference. Therefore, in order to study performance evaluation and interference mitigation techniques in a spectrum sharing scenario, the problem of 3D channel modeling is of prime importance.

In this chapter, 2D and 3D MIMO channels between MIMO radar and MIMO cellular system are designed. The rest of this chapter is organized as follows. In Section 6.1, 2D channel model is designed by considering a 1D antenna array at both the radar and cellular system. Using the proposed 2D channel model the efficacy of eigen-nulling [65] over spatial-nulling [103], for radar interference mitigation at cellular systems, is demonstrated in Section 6.1.2. In Section 6.2, power received at communication system in 2D line-of-sight (LoS) channel model is studied. Moreover, coherence time of channel is computed and discussed via numerical example. In Section 6.4, a 3D MIMO channel model between MIMO radar and MIMO cellular system is formulated by considering a 2D antenna array at the radar and a 1D array at the BS. Using the proposed channel model the efficacy of a novel null space projection algorithm in 2D which mitigates radar interference is demonstrated in Section 6.4.3. Section 6.4.4 discuss the volume illuminated by spectrum sharing MIMO radars that are subject to interference mitigation. Section 6.4.5 discusses the simulation results. Section 6.5 concludes the chapter.

6.1 Two-Dimensional (2D) Channel Modeling

Spectrum sharing between radars and cellular systems is an emerging area of research. In this section, a 2D channel between a seaborne MIMO radar and MIMO cellular system is modeled to capture the azimuth aspect of the spectrum sharing scenario. The proposed channel modeling methodology allows MIMO radar to place accurate nulls in the azimuth location of base stations (BS), thus, protecting them from harmful radar interference. A projection based approach is used, where radar waveform is projected onto null space of channel, for mitigating radar interference to BSs. This is also known as an approach based on eigen-nulling which is different from spatial-nulling commonly employed by radars. It is shown

through simulations that the proposed spatial channel model allows eigen-nulling which performs superior to traditional spatial-nulling for interference mitigation. The proposed channel model can be leveraged to use eigen-nulling that enhances target detection and beampattern resolution of MIMO radar while mitigating interference to BSs.

6.1.1 Physical Modeling of 2D Channel

In this section, a deterministic 2D channel between MIMO radar and MIMO communication system is modeled which can be extended to a statistical channel model in future.

Consider a scenario in which a BS is an area free of reflectors or scatterers and only direct paths exist between radar and BS antenna pairs. This channel consists of only direct line-of-sight paths between the radar transmit and communication system receive antennas. This scenario is typical of BS antennas mounted on building tops or outer walls of buildings in littoral areas to serve users on a beach, for example. At the BS, the inter-element spacing between antennas is $\Delta_N \lambda_c$, where Δ_N is the normalized BS antenna separation and λ_c is the carrier wavelength. Similarly, at the radar, the inter-element spacing between antennas is $\Delta_M \lambda_c$, where Δ_M is the normalized radar antenna separation. Moreover, it is assumed that the radar and BS are sufficiently apart. Then, the baseband channel gain between the k^{th} radar transmit antenna and the i^{th} BS receive antenna is as follows:

$$h_{ik} = a\exp\left(-j2\pi d_{ik}/\lambda_c\right) \tag{6.1}$$

where d_{ik} is the distance between the radar and the BS antennas, and a is the attenuation along the line-of-sight path which is assumed to be equal for all antenna pairs. Due to the geometry of the model, it is safe to assume that the antenna array sizes are much smaller

than the distance between the transmitter and the receiver, then to a first-order

$$d_{ik} = d + (i-1)\,\Delta_N \lambda_c \cos\phi_N - (k-1)\,\Delta_M \lambda_c \cos\phi_M \tag{6.2}$$

where d is the distance between radar transmit antenna 1 and BS receive antenna 1; ϕ_N and ϕ_M are the angles of incidence of the line-of-sight path on the radar and BS antenna arrays, respectively. The quantities $(i-1)\,\Delta_N \lambda_c \cos\phi_N$ and $(k-1)\,\Delta_M \lambda_c \cos\phi_M$ are respectively the displacements of receive/transmit antenna i/k from receive/transmit antenna 1 in the direction of the line-of-sight. For the simplification of notations lets define $\Omega_M \triangleq \cos\phi_M$ and $\Omega_N \triangleq \cos\phi_N$. Therefore, the channel matrix can be written as

$$\mathbf{H} = a\sqrt{NM}\exp\left(-j2\pi\frac{d}{\lambda_c}\right)\mathbf{e}_N\left(\Omega_N\right)\mathbf{e}_M^*\left(\Omega_M\right) \tag{6.3}$$

where unit spatial signature $\mathbf{e}_l$, l={N,M}, is defined to be

$$\mathbf{e}_l\left(\Omega_l\right) = \frac{1}{\sqrt{l}}\begin{bmatrix} 1 \\ \exp\left(-j2\pi\Delta_l\Omega_l\right) \\ \exp\left(-j2\pi 2\Delta_l\Omega_l\right) \\ \vdots \\ \exp\left(-j2\pi\left(l-1\right)\Delta_l\Omega_l\right) \end{bmatrix}. \tag{6.4}$$

Since propagation channel between a seaborne radar and an on-shore BS is under consideration, it is of interest to consider multiple paths reflected off sea in addition to the LoS path between the radar and the BS. Now, the i^{th} path has attenuation a_i and makes an angle

ϕ_{Mi} with the radar transmit antenna array and an angle ϕ_{Ni} with the receive antenna array of the BS. The overall channel $\mathbf{H}$ is given by

$$\mathbf{H} = \sum_{i=1}^{L} a_i \mathbf{e}_N \left(\Omega_{Ni}\right) \mathbf{e}_M^* \left(\Omega_{Mi}\right) \tag{6.5}$$

where

$$a_i = a_i \sqrt{NM} \exp\left(\frac{-j2\pi d^i}{\lambda_c}\right) \tag{6.6}$$

d^i is the distance between radar transmit antenna 1 and BS antenna 1 along path i.

In this section, scenarios where no more than one non line-of-sight (NLoS) component exist or LoS component is much much stronger than all other NLoS components except one which might be bounced of water waves is considered.

6.1.2 Spatial vs. Eigen Nulling

In radar signal processing, it is often desirable to steer nulls of the transmit beampattern for clutter and interference mitigation purposes. For this reason beamforming weights are optimally designed to maximize signal-to-interference-plus-noise ratio (SINR) so that target signal can be recovered in the presence of clutter, jammer, and interference sources. The SINR maximization can be achieved for various constraints including the constraint that the target response is unity which is mathematically expressed as

$$\begin{aligned} \min_{\mathbf{w}} \quad & \mathbf{w}^H \mathbf{R} \mathbf{w} \\ \text{subject to} \quad & \mathbf{w}^H \mathbf{x} = 1 \end{aligned} \tag{6.7}$$

where $\mathbf{w}$ is the weight vector and the solution of this optimization problem is known as minimum variance distortionless response (MVDR) beamformer [13]

$$\mathbf{w} = \frac{\mathbf{R}^{-1}\mathbf{x}}{\mathbf{x}^H\mathbf{R}^{-1}\mathbf{x}}. \tag{6.8}$$

A limitation of this approach is that covariance matrix $\mathbf{R}$ needs to be estimated. The spatial locations of nulls - i.e., location of jammers, clutter, and interference sources - are not known *a priori* in most cases and are obtained only after analyzing the received data. In traditional phased array radars, spatial-nulling locations are determined by first illuminating the desired area of interest and then configuring the beampattern with the appropriate nulls whereas in MIMO radar the transmit beampattern is configured with the help of data-dependent processing schemes. Moreover, estimation of correlation matrix of clutter/interference and multipath has to be taken into account for effective spatial transmit nulling.

In the spectrum sharing scenario under consideration where a ship-borne MIMO radar is sharing spectrum with an onshore MIMO communication systems the environmental geometry can be exploited for effective nulling. If traditional spatial nulling techniques are utilized by MIMO radars, for nulling out interference to communication systems, then the covariance matrix of interference and location of multipath scatterers needs to be estimated. Since this process may lead to estimation errors, the effect of nulling can be undermined thus leading to harmful interference for communication systems [103]. On the other hand, if eigen-nulling is utilized, i.e., nulls are placed in location of low eigen modes of the interference channel, then the transmit nulling can be very effective in mitigating interference to BSs. Assuming, the MIMO radar has channel state information, through feedback from BSs, singular value decomposition (SVD) can be performed of interference channel $\mathbf{H}$ as $\mathbf{H} = \mathbf{U}\mathbf{\Sigma}\mathbf{V}^H$. Defining

$$\widetilde{\mathbf{\Sigma}} \triangleq \text{diag}(\widetilde{\sigma}_1, \widetilde{\sigma}_2, \ldots, \widetilde{\sigma}_p) \tag{6.9}$$

where $p \triangleq \min(N, M)$ and $\widetilde{\sigma}_1 > \widetilde{\sigma}_2 > \cdots > \widetilde{\sigma}_q > \widetilde{\sigma}_{q+1} = \widetilde{\sigma}_{q+2} = \cdots = \widetilde{\sigma}_p = 0$ are the singular values of $\mathbf{H}$. Next, defining

$$\widetilde{\mathbf{\Sigma}}' \triangleq \text{diag}(\widetilde{\sigma}'_1, \widetilde{\sigma}'_2, \ldots, \widetilde{\sigma}'_M) \tag{6.10}$$

where

$$\widetilde{\sigma}'_u \triangleq \begin{cases} 0, & \text{for } u \leq q, \\ 1, & \text{for } u > q. \end{cases} \tag{6.11}$$

The above definitions leads to projection matrix defined as

$$\mathbf{P} \triangleq \mathbf{V}\widetilde{\mathbf{\Sigma}}'\mathbf{V}^H. \tag{6.12}$$

Then, in order to obtain the signal which nulls interference to BSs, radar signal is projected onto null space of BS channel $\mathbf{H}$ via $\widetilde{\mathbf{x}} = \mathbf{P}\mathbf{x}$, where $\widetilde{\mathbf{x}}$ is the null space projected radar waveform that is not going to cause interference to BS as the radar waveform is now in the low eigen modes of the interference channel $\mathbf{H}$.

In the following section two examples are provided which demonstrate the efficacy of eigen-nulling over spatial-nulling schemes.

6.1.2.1 Beampattern

In this section, a comparison of transmit-receive beampatterns of MIMO radar waveform subject to eigen- and spatial-nulling is provided. The transmit and receive beampatterns are a means to measure the beamformer's response to a target located at an angle θ, when the beam is steered digitally to a direction θ_D. The composite transmit-receive pattern can be

expressed as [13]

$$G(\theta, \theta_D) = K \frac{|\mathbf{a}^H(\theta)\mathbf{R}^T\mathbf{a}(\theta_D)|^2}{\mathbf{a}^H(\theta_D)\mathbf{R}^T\mathbf{a}(\theta_D)} \frac{|\mathbf{a}^H(\theta)\mathbf{a}(\theta_D)|^2}{M} \tag{6.13}$$

where K is the normalization constant. Only composite transmit-receive beampatterns are studied because of their advantages including narrower null-to-null beamwidths and smaller sidelobes. Moreover, composite beampatterns are unambiguous due to the presence of both transmit and receive beampatterns. An ambiguity in one beampattern, for example grating lobes, is resolved by the other [13].

Numerical Example: In Figure 6.1, transmit nulling approaches based on spatial-nulling and eigen-nulling are compared. The goal is to understand the effects of eigen-nulling and spatial-nulling for interference mitigation on the beampattern of the spectrum sharing MIMO radar. In Figure 6.1a, the case when target and BSs are far away in spatial domain is considered, i.e, it is assumed that the target is at an angle $\theta = 0°$, BS has a direct LoS angle at $\theta = -7°$ and a NLoS component is at $\theta = -6°$, this is based on the CSI exchanged between radar and BS. In the absence of such an information, traditional spatial-nulling techniques are employed that have to estimate spatial locations that need to be blocked and thus in many cases a wider range of angles have to be nulled to protect BS from radar interference. Hence, for this example spatial angles from $\theta = -10$ to -3 are blocked. It can be noticed that using the proposed 2D channel model, eigen-nulling can be leveraged which results in accurate nulling of interference at BS location and target localization. Although, spatial-nulling also results in accurate localization of target but has a large nulled area in its search space. In Figure 6.1b, the case when target and BS are very close in spatial domain is considered, i.e, it is assumed that the target is at an angle $\theta = 0°$, BS has a direct LoS angle at $\theta = -3°$ and a NLoS component is at $\theta = -2°$, this is based on the CSI exchanged between radar and BS. If traditional spatial-nulling techniques are employed then a wider range of angles have to be nulled to protect BS from radar interference. Hence, for this

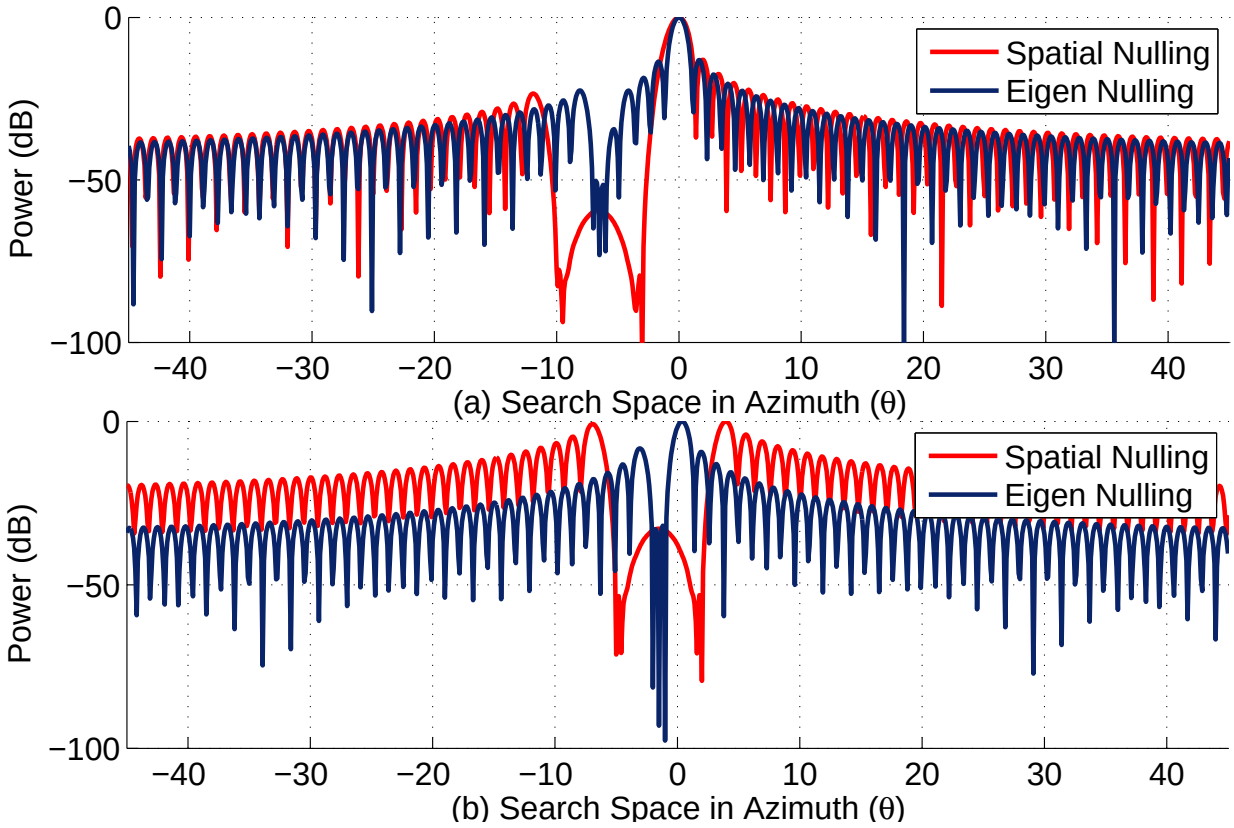

Figure 6.1: Analysis of beampattern for spatial- and eigen-nulling approaches. Eigen-nulling results in accurate nulling and target localization for targets that are both far and near to BS locations as compared to spatial-nulling.

example spatial angles from $\theta = -5$ to -2 are blocked. It can be noticed that using the proposed 2D channel model, eigen-nulling can be leveraged which results in accurate nulling of interference at BS location and target localization for even closely located BSs and target. On the other hand, spatial-nulling fails to accomplish target localization due to the nulls placed in the direction of target. Hence, using the proposed 2D channel model eigen-nulling can be leveraged which results in accurate nulling of interference and target localization for both close and far away targets.

6.1.2.2 Probability of Detection

In this section, the target detection performance of radars that utilize spatial nulling vs. eigen nulling approaches for interference mitigation are analyzed. The generalized likelihood ratio test (GLRT) for spectrum sharing MIMO radars is given by [66]

$$L_{\mathbf{y}}(\hat{\theta}_{\mathrm{ML}}) = \arg\max_{\theta} \frac{\left|\mathbf{a}^H(\hat{\theta}_{\mathrm{ML}})\mathbf{E}\mathbf{a}^*(\hat{\theta}_{\mathrm{ML}})\right|^2}{M\mathbf{a}^H(\hat{\theta}_{\mathrm{ML}})\mathbf{R}^T\mathbf{a}(\hat{\theta}_{\mathrm{ML}})} \underset{\mathcal{H}_0}{\overset{\mathcal{H}_1}{\gtrless}} \delta \tag{6.14}$$

where the asymptotic statistics of $L(\hat{\theta}_{\mathrm{ML}})$ is given by

$$L(\hat{\theta}_{\mathrm{ML}}) \sim \begin{cases} \mathcal{H}_1 : \chi_2^2\left(\dfrac{|\alpha|^2}{\sigma_n^2}|\mathbf{a}^H(\theta)\mathbf{R}^T\mathbf{a}(\theta)|^2\right) \\ \mathcal{H}_0 : \chi_2^2 \end{cases} \tag{6.15}$$

where $\hat{\theta}_{\mathrm{ML}}$ is the maximum likelihood (ML) estimate of θ, $\mathcal{H}_0$ is the null hypothesis, $\mathcal{H}_1$ is the alternate hypothesis, δ is the detector threshold, $\chi_2^2(\cdot)$ is the noncentral chi-squared distributions with two degrees of freedom, and χ_2^2 is the central chi-squared distributions with two degrees of freedom. The probability of detection is given by

$$P_{\mathrm{d}} = P(L(\mathbf{y}) > \delta|\mathcal{H}_1) = 1 - \mathcal{F}_{\chi_2^2(\rho)}\left(\mathcal{F}_{\chi_2^2}^{-1}(1 - P_{\mathrm{FA}})\right) \tag{6.16}$$

where $\mathcal{F}_{\chi_2^2(\rho)}$ is the noncentral chi-squared distribution function with two degrees of freedom and noncentrality parameter ρ and P_{FA} is the probability of false alarm.

Numerical Example: In Figure 6.2, target detection capability of the MIMO radar in a spectrum sharing environment is tudied. The goal is to understand the effects of eigen-nulling and spatial-nulling for interference mitigation on the radar's targets detection probability. It is assumed the target is at an angle $\theta = 0°$, BS has a direct LoS angle at $\theta = -7°$ and

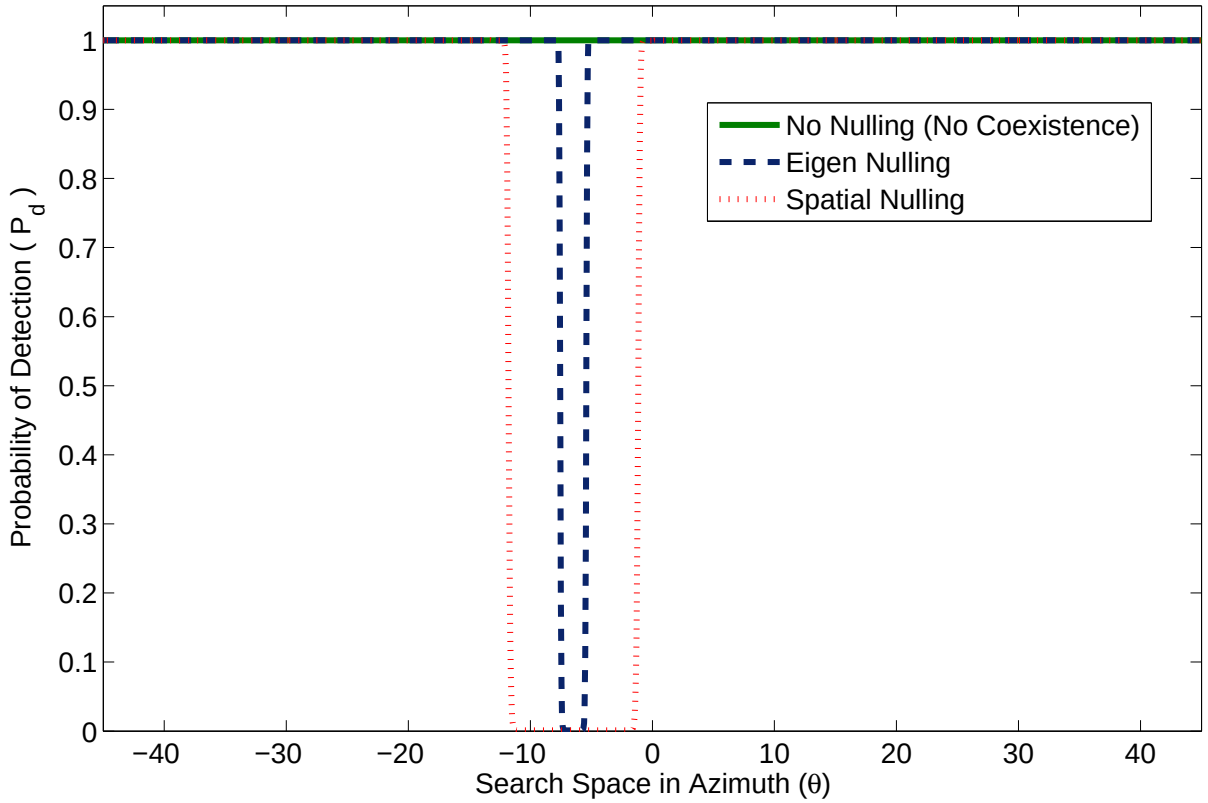

Figure 6.2: Comparison of probability of detection for spatial- and eigen-nulling approaches. Eigen-nulling results in minimum loss in search space as compared to spatial-nulling.

a NLOS component is at $\theta = -6°$, this is based on the CSI exchanged between radar and BS. For spatial-nulling, angles from $\theta = -10$ to -3 are blocked. From Figure 6.2 it can be noticed that when eigen-nulling is performed it results in zero detection probability for only the angles which strongly interfere with the BS, however, when spatial-nulling is used extra angles are nulled which leads to zero detection probability for even those angles which do not interfere with BS. Thus, the proposed 2D channel model can leverage eigen-nulling which performs much better than spatial-nulling as it provides minimum loss in radar search space as compared to spatial-nulling which blocks significant volume (azimuth space) which is not desirable for radar operations.

6.2 Performance Analysis in 2D LoS Channels

Sharing spectrum with incumbents such as radar systems is an attractive solution for cellular operators in order to meet the ever growing bandwidth requirements and ease the spectrum crunch problem. In order to realize efficient spectrum sharing, interference mitigation techniques are required. In this section, the amount of power received at BSs when radar uses null space projection (NSP)-based interference mitigation method is studied. NSP reduces the amount of projected power at targets that are in-close vicinity to BSs. This issue is studied and it is shown that this can be avoided if radar employs a larger transmit array. In addition, the coherence time of channel between radar and BSs is computed and it is shown that the coherence time of channel is much larger than the pulse repetition interval of radars. Therefore, NSP-based interference mitigation techniques which depends on accurate CSI can be effective as the problem of CSI being outdated does not occur for most practical scenarios.

6.2.1 Received Power Analysis

In this section, the amount of power received at BSs and the target is studied. The goal is to estimate the power received at BSs and target for effective interference mitigation and target detection purposes, respectively. The gain of the radar transmit array in a direction θ when the beam is steered digitally to a direction θ_D is given by [13]

$$G(\theta, \theta_D) = \Gamma \frac{|\mathbf{a}^H(\theta)\mathbf{R}^T\mathbf{a}(\theta_D)|^2}{\mathbf{a}^H(\theta_D)\mathbf{R}^T\mathbf{a}(\theta_D)}$$

where Γ is the normalization constant. It is of interest to place nulls or having minimum gain towards the direction of BSs, by using NSP-based interference mitigation scheme, and

maximum gain in the direction of target. In the following sections both the scenarios are covered in detail along with some examples.

6.2.1.1 Power Received at Cellular System

In this section, the received power at locations nulled by radar system using null space projection algorithm is studied. These nulled locations are occupied by cellular BSs and are subject to interference protection from radar system. This scenario is shown in Figure 6.3 when the target is located at 0° and BSs are located at an azimuth of 30° to 35°. Note that the received power at BS locations is much below the power projected at target and other azimuthal locations. The NSP places accurate and deep nulls at locations that are occupied by cellular BSs. The received power level is much below the noise floor of most practical BSs. Thus, radar interference can be effectively mitigated by using the proposed NSP-based algorithm.

6.2.1.2 Reduction in Power Projected at Target

In this section, the power reduction in the main beam due to NSP is evaluated. As an example, a case where BSs are present at an azimuth angle of 20° to 25° and the target first appears at an azimuth angle of 26°, with respect to (w.r.t.) radar is considered. Thus, there is a angular separation of 1° between the communication systems and the target. This angular separation is further increased to $2°, 5°, 10°, 15°, 20°, 30°$, and 50° to study reduction in mainlobe power. So the reduction in mainlobe power is presented as a function of angular difference between the communication systems and the target. Moreover, this power reduction is studied by employing $M = 10, 30, 50, 70$ and 100 antenna elements at MIMO radar while the antennas elements at communication system are fixed at $N = 5$.

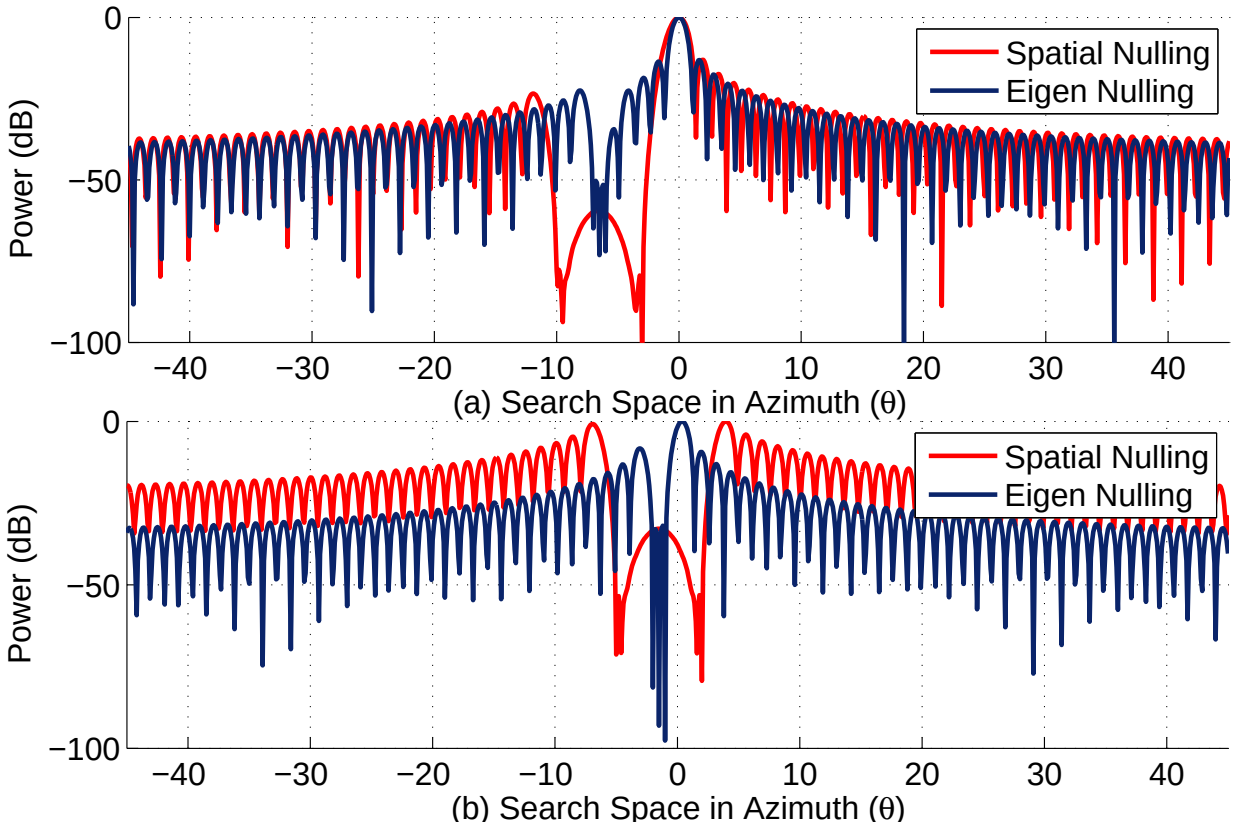

Figure 6.3: Nulls placed for effective interference mitigation: NSP-based interference mitigation scheme places accurate and deep nulls in the location of BSs (30° to 35°) for effective interference mitigation.

The results are reported in Figure 6.4. It can be noted that for a small radar array and a target immediately next to the nulled zone, i.e when $N = 10$ and target is at 1° relative to BSs, the loss in projected power is much more severe than all the other cases. As the target moves away from the communication systems the loss in power projected becomes smaller and smaller. Moreover, when the radar employs a larger antenna array, for example with 70 or 100 elements, the power reduction in mainlobe, due to NSP, is negligible.

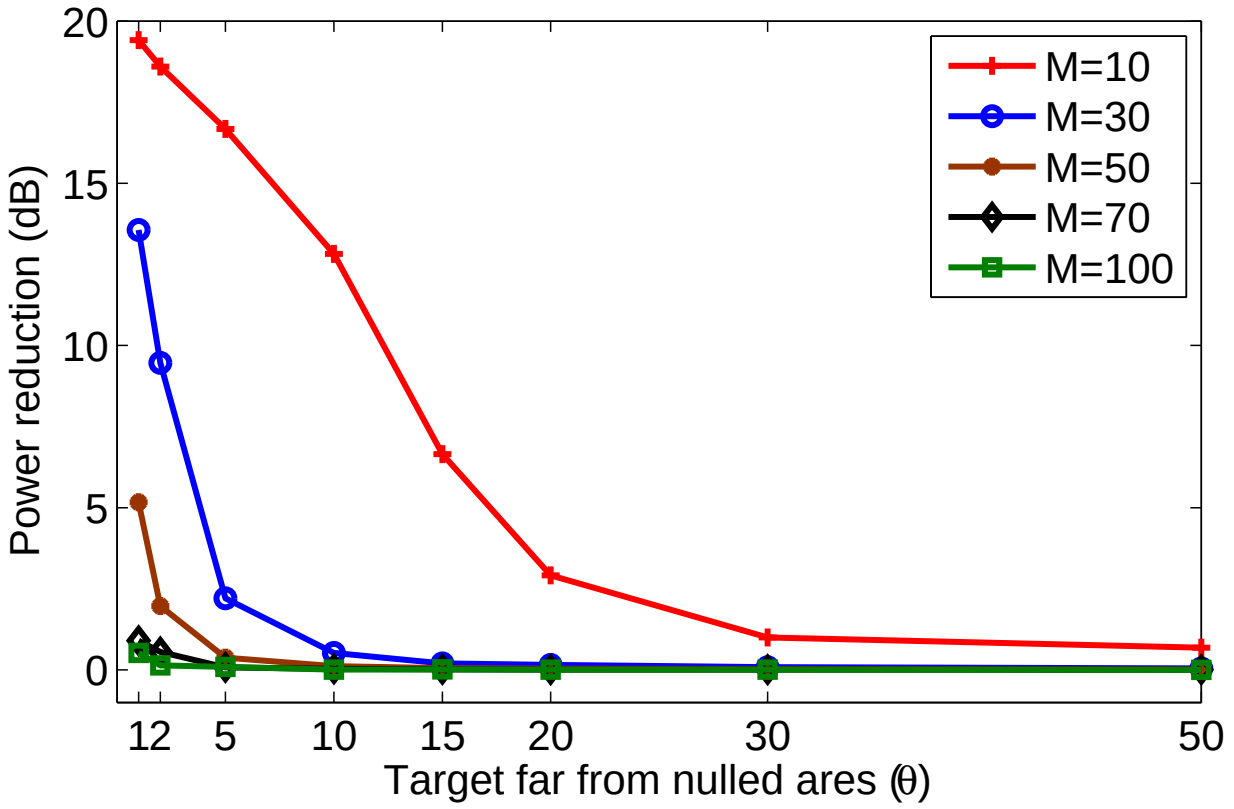

Figure 6.4: Power reduction in mainlobe due to NSP: Power reduction in mainlobe due to NSP as a function of angular separation between communication system and target.

6.2.2 Coherence Time Of A Shipborne Radar

Null-space based projection scheme requires CSI estimation. However, it has not been investigated that for how long the CSI is valid and after what time period the CSI becomes outdated. Specifically, knowledge about the coherence time of the channel between shipborne radar and cellular system is not available. This is investigated in this section. Consider a ship-borne radar, as shown in Figure 6.5, moving with a constant horizontal velocity v_s to point a. The movement of a ship, and hence radar, is affected by factors such as wind speed, length of time the wind blows, distance of open water over which the wind blows (i.e. fetch); because these factors gives rise to waves which affect the motion of a ship. Rough seas give

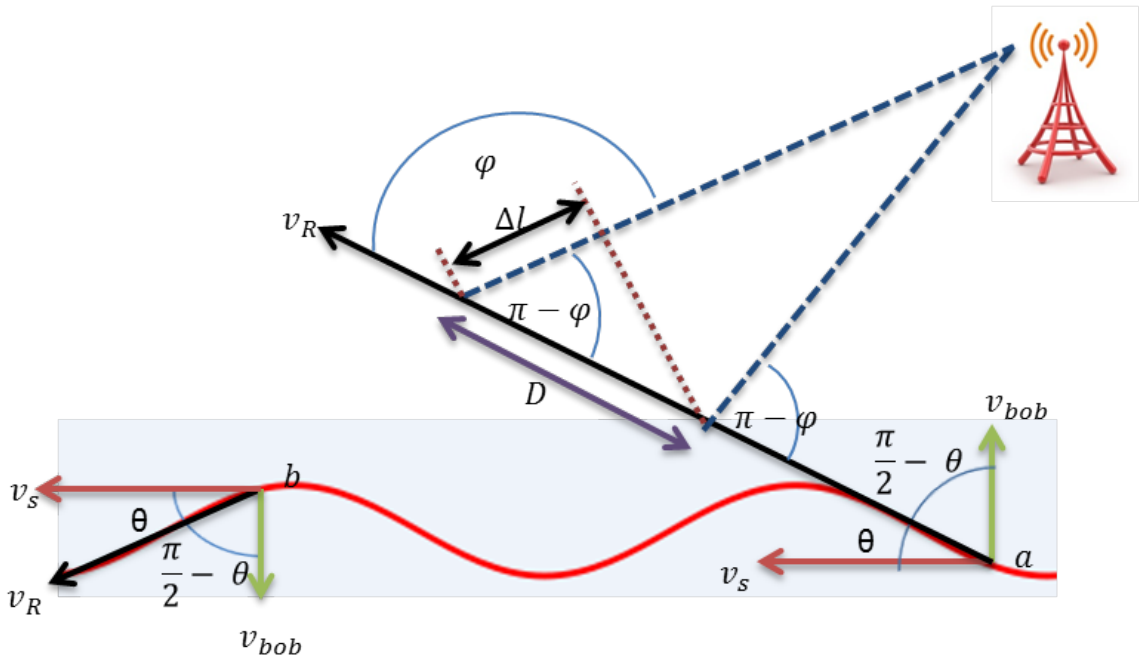

Figure 6.5: Coherence time analysis of a moving shipborne radar.

rise to waves that are steep, where steepness of a wave is the ratio of wave height to the length of wave, which in turn introduces bobbing velocity v_{bob}. Assume the ship is moving at speed v_R which is the resultant of v_s and v_{bob}. So, v_R is given by,

$$v_R = v_s \cos(\theta) + v_{bob} \cos\left(\frac{\pi}{2} - \theta\right) \tag{6.17}$$

where $\theta = \tan^{-1}(v_{bob}/v_s)$ and v_{bob} is given by

$$v_{bob} = 2\, v_s \, \frac{\text{Height of wave}}{\text{Length of wave}} \tag{6.18}$$

At speed v_R, the ship-borne radar moves along a path segment D while it illuminates its search space which also contains a remote communication system. The difference in path

length traveled by the waves between the two points along D to the communication system can be written as:

$$\Delta l \quad = \quad D\cos(\pi - \varphi) = v_R \Delta t \cos(\varphi) \tag{6.19}$$

where Δt is the time required for the ship to travel the path segment D. Since, the communication system is assumed to be far away, ϕ is assumed to be the same at the two ends of D. The phase change of the signal received at the communication system corresponding to this difference in path lengths is therefore

$$\Delta\alpha = \frac{2\pi\Delta l}{\lambda} = \frac{2\pi v_R \Delta t}{\lambda}\cos(\phi)\,. \tag{6.20}$$

So, the apparent change in frequency, or Doppler shift, is given by

$$f_d = \frac{1}{2\pi}\cdot\frac{\Delta\alpha}{\Delta t} = \frac{v_R}{\lambda}\cos(\phi)\,. \tag{6.21}$$

Consequently, coherence time, which is the time domain dual of Doppler spread, is given by [104],

$$T_c = \sqrt{\frac{9}{16\pi f_m^2}} = \frac{0.423\lambda}{v_R} \tag{6.22}$$

where f_m is the maximum Doppler shift.

Example: Coherence time analysis of a moving ship-borne radar and a static BS – In this example, the relationship between coherence time of channel and NSP is studied in order to answer the question about the applicability of NSP for a moving radar. Consider an AN/SPN-43C air traffic control (ATC) radar, used by navy in the 3.5 GHz band, with a pulse repetition rate (PRR) of 1000 Hz or pulse repetition interval (PRI) of 1 millisecond (ms) [4]. Such radars are mounted on ships that typically move with a top speed of 32 knots.

Ship Speed (knots)	Wind Speed (knots)	Wave Height (feet)	Wave Length (feet)	v_{bob} (m/s)
20	30	13.5	360	0.77
20	40	24.0	392	1.26
20	50	42.0	719	1.20
32	30	13.5	360	1.23
32	40	24.0	392	2.02
32	50	42.0	719	1.92

Table 6.1: Values of v_{bob} for various operating speeds and environmental conditions.

Also consider radars that transmit fixed-frequency carrier wave pulse modulated waveform and swept-frequency carrier wave pulse modulated waveform. These are referred to as P0N and Q3N, respectively, in the NTIA report [105]. Usually, PRI, speed, and other parameters of a military radar or ship are confidential. Sample information provided by NTIA in its assessment reports [5, 105] are used. Using this information the coherence time of channel is calculated and shown in Figure 6.6 for various operating conditions by varying ship's speed and considering different values of wind speed, wave height, wave length, for a 200 nautical mile fetch of wave. These calculations are reported in Table 6.1. It can be observed that since the PRI of radar is much smaller than the coherence time, therefore, NSP will be working perfectly even with a moving shipborne radar.

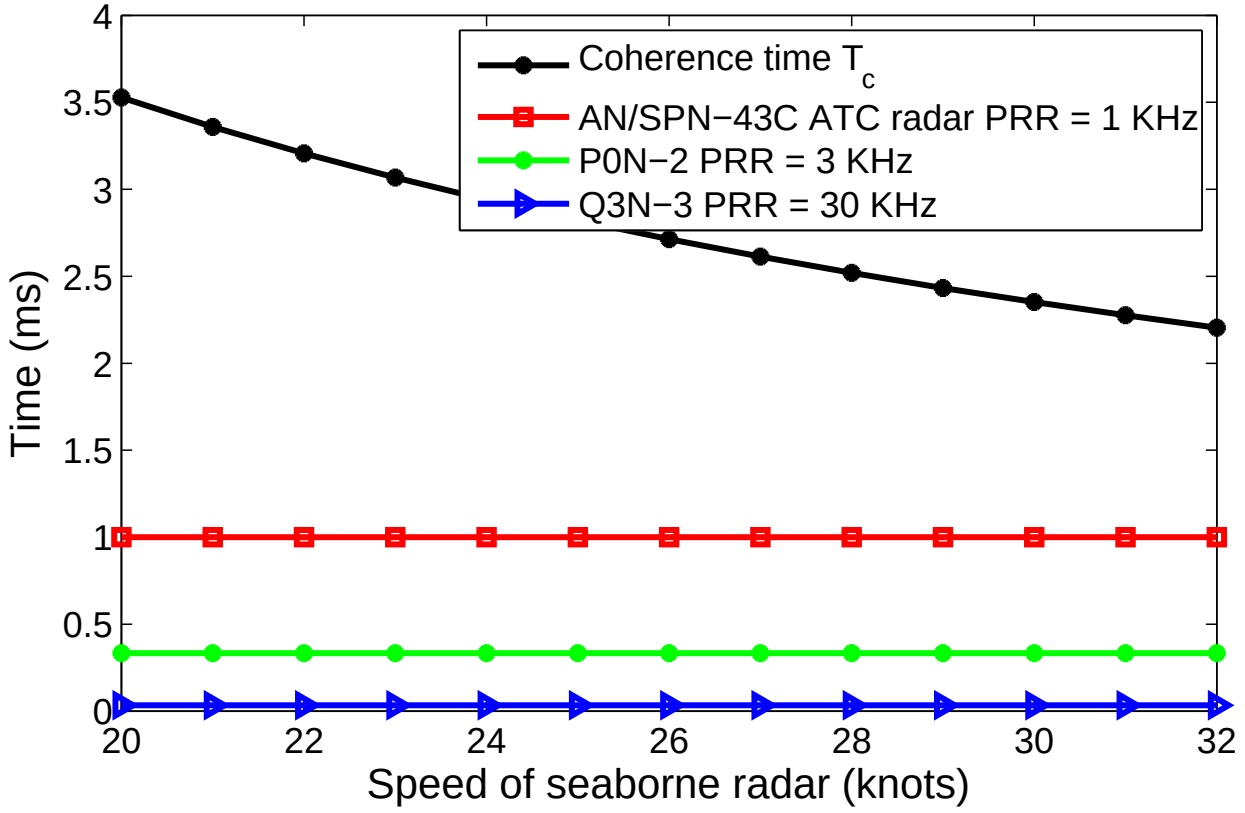

Figure 6.6: Coherence time of radar-BS channel vs. PRI of radars: The problem of CSI being outdated for the application of NSP does not occur as the coherence time of radar-BS channel is much larger than PRI of most practical radars.

6.3 Performance Analysis in Highly Mobile Environments

In previous section, performance of spectrum sharing MIMO radars was accessed in 2D LoS channels. In this chapter, this approach is extended to maritime MIMO radar which experiences time varying interference channel due to the oscillatory motion of ship, because of the breaking of sea/ocean waves. The NSP algorithm is sensitive to perturbations in the interference channel state information (ICSI) as it can alter the null space of the interference channel. This can cause interference leakage to a communication system, if it is not accounted

for, and it can also degrade the performance of a radar system, which is addressed in this chapter. The perturbation in ICSI is modeled by using the matrix perturbation theory and the statistical distribution of the breaking waves. This model is then used to study the impact of perturbed interference channel on the spatial approach of spectrum sharing. Maximum likelihood (ML) estimate of target's angle of arrival is used to study the radar's performance when its waveform is projected onto the null space of the perturbed interference channel. Through analytical and simulation results, loss in the radar's performance due to the null space projection (NSP) of its waveform on the perturbed interference channel is studied.

6.3.1 Spectrum Sharing Architecture

Due to oscillatory motion of the ship, because of sea/ocean waves even if the ship is docked at harbor, the interference channel between the radar and the communication system is perturbed. In this case, the received signal at the communication system's receiver is

$$\mathbf{y}(t) = [\mathbf{H}_{\mathrm{I}} + \Delta\mathbf{H}_{\mathrm{I}}]\mathbf{x}(t) + \mathbf{H}\mathbf{s}(t) + \mathbf{n}(t).$$

where $\Delta\mathbf{H}_{\mathrm{I}}$ denotes perturbation in ICSI and is modeled using Rayleigh distribution, see Section 6.3.2 for details, with covariance matrix

$$\mathrm{Cov}_{\Delta\mathbf{H}_{\mathrm{I}}} = \mathbb{E}\left\{vec(\Delta\mathbf{H}_{\mathrm{I}})vec(\Delta\mathbf{H}_{\mathrm{I}})^{H}\right\}$$

where $vec(\cdot)$ is the column stacking operator. This spectrum sharing scenario is shown in Figure 6.7.

As previously stated, spatial approach of interference mitigation is projection of radar

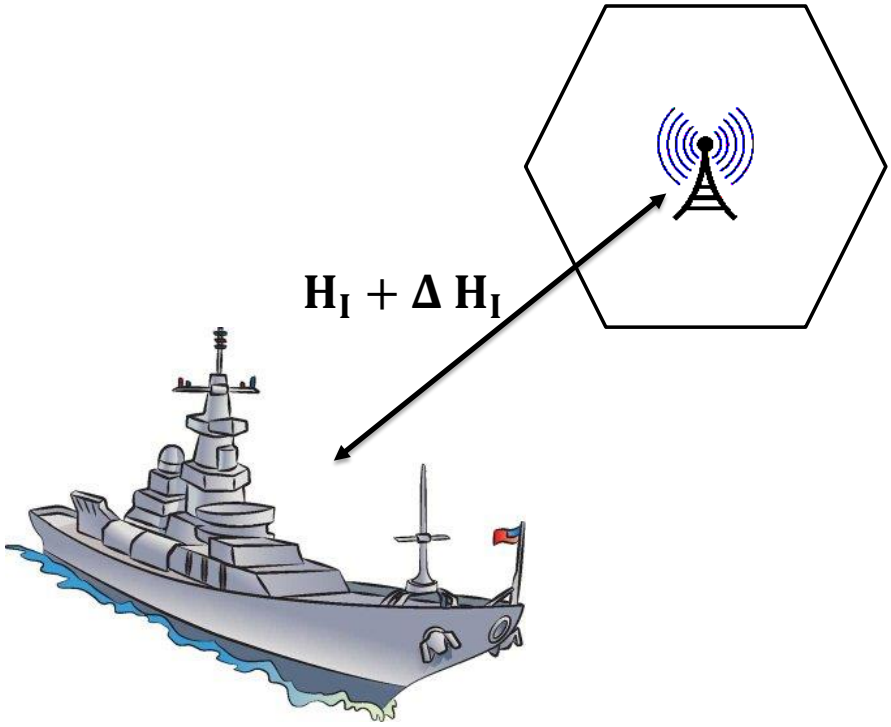

Figure 6.7: Maritime MIMO radar over perturbed channel: A maritime MIMO radar sharing spectrum with a MIMO communication system. The interference channel $\mathbf{H}_\mathrm{I}$ is perturbed by $\Delta\mathbf{H}_\mathrm{I}$ due to the motion of the ship.

signal onto the null space of interference channel [65]. After perturbation, in order for the spatial approach to work, the radar signal is projected onto the null space of the perturbed interference channel such that $[\mathbf{H}_\mathrm{I} + \Delta\mathbf{H}_\mathrm{I}]\mathbf{x}(t) = \mathbf{0}$.

6.3.2 Physical Modeling Of The Perturbed Interference Channel

In this section, the cause of perturbation in ICSI is due to the motion of the maritime radar, mounted on ship. This motion is induced by sea/ocean waves. So, in order to statistically

describe the perturbation lets look at the statistics of the wave height. The probability density function (pdf) of the wave height h is given by the Rayleigh distribution as, as in [106],

$$p(h) = \frac{2h}{h_{\text{rms}}^2} \exp\left[-\left(\frac{h}{h_{\text{rms}}}\right)^2\right]$$

where h_{rms} is the root-mean-square (rms) wave height defined as

$$h_{\text{rms}} = \left[\frac{1}{N}\sum_{n=1}^{N} h_n^2\right]^{1/2}$$

where N corresponds to the number of observed waves and the n^{th} wave has height h_n. Thus, h_{rms} can be computed by observing N wave heights. Rayleigh pdf for the wave height distribution is chosen as it gives a very good estimate of the wave properties for various nearshore conditions.

6.3.3 Impact of The Perturbed Interference Channel on the NSP Algorithm

The projection of the radar signals onto the null space of the interference channel via a projection algorithm was proposed in [11] for a stationary interference channel. However, due to the motion of the ship, the interference channel gets perturbed and can be written as

$$\mathbf{H}_{\Delta \text{I}} = \mathbf{H}_{\text{I}} + \Delta\mathbf{H}_{\text{I}}.$$

For the NSP algorithm, the null space of the perturbed interference channel can be calculated from the singular value decomposition (SVD) theorem as

$$\mathbf{H}_{\Delta \mathrm{I}} = \mathbf{U}_{\Delta \mathrm{I}} \mathbf{\Sigma}_{\Delta \mathrm{I}} \mathbf{V}_{\Delta \mathrm{I}}^{H}$$

where $\mathbf{U}_{\Delta \mathrm{I}}$ is the perturbed complex unitary matrix, $\mathbf{\Sigma}_{\Delta \mathrm{I}}$ is the diagonal matrix of the perturbed singular values, and $\mathbf{V}_{\Delta \mathrm{I}}^{H}$ is the perturbed complex unitary matrix and its columns corresponding to the vanishing singular values span the null space of $\mathbf{H}_{\Delta \mathrm{I}}$. This is denoted by $\breve{\mathbf{V}}_{\Delta \mathrm{I}}$. Now project the radar signal onto the null space of the perturbed interference-channel using the projection algorithm, as in [11],

$$\mathbf{P}_{\breve{\mathbf{V}}_{\Delta \mathrm{I}}} = \breve{\mathbf{V}}_{\Delta \mathrm{I}} \breve{\mathbf{V}}_{\Delta \mathrm{I}}^{H}.$$

The radar waveform projected onto the null space of $\mathbf{H}_{\Delta \mathrm{I}}$ can be written as

$$\breve{\mathbf{x}} = \mathbf{P}_{\breve{\mathbf{V}}_{\Delta \mathrm{I}}} \mathbf{x}. \tag{6.23}$$

By inserting the projected signal, equation (6.23) in equation (3.24), one gets the ML estimate of the target's angle of arrival for the NSP projected radar waveform as

$$(\hat{\theta}, \hat{\tau}_r, \hat{\omega}_D)_{\mathrm{ML_{NSP}}} = \underset{\theta, \tau_r, \omega_D}{\arg\max} \frac{\left| \mathbf{a}_R^H(\theta) \mathbf{E}(\tau_r, \omega_D) \mathbf{a}_T^*(\theta) \right|^2}{M_R \mathbf{a}_T^H(\theta) \mathbf{R}_{\breve{\mathbf{x}}}^T \mathbf{a}_T(\theta)}. \tag{6.24}$$

6.3.4 Numerical Results

In this section, the impact of time varying interference channel on MIMO radar-communication system spectrum-sharing scenario is simulated. The interference channel is modeled to have a Rayleigh distribution. The elements of the error channel $\Delta \mathbf{H}_{\mathrm{I}}$ are modeled as Rayleigh

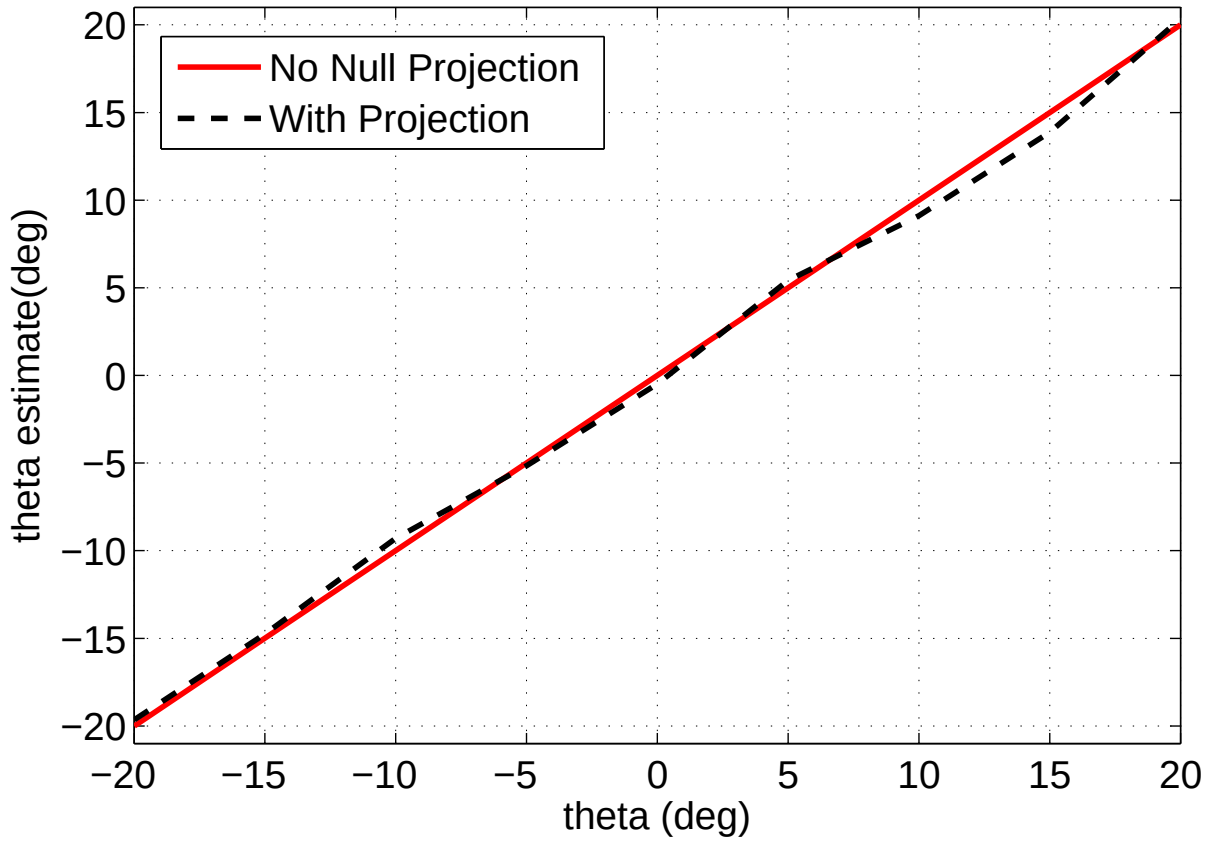

Figure 6.8: ML estimate of target's angle of arrival. The performance of the original waveform is compared with the null space projected waveform.

distribution, as it describes the pdf of the height of the waves, with h_{rms} taking values 1, 2, 3, and 4, indicating perturbation in the channel coefficients. The ML results are based on the average of 10,000 independent trials. The simulation parameters used are listed in Table 2 [11].

The ML estimate of the target's angle of arrival is calculated by equations (3.24) and (6.24) for the original radar waveform and the NSP radar waveform on the perturbed interference-channel, respectively. The impact of the NSP of the radar waveform, on the perturbed interference-channel, can be studied by the ML estimation error of the angle of arrival. First,

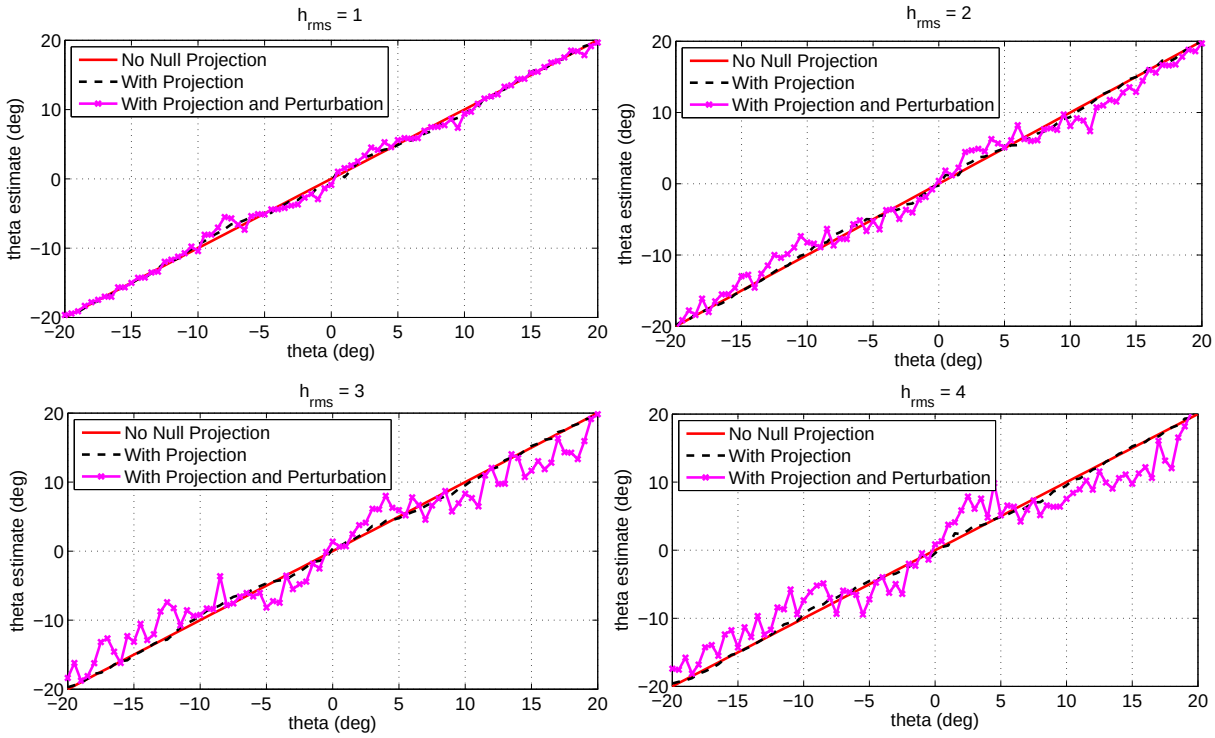

Figure 6.9: ML estimate of target's angle of arrival in perturbed channel. The performance of the original waveform is compared with the null space projected waveform onto the perturbed and un-perturbed interference channel. The values of the rms wave height, i.e., $h_{\text{rms}} = 1$, $h_{\text{rms}} = 2$, $h_{\text{rms}} = 3$, and $h_{\text{rms}} = 4$ indicate a perturbation in the channel coefficients.

in Figure 6.8, the original and the estimated angles are compared using the ML estimation for the original radar waveform and the NSP waveform onto the un-perturbed interference channel. It is important to note that the NSP waveform doesn't degrade the ML estimates or radar performance. This endorses the claims of [11] that the NSP for spectrum-sharing is a viable approach for MIMO radars. Second, the effect of the perturbation on the NSP algorithm is analyzed. In Figure 6.9, the original and the estimated angles for various magnitudes of the perturbation in the channel coefficients are compared. It is important to note that due to the perturbation of the interference-channel the degradation in the performance of the NSP waveform is significant. The degradation also depends on the magnitude of the perturbation. It is evident that as the perturbation in the channel coefficients increases the

performance of the ML, for the NSP waveform, degrades significantly. Thus, perturbation in the interference channel can have a detrimental effect on the radar performance, in a spectrum-sharing setting, when NSP approaches are used. This can be avoided by having a frequent exchange of the ICSI between radars and communication systems.

6.4 Three-Dimensional (3D) Channel Modeling

In the last two section, emphasis was given on the design of 2D channel models and performance of interference mitigation algorithms in 2D channel models. In this section, a three-dimensional (3D) channel model between radar and cellular base stations (BSs) is designed in which the radar uses a two-dimensional (2D) antenna array and the BS uses a one-dimensional (1D) antenna array. A line-of-sight (LoS) channel is formulated and then an algorithm is proposed that mitigates radar interference to BSs. The previously proposed null space projection algorithm for 2D channels is extended to 3D channels and it is shown that effective nulls can be placed by utilizing both the azimuth and elevation angle information of BSs. This results in effective interference mitigation. In addition it is shown that the 3D channel model allows to accurately classify the size of radar's search space when null space projection algorithm is used for interference mitigation.

6.4.1 3D Spectral-Coexistence Models

In this section, fundamentals of MIMO radar and radar-communication system spectrum sharing scenario are briefly discussed.

6.4.1.1 MIMO Radar

Consider a shipborne mono-static MIMO radar with $M = M_h \times M_v$ colocated antennas in a uniform rectangular array (URA), where M_h is the number of horizontal antenna elements in a given row and M_v is the number of vertical antenna elements in a given column. Assume that the inter-element distance between adjacent antenna elements on any given column and row is d_s. The target is assumed to be a point target which has azimuth and elevation angles represented by θ and ϕ, respectively.

Let $\mathbf{x}$ be the transmitted waveform vector which simultaneously illuminates the target area of interest and nulls interference to BSs present in a 2D spatial sector.

6.4.1.2 Spectral Coexistence Scenario

Consider a spectrum sharing scenario in which a cellular system is deployed in the radar band. Each BS of the cellular system is equipped with N transmit and receive antennas in a uniform linear array (ULA). Each BS antenna is at a specific azimuth and elevation angle with respect to radar. Assume a Frequency Division Duplex (FDD) cellular network in which BSs are operating in the radar band and UEs are operating at non-radar frequencies. Therefore, focus is on interference caused by the radar operation to the base stations only. Consider a single cell or a BS with $\mathcal{K}$ users, without loss of generality, that receives the following signal in the presence of radar

$$\mathbf{r} = \sum_{i=1}^{\mathcal{K}} \mathbf{G}_i \mathbf{s}_i + \mathbf{H}\mathbf{x} + \mathbf{n} \tag{6.25}$$

where $\mathbf{G}_i$ is the channel gain between the BS and the i^{th} user, $\mathbf{H}$ is the channel gain between the BS and the radar, and $\mathbf{x}$ is the interfering signal from the MIMO radar. This interference

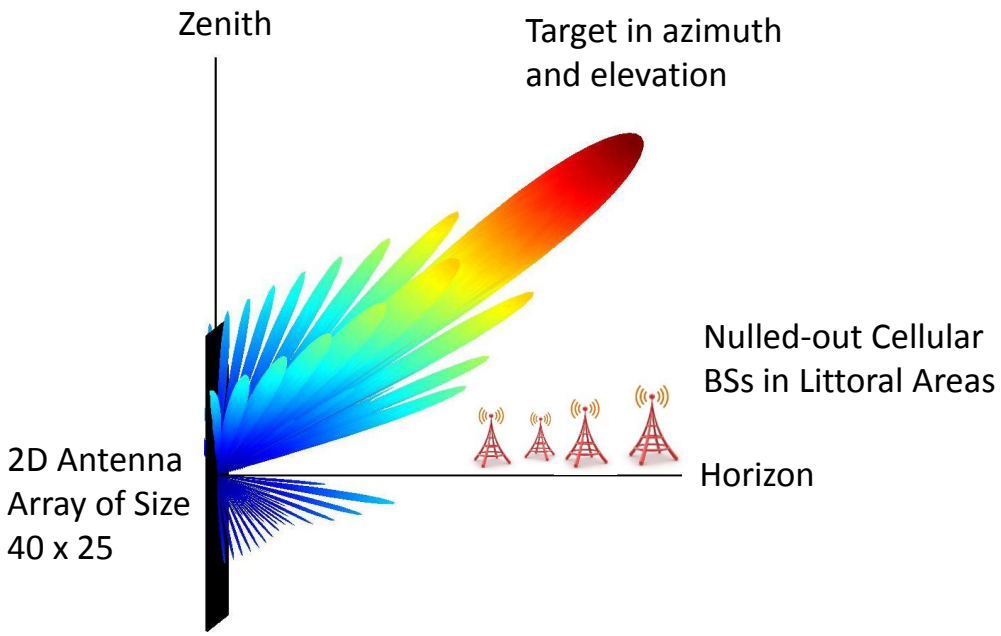

Figure 6.10: 3D spectrum sharing scenario between radar and cellular BSs. The portion containing BSs is nulled-out to protect it from the radar's interference.

from radar can be mitigated by projecting radar waveform onto null space of interference channel between radar and BS [65]. Previous work considers null space projection for 2D channels [65] which is extended in this section to 3D channels.

6.4.2 Physical Modeling of 3D Channel

In this section, a 3D channel model between radar and communication system is formulated. Consider a 2D uniform rectangular array (URA) antenna array at the radar and a 1D uniform linear array (ULA) at the BS. At radar, assume $M = M_h \times M_v$ antenna elements, where M_h antenna elements exist in the horizontal/row direction and M_v antenna elements exist in the vertical/column direction with equal element spacing d_s. Each element of the 2D antenna array can be labeled by s, where $s \triangleq (l,k) = (k-1)M_v + l$, for $k = 1, 2, \ldots, M_h$ and $l = 1, 2, \ldots, M_v$.

In this section, a 3D channel model for line-of-sight (LoS) case is modeled. In the absence of any beamforming, the 3D channel characteristics are dependent on element radiation pattern, antenna spacing, and propagation of each ray path. In the LoS case, for the two adjacent vertical antenna elements s and $s + M_v$ from the same column, the channel coefficients between receive-transmit antenna pairs (u, s) and $(u, s + M_v)$, i.e., $H_{u,s}$ and $H_{u,s+M_v}$, have the following property [107]

$$H_{u,s+M_v} \approx H_{u,s} e^{-\jmath 2\pi/\lambda d_s \cos(\phi)} \tag{6.26}$$

i.e. the difference between the two adjacent elements can be captured by the phase shift due to propagation. In equation (6.26), ϕ is the angle of departure in elevation domain.

For a BS with N antenna elements in a uniform linear array (ULA), the $N \times M$ MIMO channel is partitioned into M_h sub-matrices given by

$$\mathbf{H}_h = \begin{bmatrix} \widetilde{\mathbf{H}}_{k=1} & \widetilde{\mathbf{H}}_{k=2} & \cdots & \widetilde{\mathbf{H}}_{k=M_h} \end{bmatrix} \tag{6.27}$$

where each $\widetilde{\mathbf{H}}_k$ has size $N \times M_v$ and is given as

$$\widetilde{\mathbf{H}}_k = \begin{bmatrix} H_{1,(k-1)M_v+1} & H_{1,(k-1)M_v+2} & \cdots & H_{1,(k-1)M_v+M_v} \\ H_{2,(k-1)M_v+1} & H_{2,(k-1)M_v+2} & \cdots & H_{2,(k-1)M_v+M_v} \\ \cdots & \cdots & \cdots & \cdots \\ H_{N,(k-1)M_v+1} & H_{N,(k-1)M_v+2} & \cdots & H_{N,(k-1)M_v+M_v} \end{bmatrix}$$

for $k = 1, 2, \ldots, M_h$.

Using equation (6.26) the above channel matrix can be written as

$$\mathbf{H}_h = \begin{bmatrix} \widetilde{\mathbf{H}}_{k=1} & \widetilde{\mathbf{H}}_{k=2} & \cdots & \widetilde{\mathbf{H}}_{k=M_h} \end{bmatrix} = \mathbf{a}_h(\theta) \otimes \widetilde{\mathbf{H}}_{k=1} \tag{6.28}$$

where $\otimes$ is the Kronecker product and

$$\mathbf{a}_h(\theta) = \begin{bmatrix} 1 & e^{-\jmath 2\pi/\lambda d_s \cos(\theta)} & \cdots & e^{-\jmath 2\pi/\lambda (M_h-1) d_s \cos(\theta)} \end{bmatrix}$$

is the steering vector in azimuth domain. Using the same arguments one can write the partitioned channel model in elevation domain as

$$\mathbf{H}_v = \begin{bmatrix} \widetilde{\mathbf{H}}_{l=1} & \widetilde{\mathbf{H}}_{l=2} & \cdots & \widetilde{\mathbf{H}}_{l=M_v} \end{bmatrix} \tag{6.29}$$

and each $\widetilde{\mathbf{H}}_l$ has size $N \times M_v$. Using equation (6.26) the above equation can written as

$$\mathbf{H}_v = \begin{bmatrix} \widetilde{\mathbf{H}}_{l=1} & \widetilde{\mathbf{H}}_{l=2} & \cdots & \widetilde{\mathbf{H}}_{l=M_v} \end{bmatrix} = \mathbf{a}_v(\phi) \otimes \widetilde{\mathbf{H}}_{l=1} \tag{6.30}$$

where

$$\mathbf{a}_v(\phi) = \begin{bmatrix} 1 & e^{-\jmath 2\pi/\lambda d_s \cos(\phi)} & \cdots & e^{-\jmath 2\pi/\lambda (M_v-1) d_s \cos(\phi)} \end{bmatrix}$$

is the steering vector in elevation domain.

6.4.3 2D Null Space Projection

In this section, NSP is introduced in both azimuth and elevation domains by considering the 3D channel model designed in the previous section. A projection algorithm is defined

which projects radar signal onto null space of 3D interference channel, i.e., in elevation $\mathbf{H}_v$ and azimuth $\mathbf{H}_h$. Assuming, the MIMO radar has channel state information, singular value decomposition (SVD) is performed in both domains to find the null space and then construct a projector matrix. Lets proceed by first finding SVD of $\mathbf{H}_v$, i.e.,

$$\mathbf{H}_v = \mathbf{U}_v \mathbf{\Sigma}_v \mathbf{V}_v^H. \tag{6.31}$$

Now, define

$$\widetilde{\mathbf{\Sigma}}_v \triangleq \text{diag}(\widetilde{\sigma}_{v,1}, \widetilde{\sigma}_{v,2}, \ldots, \widetilde{\sigma}_{v,p}) \tag{6.32}$$

where $p \triangleq \min(N, M_v)$ and $\widetilde{\sigma}_{v,1} > \widetilde{\sigma}_{v,2} > \cdots > \widetilde{\sigma}_{v,q} > \widetilde{\sigma}_{v,q+1} = \widetilde{\sigma}_{v,q+2} = \cdots = \widetilde{\sigma}_{v,p} = 0$ are the singular values of $\mathbf{H}_v$. Next, define

$$\widetilde{\mathbf{\Sigma}}_v' \triangleq \text{diag}(\widetilde{\sigma}_{v,1}', \widetilde{\sigma}_{v,2}', \ldots, \widetilde{\sigma}_{v,M_v}') \tag{6.33}$$

where

$$\widetilde{\sigma}_{v,u}' \triangleq \begin{cases} 0, & \text{for } u \leq q, \\ 1, & \text{for } u > q. \end{cases} \tag{6.34}$$

Using above definitions projection matrix in elevation is defined as

$$\mathbf{P}_v \triangleq \mathbf{V}_v \widetilde{\mathbf{\Sigma}}_v' \mathbf{V}_v^H. \tag{6.35}$$

Using similar arguments projection matrix in azimuth is defined as

$$\mathbf{P}_h \triangleq \mathbf{V}_h \widetilde{\mathbf{\Sigma}}_h' \mathbf{V}_h^H. \tag{6.36}$$

Using the above defined projection matrices one can write covariance matrices of projected waveform in elevation as

$$\mathbf{R}_{Elv}^{Null} = \mathbf{P}_v \mathbf{R}_{Elv} \mathbf{P}_v^T \tag{6.37}$$

and azimuth as

$$\mathbf{R}_{Azm}^{Null} = \mathbf{P}_h \mathbf{R}_{Azm} \mathbf{P}_h^T. \tag{6.38}$$

The covariance matrix of NSP transmitted waveform is given by

$$\mathbf{R}_{NSP} = \mathbf{R}_{v,NSP} + \mathbf{R}_{h,NSP} \tag{6.39}$$

where

$$\mathbf{R}_{v,NSP} = \mathbf{R}_{Azm}^{Null} \mathbf{a}_h(\theta) \mathbf{a}_v^T(\phi) \mathbf{R}_{Elv} \tag{6.40}$$

$$\mathbf{R}_{h,NSP} = \mathbf{R}_{Azm} \mathbf{a}_h(\theta) \mathbf{a}_v^T(\phi) \mathbf{R}_{Elv}^{Null} \tag{6.41}$$

where $\mathbf{R}_{Elv}$ and $\mathbf{R}_{Azm}$ are waveform covariance matrices in elevation and azimuth, respectively. The 3D beampattern of NSP signal is given as

$$G(\theta, \phi) = |\mathbf{a}_v^T(\phi)\, \mathbf{R}_{NSP}\, \mathbf{a}_h(\theta)|. \tag{6.42}$$

6.4.4 Radar Search Space

Radar search space is normally specified by a search solid angle Ω in steradians. Defining radar search volume extent for both azimuth and elevation, in degrees, as θ and ϕ, the search

volume can be given as [108]

$$\Omega = \frac{\theta\,\phi}{(57.296)^2} \quad \text{(steradians)}. \tag{6.43}$$

Let Ω_{Null} denote the sector, azimuth and elevation angles, of cellular BSs that needs to be nulled to protect BSs from radar interference. Then, due to NSP the search volume, shown in Figure 2, can be given as

$$\Omega_{\text{NSP}} = \frac{\theta\phi - \Omega_{\text{Null}}}{(57.296)^2} \quad \text{(steradians)} \tag{6.44}$$

6.4.5 Numerical Examples

This section provides numerical examples of 3D channel modeling between radar and communication system and its applications using null space projection. The simulation setup assumes that the radar has a 40×25-element URA and the BS has a 10-element ULA. Assume that a target is located at $\theta = 0^\circ$ and $\phi = 50^\circ$ and communication systems are located in a sector of azimuth angles $\theta = -45^\circ$ to -40° and elevation angles $\phi = 5^\circ$ to 15°. It is of interest to null this sector to mitigate radar interference to this area. Two figures of the same example are provided with different views to better understand the achieved results.

Figures 6.12 and 6.13 show the impact of 2D NSP on the radar beampattern. It can be noticed that the target can be accurately localized when it is far from the nulled areas. Moreover, the power received at the target is 60 dB which is significantly higher than the power received at the BSs which is less than -40 dB in this example. Thus, the proposed approach satisfies both the radar mission objective of target detection and simultaneously mitigates interference to BSs. Moreover, only the areas where BSs are present are nulled.

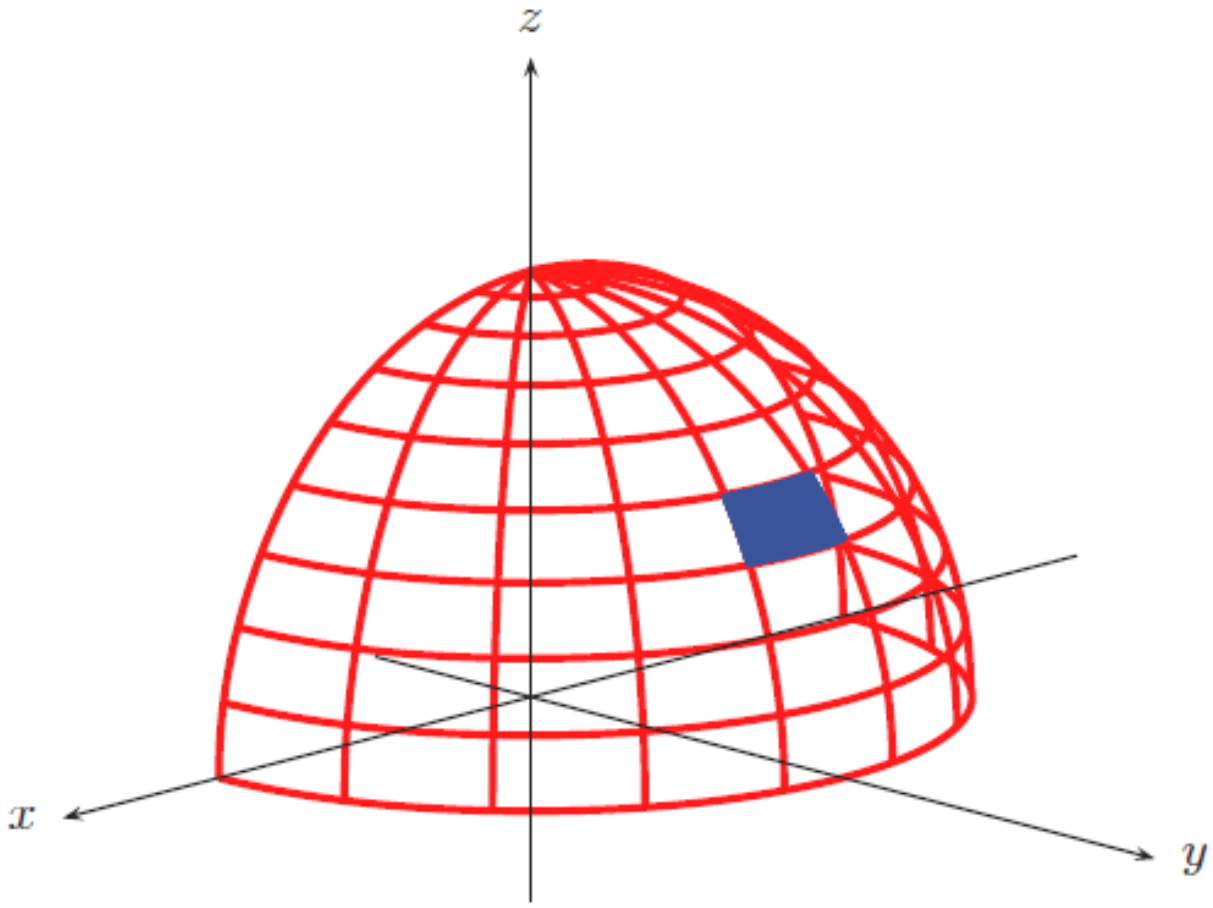

Figure 6.11: Search space of spectrum sharing MIMO radar. The part containing cellular BSs is not part of the radar's illuminated area due to the nulls placed to protect BSs from its interference. That is why the blocked-out part (blue part) of the figure is an illustration of the nulls placed in that particular azimuth-elevation sector.

Figure 6.14 shows the volume illuminated by the spectrum sharing radar as a function of its distance from nulled BSs. Assume the search-able space is 180° in azimuth, i.e., from -90° to 90° and 110° in elevation, i.e, from -20° to 90°. Note that for close-up range the difference in search volume with NSP and without NSP is significant, i.e., for ships docket at the harbor or close to shore line will experience some degradation in search volume due to NSP. However, if the radar is more than 2000 meters away from BSs the loss in search space is minimal.

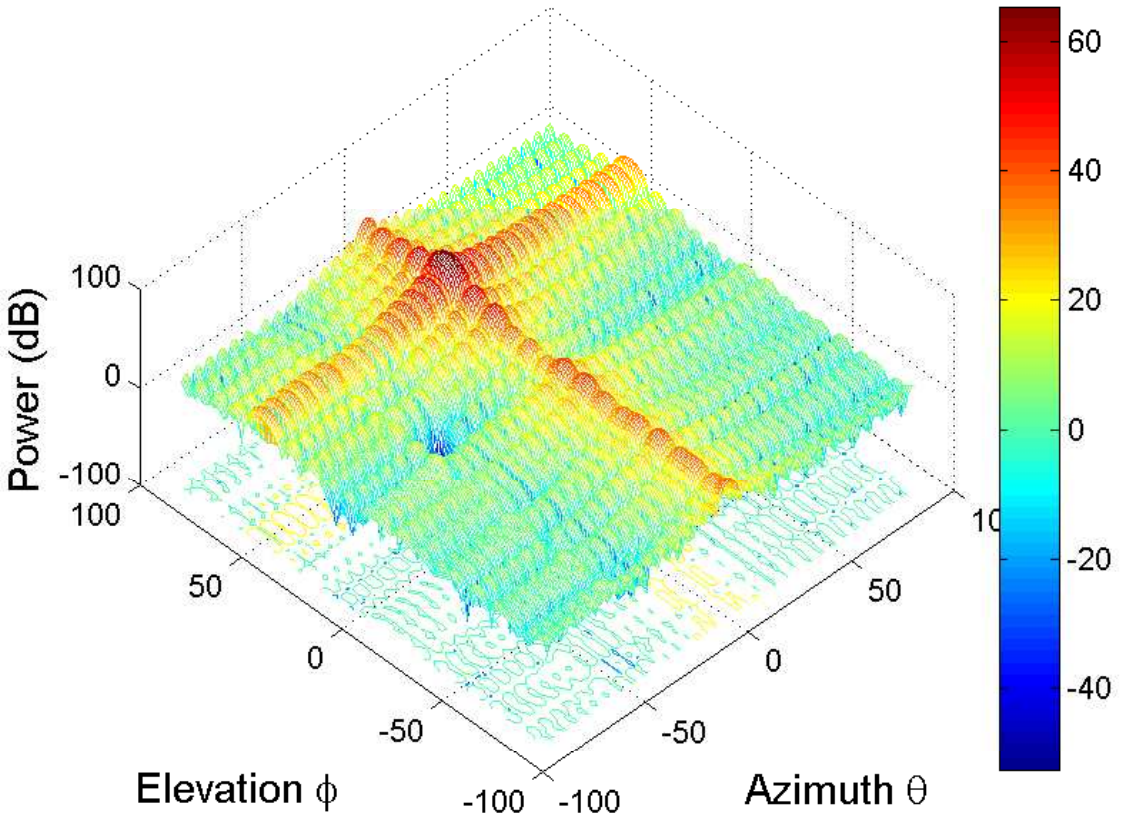

Figure 6.12: 3D view of interference mitigation at BSs. Target is located at $\theta = 0°$ and $\phi = 50°$ and BSs are located in a sector of azimuth angles $\theta = -45°$ to $-40°$ and $\phi = 5°$ to $15°$ and the intention is to null this sector to mitigate radar interference to this area.

6.5 Conclusion

In this chapter, 2D and 3D propagation channels were modeled for a seaborne MIMO radar sharing spectrum with an onshore MIMO communication system and interference mitigation capabilities and performance of MIMO radar was evaluated.

First, using the proposed 2D channel model it was shown that eigen-nulling based approaches yield better target localization, accurate interference-nulling, and minimum loss in

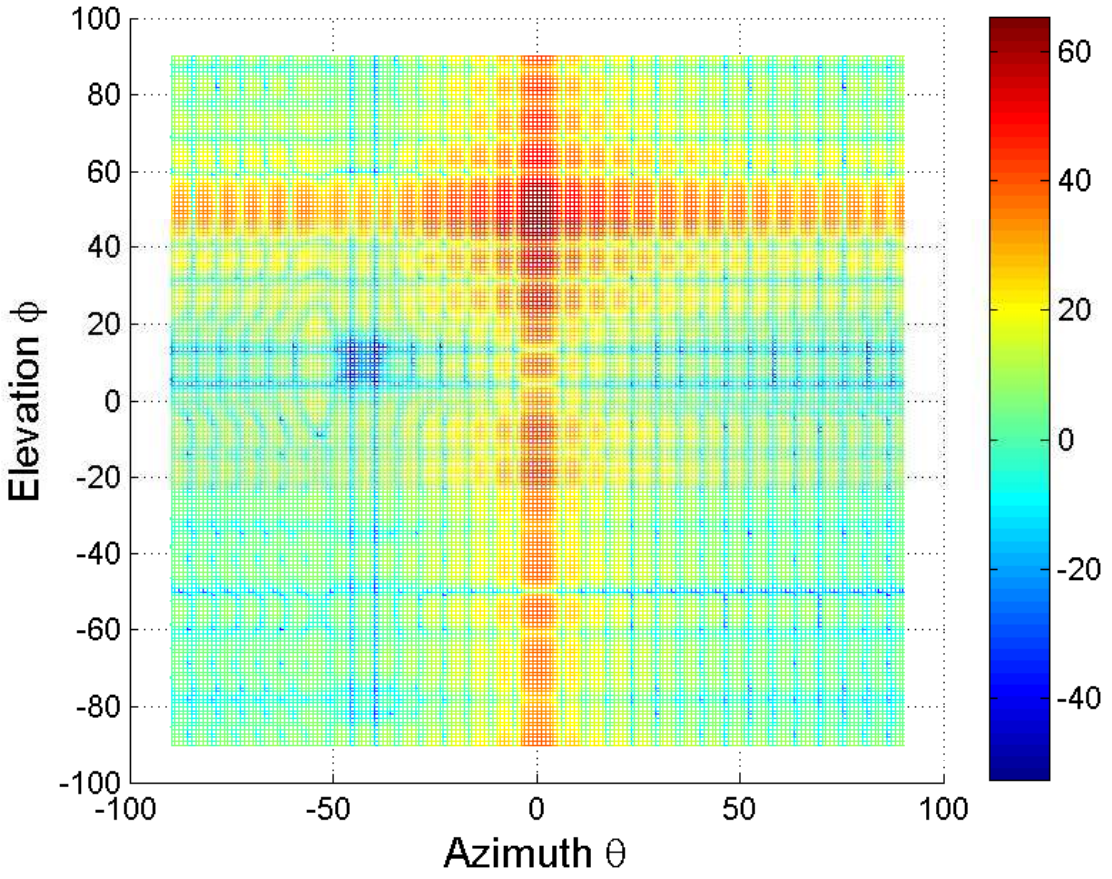

Figure 6.13: Image of interference mitigation at BSs. The intensity/magnitude of radar signal can be observed at the target and BSs. Note the difference between the power received at target vs. the power received at BSs.

radar search/detection space as compared to traditional spatial-nulling approaches widely used in radar signal processing.

Second, it was shown that the nulls placed in the direction of BSs resulted in received power well below the noise floor of commercial BSs thus mitigating radar interference. However, the interference mitigation scheme employed resulted in loss of radar's projected power at targets that were immediately next to BS locations in the azimuth. It was shown that this problem can be compensated by using a large radar antenna array. In addition, it was shown

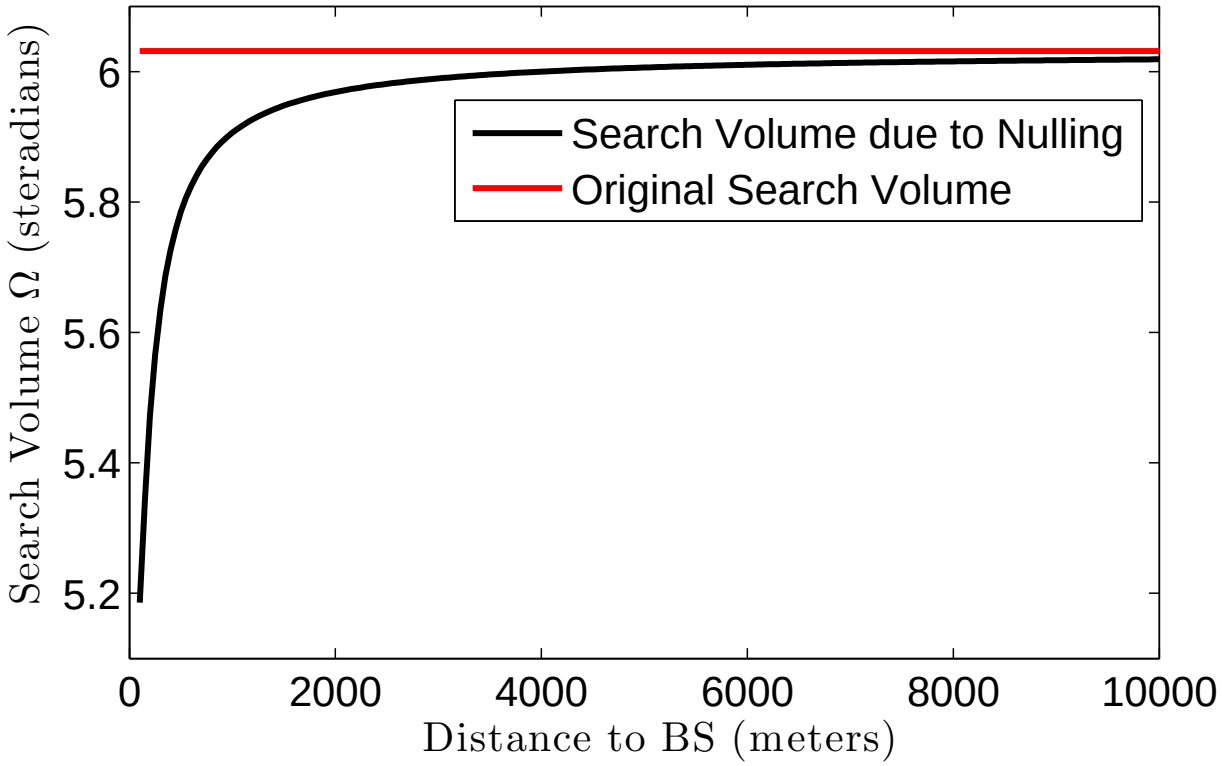

Figure 6.14: Search volume when radar is in deep sea. Search volume for radar located far from BSs. Search-able space is 180° in azimuth, i.e., from -90° to 90° and 110° in elevation, i.e, from -20° to 90°. So the searchable volume in percentage at a distance of: 500 m is 95.9%, 2 km is 99%, and at 8 km is 99.8%. At longer distances the search volume with and without NSP is very close.

that the coherence time of radar-BS channel was large enough for the application of NSP-based interference mitigation scheme which relied on CSI estimation. Thus, the issue of CSI being outdated did not arise in the radar-cellular system spectrum sharing scenario.

Third, spectrum-sharing scenario when the interference channel between radar and communication system is subjected to variations due to the oscillatory motion of ship was explored. The effects of perturbation, in the interference channel, were studied when the NSP approach of spectrum sharing is used. The NSP algorithm did not degrade the radar performance when complete ICSI was available, however, when the interference channel was perturbed, by the

waves, the radar's performance was degraded. The magnitude of the degradation depended upon the magnitude of the perturbation in the channel coefficients, which was due to the height of the waves. The radar performance, in such a scenario, could be improved by having frequent updates of the ICSI.

Fourth, a 3D channel model between radar and communication system was formulated. A 2D antenna array at the radar and a 1D antenna array at the BS was assumed. In addition, a new interference mitigation algorithm that projected radar waveform onto null space of 3D channel to mitigate radar interference to cellular BSs was introduced. The efficacy of the proposed algorithm was shown using simulation results. Search space of spectrum sharing MIMO radars using NSP was also explored and a relation to quantify the size of search space was provided. It was shown that the reduction in search space was directly related to the areas nulled to protect BSs.

Chapter 7

Resource Allocation for Spectrum Sharing

This chapter looks at optimizing communication systems for sharing spectrum with radars. A spectrum sharing scenario between a multiple-input multiple-output (MIMO) radar and Long Term Evolution (LTE) Advanced cellular system is considered. First, a rate allocation optimization problem is solved for LTE-Advanced systems supporting carrier aggregation feature in light of spectrum sharing with radars. Second, a power allocation optimization problem is solved for LTE-Advanced systems supporting carrier aggregation feature

7.1 Power Allocation

In this section, a novel approach for power allocation in cellular networks is proposed. In the proposed model, sigmoidal-like utility functions are used to represent different users' modulation schemes. Each utility function is a representation of the probability of successfully

Table 7.1: Mathematical Notations for Power Allocation

Notation	Description
M	Total number of users in a cell
P_T	Total BS power available
P_i	Power assigned to the i^{th} UE
$\mathbf{P}$	Vector of all users' powers
$\gamma_i(P_i)$	SINR of the i^{th} UE
$U_i(\gamma_i(P_i))$	Utility function of the i^{th} UE
G_i	Accounts for path loss, shadowing, and fading between BS and the i^{th} UE
I_i	Accounts for interference and background noise at the i^{th} UE
z_i	Slack variable of the i^{th} UE
p	Shadow price or the total price per unit power for all UEs
$f_i(\gamma_i(P_i))$	Probability of packet transmission success as a function of user power

transmitted packets per unit of power consumed by a user, when using a certain modulation scheme. Power allocation with utility proportional fairness policy is considered, where the fairness among users is in utility percentage, i.e., percentage of successfully transmitted packets of the corresponding modulation scheme. The power allocation optimization problem as a product of utilities of all users and it is proved that it is convex and therefore the optimal solution is tractable. A distributed algorithm is proposed to optimally allocate base station powers with priority given to users running lower modulation schemes while ensuring non-zero power allocation to users running higher modulation schemes. This algorithm prevents fluctuation in the power allocation process and is capable of traffic and modulation dependent pricing policy. This can be used to flatten traffic and decrease the service price for users.

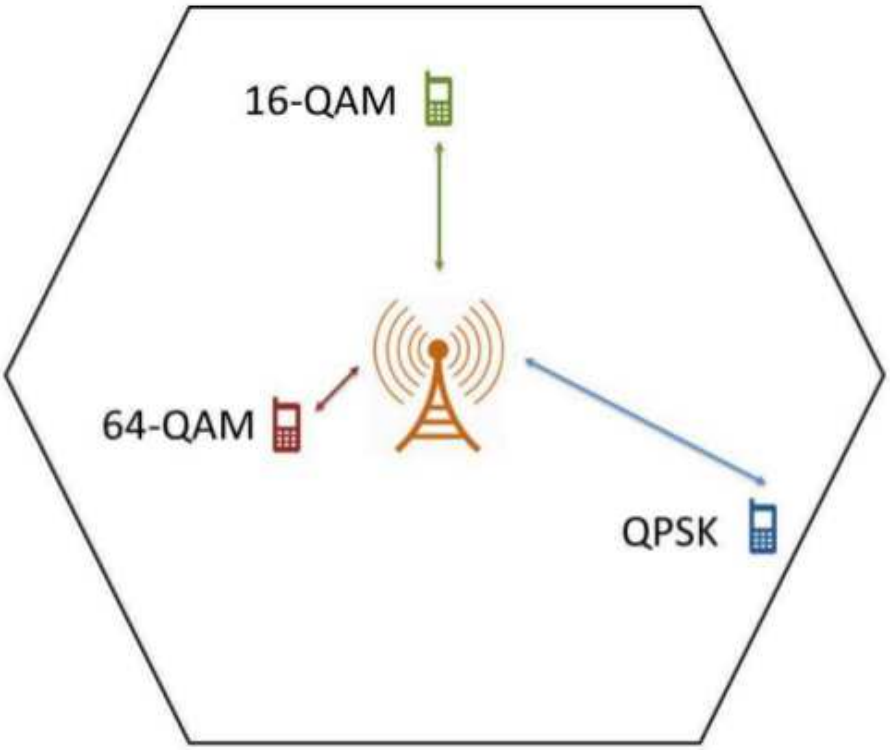

Figure 7.1: Adaptive modulation schemes: Adaptive modulation schemes are used to enhance high data-rate access to users in 3G and 4G cellular networks. When the signal-to-noise (SNR) ratio is the highest, a higher modulation scheme is used, for example 256-QAM. This usually happens for users near the BS as they share good channel quality with the BS. Higher modulation schemes require higher transmit power to maintain an acceptable SNR for successful transmission of packets, as seen from Fig. 7.2.

7.1.1 Utility Proportional Fairness

This treatment considers utility proportional fairness rather than bandwidth proportional fairness network utility maximization problem. Regular proportional fairness problem suits the case when all users have the same modulation scheme [42]. However, modern cellular network's users have different QoS needs and therefore can handle different modulation schemes. Thus, one has to give up regular proportional fairness schemes in favor of utility proportional fairness for power allocation in modern cellular systems [109, 60].

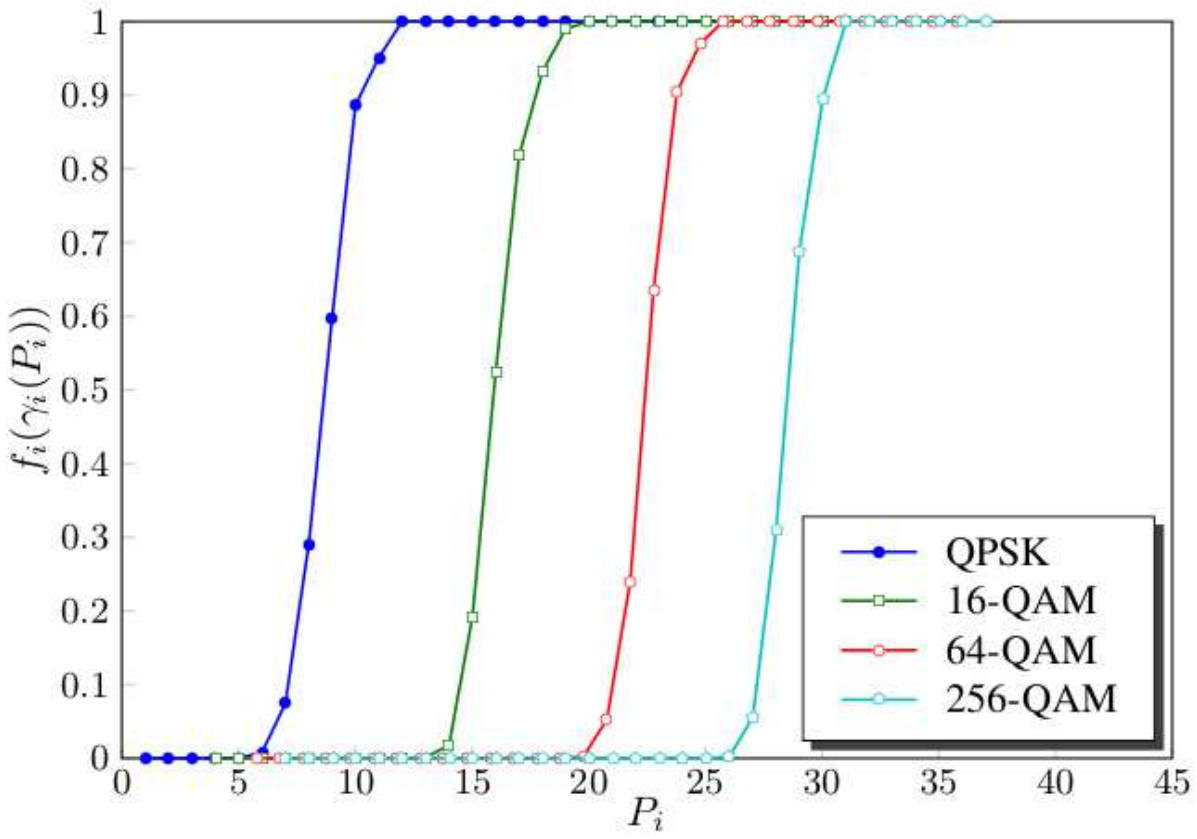

Figure 7.2: Probability of successful packet transmission. Cumulative distribution function of successful packet transmission for QPSK, 16-QAM, 64-QAM, and 256-QAM modulation schemes. Each modulation represents a user's utility function $U_i(\gamma_i(P_i))$ which is a function of power.

System Topology: This section considers, without loss of generality, a single cellular system consisting of a single BS and M UEs. The objective is to optimally allocate powers to UEs depending upon the modulation scheme used and the price paid for the power such that all UEs are served with non-zero allocation of power. A time-slotted system is assumed in which the power allocation algorithm executes in every time slot. In addition, the time slot is of arbitrary interval in which a single or several packets can be transmitted and the propagation conditions such as path loss, fading, noise and intercell interference stay the same for each UE. The BS allocates power within the power limit available such that the

power allocated to the i^{th} UE by the BS is given by P_i. Each UE has its own utility function $U_i(\gamma_i(P_i))$ that corresponds to the type of modulation scheme being handled by the UE where $\gamma_i(P_i)$ is the "generic" signal quality metric for the i^{th} UE, as in [35]. For cellular systems, this metric is commonly referred to as SINR as it not only depends on the i^{th} UE's power allocation but also on the power allocation of all other UEs. For CDMA systems, this metric represents the bit energy to interference density ratio of the i^{th} UE [35].

Sigmoidal-like Utility Functions: The objective is to assign optimal power levels to the UEs so as to have a minimum QoS for each UE. Therefore, the utility functions $U_i(\gamma_i(P_i))$ are assumed to be sigmoidal-like functions. The utility functions have the following properties:

- $U_i(0) = 0$ and $U_i(\gamma_i(P_i))$ is an increasing function of P_i.
- $U_i(\gamma_i(P_i))$ is twice continuously differentiable in P_i.

The SINR $\gamma_i(P_i)$ is represented, as in [35]

$$\gamma_i(P_i) = \frac{G_i P_i}{G_i \sum_{m=1}^{M} P_m - G_i P_i + I_i} \tag{7.1}$$

where G_i accounts for channel gain between the BS and the i^{th} UE and I_i accounts for background noise and intercell interference to the i^{th} UE. This model uses the normalized sigmoidal-like utility function, as in [35, 110, 48], that can be expressed as

$$U_i(\gamma_i(P_i)) = c_i\Big(\frac{1}{1 + e^{-a_i(P_i - b_i)}} - d_i\Big) \tag{7.2}$$

where $c_i = \frac{1+e^{a_i b_i}}{e^{a_i b_i}}$ and $d_i = \frac{1}{1+e^{a_i b_i}}$. So, it satisfies $U(0) = 0$ and $U(\infty) = 1$. The values assigned to a and b play a role in the total system utility. For example, a UE with a larger value of a or a UE with a smaller value of b requires less power to achieve the same utility,

given that other conditions are same [35]. In addition, parameters a and b can be tuned to get an approximation of utility functions of various applications.

Link Adaptation in 4G Cellular Systems: Current and emerging cellular standards adapt to the RF transmission conditions and select modulation and coding schemes which result in enhanced QoS for users. This is known as link adaptation. The choice of modulation and/or coding scheme is dynamically selected based on the channel-quality between the base station and the user. For example, in LTE systems, each user sends a signal-quality level, known as channel quality indicator (CQI) measurement, to the BS. The CQI measurement is based on the received signal-strength of the reference signal, transmitted by the BS with a constant power level and fixed modulation scheme. This CQI measurements aids the BS to assign modulation and/or coding scheme to the user. Typically, a BS can assign upto 256-QAM scheme to users that report the highest value of CQI. This is usually for the users that share good channel with the BS or are close to the BS, see Figure 7.1. However, higher power needs to be allocated in order to assure same QoS as that of a lower modulation scheme, say QPSK, see Figure 7.2.

Representing Modulations by Sigmoidal-like Utility Functions: In order to further motivate the use of sigmoidal-like utility functions, Figure 7.2, provides the probability of packet transmission success for different modulation schemes such as QPSK, 16-QAM, 64-QAM, and 256-QAM. It is assumed that the packets consist of 800 symbols and $P_T = 31$. The probability of packet success can be given by $f_i(\gamma_i(P_i)) = \text{Prob}(\gamma_i(P_i) \geq \Gamma)$, where Γ is some pre-established threshold. This packet transmission success probability depends on many parameters including modulation schemes, coding rate, packet size, hybrid automatic repeat request (H-ARQ) schemes, SINR, and power. It is important to note that the cumulative distribution function of modulation schemes has a sigmoidal-like shape i.e. first convex and then concave. Thus, a modulation can indeed be represented by sigmoidal-like utility

function of its power allocation [35]. For this reason, this work represents different user modulations by sigmoidal- like utility functions.

7.1.2 Problem Formulation

The utility proportional fairness objective function is given by

$$\max_{\mathbf{P}} \prod_{i=1}^{M} U_i(\gamma_i(P_i)) \tag{7.3}$$

where $\mathbf{P} = \{P_1, P_2, ..., P_M\}$ and M is the number of UEs in the coverage area of the BS. The goal of this power allocation objective function is to allocate power to each UE that maximizes the total mobile system objective (i.e. the product of the utilities of all the UEs) while ensuring proportional fairness among individual utilities. This power allocation objective function ensures non-zero power allocation for all users. Therefore, the corresponding power allocation optimization problem guarantees minimum QoS for all users. In addition, this approach allocates more power to users with lower modulation schemes providing improvement in the QoS of cellular system.

Optimization Problem: The basic formulation of the utility proportional fairness power allocation problem is given by the following optimization problem with two constraints:

$$\begin{aligned} \max_{\mathbf{P}} \quad & \prod_{i=1}^{M} U_i(\gamma_i(P_i)) \\ \text{subject to} \quad & \sum_{i=1}^{M} P_i \leq P_T \\ & P_i \geq 0, \quad \text{for } i = 1, 2, ..., M \text{ and } P_T \geq 0. \end{aligned} \tag{7.4}$$

where P_T is the total power of the BS covering the M UEs, and $\mathbf{P} = \{P_1, P_2, ..., P_M\}$. The

optimization problem has two constraints which are discussed as follows.

Total BS Power Constraint i.e. $\sum_{i=1}^{M} P_i \leq P_T$**:** The BS has to allocate powers to all users by staying within its available power budget.

Minimum QoS Constraint i.e. $P_i \geq 0$ **for** $i = 1, 2, ..., M$ **and** $P_T \geq 0$**:** It is ensured that all UEs are served by the BS by allocating non-zero powers to all UEs, i.e., when $P_T \neq 0$, $P_i > 0$ for all users. This is to meet a minimum QoS criteria for all users of the network. The case $P_i = 0$ is only when $P_T = 0$ and is included to make the problem as general as possible.

In Section 7.1.3, it is proved that there exists a tractable global optimal solution to the optimization problem (7.4).

7.1.3 The Global Optimal Solution

In the optimization problem (7.4), since the objective function $\arg\max_{\mathbf{P}} \prod_{i=1}^{M} U_i(\gamma_i(P_i))$ is equivalent to $\arg\max_{\mathbf{P}} \sum_{i=1}^{M} \log(U_i(\gamma_i(P_i)))$, it can be expressed as:

$$\begin{aligned} \max_{\mathbf{P}} \quad & \sum_{i=1}^{M} \log(U_i(\gamma_i(P_i))) \\ \text{subject to} \quad & \sum_{i=1}^{M} P_i \leq P_T \\ & P_i \geq 0, \quad \text{for } i = 1, 2, ..., M \text{ and } P_T \geq 0. \end{aligned} \tag{7.5}$$

Lemma 7.1.1. *The utility functions* $\log(U_i(\gamma_i(P_i)))$*, in the optimization problem (7.5), are strictly concave functions.*

Proof. In this section, it is assumed that all the utility functions of the UEs are sigmoidal-like

functions. The utility function of the normalized sigmoidal-like function is given by equation (7.2) as $U_i(\gamma_i(P_i)) = c\Big(\frac{1}{1+e^{-a_i(P_i-b_i)}} - d\Big)$. For $0 < P_i < P_T$,

$$0 < 1 - d_i(1 + e^{-a_i(P_i-b_i)}) < \frac{1}{1 + c_i d_i}$$

It follows that for $0 < P_i < P_T$, the first and second derivative are

$$\begin{aligned}
\frac{d}{dP_i} \log U_i(\gamma_i(P_i)) =& \frac{a_i d_i e^{-a_i(P_i-b_i)}}{1 - d_i(1 + e^{-a_i(P_i-b_i)})} + \frac{a_i e^{-a_i(P_i-b_i)}}{(1 + e^{-a_i(P_i-b_i)})} > 0 \\
\frac{d^2}{dP_i^2} \log U_i(\gamma_i(P_i)) =& \frac{-a_i^2 d_i e^{-a_i(P_i-b_i)}}{c_i\Big(1 - d_i(1 + e^{-a(P_i-b_i)})\Big)^2} + \frac{-a_i^2 e^{-a_i(P_i-b_i)}}{(1 + e^{-a_i(P_i-b_i)})^2} < 0.
\end{aligned}$$

Therefore, the sigmoidal-like utility function's $U_i(\gamma_i(P_i))$ natural logarithm $\log(U_i(\gamma_i(P_i)))$ is strictly concave function. Therefore, all the utility functions in the system model have strictly concave natural logarithms. □

The natural logarithms of the utility functions of Figure 7.3 are shown in Figure 7.4 and the derivatives of natural logarithms of the utility functions are shown in Figure 7.5.

Theorem 7.1.2. *The optimization problem (7.4) is a convex optimization problem and there exists a unique tractable global optimal solution.*

Proof. It follows from Lemma 7.1.1 that all UEs' utility functions are strictly concave. Therefore, the optimization problem (7.5) is a convex optimization problem [111]. The optimization problem (7.5) is equivalent to the optimization problem (7.4), therefore it is also a convex optimization problem. For a convex optimization problem there exists a unique tractable global optimal solution [111]. □

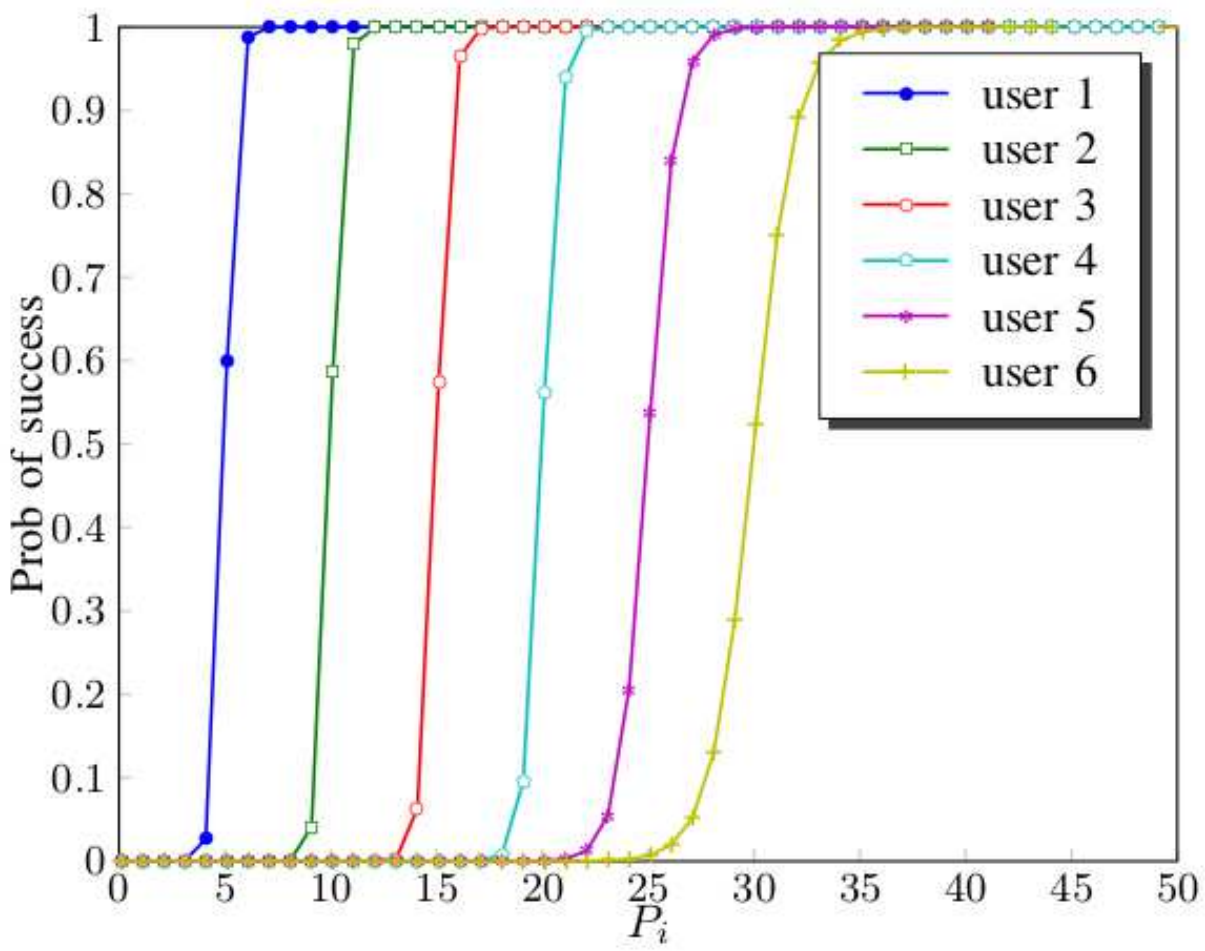

Figure 7.3: Sigmoidal-like utility functions: The sigmoidal-like utility functions (representing users with different modulation schemes) $U_i(\gamma_i(P_i))$. We use sigmoidal-like utility functions as their shape resembles cumulative distribution function of successful packet transmission of modulation schemes, see Figure 7.2.

7.1.4 The Dual Problem

The key to a distributed and a decentralized optimal solution of the primal problem in (7.5) is to convert it to the dual problem, similar to [42] and [43]. The optimization problem (7.5) can be divided into two simpler problems by using the dual problem. The Lagrangian is

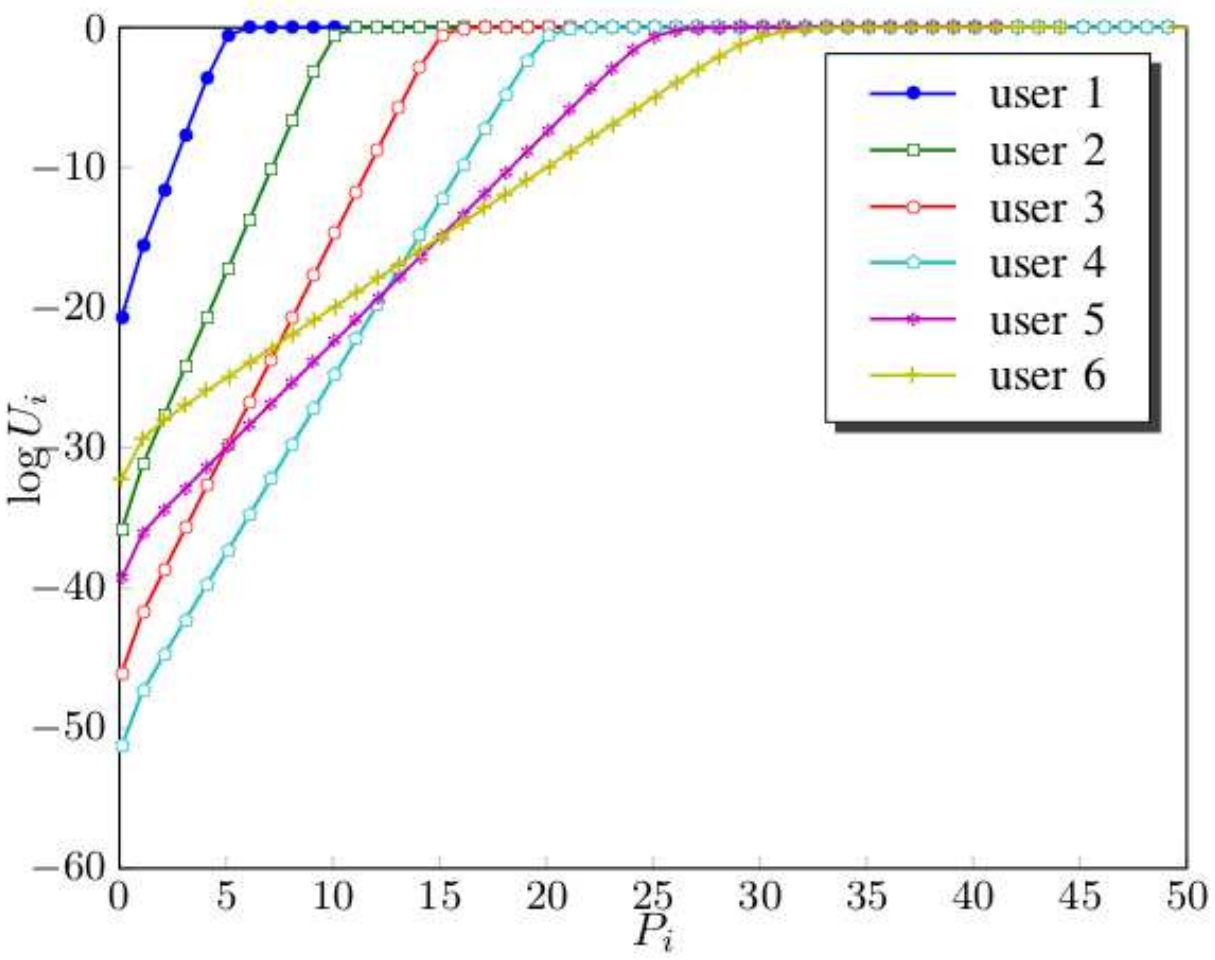

Figure 7.4: Natural logarithm of sigmoidal-like utility functions: The natural logarithm of sigmoidal-like utility functions $\log U_i(\gamma_i(P_i))$ which are strictly concave. Thus all modulation schemes considered can be represented by sigmoidal-like utility functions that are strictly concave.

defined as

$$\begin{aligned} L(\mathbf{P}, p) &= \sum_{i=1}^{M} \log(U_i(\gamma_i(P_i))) - p(\sum_{i=1}^{M} P_i + z_i - P_T) \\ &= \sum_{i=1}^{M} \Big(\log(U_i(\gamma_i(P_i))) - pP_i\Big) + p\sum_{i=1}^{M}(P_T - z_i) \\ &= \sum_{i=1}^{M} L_i(P_i, p) + p\sum_{i=1}^{M}(P_T - z_i) \end{aligned} \tag{7.6}$$

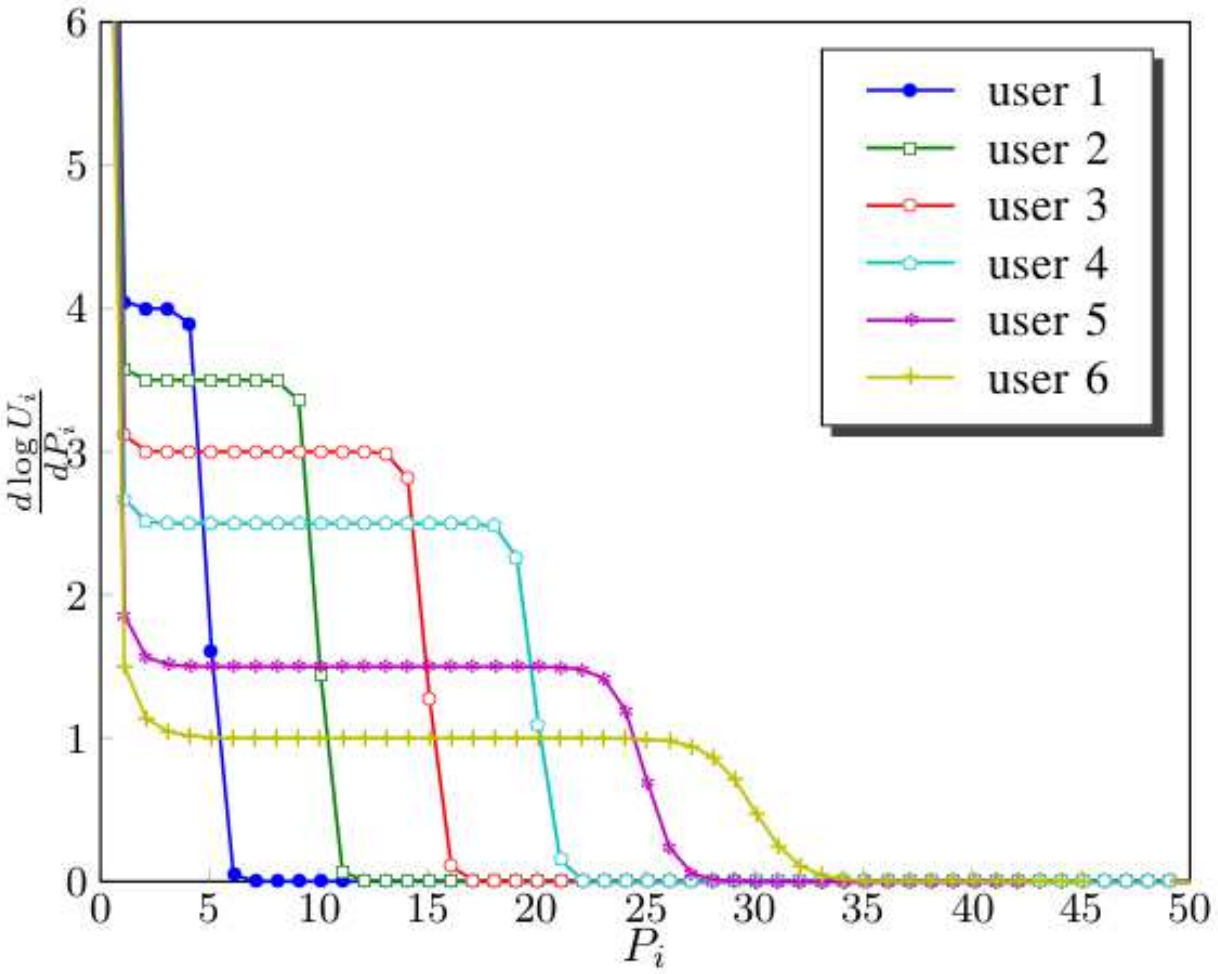

Figure 7.5: First derivative of the natural logarithm of sigmoidal-like utility functions: The first derivative of the natural logarithm of sigmoidal-like utility functions $\frac{\partial \log U_i(\gamma_i(P_i))}{\partial P_i}$.

where $z_i \geq 0$ is the slack variable and p is Lagrange multiplier or the shadow price (i.e. the total price per unit power for all the M channels). Therefore, the i^{th} UE bid for power can be given by $w_i = pP_i$ and thus $\sum_{i=1}^{M} w_i = p \sum_{i=1}^{M} P_i$. The first term in equation (7.6) is separable in P_i. Thus, $\max_{\mathbf{P}} \sum_{i=1}^{M} (\log(U_i(\gamma_i(P_i))) - pP_i) = \sum_{i=1}^{M} \max_{P_i} (\log(U_i(\gamma_i(P_i))) - pP_i)$.

The dual problem objective function can be written as

$$\begin{aligned} D(p) =& \max_{\mathbf{P}} L(\mathbf{P}, p) \\ &= \sum_{i=1}^{M} \max_{P_i} \Big(\log(U_i(\gamma_i(P_i))) - pP_i \Big) + p \sum_{i=1}^{M} (P_T - z_i) \\ &= \sum_{i=1}^{M} \max_{P_i} (L_i(P_i, p)) + p \sum_{i=1}^{M} (P_T - z_i). \end{aligned} \tag{7.7}$$

The dual problem is given by

$$\begin{aligned} \min_{p} \quad & D(p) \\ \text{subject to} \quad & p \geq 0. \end{aligned} \tag{7.8}$$

Thus,

$$\frac{\partial D(p)}{\partial p} = P_T - \sum_{i=1}^{M} (P_i - z_i) = 0 \tag{7.9}$$

Substituting by $\sum_{i=1}^{M} w_i = p \sum_{i=1}^{M} P_i$ gives

$$p = \frac{\sum_{i=1}^{M} w_i}{P_T - \sum_{i=1}^{M} z_i}. \tag{7.10}$$

Now, we divide the primal problem (7.5) is divided into two simpler optimization problems in the UEs and the BS. The i^{th} UE optimization problem is given by:

$$\begin{aligned} \max_{P_i} \quad & \log U_i(\gamma_i(P_i)) - pP_i \\ \text{subject to} \quad & p \geq 0 \\ & P_i \geq 0, \quad \text{for } i = 1, 2, ..., M \text{ and } P_T \geq 0. \end{aligned} \tag{7.11}$$

The BS optimization problem is given by:

$$\begin{aligned} \min_{p} \quad & D(p) \\ \text{subject to} \quad & p \geq 0. \end{aligned} \tag{7.12}$$

The minimization of shadow price p is achieved by the minimization of the slack variable $z_i \geq 0$ from equation (7.10). Therefore, the maximum utilization of the available BS power is achieved by setting the slack variable $z_i = 0$. In this case, the inequality in primal problem (7.5) constraint is replaced by equality constraint and thus $\sum_{i=1}^{M} w_i = pP_T$. Therefore, we have $p = \frac{\sum_{i=1}^{M} w_i}{P}$ where $w_i = pP_i$ is transmitted by the i^{th} UE to the BS. The utility proportional fairness in the objective function of the optimization problem (7.4) is guaranteed in the solution of the optimization problems (7.11) and (7.12).

7.1.5 Distributed Algorithm

A distributed power allocation algorithm can be directly constructed form the dual problem. The distributed power allocation algorithm is an iterative solution for allocating the network resources with bandwidth proportional fairness. The algorithm allocates powers with utility proportional fairness, which is the objective of the new problem formulation. The algorithm is divided into an UE algorithm shown in Algorithm (7) and an BS algorithm shown in Algorithm (8). For the Algorithm in (7) and (8), each UE starts with an initial bid $w_i(1)$ which is transmitted to the BS. The BS calculates the difference between the received bid $w_i(n)$ and the previously received bid $w_i(n-1)$ and exits if it is less than a pre-specified threshold δ, $w_i(0)$ is set to zero. If the value is greater than the threshold δ, BS calculates the shadow price $p(n) = \frac{\sum_{i=1}^{M} w_i(n)}{P}$ and sends that value to all the UEs. Each UE receives the shadow price to solve for the power P_i that maximizes $\log U_i(\gamma_i(P_i)) - p(n)P_i$. That

power is used to calculate the new bid $w_i(n) = p(n)P_i(n)$. Each UE sends the value of its new bid $w_i(n)$ to the BS. This process is repeated until $|w_i(n) - w_i(n-1)|$ is less than the pre-specified threshold δ.

Algorithm 7 Power Allocation: UE Algorithm

Send initial bid $w_i(1)$ to BS
loop
  Receive shadow price $p(n)$ from BS
  if STOP from BS **then**
    Calculate allocated power $P_i^{\text{opt}} = \frac{w_i(n)}{p(n)}$
    STOP
  else
    Solve $P_i(n) = \arg\max_{P_i} \Big(\log U_i(\gamma_i(P_i)) - p(n)P_i \Big)$
    Send new bid $w_i(n) = p(n)P_i(n)$ to BS
  end if
end loop

Algorithm 8 Power Allocation: BS Algorithm

loop
  Receive bids $w_i(n)$ from UEs {Let $w_i(0) = 0 \ \forall i$}
  if $|w_i(n) - w_i(n-1)| < \delta \ \forall i$ **then**
    Allocate powers, $P_i^{\text{opt}} = \frac{w_i(n)}{p(n)}$ to user i
    STOP
  else
    Calculate $p(n) = \frac{\sum_{i=1}^{M} w_i(n)}{P}$
    Send new shadow price $p(n)$ to all UEs
  end if
end loop

The solution P_i of the optimization problem $P_i(n) = \arg\max_{P_i} \Big(\log U_i(\gamma_i(P_i)) - p(n)P_i \Big)$ in Algorithm (7), is the value of P_i that solves equation $\frac{\partial \log U_i(\gamma_i(P_i))}{\partial P_i} = p(n)$.

7.1.6 Convergence

This section presents the convergence analysis of Algorithm (7) and (8) for different values of P_T.

Lemma 7.1.3. *For sigmoidal-like utility function $U_i(\gamma_i(P_i))$, the slope curvature function $\frac{\partial \log U_i(\gamma_i(P_i))}{\partial P_i}$ has an inflection point at $P_i = P_i^s \approx b_i$ and is convex for $P_i > P_i^s$.*

Proof. For the sigmoidal-like function $U_i(\gamma_i(P_i)) = c_i\Big(\frac{1}{1+e^{-a_i(P_i-b_i)}} - d_i\Big)$, let $S_i(P_i) = \frac{\partial \log U_i(\gamma_i(P_i))}{\partial P_i}$ be the slope curvature function. Then,

$$\frac{\partial S_i}{\partial P_i} = \frac{-a_i^2 d_i e^{-a_i(P_i-b_i)}}{c_i\Big(1-d_i(1+e^{-a_i(P_i-b_i)})\Big)^2} - \frac{a_i^2 e^{-a_i(P_i-b_i)}}{\Big(1+e^{-a_i(P_i-b_i)}\Big)^2}$$

and (7.13)

$$\frac{\partial^2 S_i}{\partial P_i^2} = \frac{a_i^3 d_i e^{-a_i(P_i-b_i)}(1-d_i(1-e^{-a_i(P_i-b_i)}))}{c_i\Big(1-d_i(1+e^{-a_i(P_i-b_i)})\Big)^3} + \frac{a_i^3 e^{-a_i(P_i-b_i)}(1-e^{-a_i(P_i-b_i)})}{\Big(1+e^{-a_i(P_i-b_i)}\Big)^3}.$$

The curvature of the slope of the natural logarithm of sigmoidal-like utility function is analyzed. For the first derivative, $\frac{\partial S_i}{\partial P_i} < 0 \ \ \forall\, P_i$. The first term S_i^1 of $\frac{\partial^2 S_i}{\partial P_i^2}$ in equation (7.13) can be written as

$$S_i^1 = \frac{a_i^3 e^{a_i b_i}\big(e^{a_i b_i} + e^{-a_i(P_i-b_i)}\big)}{\big(e^{a_i b_i} - e^{-a_i(P_i-b_i)}\big)^3} \tag{7.14}$$

and

$$\lim_{P_i \to 0} S_i^1 = \infty, \ \text{ and } \ \lim_{P_i \to b_i} S_i^1 = 0 \ \text{ for } \ b_i \gg \frac{1}{a_i}. \tag{7.15}$$

For second term S_i^2 of $\frac{\partial^2 S_i}{\partial P_i^2}$ in equation (7.13), the following properties exist

$$S_i^2(b_i) = 0, \ \ S_i^2(P_i > b_i) > 0, \ \text{ and } \ S_i^2(P_i < b_i) < 0. \tag{7.16}$$

From equation (7.15) and (7.16), S_i has an inflection point at $P_i = P_i^s \approx b_i$. In addition, the curvature of S_i changes from a convex function close to origin to a concave function before the inflection point $P_i = P_i^s$ then to a convex function after the inflection point. □

Corollary 7.1.4. *If $\sum_{i=1}^{M} P_i^{inf} \ll P_T$ then Algorithm in (7) and (8) converges to the global*

optimal powers which correspond to the steady state shadow price $p_{ss} < \frac{a_{i_{\max}} d_{i_{\max}}}{1-d_{i_{\max}}} + \frac{a_{i_{\max}}}{2}$ *where* $i_{\max} = \arg\max_i b_i$.

Proof. For the sigmoidal-like function $U_i(\gamma_i(P_i)) = c_i\Big(\frac{1}{1+e^{-a_i(P_i-b_i)}} - d_i\Big)$, the optimal solution is achieved by solving the optimization problem (7.5). In Algorithm (7), an important step to reach to the optimal solution is to solve the optimization problem $P_i(n) = \arg\max_{P_i}\Big(\log U_i(\gamma_i(P_i)) - p(n)P_i\Big)$ for every UE. The solution of this problem can be written, using Lagrange multipliers method, in the form

$$\frac{\partial \log U_i(\gamma_i(P_i))}{\partial P_i} - p = S_i(P_i) - p = 0. \tag{7.17}$$

From equation (7.15) and (7.16) in Lemma 7.1.3, the curvature of $S_i(P_i)$ is convex for $P_i > P_i^s \approx b_i$. The Algorithm in (7) and (8) is guaranteed to converges to the global optimal solution when the slope $S_i(P_i)$ of all the utility functions' natural logarithm $\log U_i(\gamma_i(P_i))$ are in the convex region of the functions, similar to the analysis of logarithmic functions in [42] and [43]. Therefore, the natural logarithm of sigmoidal-like functions $\log U_i(\gamma_i(P_i))$ converge to the global optimal solution for $P_i > P_i^s \approx b_i$. The inflection point of sigmoidal-like function $U_i(\gamma_i(P_i))$ is at $P_i^{\inf} = b_i$. For $\sum_{i=1}^{M} P_i^{\inf} \ll P_T$, Algorithm in (7) and (8) allocates powers $P_i > b_i$ for all users. Since $S_i(P_i)$ is convex for $P_i > P_i^s$ *approx*b_i then the optimal solution can be achieved by Algorithm (7) and (8). From equation (7.17) and as $S_i(P_i)$ is convex for $P_i > P_i^s \approx b_i$, that $p_{ss} < S_i(P_i = \max b_i)$ where $S_i(P_i = \max b_i) = \frac{a_{i_{\max}} d_{i_{\max}}}{1-d_{i_{\max}}} + \frac{a_{i_{\max}}}{2}$ and $i_{\max} = \arg\max_i b_i$. □

Corollary 7.1.5. *For* $\sum_{i=1}^{M} P_i^{inf} > P_T$ *and the global optimal shadow price* $p_{ss} \approx \frac{a_i d_i e^{\frac{a_i b_i}{2}}}{1-d_i(1+e^{\frac{a_i b_i}{2}})} + \frac{a_i e^{\frac{a_i b_i}{2}}}{(1+e^{\frac{a_i b_i}{2}})}$, *then the solution by Algorithm in (7) and (8) fluctuates about the global optimal solution.*

Proof. It follows from lemma 7.1.3 that for $\sum_{i=1}^{M} P_i^{\inf} > P_T \ \exists \ i$ such that the optimal powers $P_i^{\text{opt}} < b_i$. Therefore, if $p_{ss} \approx \frac{a_i d_i e^{\frac{a_i b_i}{2}}}{1-d_i(1+e^{\frac{a_i b_i}{2}})} + \frac{a_i e^{\frac{a_i b_i}{2}}}{(1+e^{\frac{a_i b_i}{2}})}$ is the optimal shadow price for optimization problem (7.12). Then, a small change in the shadow price $p(n)$ in the n^{th} iteration can lead the power $P_i(n)$ (root of $S_i(P_i) - p(n) = 0$) to fluctuate between the concave and convex curvature of the slope curve $S_i(P_i)$ for the i^{th} user. Therefore, it causes fluctuation in the bid $w_i(n)$ sent to the BS and fluctuation in the shadow price $p(n)$ set by BS. Therefore, the iterative solution of Algorithm in (7) and (8) fluctuates about the global optimal powers P_i^{opt}. □

Theorem 7.1.6. *Algorithm in (7) and (8) does not converge to the global optimal solution for all values of P_T.*

Proof. It follows from Corollary 7.1.4 and 7.1.5 that Algorithm in (7) and (8) does not converge to the global optimal solution for all values of P_T. □

Fluctuation Example

An example of six users is considered using sigmoidal-like utility functions. The sigmoidal-like utility functions' parameters are $a = \{4, 3.5, 3, 2.5, 1.5, 1\}$ and $b = \{5, 10, 15, 20, 25, 30\}$, respectively. It is assumed that the BS's maximum power is $P_T = 100$, therefore, $\sum_{i=1}^{6} P_i^{\inf} = 105 > P_T = 100$. Hence, convergence with Algorithm in (7) and (8) can not be guaranteed as stated by Corollary 7.1.5. Figure 7.6 shows that the shadow price $p(n)$ fluctuates between a concave and convex curvature of the $\frac{\partial \log U_i(\gamma_i(P_i))}{\partial P_i}$ curve. The fluctuation in the shadow price $p(n)$ causes fluctuation in the allocated powers and hinders the convergence to the optimal powers. Therefore, the optimal power allocation is not achievable by Algorithm in (7) and (8).

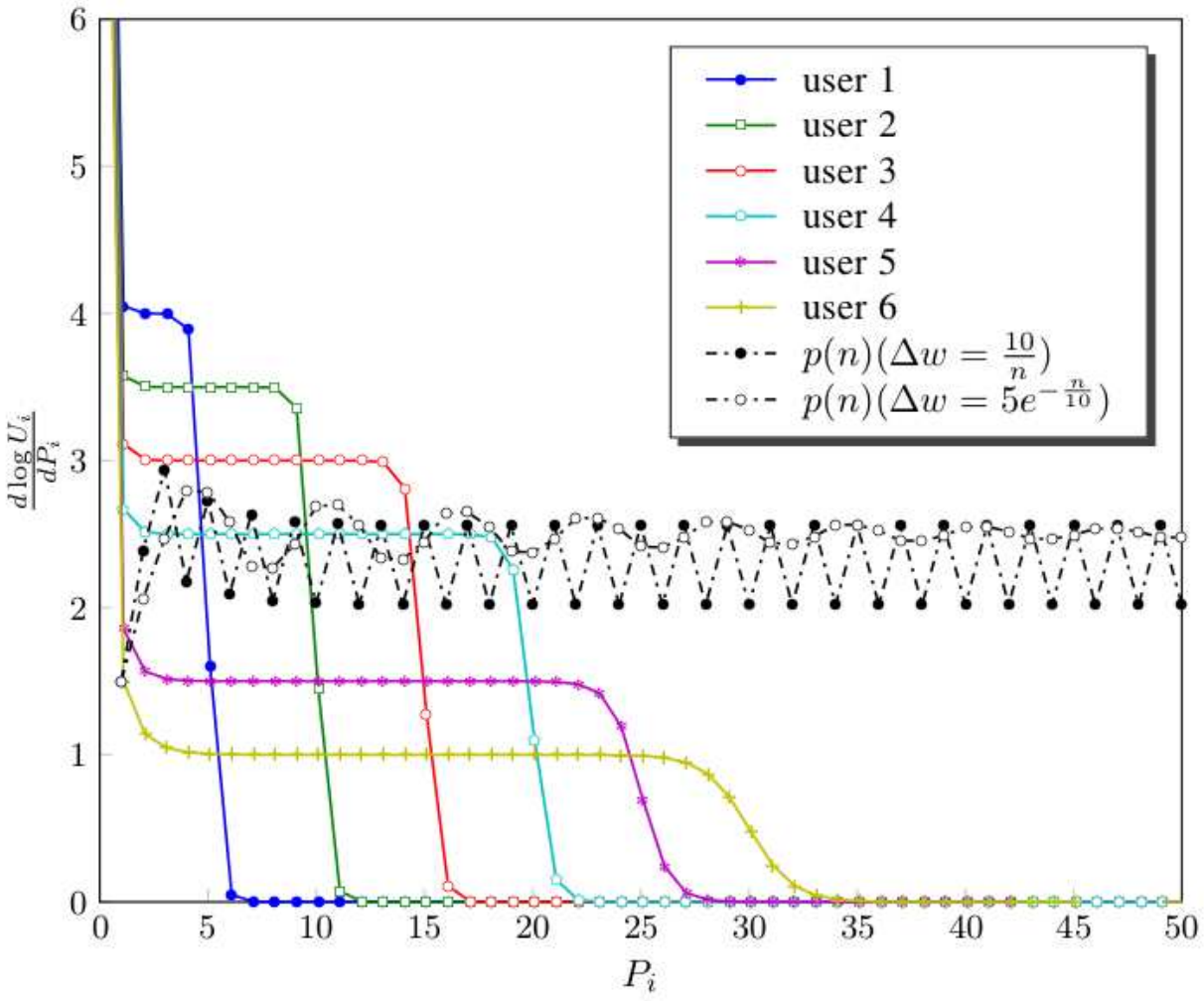

Figure 7.6: Fluctuation curve: The $\frac{\partial \log U_i(\gamma_i(P_i))}{\partial P_i}$ curve of fluctuation example in Section 7.1.6 and the shadow price $p(n)$ from Algorithm in (7) and (8) for $P_T = 100$ (i.e. $\sum P_i^{\text{inf}} > P_T$). When BS has scarce power, Algorithm in (7) and (8) don't guarantee convergence for shadow price and thus optimal power allocation is not possible with these algorithms.

7.1.7 Robust Distributed Algorithm

This section presents a modified version of distributed algorithm in Section 7.1.5 to avoid the drawback discussed in section 7.1.6. The modified algorithm is robust and it guarantees convergence for all values of the BS maximum power P_T. The algorithm allocates powers that coincide with the Algorithm in (7) and (8) for $\sum P_i^{\text{inf}} \ll P_T$. For $\sum P_i^{\text{inf}} > P_T$, the algorithm

avoids fluctuations in the non-convergent region, as discussed in the previous section. This is achieved by adding a convergence measure $\Delta w(n)$ that senses the fluctuation in the bids w_i. In the case of fluctuation, the algorithm decreases the step size between the current and the previous bid $w_i(n) - w_i(n-1)$ for every user i using *fluctuation decay function*. The fluctuation decay function could be in the following forms:

- *Exponential function*: It takes the form $\Delta w(n) = l_1 e^{-\frac{n}{l_2}}$.
- *Rational function*: It takes the form $\Delta w(n) = \frac{l_3}{n}$.

where l_1, l_2, l_3 can be adjusted to change the power of decay of the bids w_i. The new algorithm with the fluctuation decay function is in Algorithm (9) and (8).

Remark 7.1.7. *The fluctuation decay function can be included in Algorithm (7) of the UE or Algorithm (8) of the BS.*

The model considered adds the decay part in Algorithm (7) of the UE. Thus, the modified UE algorithm with the decay part becomes Algorithm (9).

Algorithm 9 Power Allocation: UE Algorithm with Fluctuation Decay

```
Send initial bid w_i(1) to BS
loop
  Receive shadow price p(n) from BS
  if STOP from BS then
    Calculate allocated power P_i^opt = w_i(n)/p(n)
  else
    Calculate new bid w_i(n) = p(n)P_i(n)
    if |w_i(n) − w_i(n−1)| > Δw(n) then
      w_i(n) = w_i(n−1) + sign(w_i(n) − w_i(n−1))Δw(n) {Δw = l_1 e^{−n/l_2} or Δw = l_3/n}
    end if
    Send new bid w_i(n) to BS
  end if
end loop
```

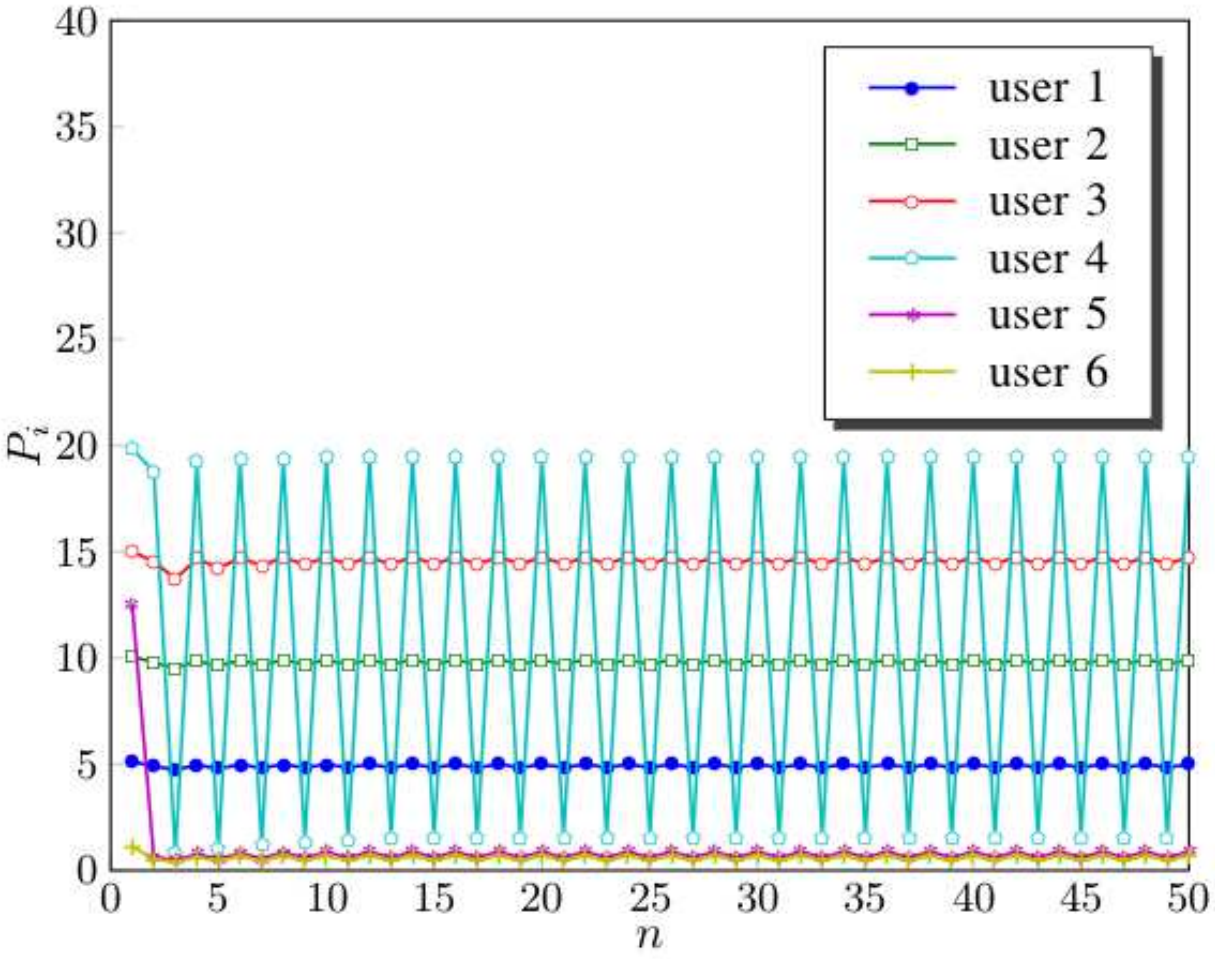

Figure 7.7: Convergence of powers $P_i(n)$ of Algorithm in (7) and (8). The convergence of powers $P_i(n)$ of Algorithm in (7) and (8) with number of iterations n for different users and $P_T = 45$. It can be observed that powers don't converge and fluctuate around optimal powers. Thus the power allocation algorithm is not optimal even though the power allocation optimization problem has optimal solution.

7.1.8 Numerical Examples

This section presents the simulation results of six utility functions corresponding to six UEs, as shown in Figure 7.3. Algorithm in (9) and (8) was applied to sigmoidal-like utility functions with different parameters using MATLAB. The simulation results showed convergence to the optimal global powers for all values of the BS power P_T.

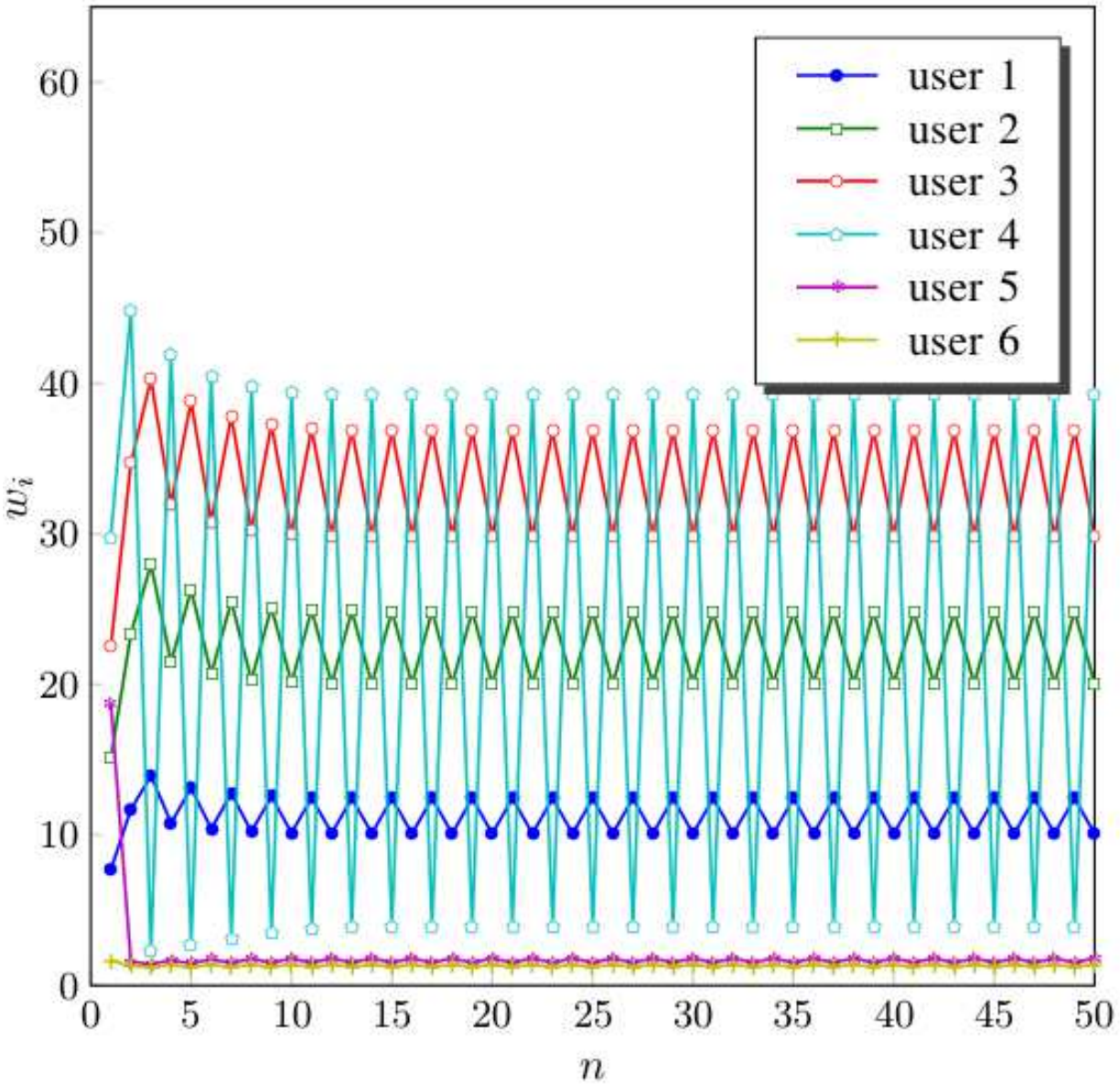

Figure 7.8: Convergence of bids $w_i(n)$ of Algorithm in (7) and (8). The convergence of bids $w_i(n)$ of Algorithm in (7) and (8) with number of iterations n for different users and $P_T = 45$. For these algorithms the process of bidding doesn't converge for all users and bids fluctuate around optimal bid values.

7.1.8.1 Convergence Dynamics for $P_T = 45$

In the following simulations, P_T is set to 45 and the number of iterations is set to $n = 40$.

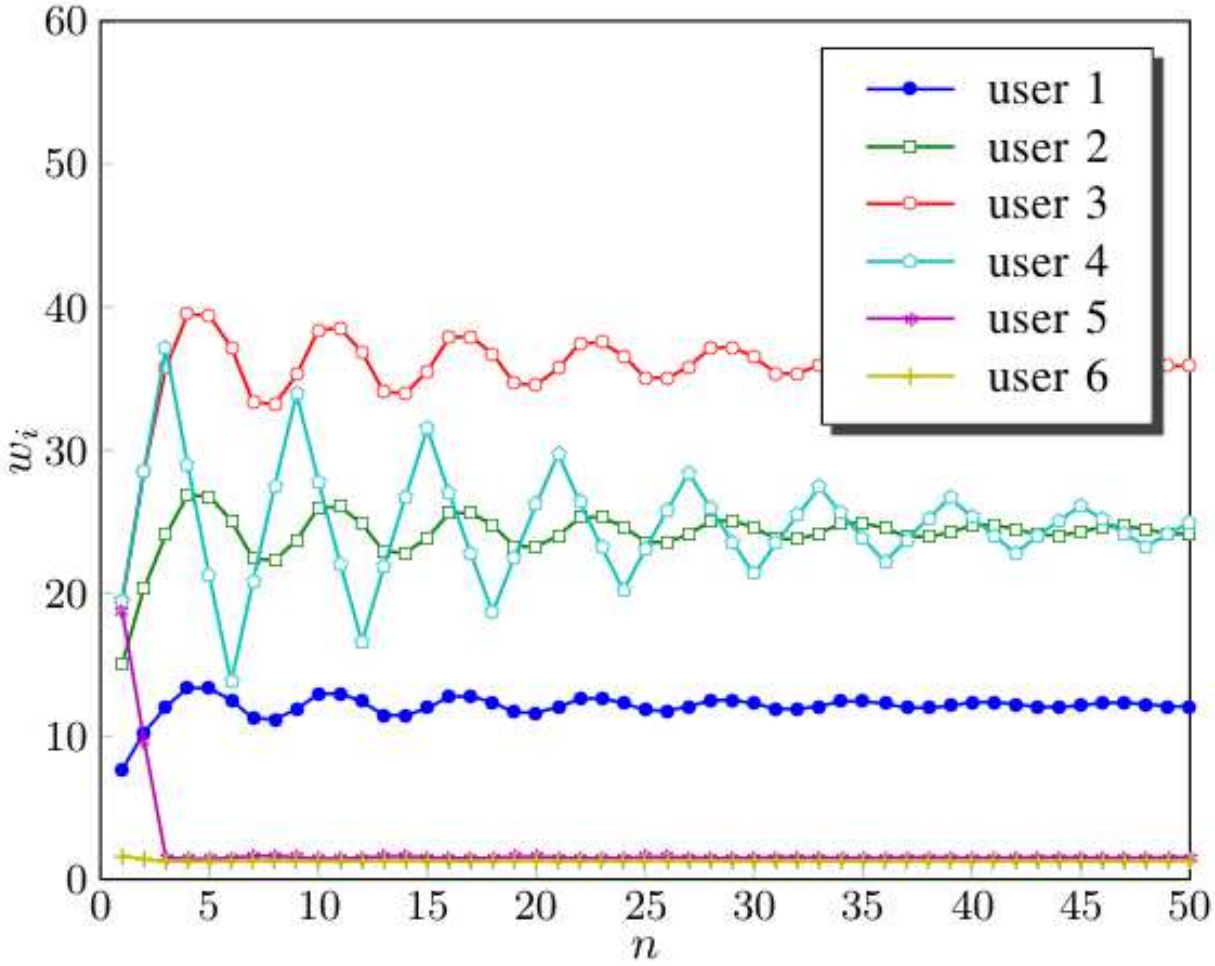

Figure 7.9: Convergence of power $P_i(n)$ with the number of iterations n. The convergence of powers $P_i(n)$ of Algorithm in (9) and (8) with number of iterations n for different users and $P_T = 45$. It can be observed that there is no fluctuation in powers when using Algorithm (9) and (8). This is due to the introduction of fluctuation decay function in our algorithm which damps the fluctuations and the powers converge for all users.

Algorithm (7) and (8): Non-convergent Powers and Bids Here, the total BS power P_T is chosen to be less than the sum of users' inflection points $\sum b_i$. Therefore, Algorithm in (7) and (8) does not converge in this region. Figure 7.7 shows the powers $P_i(n)$ of different users with the number of iterations n for Algorithm in (7) and (8). It is shown that the powers fluctuate around the optimal powers and so the optimal powers are not achieved and

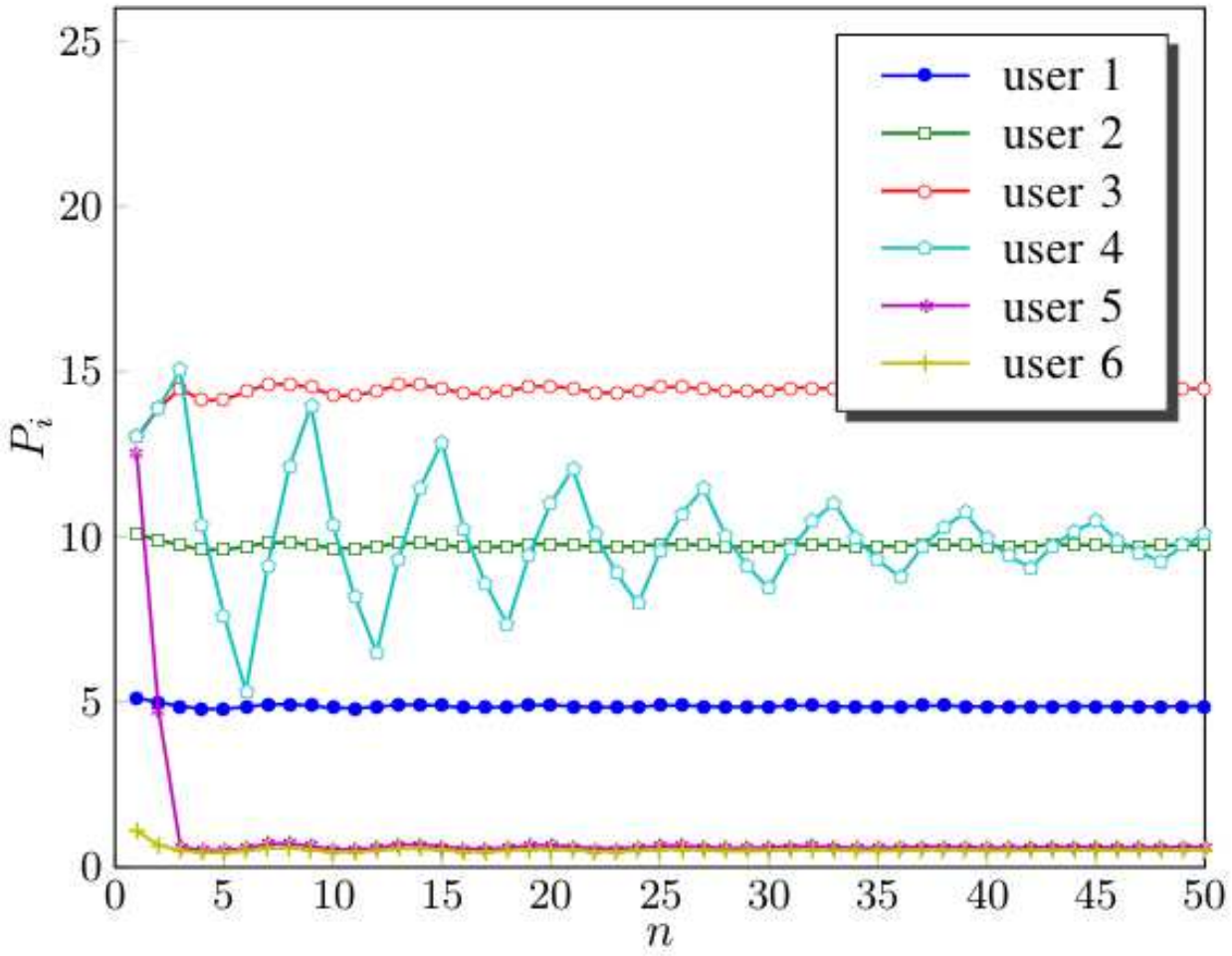

Figure 7.10: Convergence of bids $w_i(n)$ with the number of iterations n: The convergence of bids $w_i(n)$ of Algorithm in (9) and (8) with number of iterations n for different users and $P_T = 45$. It can be observed that there is no fluctuation in bids $w_i(n)$ when using Algorithm (9) and (8). This is due to the introduction of fluctuation decay function in our algorithm which damps the fluctuations and the bidding process converges for all users.

the exit condition is not satisfied (i.e., endless iterations). Similar behavior for bids $w_i(n)$ with the number of iterations n is shown in Figure 7.8.

Algorithm (9) and (8): Convergent Powers and Bids The behavior is more robust in Algorithm (9) and (8) due to the fluctuation decay function. It damps the fluctuation with every iteration so the network reaches the optimal powers of the optimization problem

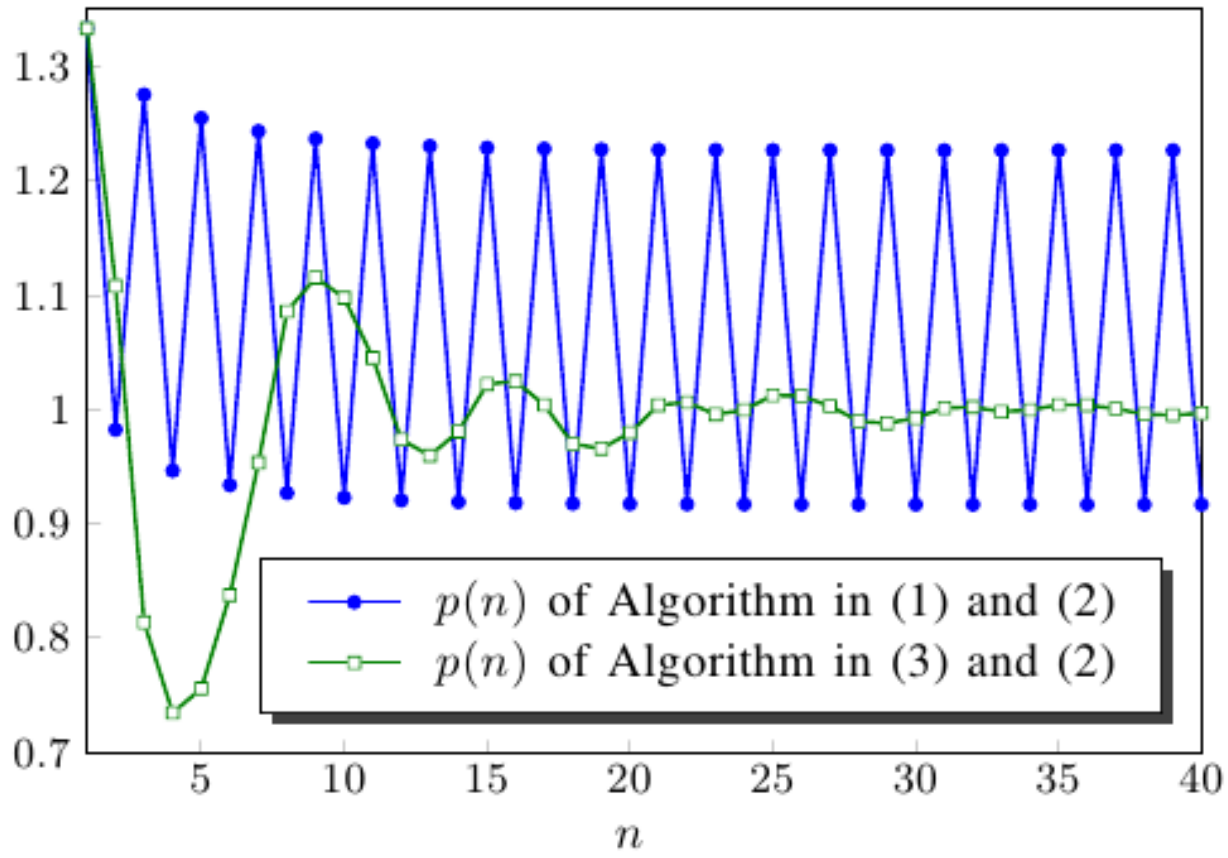

Figure 7.11: Convergence of shadow price $p(n)$ with the number of iterations n. There is fluctuation in the shadow price $p(n)$ when using Algorithm (7) and (8). However, there is no fluctuation in the shadow price $p(n)$ when using Algorithm (9) and (8). This is due to the introduction of fluctuation decay function in our algorithm which damps the fluctuations and the optimal price converges.

(7.11). The powers $P_i(n)$ and bids $w_i(n)$ of Algorithm in (9) and (8) are shown in Figures 7.9 and 7.10, respectively.

Optimal Shadow Price $p(n)$**:** Figure 7.11 shows the new shadow price $p(n)$ of the fluctuation example in Section 7.1.6 when using Algorithm in (9) and (8). The shadow price $p(n)$ fluctuation decreases with every iteration n and converges to the optimal shadow price that corresponds to the optimal powers. On the contrary, when using Algorithm in (7) and (8), the shadow price fluctuates and doesn't reach optimal value.

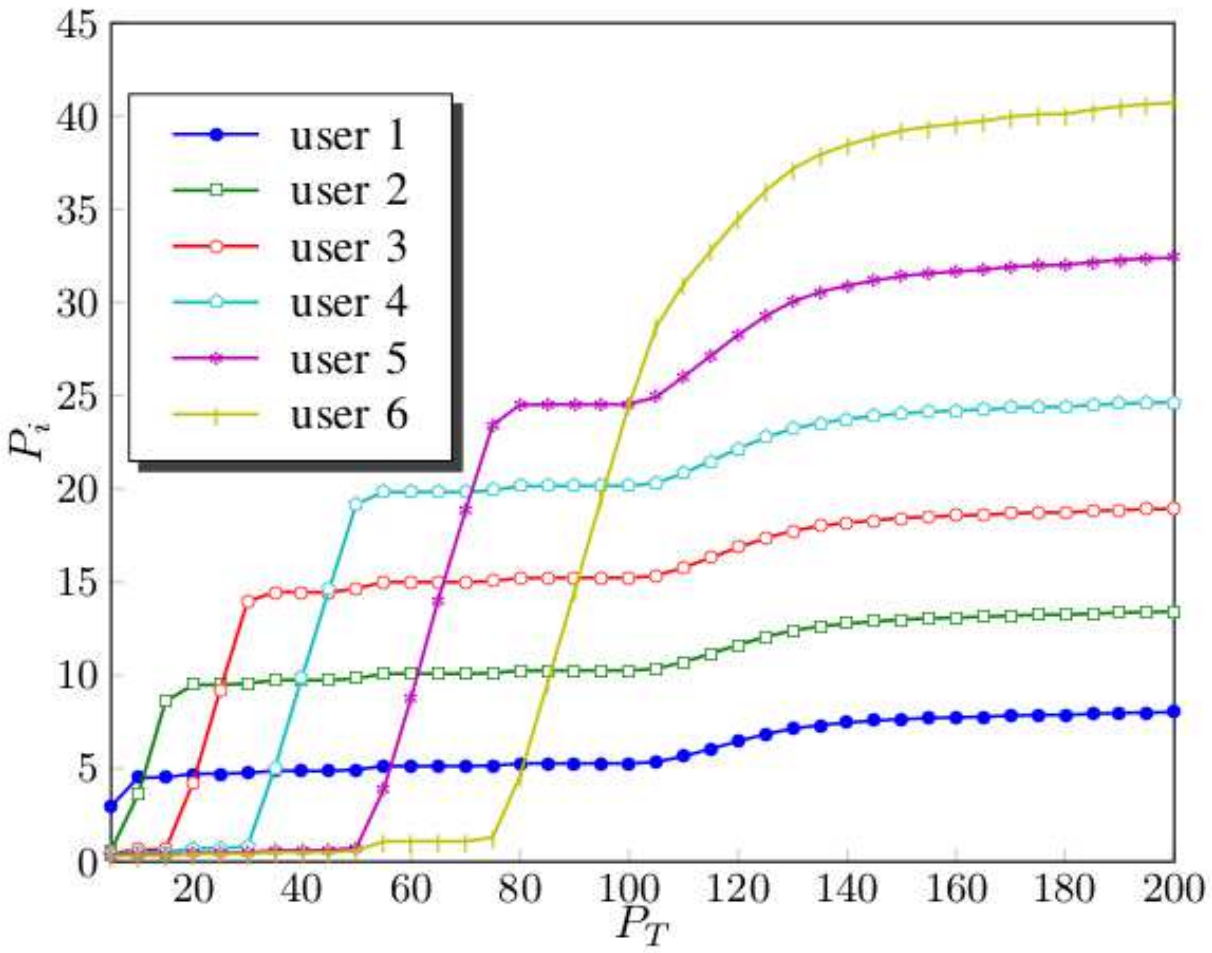

Figure 7.12: Allocated powers P_i for different values of P_T, $n_0 = 20$ and $\delta = 10^{-3}$ for Algorithm in (9) and (8). Our algorithm gives priority to users running lower modulation schemes and thus first allocates powers to them until they reach their inflection point. Users running higher modulation schemes are followed by this. However, our algorithm ensures non-zero allocation of powers to all users thus maintaining a minimum QoS of all users.

7.1.8.2 Power Allocation and Pricing for $5 \leq P_T \leq 100$

In the following simulations, δ is set to 10^{-3} and the total power of the BS P_T takes values between 5 and 100 with a step of 5.

Optimal Power Allocation: Figure 7.12 shows the final powers of different users with different BS power P_T. The distributed algorithm is set to avoid the situation of allocating

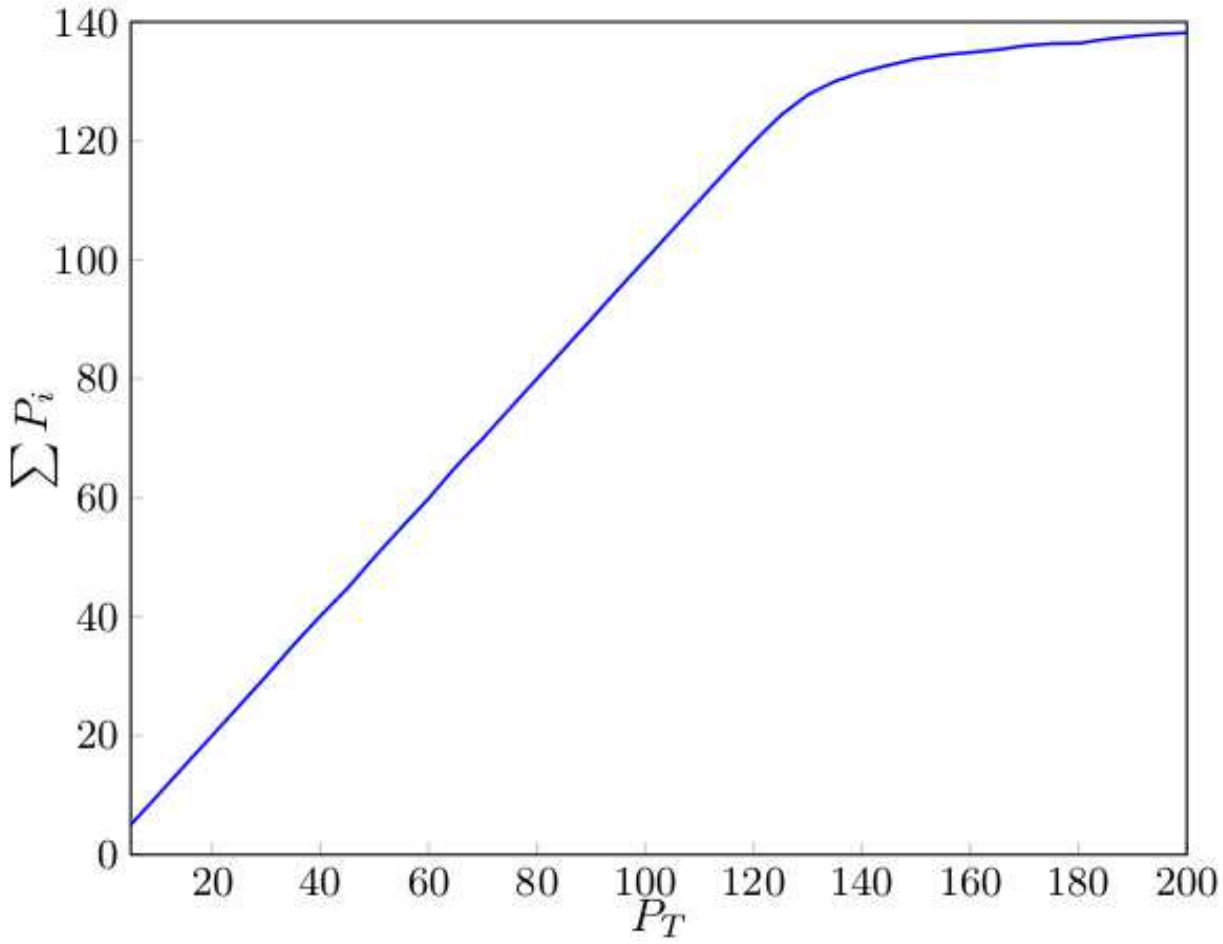

Figure 7.13: Sum of power $\sum P_i$ for different values of P_T and $\delta = 10^{-3}$ for Algorithm in (9) and (8). It can be seen that when the total power P_T exceeds the sum of the inflection power $\sum P_i = \sum b_i$ of all the users, all the users are assigned power according to their desired modulation scheme's requirement. Thus satisfying users' demands and the power allocation algorithm reaches a steady state.

zero power to any user (i.e. no user is dropped). However, the BS allocates the majority of the powers to the UEs running low modulation schemes until they reach the inflection power $P_i = b_i$. When the total power P_T exceeds the sum of the inflection powers $\sum b_i$ of all the users with lower modulation schemes, BS allocates more powers to the UEs with higher modulation schemes, as shown in Figure 7.12, when BS power exceeds $P_T = 65$. This behavior is similar to that in Figure 7 but with including BS power $P_T < 60$ where the

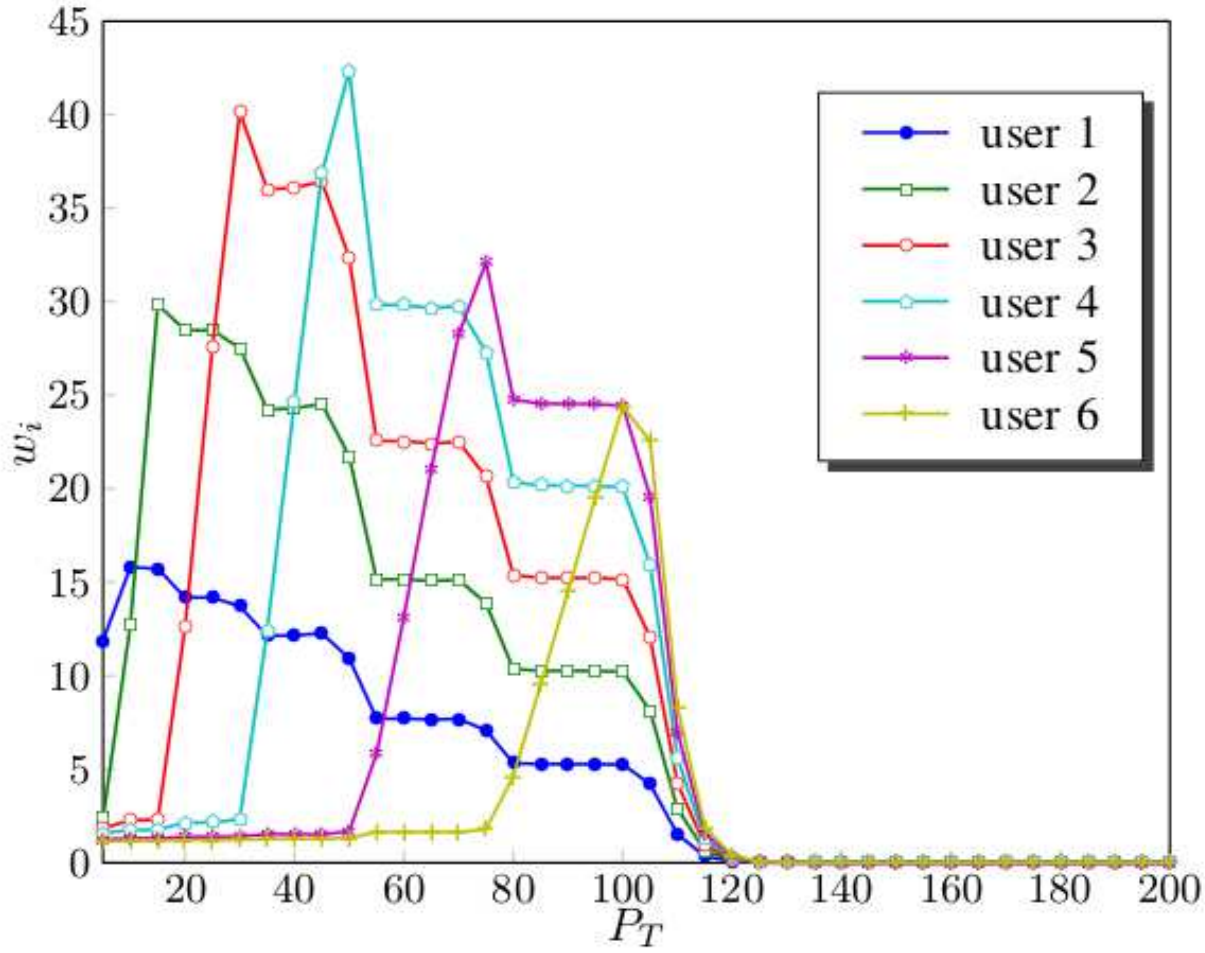

Figure 7.14: Final bids w_i for different values of P_T and $\delta = 10^{-3}$ for Algorithm in (9) and (8). It can be seen that as the users bid higher they are allocated higher power. Since our algorithm gives priority to lower modulation schemes we start by allocating powers to users with lower modulation schemes. The users with lower modulation schemes bid higher when the resources are scarce and their bids decrease as P_T increases. Therefore, the pricing which is proportional to the bids is traffic-dependent.

power is scarce with respect to the users' modulation schemes. Figure 7.13 shows the sum of powers $\sum P_i$ for different BS power P_T values. When the total power P_T exceeds the sum of the inflection power $\sum P_i = \sum b_i$ of all the users, the users demands are met and the power allocation reaches a steady state. This is similar in behavior to individual users, Figure 7.12, where after the inflection point the power allocation is steady. However, Figure 7.13 gives

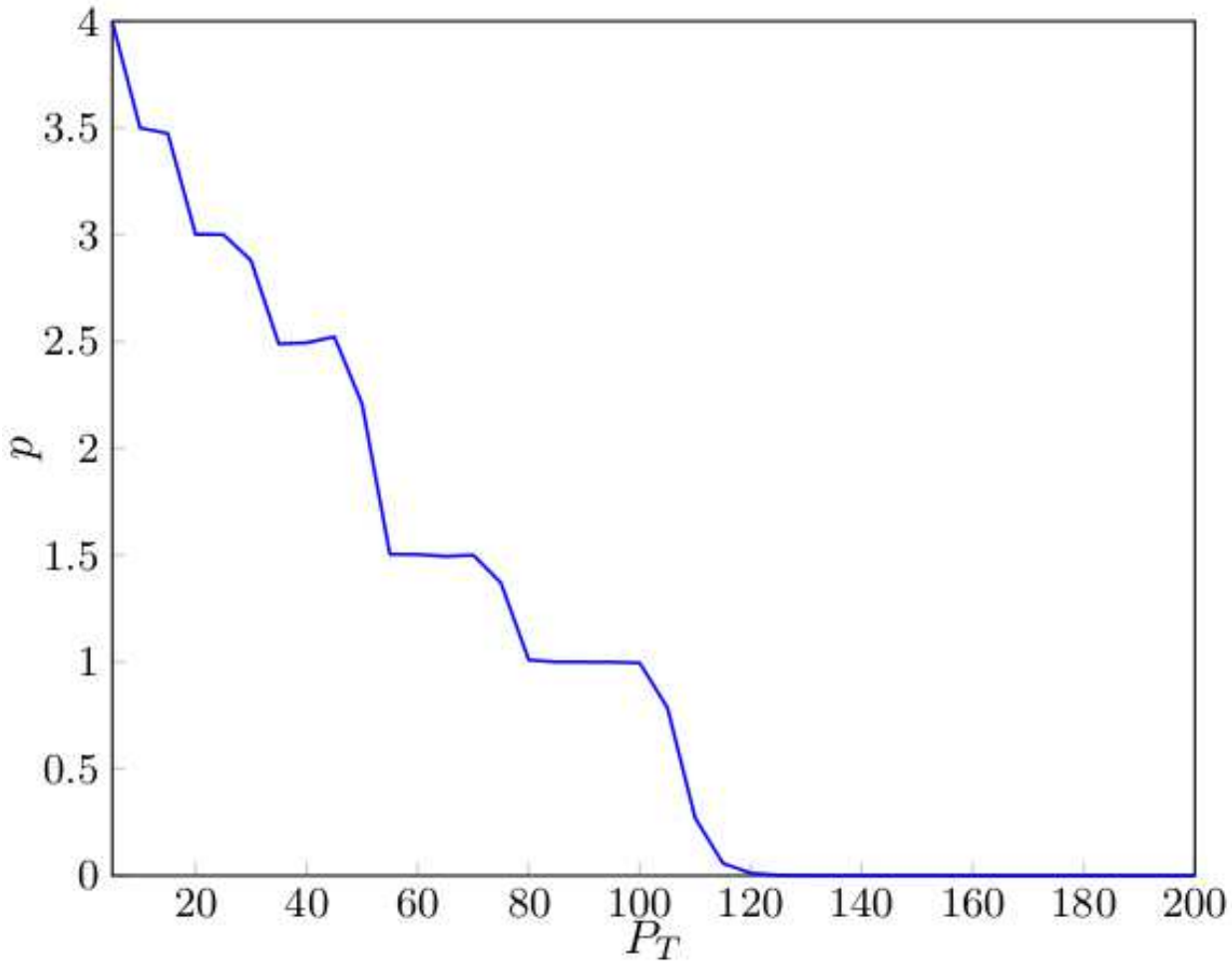

Figure 7.15: Final shadow price p for different values of P_T and $\delta = 10^{-3}$ for Algorithm in (9) and (8). It can be seen that for high-traffic periods or when the power is scarce the network providers charge higher price for the same amount of per unit power. This traffic-dependent pricing regimen provides incentive to users to use network during off-peak hours as they'll pay less for the same amount of per unit power.

an overall relation between total power available and demands of users in the network.

Traffic-dependent Bidding/Pricing: Figure 7.14 shows the final bids of different users with different BS total power P_T. The higher the user bids the higher the allocated power. The users with lower modulation schemes bid higher when the resources are scarce and their bids decrease as P_T increases. Therefore, the pricing which is proportional to the bids is

traffic-dependent. This gives service providers an option to increase the service price for subscribers when the traffic load on the system is high. Therefore, service providers can motivate subscribers to use the network when the traffic load on the network is low, as they pay less for the same service. The shadow price $p(n)$ represents the total price per unit power for all users. Figure 7.15 shows the shadow price $p(n)$ with BS power P_T. The price is high for high-traffic (i.e. fixed number of users but less resources, P_T is small) which decreases for low-traffic (i.e. same number of users but more resources, P_T is large). A large decrease in the price is apparent after $P = \{10, 30, 60\}$ which are the points where one of the users utility exceed the inflection point. This large decrease occurs at the sum of inflection points $\sum_{i=1}^{k} P_i^{\text{inf}}$, where $k = \{1, 2, ..., M\}$ is the users index and M is the number of users.

7.2 Conclusion

In this chapter, resource and power allocation at communication system was proposed in order to share radar spectrum. In the previous chapters, radar systems were optimized for spectrum sharing but in this chapter an alternate approach for spectrum sharing was proposed.

First, the problem of spectrum sharing was addressed from a rate allocation perspective. An optimal rate allocation with carrier aggregation approach was proposed to allocate LTE-Advanced and MIMO radar carriers' rates optimally among LTE Advanced users in a cell. The two systems shared spectrum such that the MIMO radar did not interfere with the LTE-Advanced system through a spatial approach proposed in [65]. Two utility functions were considered based on the application type running on the UE. Sigmoidal-like utility functions represented real time applications and logarithmic utility functions represented delay tolerant applications. The RA with carrier aggregation problem was divided into two optimization

problems, one for the LTE-Advanced carrier and the other for the radar carrier. The solution to this was characterized by utility proportional fairness. An iterative distributed RA with carrier aggregation algorithm was proposed for the UEs and both LTE Advanced and radar carriers. The algorithm provided a utility proportional fair rate allocation which guaranteed a minimum QoS to each user while giving priority to users running real-time applications. It was shown through simulations that the proposed algorithm converged to the optimal rates in its two stages. In addition, it was showed that the spectrum sharing approach between LTE Advanced and radar carriers provided a significant gain in the LTE Advanced total available rates.

Second, the problem of optimal allocation of BS powers was addressed for users running different modulation schemes by taking into account the price paid per unit power by each user and the total power available at the BS. Sigmoidal-like utility functions were used to represent different users' modulation schemes due to the resemblance in shape of sigmoidal-like utility functions and the probability of packet transmission success of modulation schemes. It was shown that the network utility maximization problem is convex and thus has optimal solution. The proposed distributed power allocation algorithm ensured fairness in the allocation of powers as it gave priority to users running lower modulation schemes while ensuring non-zero power allocation to users running higher modulation schemes. Moreover, the power allocation algorithm was convergent, for all network traffic conditions, and there was no oscillation in the power allocation process due to the introduction of fluctuation damping parameter in our algorithm. It was also illustrated that the proposed algorithm provided a pricing approach for network providers that could be used to reduce the demand in power i.e. flatten traffic loads during peak traffic hours. It was shown that the price per unit power, the power allocation algorithm charged from users depended upon the modulation scheme used and the total power available at the BS. This provided an opportunity for network providers

to flatten load on their network by motivating users to use the network at off-peak hours as they paid more for the same amount of per unit power in peak hours than in off-peak hours.

Chapter 8

Conclusions and Future Research

Spectrum sharing between radar and communication systems is an important cross-disciplinary research area of federal and commercial interest. The methods proposed for spectrum sharing in this research allow radar and communication systems to operate in a geographical area without the need for exclusion zones, required to protect both systems from each other's interference, and promise highly sought-after capacity gains for communication systems. This chapter provides some conclusions that were deduced through the course of this research and also points out some future research directions.

8.1 Conclusions

Spectrum sharing between radars and communication systems is an emerging area of research. The goal of this thesis was to investigate spectrum sharing approaches between radar and communication systems. During the course of this research spectrum sharing algorithms were designed that ensured spectral, temporal, and spatial coexistence of radar and

communication systems without creating harmful interference and meeting objectives of the respective systems. In order to efficiently share spectrum between radars and communication systems at the same time and in the same geographical area, a novel method was proposed that transformed radar signal in such a way that it did not interfere with communication systems. This was accomplished by projecting the radar signal onto null space of the wireless channel between radar and communication system. Basically, nulls were formed in radar beampattern in the direction of communication systems. Previous approaches either allowed spectrum sharing in time or space but not both. In order to understand the effects of the proposed sharing mechanism - in urban, sub-urban, and littoral areas - new channel models were designed keeping in view the different antenna geometries of radar and communication systems. In this regard two- and three-dimensional channel models were designed that captured azimuth and elevation angles of communication systems and helped in placing accurate nulls. In addition, interference coming from communication systems into radar receivers was analyzed and radar performance was accessed. Using this information, resource allocation schemes were designed for communication systems that took advantage of the carrier aggregation feature of the LTE-Advanced systems. This further helped in dynamic sharing of spectrum between radars and communication systems. The proposed signal shaping/design approach not only met radar objectives but also met spectrum sharing objectives. However, there was a tradeoff as signal shaping or designing new radar signal, with spectrum sharing constraint, resulted in some performance degradation for radars. Therefore, it was of interest to study the impact of projection on radar performance. Performance metrics such as probability of target detection, Cramér Rao bound and maximum likelihood estimate of target's angle of arrival, and beampattern of radar were studied for performance degradation. The results showed minimal degradation in radar performance and reduction in exclusion zones, thus, showing the efficacy of the proposed approach. At the same time, resource allocation

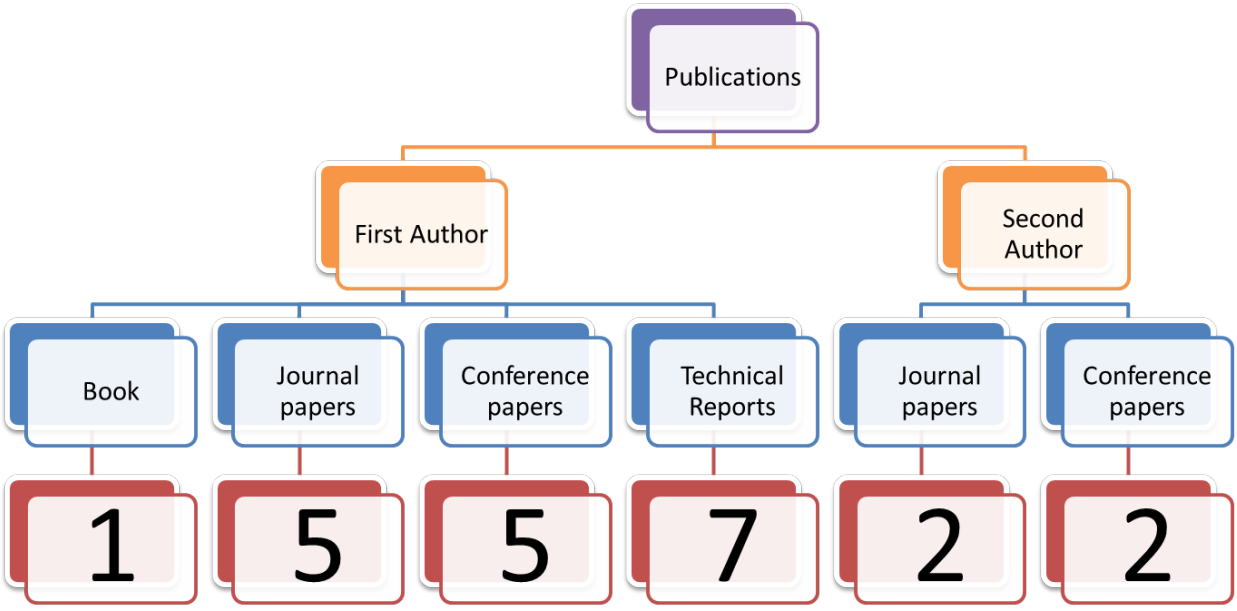

Figure 8.1: Publication chart: A breakdown of contributions made in terms of publications of this research.

schemes benefited from extra spectrum provided by radars, thus, resulting in capacity gains for communication systems. The research conducted for this thesis resulted in a number of publication including a book, seven journal articles, seven conference papers, and seven technical reports. A breakdown of publications is shown in Figure 8.1 and a list of publications is provided in Appendix A.

8.2 Future Research Directions

In order to realize spectrum sharing between radars and communications systems, contributions were made at both ends, i.e, waveform shaping, waveform design, and interference modeling were explored for radar systems and resource allocation algorithms were explored

for communication systems. In addition new channel models were designed. All of these areas can be further extended and refined for the purpose of spectrum sharing. An outline of future research direction is as follows:

- **Waveform Shaping:** A projection based waveform shaping algorithm was proposed to project radar waveform onto null space of interference channel to mitigate interference to single- and multi-cell communication systems. This can be further extended to different cellular architectures, for example heterogeneous networks. In addition new waveform shaping algorithms and performance metrics can be considered.

- **Waveform Design:** Finite alphabet BPSK and QPSK waveforms were designed with spectrum sharing constraints. Due to the spectrum sharing constraint the designed waveforms were no longer constant envelope. A further extension of this work would be looking into algorithms that design finite alphabet constant-envelope spectrum sharing radar waveforms.

- **Interference Modeling:** Aggregate interference originating from cellular base stations was modeled as a log-normal distribution at radar receiver. A limitation of this approach was the assumption of high power cellular base stations with deterministic locations. A further extension of this work would be interference considerations from randomly deployed small cells and its impact on radar's target detection performance.

- **Channel Modeling:** Two- and three-dimension channels were modeled between radar and communication systems. A limitation of this work was that line-of-sight and deterministic cases were considered. A further extension of this work would be stochastic two- and three-dimensional channel models.

- **Resource Allocation:** Resource allocation algorithms for cellular systems were designed which exploited the carrier aggregation feature of LTE-Advanced systems to

increase system capacity and avoid radar interference. A further extension of this work would be optimal resource allocation for spectrum sharing with interference and energy efficiency constraints.

Appendices

Appendix A

List of Publications

A.1 Book

Awais Khawar, Ahmed Abdelhadi, T. Charles Clancy, "*MIMO Radar Waveform Design for Spectrum Sharing with Cellular Systems: A MATLAB Based Approach*", Springer (in press).

A.2 Journal Articles

7. **A. Khawar**, A. Abdelhadi, T. Clancy, "*3D Channel Modeling between Seaborne Radar and Cellular System*", under submission.

6. **A. Khawar**, A. Abdelhadi, T. Clancy, "*Performance Analysis of Coexisting Radar and Cellular System in LoS Channel*", under submission.

5. **A. Khawar**, A. Abdelhadi, T. Clancy, "*Channel Modeling between MIMO Seaborne Radar and MIMO Cellular System*", under submission.

4. J. Mahal, **A. Khawar**, A. Abdelhadi, T. Clancy, "*Radar Precoder Design for Spectral Coexistence with Coordinated Multi-point (CoMP) System*", under submission.

3. **A. Khawar**, A. Abdelhadi, T. Clancy, "*Target detection performance of spectrum sharing MIMO radars*", to appear in IEEE Sensors Journal.

2. **A. Khawar**, A. Abdelhadi, T. Clancy, "*QPSK waveform for MIMO radar with spectrum sharing constraints*", to appear in ELSEVIER Physical Communication.

1. A. Abdelhadi, **A. Khawar**, T. Clancy, "*Optimal Downlink Power Allocation in Cellular Networks*", to appear in ELSEVIER Physical Communication.

A.3 Conference Proceedings

7. **A. Khawar**, A. Abdelhadi, T. Clancy, "*On the Impact of a Time-Varying Interference-Channel on the Spatial Approach of Spectrum Sharing between S-band radar and Communication System*", IEEE Military Communications Conference, (Baltimore, USA), Oct. 2014.

6. Haya Shajaiah, **A. Khawar**, A. Abdel-Hadi, T. Clancy, "*Resource Allocation with Carrier Aggregation in LTE Advanced Cellular System sharing Spectrum with S-band Radar*", IEEE International Symposium on Dynamic Spectrum Access Networks: SSPARC Workshop (IEEE DySPAN 2014 - SSPARC Workshop), (McLean, USA), Apr. 2014.

5. **A. Khawar**, A. Abdel-Hadi, T. Clancy, "*MIMO Radar Waveform Design for Coexistence With Cellular Systems*", IEEE International Symposium on Dynamic Spectrum

Access Networks: SSPARC Workshop (IEEE DySPAN 2014 - SSPARC Workshop), (McLean, USA), Apr. 2014.

4. **A. Khawar**, A. Abdel-Hadi, T. Clancy, "*Spectrum Sharing between S-band Military Radar and LTE Cellular System: A Spatial Approach*", IEEE International Symposium on Dynamic Spectrum Access Networks: SSPARC Workshop (IEEE DySPAN 2014 - SSPARC Workshop), (McLean, USA), Apr. 2014.

3. **A. Khawar**, A. Abdel-Hadi, T. Clancy, "*A Mathematical Analysis of LTE Interference on the Performance of S-band Military Radar System*", 13th Annual Wireless Telecommunications Symposium (WTS), (Washington, DC, USA), Apr. 2014.

2. **A. Khawar**, A. Abdel-Hadi, T. Clancy, "*Beampattern Analysis for MIMO Radar and Communication System Coexistence*", IEEE International Conference on Computing, Networking and Communications, 2014.

1. S. Sodagari, **A. Khawar**, T. Clancy, R. McGwier, "*A Projection Based Approach for Radar and Telecommunication Systems Coexistence*", IEEE Global Communications Conference (Globecom), 2012.

A.4 Technical Reports

7. **A. Khawar**, A. Abdel-Hadi, T. Clancy, "*Shared Spectrum Access for Radar and Communications*", Virginia Tech Hume Center Technical Report HC-R140013, September 2014

6. **A. Khawar**, A. Abdel-Hadi, T. Clancy, "*On the Coherence Time of Wireless Channel under Various Operating Conditions at Sea*", Virginia Tech Hume Center Technical

Report HC-R140009, September 2014

5. **A. Khawar**, A. Abdel-Hadi, T. Clancy, "*Performance of Spectrum Sharing MIMO Radars in LoS Channel Models*", Virginia Tech Hume Center Technical Report HC-R140012, August 2014

4. **A. Khawar**, A. Abdel-Hadi, T. Clancy, "*3D Channel Modeling between Radar and Communication Systems for Spectrum Sharing*", Virginia Tech Hume Center Technical Report HC-R140011, August 2014

3. **A. Khawar**, A. Abdel-Hadi, T. Clancy, "*Limits on Search/Track/Detect Volume Illuminated by Spectrum Sharing MIMO Radars*", Virginia Tech Hume Center Technical Report HC-R140010, August 2014

2. **A. Khawar**, J. Mahal, A. Abdel-Hadi, T. Clancy, "*A Realistic Channel Model for Radar/Cellular Coexistence in the 3.5 GHz band*", Virginia Tech Hume Center Technical Report HC-R140007, July 2014

1. **A. Khawar**, A. Abdel-Hadi, T. Clancy, "*Spectral Coexistence Using MIMO Radar Platforms*", Virginia Tech Hume Center Technical Report HC-R140002, Apr. 2014

References

[1] Federal Communications Commission (FCC), "Connecting America: The national broadband plan." Online, 2010.

[2] The Presidents Council of Advisors on Science and Technology (PCAST), "Realizing the full potential of government-held spectrum to spur economic growth," July 2012.

[3] Federal Communications Commission (FCC), "FCC proposes innovative small cell use in 3.5 GHz band." Online: http://www.fcc.gov/document/fcc-proposes-innovative-small-cell-use-35-ghz-band, December 12, 2012.

[4] National Telecommunications and Information Administration (NTIA), "An assessment of the near-term viability of accommodating wireless broadband systems in the 1675-1710 MHz, 1755-1780 MHz, 3500-3650 MHz, 4200-4220 MHz, and 4380-4400 MHz bands (Fast Track Report)." `http://www.ntia.doc.gov/files/ntia/publications/fasttrackevaluation_11152010.pdf`, October 2010.

[5] National Telecommunications and Information Administration (NTIA), "Analysis and resolution of RF interference to radars operating in the band 27002900 MHz from broadband communication transmitters." Online, October 2012.

[6] Presidential Memorandum, "Unleashing the wireless broadband revolution," 2010.

[7] Federal Communications Commission (FCC), "In the matter of revision of parts 2 and 15 of the commissions rules to permit unlicensed national information infrastructure (U-NII) devices in the 5 GHz band." MO&O, ET Docket No. 03-122, June 2006.

[8] A. Lackpour, M. Luddy, and J. Winters, "Overview of interference mitigation techniques between WiMAX networks and ground based radar," in *Proc. 20th Annual Wireless and Optical Comms. Conf.*, 2011.

[9] R. Saruthirathanaworakun, J. Peha, and L. Correia, "Performance of data services in cellular networks sharing spectrum with a single rotating radar," in *IEEE International Symposium on a World of Wireless, Mobile and Multimedia Networks (WoWMoM)*, pp. 1–6, 2012.

[10] H. Deng and B. Himed, "Interference mitigation processing for spectrum-sharing between radar and wireless communications systems," *IEEE Transactions on Aerospace and Electronic Systems*, vol. 49, no. 3, pp. 1911–1919, 2013.

[11] S. Sodagari, A. Khawar, T. C. Clancy, and R. McGwier, "A projection based approach for radar and telecommunication systems coexistence," in *IEEE Global Communications Conference (GLOBECOM)*, 2012.

[12] A. Khawar, A. Abdel-Hadi, and T. C. Clancy, "MIMO radar waveform design for coexistence with cellular systems," in *2014 IEEE International Symposium on Dynamic Spectrum Access Networks: SSPARC Workshop (IEEE DySPAN 2014 - SSPARC Workshop)*, (McLean, USA), Apr. 2014.

[13] J. Li and P. Stoica, *MIMO Radar Signal Processing*. Wiley-IEEE Press, 2008.

[14] J. Tan and G. Stuber, "Constant envelope multi-carrier modulation," in *MILCOM 2002. Proceedings*, vol. 1, pp. 607–611 vol.1, Oct 2002.

[15] S. Thompson, A. Ahmed, J. Proakis, J. Zeidler, and M. Geile, "Constant envelope OFDM," *IEEE Transactions on Communications*, vol. 56, pp. 1300–1312, August 2008.

[16] P. Stoica, J. Li, and X. Zhu, "Waveform synthesis for diversity-based transmit beampattern design," *IEEE Transactions on Signal Processing*, vol. 56, pp. 2593–2598, June 2008.

[17] S. Ahmed, J. S. Thompson, Y. R. Petillot, and B. Mulgrew, "Finite alphabet constant-envelope waveform design for MIMO radar," *IEEE Transactions on Signal Processing*, vol. 59, no. 11, pp. 5326–5337, 2011.

[18] S. Sodagari and A. Abdel-Hadi, "Constant envelope radar with coexisting capability with LTE communication systems," *under submission.*

[19] D. Fuhrmann and G. San Antonio, "Transmit beamforming for MIMO radar systems using signal cross-correlation," *IEEE Transactions on Aerospace and Electronic Systems*, vol. 44, pp. 171–186, January 2008.

[20] T. Aittomaki and V. Koivunen, "Signal covariance matrix optimization for transmit beamforming in MIMO radars," in *in Proc. of the Forty-First Asilomar Conference on Signals, Systems and Computers (ASILOMAR)*, pp. 182–186, Nov 2007.

[21] P. Gong, Z. Shao, G. Tu, and Q. Chen, "Transmit beampattern design based on convex optimization for {MIMO} radar systems," *Signal Processing*, vol. 94, no. 0, pp. 195 – 201, 2014.

[22] G. Hua and S. Abeysekera, "MIMO radar transmit beampattern design with ripple and transition band control," *IEEE Transactions on Signal Processing*, vol. 61, pp. 2963–2974, June 2013.

[23] L. Fenton, "The sum of log-normal probability distributions in scatter transmission systems," *IRE Transactions on Communications Systems*, vol. 8, no. 1, pp. 57–67, 1960.

[24] S. Schwartz and Y. S. Yeh, "On the distribution function and moments of power sums with log-normal components," *Bell Syst. Tech. Journal*, vol. 61, pp. 1441–1462, 1982.

[25] K. Ruttik, K. Koufos, and R. Jantti, "Model for computing aggregate interference from secondary cellular network in presence of correlated shadow fading," in *IEEE 22nd International Symposium on Personal Indoor and Mobile Radio Communications (PIMRC)*, pp. 433–437, 2011.

[26] K. W. Sung, E. Obregon, and J. Zander, "On the requirements of secondary access to 960-1215 mhz aeronautical spectrum," in *IEEE Symposium on New Frontiers in Dynamic Spectrum Access Networks (DySPAN)*, pp. 371–379, 2011.

[27] A. F. Molisch, *Wireless Communications*. John Wiley & Sons, 2010.

[28] A. Kammoun, H. Khanfir, Z. Altman, M. Debbah, and M. Kamoun, "Preliminary results on 3D channel modeling: From theory to standardization," *IEEE Journal on Selected Areas in Communications*, vol. 32, pp. 1219–1229, June 2014.

[29] G. Yuan, X. Zhang, W. Wang, and Y. Yang, "Carrier aggregation for LTE-advanced mobile communication systems," in *Communications Magazine, IEEE*, vol. 48, pp. 88–93, 2010.

[30] A. Abdel-Hadi and T. C. Clancy, "A utility proportional fairness approach for resource allocation in 4G-LTE," in *IEEE International Conference on Computing, Networking and Communications: Computing, Networking and Communications Symposium (ICNC'14 - CNC)*, 2014.

[31] H. Shajaiah, A. Abdel-Hadi, and T. C. Clancy, "Utility proportional fairness resource allocation with carrier aggregation in 4G-LTE," in *IEEE Military Communications Conference (MILCOM)*, 2013.

[32] F. Kelly, A. Maulloo, and D. Tan, "Rate control in communication networks: shadow prices, proportional fairness and stability," in *Journal of the Operational Research Society*, vol. 49, 1998.

[33] S. Shenker, "Fundamental design issues for the future internet," *Selected Areas in Communications, IEEE Journal on*, vol. 13, no. 7, pp. 1176–1188, 1995.

[34] R. L. Kurrle, "Resource Allocation for Smart Phones in 4G LTE Advanced Carrier Aggregation," Master Thesis, Virginia Tech, Nov. 2012.

[35] J.-W. Lee, R. R. Mazumdar, and N. B. Shroff, "Downlink power allocation for multi-class wireless systems," *IEEE/ACM Trans. Netw.*, vol. 13, pp. 854–867, Aug. 2005.

[36] H. Shajaiah, A. Abdel-Hadi, and T. C. Clancy, "Spectrum sharing between public safety and commercial users in 4G-LTE," in *IEEE International Conference on Computing, Networking and Communications (ICNC)*, 2014.

[37] H. Shajaiah, A. Abdel-Hadi, and C. Clancy, "Multi-Application Resource Allocation with Users Discrimination in Cellular Networks," in *Submitted to DySPAN, 2014*, 2014.

[38] A. Abdel-Hadi and T. C. Clancy, "A robust optimal rate allocation algorithm and pricing policy for hybrid traffic in 4G-LTE," in *IEEE 24th International Symposium on Personal, Indoor and Mobile Radio Communications (PIMRC)*, 2013.

[39] A. Abdel-Hadi, T. C. Clancy, and J. Mitola, "A resource allocation algorithm for multi-application users in 4G-LTE," in *ACM Proceedings of the 19th Annual International Conference on Mobile Computing and Networking (MobiCom)*, 2013.

[40] "LTE release 12 - Taking another step toward the networked society." Online, January 2013. White paper.

[41] "The second phase of LTE-Advanced – LTE-B : 30-fold capacity boosting to LTE." Online. White paper.

[42] F. Kelly, A. Maulloo, and D. Tan, "Rate control in communication networks: shadow prices, proportional fairness and stability," in *Journal of the Operational Research Society*, vol. 49, 1998.

[43] S. H. Low and D. E. Lapsley, "Optimization flow control, i: Basic algorithm and convergence," *IEEE/ACM Transactions on Networking*, vol. 7, no. 6, pp. 861–874, 1999.

[44] P. Marbach and R. Berry, "Downlink resource allocation and pricing for wireless networks," in *Proceedings of IEEE INFOCOM*, vol. 3, pp. 1470–1479 vol.3, 2002.

[45] F. Meshkati, H. V. Poor, S. C. Schwartz, and N. B. Mandayam, "A utility-based approach to power control and receiver design in wireless data networks," *CoRR*, vol. abs/cs/0507011, 2005.

[46] D. Goodman and N. Mandayam, "Power control for wireless data," in *IEEE International Workshop on Mobile Multimedia Communications (MoMuC '99)*, pp. 55–63, 1999.

[47] J.-W. Lee and J.-A. Kwon, "Downlink power allocation for wireless systems through network utility maximization," in *14th Asia-Pacific Conference on Communications (APCC'08)*, pp. 1–5, Oct 2008.

[48] M. Xiao, N. Shroff, and E. K. P. Chong, "A utility-based power-control scheme in wireless cellular systems," *IEEE/ACM Transactions on Networking*, vol. 11, no. 2, pp. 210–221, 2003.

[49] P. Viswanath, D. Tse, and R. Laroia, "Opportunistic beamforming using dumb antennas," *Information Theory, IEEE Transactions on*, vol. 48, no. 6, pp. 1277–1294, 2002.

[50] H. Shi, R. Prasad, E. Onur, and I. Niemegeers, "Fairness in wireless networks: Issues, measures and challenges," *IEEE Communications Surveys Tutorials*, vol. PP, no. 99, pp. 1–20, 2013.

[51] A. Tang, J. Wang, S. Low, and M. Chiang, "Equilibrium of heterogeneous congestion control: Existence and uniqueness," *IEEE/ACM Transactions on Networking*, vol. 15, pp. 824–837, Aug 2007.

[52] C. Saraydar, N. B. Mandayam, and D. Goodman, "Efficient power control via pricing in wireless data networks," *IEEE Transactions on Communications*, vol. 50, pp. 291–303, Feb 2002.

[53] L. Chen and J. Leneutre, "A game theoretic framework of distributed power and rate control in ieee 802.11 wlans," in *IEEE International Conference on Network Protocols (ICNP'07)*, pp. 338–339, Oct 2007.

[54] X. Wang and L. Cai, "Proportional fair scheduling in hierarchical modulation aided wireless networks," *Wireless Communications, IEEE Transactions on*, vol. 12, no. 4, pp. 1584–1593, 2013.

[55] G. Tychogiorgos, A. Gkelias, and K. K. Leung, "A new distributed optimization framework for hybrid ad-hoc networks," in *GLOBECOM Workshops*, pp. 293–297, 2011.

[56] G. Tychogiorgos, A. Gkelias, and K. K. Leung, "Towards a fair non-convex resource allocation in wireless networks," in *PIMRC*, pp. 36–40, 2011.

[57] F. Pantisano and V. Corvino, "Position-based power planning for fair resource allocation in LTE-A," in *Proceedings of the IEEE 21st International Symposium on Personal, Indoor and Mobile Radio Communications, PIMRC 2010, 26-29 September 2010, Istanbul, Turkey*, pp. 1493–1498, IEEE, 2010.

[58] L. Li, G. Wu, H. Xu, G. Y. Li, and X. Feng, "Joint power control and resource allocation for interference mitigation in lte uplink systems.," in *CISS*, pp. 1–5, IEEE, 2011.

[59] T. Harks, "Utility proportional fair bandwidth allocation: An optimization oriented approach," in *QoS-IP*, pp. 61–74, 2005.

[60] G. Tychogiorgos, A. Gkelias, and K. K. Leung, "Utility-proportional fairness in wireless networks.," in *PIMRC*, pp. 839–844, IEEE, 2012.

[61] T. Nandagopal, T.-E. Kim, X. Gao, and V. Bharghavan, "Achieving mac layer fairness in wireless packet networks," in *Proceedings of the 6th annual international conference on Mobile computing and networking*, MobiCom '00, (New York, NY, USA), pp. 87–98, ACM, 2000.

[62] C. Yang and S. Jordan, "Power and rate allocation for video conferencing in cellular networks," *EURASIP J. Wireless Comm. and Networking*, vol. 2013, p. 31, 2013.

[63] C. Yang and S. Jordan, "Power and rate allocation for video conferencing in cellular networks," in *Communication, Control, and Computing (Allerton), 2011 49th Annual Allerton Conference on*, pp. 127–134, 2011.

[64] J. Huang, Z. Li, M. Chiang, and A. Katsaggelos, "Joint source adaptation and resource allocation for multi-user wireless video streaming," *Circuits and Systems for Video Technology, IEEE Transactions on*, vol. 18, no. 5, pp. 582–595, 2008.

[65] A. Khawar, A. Abdel-Hadi, and T. C. Clancy, "Spectrum sharing between S-band radar and LTE cellular system: A spatial approach," in *2014 IEEE International Symposium on Dynamic Spectrum Access Networks: SSPARC Workshop (IEEE DySPAN 2014 - SSPARC Workshop)*, (McLean, USA), Apr. 2014.

[66] A. Khawar, A. Abdelhadi, and T. C. Clancy, "Target detection performance of spectrum sharing MIMO radars," *arXiv:1408.0540*.

[67] J. A. Mahal, A. Khawar, A. Abdelhadi, and T. C. Clancy, "Radar precoder design for spectral coexistence with coordinated multi-point (CoMP) system," *CoRR*, vol. abs/1503.04256, 2015.

[68] A. Khawar, A. Abdel-Hadi, T. C. Clancy, and R. McGwier, "Beampattern analysis for MIMO radar and telecommunication system coexistence," in *IEEE International Conference on Computing, Networking and Communications, Signal Processing for Communications Symposium (ICNC'14 - SPC)*, 2014.

[69] A. Khawar, A. Abdelhadi, and T. C. Clancy, "QPSK waveform for MIMO radar with spectrum sharing constraints," *arXiv:1407.8510*.

[70] A. Khawar, A. Abdelhadi, and T. Clancy, "A mathematical analysis of cellular interference on the performance of S-band military radar systems," in *Wireless Telecommunications Symposium*, April 2014.

[71] A. Khawar, A. Abdelhadi, and T. C. Clancy, "Channel modeling between MIMO seaborne radar and MIMO cellular system," *CoRR*, vol. abs/1504.04325, 2015.

[72] A. Khawar, A. Abdelhadi, and T. C. Clancy, "Performance analysis of coexisting radar and cellular system in LoS channel," *under submission*.

[73] A. Khawar, A. Abdel-Hadi, and T. C. Clancy, "On the impact of time-varying interference-channel on the spatial approach of spectrum sharing between S-band radar and communication system," in *IEEE Military Communications Conference (MILCOM)*, 2014.

[74] A. Khawar, A. Abdelhadi, and T. C. Clancy, "3D channel modeling between seaborne radar and cellular system," *CoRR*, vol. abs/1504.04333, 2015.

[75] H. Shajaiah, A. Khawar, A. Abdel-Hadi, and T. C. Clancy, "Resource allocation with carrier aggregation in LTE Advanced cellular system sharing spectrum with S-band radar," in *IEEE International Symposium on Dynamic Spectrum Access Networks: SSPARC Workshop (IEEE DySPAN 2014 - SSPARC Workshop)*, (McLean, USA), Apr. 2014.

[76] A. Abdelhadi, A. Khawar, and T. C. Clancy, "Optimal downlink power allocation in cellular networks," *arXiv:1405.6440*.

[77] A. Hassanien and S. Vorobyov, "Phased-mimo radar: A tradeoff between phased-array and mimo radars," *IEEE Transactions on Signal Processing*, vol. 58, pp. 3137–3151, June 2010.

[78] C. Shahriar, A. Abdelhadi, and T. C. Clancy, "Overlapped-MIMO radar waveform design for coexistence with communication systems," in *IEEE WCNC*, March 2015.

[79] A. Khawar, *Spectrum Sensing Security in Cognitive Radio networks*. PhD thesis, University of Maryland at College Park, December 2010.

[80] H. Yi, H. Hu, Y. Rui, K. Guo, and J. Zhang, "Null Space-Based Precoding Scheme for Secondary Transmission in a Cognitive Radio MIMO System Using Second-Order Statistics," in *Proc. IEEE Int. Conf. Communications ICC '09*, pp. 1–5, 2009.

[81] H. Yi, "Nullspace-based secondary joint transceiver scheme for cognitive radio MIMO networks using second-order statistics," in *IEEE International Communications Conference (ICC)*, 2010.

[82] M. Skolnik, *Radar Handbook*. McGraw-Hill Professional, 3^{rd} ed., 2008.

[83] D. Tse and P. Viswanath, *Fundamentals of Wireless Communication*. Cambridge University Press, 2005.

[84] A. Babaei, W. H. Tranter, and T. Bose, "A nullspace-based precoder with subspace expansion for radar/communications coexistence," *IEEE Global Communications Conference (GLOBECOM)*, 2013.

[85] M. Ghorbanzadeh, A. Abdelhadi, and T. C. Clancy, "A utility proportional fairness resource allocation in spectrally radar-coexistent cellular networks," in *IEEE MILCOM*, October 2014.

[86] I. Bekkerman and J. Tabrikian, "Target detection and localization using mimo radars and sonars," *IEEE Transactions on Signal Processing*, vol. 54, pp. 3873–3883, Oct 2006.

[87] S. Kay, *Fundamentals of Statistical Signal Processing: Detection Theory*. Prentice Hall, 1998.

[88] S. Ahmed, J. Thompson, Y. Petillot, and B. Mulgrew, "Unconstrained synthesis of covariance matrix for MIMO radar transmit beampattern," *Signal Processing, IEEE Transactions on*, vol. 59, pp. 3837–3849, aug. 2011.

[89] A. Hyvärinen, J. Karhunen, and E. Oja, *Independent Component Analysis*. Wiley-Interscience, 2001.

[90] J. Brown, Jr., "On the expansion of the bivariate gaussian probability density using results of nonlinear theory (corresp.)," *IEEE Transactions on Information Theory*, vol. 14, pp. 158–159, Sept. 1968.

[91] A. De Maio, S. De Nicola, A. Farina, and S. Iommelli, "Adaptive detection of a signal with angle uncertainty," *IET Radar, Sonar Navigation*, vol. 4, pp. 537–547, August 2010.

[92] D. S. Bernstein, *Matrix Mathematics: Theory, Facts, and Formulas*. Princeton University Press, second ed., 2009.

[93] R. A. Horn and C. R. Johnson, *Matrix Analysis*. Cambridge, U.K.: Cambridge University Press, 1985.

[94] A. Rabbachin, T. Quek, H. Shin, and M. Win, "Cognitive network interference," *IEEE Journal on Selected Areas in Communications*, vol. 29, no. 2, pp. 480–493, 2011.

[95] N. Beaulieu, "An extended limit theorem for correlated lognormal sums," *IEEE Transactions on Communications*, vol. 60, no. 1, pp. 23–26, 2012.

[96] R. Jantti, J. Kerttula, K. Koufos, and K. Ruttik, "Aggregate interference with FCC and ECC white space usage rules: Case study in finland," in *IEEE Symposium on New Frontiers in Dynamic Spectrum Access Networks (DySPAN)*, pp. 599–602, 2011.

[97] C. Cordeiro, K. Challapali, D. Birru, and S. S. N, "IEEE 802.22: The first worldwide wireless standard based on cognitive radios," in *IEEE Int. Symp. New Frontiers Dynamic Spectrum Access Networks (DySPAN)*, pp. 328–337, 2005.

[98] J. Di Franco and W. Rubin, *Radar Detection*. Artech House, Inc, 1980.

[99] P. Beckmann, "Rayleigh distribution and its generalizations," *Journal of Research of the National Bureau of Standards*, vol. 68D, pp. 927–932, 1964.

[100] H. Goldstein, *The origins of echo fluctuations*, vol. 13 of *M.I.T. Radiation Laboratory Series*. New York: McGraw-Hill, 1951.

[101] G. R. Heidbreder and R. L. Mitchell, "Detection probabilities for log-normally distributed signals," *IEEE Transactions on Aerospace and Electronic Systems*, vol. AES-3, no. 1, pp. 5–13, 1967.

[102] F. Berggren and S. Slimane, "A simple bound on the outage probability with lognormally distributed interferers," *IEEE Communications Letters*, vol. 8, no. 5, pp. 271–273, 2004.

[103] P. G. Vouras and T. D. Tran, "Robust transmit nulling in wideband arrays," *IEEE Trans. on Signal Processing*, vol. 62, pp. 3706–3719, July 2014.

[104] A. Goldsmith, *Wireless Communications*. Cambridge University Press, 2005.

[105] NTIA, "Effects of radar interference on LTE base station receiver performance." Online, December 2013.

[106] M. S. Longuet-Higgins, "On the statistical distribution of the heights of sea waves," *Journal of Marine Research*, vol. 11, no. 3, pp. 245–266, 1952.

[107] M. Jiang, M. Hosseinian, M.-i. Lee, and J. Stern-Berkowitz, "3D channel model extensions and characteristics study for future wireless systems," in *IEEE 24th International Symposium on Personal Indoor and Mobile Radio Communications (PIMRC)*, pp. 41–46, Sept 2013.

[108] M. A. Richards, J. A. Scheer, and W. A. Holm, eds., *Principles of Modern Radar: Basic Principles*. SciTech Publishing, 2010.

[109] W.-H. Wang, M. Palaniswami, and S. Low, "Application-oriented flow control: Fundamentals, algorithms and fairness," *IEEE/ACM Transactions on Networking*, vol. 14, no. 6, pp. 1282–1291, 2006.

[110] M. Xiao, N. Shroff, and E. Chong, "Utility-based power control in cellular wireless systems," in *IEEE INFOCOM*, vol. 1, pp. 412–421 vol.1, 2001.

[111] S. Boyd and L. Vandenberghe, *Convex Optimization*. New York, NY, USA: Cambridge University Press, 2004.